GLOBAL POSITIONING SYSTEM STUDIES OF EQUATORIAL SCINTILLATIONS

A Dissertation

Presented to the Faculty of the Graduate School

of Cornell University

in Partial Fulfillment of the Requirements for the Degree of

Doctor of Philosophy

by

Theodore Lyman Beach

May 1998

GLOBAL POSITIONING SYSTEM STUDIES OF EQUATORIAL SCINTILLATIONS

Theodore Lyman Beach, Ph.D.

Cornell University 1998

The Global Positioning System (GPS) satellites provide an extensive array of beacon signals for probing the ionosphere. Studies of ionospheric propagation at the GPS L band frequencies (1.2 and 1.6 GHz) are of great interest for proposed communications satellite systems as well as for GPS itself. This dissertation describes the development and use of a specialized GPS receiver which measures signal strength at a high data rate (50 samples per second). The instrument monitors amplitude scintillations and the present application studies scintillations produced by propagation through equatorial ionospheric irregularities, particularly equatorial spread *F*. Several observations of GPS scintillations from stations near the geomagnetic equator (primarily Ancon, Peru) during equinox seasons are presented. Studies performed include drift measurements by correlation between spaced receivers and multiple instrument studies encompassing GPS scintillations, 50 MHz radar observations (at the Jicamarca observatory) and 630 nm airglow images (from Arequipa, Peru). Observations of possible diffraction patterns generated by sharply defined differences in ionospheric electron density are also presented. Modeling suggests that the conditions required

to obtain such patterns are gradients with widths of ~ 16 meters and a change in E or F region total electron content (TEC) of about 1×10^{16} electrons per m^2, narrower and steeper than previous VHF observations of similar patterns imply. Finally, comparisons between TEC fluctuations, as measured by a dual frequency GPS receiver, and GPS amplitude scintillations are made for co-located receivers at Ancon. Such comparisons are important because of the availability of global networks of GPS receivers which can be used to study TEC fluctuations at low sample rates (typically 30 seconds per sample). Several researchers currently conduct irregularity studies using the low rate TEC data from these networks, but the relationship between measures of low frequency TEC fluctuations and L band scintillations has not been investigated. This study concludes that, for the same line of sight, TEC fluctuations and scintillations are often related and that relationship is explored here using a simple, one dimensional phase screen model.

Biographical Sketch

Ted Beach was born in Lima, Ohio on 25 November 1966. He grew up in Columbus and in rural Vinton County, Ohio, attending public schools throughout. After early release from high school in 1983 (officially graduating with his class in 1984), he attended Ohio University, obtaining a bachelor's degree in electrical engineering in 1987. He went on to complete a master's in electrical engineering there in 1988, working at the Avionics Engineering Center on Global Positioning System research. Also, that year he entered the United States Naval Reserve as an officer, teaching at the Naval Nuclear Power School in Orlando, Florida. After four years in Orlando, he returned briefly to Ohio for a stint in the tool and die industry while investigating a business opportunity with a friend. He returned to school at Cornell in the fall of 1994, having only taken a course on modern poetry at the University of Central Florida in the intervening six years.

Dedicated to Robert L. Beach, Barbara L. Beach,

Wilma W. Beach,

and to the memory of Cora Lee Staker (1905–1996)

Acknowledgements

First and foremost, I thank the members of my special committee. Prof. Paul Kintner has been an excellent chair, providing guidance, pointed wit, great enthusiasm for GPS and free rein to get some work done. Prof. Mike Kelley contributed some of his legendary enthusiasm for science and his longstanding interest in multi-instrument studies influenced many experimental campaigns. Prof. Don Farley provided guidance from his long experience with equatorial phenomena and, through his outstanding lectures, gave penetrating insight into radar processing (ambiguity functions, pulse compression, etc.), a great foundation for understanding GPS receiver operation. Prof. Dick Lovelace, a relative newcomer to the committee, provided excellent guidance through the scintillation literature from his years of experience in that field and contributed many interesting discussions.

Many other people at Cornell contributed valuable discussions or guidance. Dr. Jon Hagen of the National Astronomy and Ionosphere Center (NAIC) provided feedback for some of the RF setup and testing of the scintillation monitor. Steve Powell helped out with the selection of GPS hardware and provided invaluable guidance in such practical matters as ordering needed equipment and shipping it to the field. Steve Baker gave many UNIX and LaTeX tips plus excellent advice on international shipping of equipment. Dr. John Bonnell was always interested to discuss the project, from ba-

sic science to ideas for signal processing, and provided many thoughtful suggestions. Jason Franz also gave helpful input through innumerable casual conversations around the office on science and data analysis and, specifically, he volunteered to review the scintillation theory material for readability. Pete Schuck contributed discussions of basic plasma physics and electromagnetics. Nestor Aponte was kind enough to answer ceaseless questions about Spanish for correspondence. Thanks go to Andy Clark for sharing his voluminous library of mathematics and physics references. I appreciate talks with Dr. Clark Miller on mid-latitude irregularities. Of course, work would grind to a standstill in the Space Plasma Physics group without the tireless efforts of Sally Bird and Laurie Shelton.

Many people helped to make mid-latitude and equatorial campaigns successful. For earlier work with traveling ionospheric disturbances in Puerto Rico, my thanks go out to the following people: at Los Alamos National Laboratory, Dr. Abe Jacobson, Dr. Tom Armstrong, Bob Carlos and Hal DeHaven; at the University of Puerto Rico, Mayagüez, Prof. Mario Ierkic and Raymond Arce; at Boston University, Prof. Michael Mendillo, Marlene Colerico and Dan Nottingham; at Cornell, Dr. Wes Swartz, Mike Buckler and Levina Wong. In the equatorial work, I would like to acknowledge the following individuals: at Instituto Geofísico del Perú, Dr. Ron Woodman, Dr. Mutsumi Ishitsuka, Ing. Edmundo Norabuena, Ing. Jorge Espinoza, Ing. Rubén Villafani and Jesús Caballero; at Universidad Nacional de Tucumán, Argentina, Prof. Rudi Ezquer; at Universidade Federal do Rio Grande do Norte, Brazil, Prof. Enivaldo Bonelli; at Instituto Nacional de Pesquisas Espaciais, Brazil, Dr. Eurico de Paula; from Johns Hopkins Applied Physics Laboratory, Dr. Jim Gary; from Boston University, Joei Wroten (in addition to those listed above); from Clemson University, Prof. Dave Hysell; from the University of Massachusetts at Lowell, Dr. Jim Scali; at Cornell, Greg

Weber.

In GPS total electron content work, Dr. Steve Musman of the National Oceanic and Atmospheric Administration and Drs. Clayton Coker and Gary Bust of the Applied Research Laboratory, University of Texas Austin, were valuable resources. For help with AE-E data I thank Dr. Robin Coley of the University of Texas at Dallas and Dr. Hyosub Kil (now at Cornell). For helpful advice on GPS, I appreciate discussions with the following people at the Air Force Research Laboratory, Hanscom AFB (formerly AFGL or Geophysics Directorate, Phillips Laboratory): John A. Klobuchar (now retired), Greg Bishop and Dr. Keith Groves. Finally, I have been greatly privileged to have had helpful discussion with several whose names are intimately associated with ionospheric scintillation research: Dr. Jules Aarons, Dr. Santi Basu and Dr. Sunanda Basu.

Of course, many thanks are due my colleagues, neighbors and friends of the past four years for keeping me human and sane, whether watching movies, going to plays, eating out, discussing current events, celebrating Thanksgiving, playing softball, attending wine tastings, having barbecues, watching fireworks on the 4th of July or sailing on Cayuga Lake (alas, only once).

Cornell University and the School of Electrical Engineering provided support for my 1994–5 studies through a John McMullen fellowship. Thereafter, the Department of the Air Force supported me through the Palace Knight/Senior Knight program. My mentor and supervisor for that program was Dr. Dave Anderson, who has shown great interest in my research and in employing that expertise in my future career at the Air Force Research Laboratory. The Office of Naval Research supplied the funding for GPS research at Cornell.

This work is dedicated to my parents and to my two grandparents who lived to see

me return to graduate school at this slightly later than usual stage. Needless to say, without them I would not be here. I thank them for their love and support—tolerance and understanding, in some cases—over the years.

Table of Contents

1 Introduction **1**
- 1.1 Beginnings . . . 1
- 1.2 GPS . . . 3
- 1.3 Equatorial Irregularities and Scintillations . . . 9
- 1.4 Outline of Dissertation . . . 17

2 GPS Receivers **21**
- 2.1 Motivation . . . 21
- 2.2 GPS Signal Structure . . . 22
- 2.3 Signal Acquisition . . . 26
  - 2.3.1 Code Lock . . . 28
  - 2.3.2 Carrier Lock . . . 35
  - 2.3.3 Bit and Subframe Lock . . . 39
- 2.4 Noise and Power Estimation . . . 41
- 2.5 Other Concerns . . . 44

3 Scintillation Monitor **47**
- 3.1 Introduction . . . 47
- 3.2 Plessey Overview . . . 47
- 3.3 Software Modifications . . . 51
  - 3.3.1 Overview . . . 51
  - 3.3.2 File Format . . . 55
- 3.4 Receiver Operation . . . 61
- 3.5 Power Measurements . . . 64
- 3.6 Measurement Examples . . . 74
  - 3.6.1 Power Variations . . . 75
  - 3.6.2 Multipath . . . 77
  - 3.6.3 Noise and Gain . . . 84

4 Scintillations **89**
- 4.1 Introduction . . . 89

4.2 Scattering Example . . . 95
4.3 Phase Screen . . . 101
4.4 Model Properties . . . 107
4.4.1 Amplitude Scintillations . . . 108
4.4.2 Sinusoidal Phase Screen . . . 111
4.4.3 Phase Scintillations . . . 121
4.5 Time Variations . . . 122
4.6 Concluding Remarks . . . 130

5 Measurement Examples **131**
5.1 Campaigns . . . 131
5.2 Scintillation Index . . . 136
5.3 Time Scales . . . 144
5.4 Case Study . . . 159
5.5 Summary . . . 176

6 Edge Diffraction **178**
6.1 Background . . . 178
6.2 Observations . . . 180
6.3 Phase Screen Model . . . 190
6.4 Model Refinements . . . 202
6.5 AE-E Data . . . 215
6.6 Summary . . . 224

7 TEC Fluctuations **227**
7.1 Introduction . . . 227
7.2 TEC Measurements . . . 229
7.2.1 Available Data . . . 229
7.2.2 Measurement Techniques . . . 231
7.2.3 Fluctuation Studies . . . 234
7.3 Comparison of Fluctuation Measures . . . 238
7.4 Case Studies . . . 246
7.4.1 Data . . . 246
7.4.2 Summary . . . 253
7.5 Theoretical Relationships . . . 257
7.6 Discussion and Conclusions . . . 267

8 Conclusion **271**
8.1 Summary . . . 271
8.2 Major Results . . . 274
8.3 Future Directions . . . 275

A Receiver Program Modifications **277**
A.1 Overview 277
A.2 Power Measurements 277
A.3 Noise Channel 283
A.4 FSL Logging 286
A.5 Delayed Commands 300

B Reading FSL Files **310**
B.1 Description 310
B.2 Usage 310
B.3 Listing 313

C Phase Screen Program **322**
C.1 Description 322
C.2 Usage 323
C.3 Listing 324

D Photos of Author **326**

Bibliography **327**

List of Tables

3.1 Modified source code modules. 52
3.2 FSL file header contents. 57
3.3 FSL satellite entry contents. 60

5.1 Instruments for October 1996 campaign. 132
5.2 Instruments for April 1997 campaign. 133
5.3 Nights with Observed Scintillations at Ancon, Peru. 136

6.1 Auxiliary data for Figure 6.16 observations. 217

List of Figures

1.1 Sketch of magnetic field geometry near the dip equator. 10
1.2 Sketch of ionosphere supported by a magnetic field **B** against gravity g with a bottomside perturbation. 12
1.3 Electron density (N_e in electrons per cubic meter) measured by the AE-E satellite during orbit 21,093. 14
1.4 Range-time-intensity (RTI) plot of backscatter from equatorial spread F irregularities observed over the Jicamarca Radio Observatory on 22 October 1996. 15

2.1 Sketch of GPS signal structure. 25
2.2 Simplified block diagram of one channel of a GPS receiver. 27
2.3 Autocorrelation function R(τ) of GPS Coarse/Acquisition code. . . . 32
2.4 Block diagram of "early-late" correlation scheme. 34
2.5 Rotation of (I_n, Q_n) vector between correlator output samples. . . . 37

3.1 Structure of FSL files. 56
3.2 Normalized deviation of signal plus noise power, WBP_k, as a function of carrier to noise ratio. 66
3.3 Setups used for laboratory testing of the scintillation monitor. 67
3.4 Simulation runs for simulator setups (a) and (b). 69
3.5 Sweep frequency, or "chirp," test of scintillation monitor. 71
3.6 Spectrogram of receiver output during chirp test. 72
3.7 Amplitude of transfer function between simulated signal and scintillation monitor response. 73
3.8 Comparison of power measurements on successive days for the Ancon east receiver. 76
3.9 Comparison of power measurements on successive days for the Tucuman receiver. 78
3.10 Fine time scale comparison of power measurements on successive days for the Tucuman receiver. 79
3.11 Sketch of hypothesized diffraction of multipath signal around edge of the ground plane. 82

3.12 Noise channel measurements from Ancon east station for night of 10–11 Apr 1997. 86
3.13 Measurements from the Ancon east station for PRN 9, processed using low pass filtered noise WBP_{1s}. 87

4.1 Scattering of an incident electromagnetic wave by a single electron. . 93
4.2 Scattering geometry for single scatter example. 96
4.3 Sketch of Fresnel zone geometry 98
4.4 Phase screen model 103
4.5 Cross section of sinusoidal profile lens. 112
4.6 Development of intensity patterns below shallow and deep sinusoidal phase screens. 115
4.7 Modulation index as a function of normalized distance for deep and shallow sinusoidal phase screens. 119
4.8 Top view of ionospheric irregularities passing over spaced receivers. . 125
4.9 Ionospheric penetration point velocities at Ancon, Peru. 126
4.10 Simple ionospheric model for a non-zenith satellite. 128

5.1 Site sketch of Ancon GPS station. 134
5.2 Example wide band power autocorrelation functions. 138
5.3 Comparison of wide band power measurements with scintillation index. 141
5.4 Example screen capture from SCANFILE diagnostic program. 143
5.5 Phase screen numerical experiment to illustrate Fresnel filtering. . . . 144
5.6 Comparison of scintillation fading rates from two satellites with different east-west puncture point velocities. 146
5.7 Comparison of scintillation fading rates from two satellites with the same east-west velocity. 147
5.8 Example of spaced receiver drift measurements. 149
5.9 Comparison of spaced receiver drift measurements with scintillation period. 150
5.10 Comparison of spaced receiver drift measurements with scintillation period. 152
5.11 Comparison of spaced receiver drift measurements with scintillation period (binned by time). 154
5.12 Height of the F layer as seen by the Jicamarca digisonde for the two nights studied in the text. 156
5.13 Range-time-intensity (RTI) plot from the JULIA radar at Jicamarca for the night of 18–19 October 1996. 158
5.14 RTI plot from the JULIA radar for the night of 15–16 October 1996. 160
5.15 Map of scintillation activity from Ancon to PRN 29, 16 October 1996. 161

5.16 Scintillation map over Ancon for the period 0100–0200 UT on 16 October 1996. 163
5.17 Scintillation map over Ancon for the period 0200–0300 UT on 16 October 1996. 166
5.18 Scintillation map over Ancon for the period 0300–0400 UT on 16 October 1996. 168
5.19 Sequence of 630 nm airglow images from Arequipa on 16 October 1996. 171
5.20 Unwarped 630 nm airglow image from Arequipa for 0242 UT on 16 October 1996. 172
5.21 Unwarped 630 nm airglow image from Arequipa for 0301 UT on 16 October 1996. 174
5.22 Unwarped 630 nm airglow image from Arequipa for 0325 UT on 16 October 1996. 175

6.1 "Spectral V" in spectrogram of PRN 29 intensity data on 16 October 1996 from Ancon. 181
6.2 Concurrent spectral Vs observed on PRN 29 signal at western and eastern stations (Ancon, Peru on 16 October 1996). 183
6.3 Pair of spectral Vs observed on PRN 26 signal at western and eastern stations (Ancon, Peru on 10 April 1997). 185
6.4 Possible multipath models for spectral Vs. 187
6.5 Plot of normalized field intensity observed below the boundary at $x = 0$ between a perfectly conducting half plane (on the left) and free space. 191
6.6 The diffraction pattern observed below a phase screen with a discontinuity in phase at $x = 0$ as calculated by the one dimensional phase screen code of Chapter 4. 192
6.7 Maximum percentage fluctuation in intensity for a step phase screen as a function of $\Delta\phi$. 195
6.8 Cornu spiral used to characterize the behavior of the Fresnel functions. 196
6.9 Spectrogram of intensity for numerical example of a phase screen with a $\Delta\phi = 0.1$ rad step in the middle (otherwise uniform). 199
6.10 Slab model to illustrate how slanted ray paths through a depletion can generate a graded transition in phase. 203
6.11 Intensity patterns observed below a phase screen with a linear transition in phase at $x = 0$ of width δ, for various values of δ (expressed in grid spacings) with $\Delta\phi = \pi/2$. 206
6.12 Intensity patterns observed below a graded phase screen with a transition of width $\delta = r_F/4$ for increasing $\Delta\phi$. 208
6.13 Maximum modulation index $m_{\max}$ as a function of $\Delta\phi$ and δ for a phase screen with a finite, linear transition in phase and $r_F = 512$ wavelengths of the illuminating plane wave. 210

6.14 Intensity pattern width W over the parameter space explored in Figure 6.13 for the graded transition model. 211
6.15 Comparison of the widths of two intensity patterns for $\Delta\phi = 2.2\pi$. . 212
6.16 Examples of sharp gradients in *in situ* electron density from AE-E RPA duct mode measurements. 216
6.17 Averaged AE-E RPA duct mode density data for orbit 20,908 on 16 Aug 1979. 219
6.18 Averaged AE-E RPA duct mode density data for orbit 23,834 on 22 Feb 1980. 219
6.19 Equivalent phase screen and calculated intensity pattern for 22.13 MLT on 79228 (orbit 20,908). 221
6.20 Equivalent phase screen and calculated intensity pattern for 20.26 MLT on 80053 (orbit 23,834). 223

7.1 Simultaneous amplitude and total electron content (TEC) observations from Ancon for PRN 26, 10–11 April 1997. 239
7.2 Simultaneous amplitude and total electron content (TEC) observations from Ancon for PRN 5, 10–11 April 1997. 241
7.3 Comparative measures of TEC fluctuation strength from PRN 26 data at Ancon, 10–11 April 1997. 243
7.4 Comparative measures of TEC fluctuation strength from PRN 5 data at Ancon, 10–11 April 1997. 245
7.5 Scintillation map from Ancon, 09 April 1997. 247
7.6 Comparison of scintillation index m and TEC fluctuation measures at Ancon for 09 April 1997 UT. 249
7.7 Comparison of scintillation index m and TEC fluctuation measures at Ancon for 11 April 1997 UT. 250
7.8 Comparison of scintillation index m and TEC fluctuation measures at Ancon for 17 April 1997 UT. 252
7.9 Observations of changes in drifting irregularity structure on 09 April 1997. 255
7.10 Observations of change in drifting irregularity structure on 17 April 1997. 256
7.11 Sample TEC fluctuation power spectra at Ancon, Peru from April 1997 campaign. 259
7.12 Ratios of scintillation index to TEC variance (σ_{TEC}) and rate of TEC index (ROTI) for various outer scale (ℓ_0) and power law index (p) values. 265
7.13 Illustration of the insensitivity of m/ROTI versus power law index p to the perpendicular ionospheric drift velocity V. 266

Chapter 1

Introduction

We shall not cease from exploration
And the end of all our exploring
Will be to arrive where we started
And know the place for the first time.

—T. S. Eliot, *Little Gidding*, ll. 239–42

Where is the horse that doth untread again
His tedious measures with the unbated fire
That he did pace them first? All things that are,
Are with more spirit chased than enjoy'd.

—W. Shakespeare, *The Merchant of Venice*, Act II, Scene VI

1.1 Beginnings

It is an irony. We live in an age which has all but dismissed space flight as routine or relegated it to the status of a luxury, a symbol of international prestige. We had, after all, chased the moon and caught it. Yet now space based applications are poised to enter our daily lives as never before. No, manufacturing in space remains infeasible and unnecessary. We do not yet mine asteroids for scarce resources. Huge solar

power arrays do not loom overhead, beaming power to the surface. Nothing truly revolutionary came about. What transpired was a quiet, far more logical progression, a progression as sensible in hindsight as the transition from rail to truck shipment with the construction of the Interstates.

What happened? Computers came down off their lofty pedestals and into the shopping malls. Television saturated our lives and multiplied in its forms. People suddenly discovered that they needed mobile phones, pagers and fax machines, services that had been available to some extent for decades. Competition increased in the telephone industry to the point where it is now virtually impossible to answer the phone at dinner time without hearing yet another sales pitch by a long distance carrier. The Internet exploded after years of failed attempts by proprietary on line services to survive. In short, the whole information-communications-electronics-computer "revolution" happened.

As a result, space based applications are newly ascendant. They range from conventional satellite television services to the cutting edge of worldwide digital messaging and glorified cellular telephony. Countries now sell old spy satellite imagery for commercial use. And satellite navigation systems, such as the Global Positioning System (GPS) and the Russian GLONASS, have reached fruition after years of planning and development.

It is with GPS that this dissertation concerns itself, but we should not forget the other systems for the moment. All of these systems provide an unprecedented amount of interaction with the earth's ionosphere on a daily, global basis, primarily through transionospheric radio wave propagation. As we head into the next solar maximum shortly after the year 2000, these new systems face the challenges of day to day ionospheric variability, to be enhanced by greater ionospheric electron densities

and increased solar activity.

The consequences of increased interaction with the ionosphere will be twofold. On one hand, these systems may suffer in their ionospheric interactions. As such, immediate practical significance attaches itself to up to date knowledge of ionospheric climatology and its current "weather patterns." On the other hand, the existence of these systems provides for unparalleled probing of the ionosphere under a host of different conditions. Already, for example, many researchers use GPS measurements to study the ionosphere on a routine basis [*Mannucci et al.*, 1993; *Aarons et al.*, 1997; *Aarons*, 1997; *Pi et al.*, 1997]. Of course, ground based measurements from satellite beacons can be limited and often require care in interpretation [*Evans*, 1977]. Nevertheless, given increased satellite availability, the potential for global or regional coverage from relatively inexpensive arrays of receivers is excellent.

1.2 GPS

The development of the Global Positioning System dates from the early 1970s. The United States Department of Defense conceived the system as a worldwide, continuously available navigation aid for its ships, troops and aircraft. Furthermore, its accuracy was to be unprecedented for a worldwide system, on the order of tens of meters or better for authorized users. The military launched the first test satellite in 1978. Then the Challenger disaster in 1986, and the coincidental failure of several unmanned launch vehicles in the same time period, delayed the launch of operational satellites until 1989. From 1989 to 1993, new GPS satellite launches proceeded on a regular basis. In 1994, the Defense Department declared GPS to be a fully operational navigation system. (See *Parkinson* [1996] for a more detailed history of the

program.)

Conceptually, GPS is simple. Each satellite continuously broadcasts a ranging signal. The receiver estimates its distance from the various satellites by straightforward time of flight calculations. From range measurements and calculated positions of the satellites, the receiver can estimate its position. In the simplest picture, a receiver requires ranges from three separate satellites to calculate its three dimensional position. Because the user's clock usually does not keep GPS system time, however, receivers typically need another satellite's ranging measurement to calculate the clock offset (the difference between the user's clock and GPS system time).

In order to achieve all this, the Defense Department maintains a constellation of 24 GPS satellites in 12 hour ($\sim 20,000$ km altitude), 55° inclination orbits. Most of the time, users can see the minimum four satellites required for navigation from any point on earth. Under unusual circumstances, particularly with extra satellites in orbit as "active spares," we have observed as many as 12 at one time. Each satellite contains an atomic frequency standard to generate the precise timing signals required (10 ns of timing error translates into 3 m of ranging error and long term clock stability is very important). Several ground stations monitor the status of the satellites, including their orbits, and compare the satellite clock settings with a reference bank of atomic clocks. These ground stations then uplink values of each satellite's ephemeris, clock offset and frequency drift to be rebroadcast by the satellite to its users.

The satellites broadcast on L band carrier frequencies. The higher frequency is called L1 and is 1.57542 GHz. The lower, L2, is 1.2276 GHz. Broadcasting on two frequencies allows users to estimate and correct for the ionosphere's group delay by the dispersion of the two signals. All satellites share the same two frequencies by using a code division multiple access (CDMA) spread spectrum scheme. Unique

pseudorandom noise (PRN) codes multiply each satellite's carrier signals to identify the satellites and to allow them to share the same radio spectrum. In fact, the codes provide the most basic timing information to the receiver concerning the time of transmission. From the clock difference Δt between transmission and reception, the receiver estimates the range as $c\Delta t$ (called a "pseudorange" since this range estimate contains effects of the receiver and satellite clock offsets, as well as other errors).

Each satellite broadcasts two types of codes. The coarse/acquisition (C/A) code is a short code designed to enable receivers to acquire the satellite signal relatively quickly. It repeats every millisecond and is 1023 "chips" (PRN code bits) long. The precise (P) code is a much longer code that repeats once a week and has a chipping rate ten times that of the C/A code. The faster chipping rate provides higher accuracy in ranging measurements. The L1 signal shares the C/A code with the P code in quadrature while the L2 signal contains only the P code.

Of course, because GPS is a Department of Defense system, national security concerns come into play. The military reserves to itself the most accurate positioning services and keeps some of the PRN codes classified so that adversaries cannot mimic GPS signals as a form of electronic warfare. Selective Availability (SA) is the name of the policy wherein the Defense Department denies full navigation accuracy to non-authorized users by broadcasting ephemerides containing deliberate, small errors and by other means. Under this policy, ranging accuracy drops from 6 m to 20 m for the so called standard positioning service (SPS), with an attendant decrease in positioning accuracy [*Parkinson*, 1996]. Another policy, Anti-Spoofing (AS), substitutes classified PRN codes ("Y codes") for the P codes that each satellite broadcasts. Effectively, AS denies non-authorized users access to both GPS frequencies because each satellite broadcasts its C/A code only on the L1 frequency. Clever signal processing can

recover some information on L2 but at the cost of decreased receiver performance [*Hofmann-Wellenhof et al.*, 1994].

Cost also makes dual frequency operation impractical for any uses except those that specifically require it. Civil dual frequency receivers, the kind that use special processing to recover information from L2, currently run US$14,000 and up. Inexpensive single frequency receivers can be purchased for under US$200 while higher end, L1 only receivers sell for several thousand dollars. Although market factors partially determine this price differential, one key difference is receiver complexity. Dual frequency receivers require faster signal processing (by an order of magnitude) and have more radio frequency (RF) channels, in addition to being produced in smaller quantities; therefore, they are more expensive.

The ionosphere affects GPS receivers by introducing group delays into the GPS signals. Free electrons modify the refractive index in the ionosphere and slow the propagation of the ranging signals. The amount of delay depends on the total electron content (TEC) of the ionosphere, the integrated electron density along the ray path (essentially the line of sight) between the receiver and the satellite. For example, if the TEC is 2×10^{17} electrons per m^2, the group delay at L1 is about 10 ns which translates into a ranging error of 3 m. For comparison, three meters is half the nominal ranging accuracy of the standard positioning service when SA is off, and this TEC value is not atypical.

Another important ionospheric effect stems from the phase advance that the ionosphere imparts to signals. The phase advance is also proportional to TEC so that 1.17×10^{16} electrons per m^2 give 2π radians, or one cycle, of phase advance at the L1 frequency. Phase advance can directly affect positioning estimates in GPS receivers which utilize carrier phase measurements. Moreover, changes in phase can lead to

variations in signal amplitude due to interference effects. When the ionosphere contains electron density irregularities of a certain scale, roughly $\sqrt{2\lambda z}$ (where λ is the radio wavelength and z is the distance to the centroid of electron density from the receiver), the radio waves scattering from these irregularities interfere to produce a diffraction pattern on the ground. Growth or decay of irregularities, irregularity drift and satellite motion cause the signal power observed by a stationary receiver to fluctuate with time. These fluctuations are called amplitude scintillations.

The topic of this dissertation concerns observations of amplitude scintillations by GPS in regions near the geomagnetic equator. The investigation of scintillations on GPS signals is important from a practical standpoint because of concern over the reliability of the system in adverse conditions. If a GPS satellite's signal strength fades to a low enough level, and for a long enough period, a receiver may lose lock on that signal or have difficulty acquiring the satellite in the first place. One missing satellite signal could affect navigation accuracy; several missing signals could render navigation impossible. The assessment of receiver performance under scintillation conditions is beyond the scope of this dissertation, however. Primarily, we develop the means to monitor amplitude scintillations using a specially modified GPS receiver and demonstrate the ability of that receiver to monitor the local ionospheric environment.

We have developed a GPS scintillation monitor to fulfill a need that commercially available receivers do not meet. Specifically, many commercial receivers do not provide indicators of signal strength that are suitable for scientific use. The given indicators are often too crude ("signal present or absent") or they are stated in terms of manufacturer's arbitrary units. Furthermore, most available GPS receivers do not provide high time resolution measurements of signal strength from the various satellites. Quantitative measurements of GPS amplitude scintillations require known, well

defined indicators of signal strength; detailed studies of scintillation power spectra need high sampling rates.

In other quarters, the Air Force, through the Air Force Research Laboratory (AFRL, formerly Phillips Laboratory, Geophysics Directorate), has contracted for the development of a similar receiver [*Van Dierendonck et al.*, 1993; *Klobuchar et al.*, 1994]. These receivers will have higher quality clocks than the current incarnation of the Cornell scintillation monitor, so they are better suited to monitoring L1 phase scintillations (fluctuations in phase due to ionospheric irregularities). Also, they have been designed for remote operation via the Internet or phone lines. The AFRL receivers are not yet generally available, however.

Three main criteria guided the design of the Cornell scintillation monitor. First and foremost, the receiver was to take signal strength data, based on the output of the C/A code correlators, at a 50 Hz rate. Second, the receiver was to be designed to allow drift measurements of scintillations between spaced receivers. Third, the receiver was to have the capability (at least a rudimentary one) of automatic operation, so that it could stop and restart data logging during weekends or other periods when the station might be unattended.

In order to satisfy these criteria, we used a GPS receiver development system sold by GEC Plessey Semiconductors under the trade name "GPS Builder-2." The philosophy of the Plessey development system and its associated chip set are unique among GPS receivers on the market. Rather than keeping the low level details of receiver operation locked up in custom microcontrollers integral to the digital signal processing chip, the Plessey system supplies two very fundamental building blocks: the RF front end and a correlator chip (correlates the incoming C/A codes with locally generated replicas). A standard, general purpose microprocessor provides

the remainder of the data processing, including such tasks as maintaining lock on the satellite signals, interpreting the data messages broadcast by the satellites and computing navigation solutions.

In the case of the Plessey GPS development system, the processor is an 80486 or Pentium in a standard personal computer. The receiver hardware goes on a standard 16 bit card that plugs into the PC bus. Receiver software is written in C and assembly language, with the source code provided as part of the development package. Consequently, modifying the receiver to take high data rate power measurements is relatively simple. Using a PC also allows for data logging to the computer's hard drive and archiving using standard PC peripherals and software. Following about eight months of software development, and an early field trial in April 1996, the scintillation monitor was ready for an experimental campaign in October 1996.

1.3 Equatorial Irregularities and Scintillations

The purpose for developing the scintillation monitor was the study of L band scintillations in equatorial regions. The equatorial ionosphere is one of two areas on the globe with significant L band scintillation activity, the other being high latitudes near the aurora [*Basu et al.*, 1988]. From a practical standpoint, scintillations near the magnetic equator are perhaps more significant than high latitude scintillations. First, human population concentrates itself more in equatorial regions than near the poles. Consequently, people are more likely to use GPS or communications satellites in equatorial regions. Also, the equatorial anomalies (regions of high ionospheric plasma density several (about ± 15) degrees north and south of the geomagnetic dip equator) produce the largest L band scintillations observed, with fading by as much

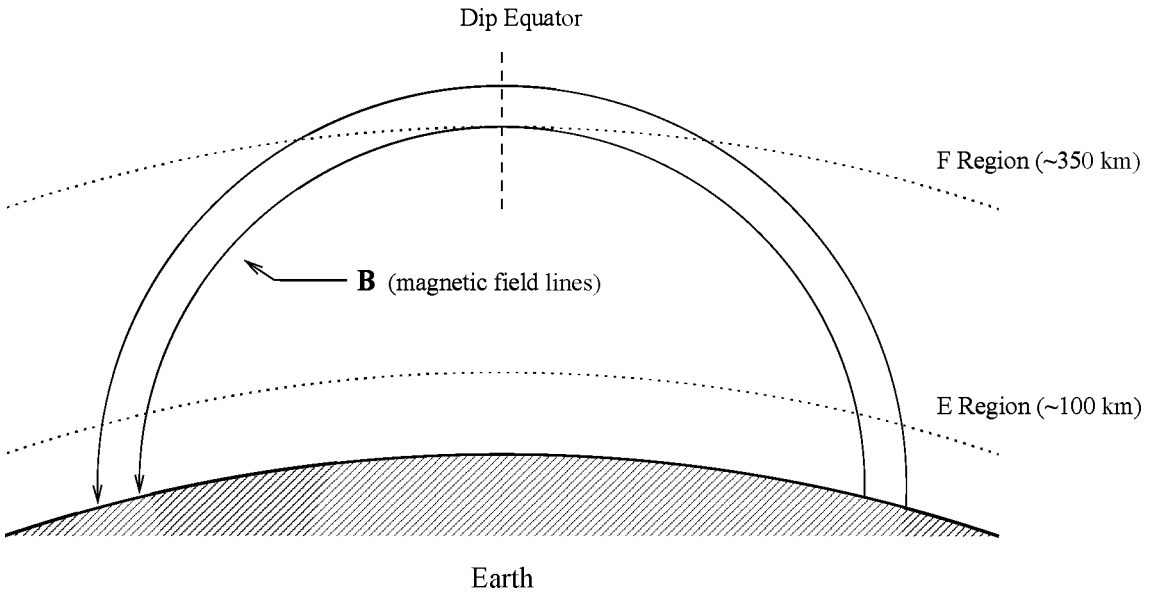

Figure 1.1: Sketch of magnetic field geometry near the dip equator. (Not to scale.)

as 20 dB during solar maximum periods [*Aarons*, 1982; *Basu et al.*, 1988].

Irregularities develop in the equatorial ionosphere through plasma instabilities fostered by the unique horizontal orientation of the magnetic field lines. It is important to note that throughout this dissertation "equator" and "equatorial" refer to the dip equator, the place where the earth's magnetic field lines are parallel to its surface (Figure 1.1). The dip equator lies roughly 12° south of the geographic equator on the western coast of South America, for example.

At the equator, the magnetic field supports the charged particles in the ionosphere against gravity. Electrons and ions that attempt to move vertically, perpendicular to the magnetic field lines, are guided into orbits around the field lines. (They are still free to move north and south along the field lines, however.) The equilibrium is unstable, though, in the manner of a layer of dense fluid sitting on less dense fluid. If any perturbation of the boundary layer occurs, the perturbation grows and the lighter fluid wells up through the heavier fluid (see *Kelley* [1989] for pictures), with

the final state that the more dense fluid is on the bottom and the less dense fluid is on top.

In the case of the ionosphere, the more dense fluid consists of the plasma, the collection of charged particles in approximate electrical neutrality (i.e., in any small volume the number density of singly charged ions and electrons is nearly identical). The lighter fluid is the absence of charged particles below the ionosphere or "vacuum." (Although there are still neutral gas particles at these altitudes, the magnetic field does not affect their motion and they do not play a direct role in the instability.) So, when the instability occurs, regions of low plasma density ("depletions") well upward into the plasma.

Actually, the situation is somewhat more complicated. When the earth's magnetic field supports the ionospheric plasma against gravity, a current flows along the bottom of the ionosphere, perpendicular to both the gravitational force and the magnetic field direction (Figure 1.2). If the bottom of the ionosphere is vertically perturbed, the perturbation tends to block the current flow and charge builds up on either side. The resulting electric fields, combined with the background magnetic field, tend to drive the plasma further upward where it initially went up and further downward where it initially went down.

Two factors offset this process of instability generation during the day. First, illumination by solar extreme ultraviolet (EUV) radiation produces an ionosphere with a relatively gradual dropoff in electron density toward the bottom (toward the E region, around 100 km in altitude). Second, since charges can move freely along the magnetic field lines, they act as electrical conductors, conducting any perpendicular electric field generated at the equator down into the E region. There, at lower altitudes, the number density of background neutral gas particles is higher. Charged

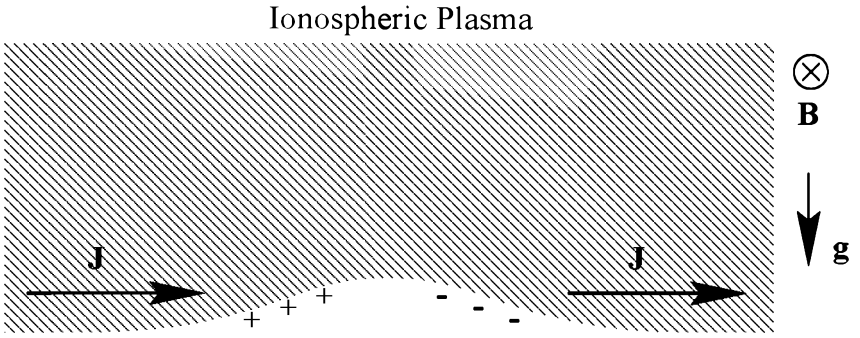

Figure 1.2: Sketch of ionosphere supported by a magnetic field **B** against gravity **g** with a bottomside perturbation. The perturbation disrupts current flow **J** through the bottom of the ionosphere and causes polarization charges to build up on either side of the perturbation. The resulting electric field acts to increase the ionospheric displacement.

particles collide with these neutral particles, disrupting the normal charged particle orbits about the field lines and allowing them to move perpendicularly in response to electric fields. In other words, the perpendicular (Pedersen) conductivity of the E region is higher during the day and tends to "short out" any instability-driving electric fields developed at the dip equator.

Just after sunset, the situation drastically changes. Without any direct solar illumination to generate ionization, the E region recombines. The higher altitude F region persists, however, because there the predominant species of ion is singly charged atomic oxygen, O^+. Free electrons recombine slowly with atomic ion species because of the difficulty of matching velocities between randomly moving particles so that momentum and energy are conserved in the recombination process. (The same is not true at lower altitudes, where diatomic molecular ion species dominate, since the extra atom involved in the recombination process can "take up the slack," so to speak, if the molecule dissociates, for example.)

At any rate, the disappearance of the E region leads to two profound consequences

for generating the instability outlined above: (1) the vertical gradient in electron density at the bottomside of the F region can become quite sharp, and (2) E region conductivity no longer "shorts out" the instability electric fields. As a result, if no other mitigating factors exist, the instability takes off and depleted regions well up into the ionosphere.

Through nonlinear processes (reviewed by *Kelley* [1989]), these depletions can reach significant altitudes, above the peak in electron density in the F region. Figure 1.3 illustrates *in situ* satellite measurements of electron density showing depletions, taken at 445 km altitude as the satellite moved from west to east in its equatorial orbit. Furthermore, many subsidiary instabilities develop at smaller scales than the original depletion size, generating more detailed structuring of the plasma. For example, electron density irregularities formed in this instability process cause radar returns at 50 MHz at the Jicamarca Radio Observatory near Lima, Peru (Figure 1.4). These radar returns indicate the presence of fluctuations in electron density at half the radio wavelength (i.e., at the 3 m scale).

We should note that Figure 1.4 represents a spectacular case and that the irregularities are not always so dramatically structured. Historically, equatorial irregularities of this nature are termed equatorial spread F, although the term strictly refers to the effects of the irregularities on ionosonde plots. (More specifically, since the irregularity structure here appears at altitudes above the peak of F region electron density, it is "topside" equatorial spread F.) The literature refers to the towering structures observed by radar as plumes. Note that the the ionosphere drifts from west to east through the radar beam after sunset, so that the interesting structure at later times represents the westward portion of the plumes. It is generally the case that the westward portion of the plumes is more structured than the eastward edge

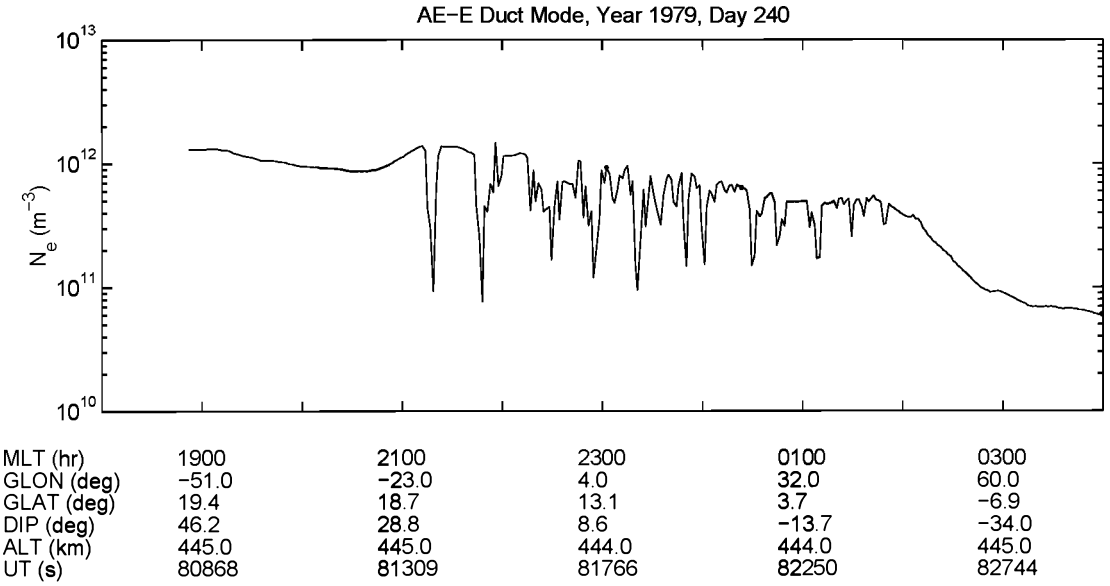

Figure 1.3: Electron density (N_e in electrons per cubic meter) measured by the AE-E satellite during orbit 21,093. Several electron density depletions are evident between 2100 and 0100 magnetic local time (MLT). (Data courtesy H. Kil, UT Dallas.)

[*Woodman and La Hoz*, 1976; *Kelley*, 1989].

Ionospheric structure in equatorial spread F encompasses a wide range of scales, from the several hundred kilometer widths and heights of the plumes to 3 m. That range includes the several hundred meter scale size required to generate scintillations at the GPS L1 frequency. As the GPS signals propagate through the irregular ionospheric density, the different parts of the wave fronts acquire different phasings. The result is a complex interference pattern by the time the signal reaches the ground. Furthermore, the pattern varies with time as the ionospheric irregularities drift, develop or decay. The effect is similar to the twinkling of stars caused by the passage of their light through turbulence in the lower atmosphere or the shimmering seen above hot asphalt on a sunny summer day.

In fact, scintillations (on several frequency bands) are one primary indicator of

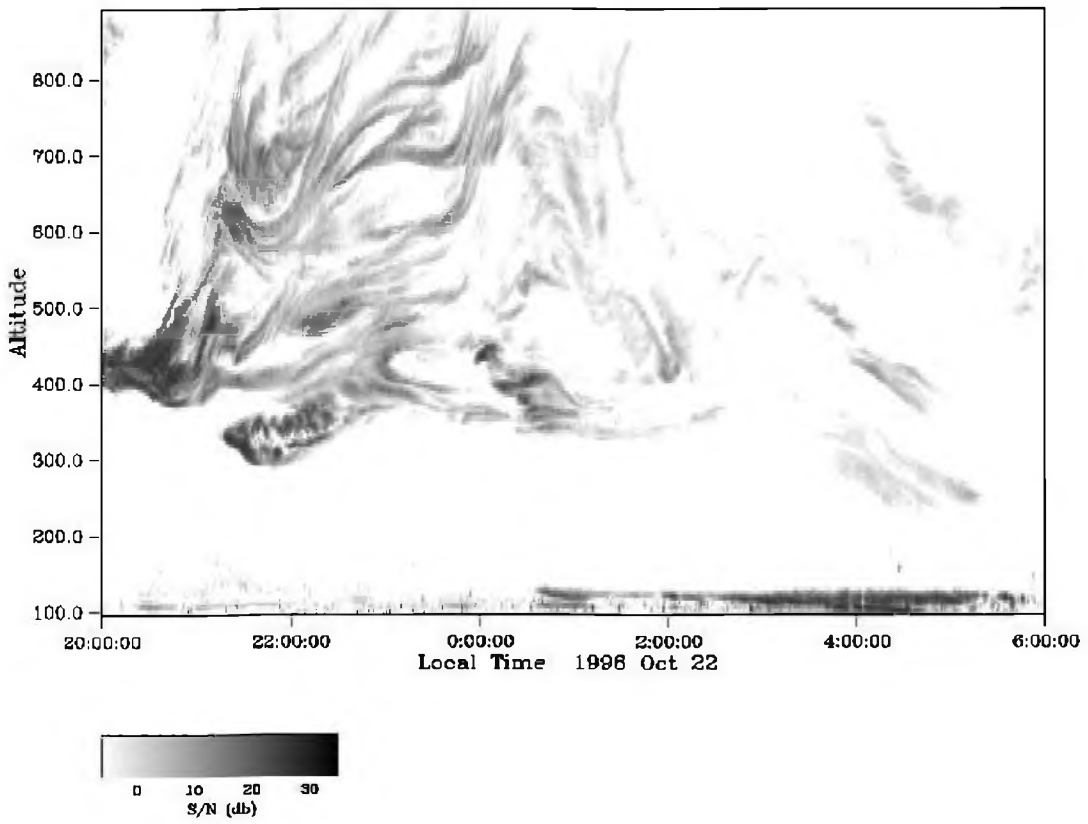

Figure 1.4: Range-time-intensity (RTI) plot of backscatter from equatorial spread F irregularities observed over the Jicamarca Radio Observatory on 22 October 1996. The plot shows the echos returned from 3 m irregularities at altitudes up to 900 km for each time. The grayscale indicates the strength of the echo returns. (Courtesy D. Hysell)

the formation of equatorial ionospheric irregularities in areas not fortunate enough to have ionospheric radar observatories. Scintillation observations from several stations worldwide provide insight into diurnal, seasonal and solar cycle dependence of equatorial irregularities. In general, scintillations appear to peak in strength and occurrence around 2100 local time, around the equinoxes and during solar maximum periods [*Aarons*, 1993]. Still, there exists much day to day and station to station variability in equatorial scintillation occurrence that remains the subject of ongoing, active research.

There is also an important way in which scintillation observations do not accurately track the state of ionospheric irregularities. Scintillations depend upon the accumulated effect of passage through several electron density irregularities to form the phase variations required for their generation. As such, they depend on the total electron content (TEC) along the signal path and the deviations in electron density (ΔN_e) govern the magnitude of TEC fluctuations. On the other hand, irregularity strength is usually characterized by the relative fluctuation strength $\Delta N_e/N_e$, where N_e is the background local electron density. Consequently, irregularities with relatively strong $\Delta N_e/N_e$ may not provide significant levels of TEC fluctuations, and hence scintillation activity, if N_e is low. This effect predisposes equatorial scintillations to be more prominent during solar maximum (when ionospheric electron densities are greatest) and near the equatorial anomaly regions (where electron densities are greatest, $\sim 15^\circ$ north and south of the dip equator), even if the average $\Delta N_e/N_e$ remains constant.

Another factor comes into play as the frequency of scintillation observations increases. The effect of TEC on the signal's phase decreases as the square of the frequency. So scintillation effects at the GPS L1 frequency, compared to, say, VHF

observations at 250 MHz, are far weaker for a given set of ionospheric conditions. Put the other way around, the attainment of strong scintillations on L1 requires relatively high $\Delta N_e/N_e$ and N_e values and a relatively thick layer of irregularities. Thus, if the Jicamarca radar observes a thin layer of irregularities on the bottomside of the F region, these irregularities probably will not produce L band scintillations, even though fluctuation scales of hundreds of meters and smaller are present. Meanwhile, VHF scintillations may last throughout the night.

Armed with this knowledge of scintillation morphology, we established our field campaigns to guarantee a good chance of capturing scintillation activity with the new GPS scintillation monitors during the present solar minimum. The campaigns took place around equinox. One station (Tucuman, Argentina) was established near the southern equatorial anomaly; the other (Ancon, Peru) was located near the dip equator to take advantage of the nearby Jicamarca radar. We collected data throughout the nights during the campaign period, typically from 1600 to 0600 in local time. As implied above, comparison of the Ancon GPS scintillation data with radar plots (when available) shows that L band scintillations developed overhead only when plumes occurred (i.e., when the layer of irregularities was comparatively thick). The next section outlines other major thrusts of the research.

1.4 Outline of Dissertation

This dissertation divides roughly into two parts. The first part concerns the design of GPS receivers, particularly the design of the Cornell GPS scintillation monitor. Then, following an introductory chapter on the propagation physics of scintillations, the remainder of dissertation discusses observations of scintillations using the GPS

scintillation monitor. These observations illustrate some of the unique potential of GPS as an ionospheric research tool and provide some early, important results.

Chapter 2 describes the basic RF electronics aspects of GPS receivers. Specifically, it outlines the process by which a receiver acquires and tracks the GPS satellite signals. The motivation for this discussion is twofold. First, it reinforces the idea that GPS is a code division multiple access (CDMA) system, emphasizing some of the complexity of "tuning in" and measuring signal strength from each of the satellites in view. Second, the discussion provides a reference for terminology and concepts to be used throughout the remainder of the dissertation.

Chapter 3 builds on the concepts developed in Chapter 2 to sketch the process of designing and testing the Cornell scintillation monitor. It presents an overview of the Plessey development system, from which the scintillation monitor was derived, then summarizes the modifications performed. The key modification is the addition of the capability to log power data at a high rate, so this chapter describes the power measurements in detail, including tests of the receiver with a GPS signal simulator. Various factors which affect signal strength are discussed, with particular emphasis on distinguishing multipath effects from scintillations.

Chapter 4 provides the transition from the design of the scintillation monitor to its use. It describes the physics of scintillations, starting with the propagation of electromagnetic waves through media having irregular variations in refractive index. Quickly moving from the general case, where the important concept of the Fresnel radius (r_F) is developed as a fundamental unit of irregularity scale transverse to the direction of wave propagation, the remainder of the chapter devotes itself to discussion of the phase screen model of scintillation generation. The phase screen model was a very early means to characterize the effects of ionospheric irregularities

on radio wave propagation [*Booker et al.*, 1950; *Hewish*, 1951], and remains a useful tool. Discussion of the phase screen model emphasizes the development of amplitude scintillations, fluctuations in signal intensity as the wave front propagates away from the screen. Chapters 6 and 7 rely extensively on the properties of the phase screen model as developed in Chapter 4.

Chapter 5 goes from theory to practice, summarizing observations using Cornell scintillation monitors from two experimental campaigns in equatorial regions. These campaigns took place in October 1996 and in April 1997 in South America. Chapter 5 discusses the data available from these campaigns and some basic data processing techniques. Two key ideas presented are the computation of the scintillation (or modulation) index, the normalized root-mean-square fluctuation of signal power over time, and the process of correlating power fluctuations between spaced receivers to obtain drift measurements. Other instruments were also trained on the ionosphere during these time periods, especially in October 1996 when a MISETA (Multi-Instrumented Study of Equatorial Thermospheric Aeronomy) campaign occurred. Chapter 5 includes a detailed case study of the scintillations which occurred on the night of 15–16 October 1996, with comparisons to 50 MHz radar observations at the Jicamarca Radio Observatory near Lima, Peru and to 630 nm wavelength all sky airglow images from Arequipa, Peru. This case study highlights the advantages of having data from several GPS lines of sight at one time.

Chapter 6 discusses particular observations of unusual patterns found in spectrograms of the signal power data. These observations, termed "spectral Vs" because of their signature shape in spectrograms, appear to be the result of edge diffraction from sharp electron density gradients in the ionosphere, from somewhere between 95 km altitude and the F peak. Interpreted as such, they resemble VHF observations

of so called quasiperiodic scintillations [*Hajkowicz*, 1977]. The chapter investigates two diffraction models using a phase screen, an instantaneous step in phase and a linear transition in phase of finite width. The latter model is physically more realistic because it requires far less drastic gradients in ionospheric electron density and, importantly, it provides stronger diffraction patterns which are more likely to be noticed. Finally, *in situ* electron density data from the AE-E satellite are examined for evidence of steep enough gradients to form spectral Vs.

Chapter 7 tackles an important practical question: what is the relationship between amplitude scintillations and low rate total electron content (TEC) data? Most ground based GPS research analyzes the latter, since it is the most widely available [*Aarons et al.*, 1996; *Musman et al.*, 1997; *Pi et al.*, 1997]; only recently have specialized GPS receivers been developed to record high rate amplitude scintillation data. For the comparison, we use data from a dual frequency GPS receiver co-located with the scintillation monitors at Ancon, Peru during the April 1997 campaign. In addition to the comparison of TEC fluctuations and scintillation data for the nights which had GPS scintillations, the chapter presents a theoretical discussion of the relationship between scintillations and measures of TEC fluctuation strength, based on a one dimensional phase screen model.

Chapter 8 summarizes the major results of the dissertation and gives suggestions for future research. Several appendices are provided which contain program listings. Appendix A contains details of the conversion of the original GPS receiver software into the present scintillation monitor system. Appendix B sketches some of the details involved in reading the fast scintillation logging (FSL) binary files produced by the scintillation monitor. Appendix C provides a listing of the one dimensional phase screen code used throughout the dissertation.

Chapter 2

GPS Receivers

2.1 Motivation

This chapter describes the rudiments of GPS signal reception with an eye toward the background needed to understand the details of the Cornell scintillation monitor. Although many elements of traditional radio engineering appear throughout the following analysis, two factors make this in depth treatment helpful. First, GPS uses spread spectrum, code division multiple access signals rather than conventionally modulated carriers. Consequently, the measurable outputs, including signal strength, result from the correlation of a received pseudorandom noise code with a locally generated code, not from simple detection. Second, a GPS receiver gains timing information from the particular structure of the GPS signal, on scales ranging from tens of nanoseconds to seconds. Data collection in the scintillation monitor depends on this timing for the organization of the data samples.

The discussion in this chapter will emphasize several major points concerning GPS receiver operation from a radio engineering standpoint. Foremost among its

goals is to describe the correlation process and the measurements it yields, the I_n and Q_n samples. The discussion includes details on how the scintillation monitor receiver computes two quantities which it records in its data records: pseudorange and "wide band power." Additionally, this chapter describes how the receiver synchronizes timing in a channel to the incoming GPS signal that the channel "tunes in." Such synchronization is important for making irregularity drift measurements using spaced receivers.

2.2 GPS Signal Structure

The primary purpose of the Global Positioning System is radio navigation. As such, its signals must convey timing information, satellite ephemeris and system status to its intended users. Additionally, GPS is a spread spectrum system; all signals share exactly the same portion of the radio spectrum. In order to satisfy these requirements, the GPS signals are relatively complicated, incorporating several layers of structure.

The carriers, L1 at 1.57542 GHz and L2 at 1.2276 GHz, form the backbone of the signals. Pseudorandom noise codes modulate the carriers, allowing receivers to identify the broadcasting satellites and also providing the most basic level of timing information. Each satellite transmits two types of pseudorandom noise codes, codes unique to that satellite: the Coarse/Acquisition (C/A) code and the Precise (P) code. The P code has a higher bit, or chipping, rate, 10.23 MBps, than the 1.023 MBps of the C/A code, allowing for more precise measurement of signal timing. It also has a much longer period before the sequence repeats: one week compared to the 1 ms code period of the C/A code. Each satellite broadcasts its P code on both the L1 and L2 signals. The C/A code only appears on the L1 frequency, sharing it with the

P code in quadrature.

Unfortunately for civilian users, the United States Department of Defense encrypts or scrambles the publicly known P codes into "Y codes" under its program called "Anti-Spoofing." Since the Y codes are only available to authorized users, this policy effectively denies civilian users access to the L2 frequency, as well as to the more precise timing ability of the P code. Civil dual frequency receivers may, however, use clever processing techniques to recover some information from the L2 signal when Anti-Spoofing is on. For example, since the Y code is the same on both GPS frequencies, a receiver can cross correlate between the two signals, measuring the time delay between the channels to estimate relative ionospheric dispersion. Nonetheless, such receivers remain substantially more expensive than single frequency receivers and require higher signal to noise ratios to operate than for normal P code reception when Anti-Spoofing is off. The book by *Hofmann-Wellenhof et al.* [1994] contains a brief survey of dual frequency techniques available to non-authorized users.

Concentrating on the Coarse/Acquisition code only, the L1 signal broadcast from satellite n may be expressed roughly in the following form:

$$s_n(t) = A_n C_n(t) \cos(\omega_1 t), \tag{2.1}$$

where A_n is the signal amplitude, $C_n(t)$ is the C/A code bit (± 1) and ω_1 is the angular frequency corresponding to 1.57542 GHz. Normal practice refers to each satellite by the number of the pseudorandom noise (PRN) code assigned to it, out of a set of 32 available codes. Thus, if the builders assign code number 23 to a satellite, for example, one refers to the satellite as PRN 23 or SV 23 (for "Space Vehicle"). The latter usage, although common, is inaccurate and somewhat confusing since the satellites are assigned separate SVNs (space vehicle numbers), which often correspond to the PRN, but not always (see satellite table in [*Parkinson*, 1996]). This dissertation

will adhere to the standard of labeling GPS satellites with "PRN" rather than "SV," unless quoting the work of others.

Returning to the characteristics of the satellite signals, the C/A code repeats itself each 1 ms, as previously mentioned. Since the C/A chipping rate is 1.023 MBps, each code sequence is 1023 bits long. The shortness of the code implies that if a receiver is locked to the C/A code, it only knows the time of broadcast modulo 1 ms. On the other hand, the propagation time from the GPS satellites (in 26,600 km radius orbits) to the ground is of the order of hundreds of milliseconds. Alternatively, even 1 ms of timing ambiguity leads to ranging errors of 300 km. Clearly, accurate navigation cannot result if these ambiguities remain.

In order to resolve the 1 ms timing ambiguities incurred by using the C/A code, single frequency receivers use the navigation message. The navigation message contains satellite ephemeris and status information. It also provides additional timing marks and a count (the "truncated Z-count") which help to resolve C/A code timing ambiguity. The navigation message modulates the C/A code at a very slow rate, 50 Bps, such that each data bit holds constant for 20 C/A code periods. The broadcast signal then becomes

$$s_n(t) = A_n D_n(t) C_n(t) \cos(\omega_1 t), \tag{2.2}$$

where $D_n(t)$ (± 1) is the 50 Bps data stream.

From the fastest to the slowest time scales, then, the broadcast GPS signals contain the following, for single frequency users (summarized in Figure 2.1). Each satellite sends out a 1.57542 GHz carrier signal. A pseudorandom noise code, the C/A code, modulates the carrier at 1.023 MHz, repeating itself every millisecond. The navigation message then modifies the polarity of the the composite signal at a rate of 50 Hz. Further structure exists within the navigation message. The main feature

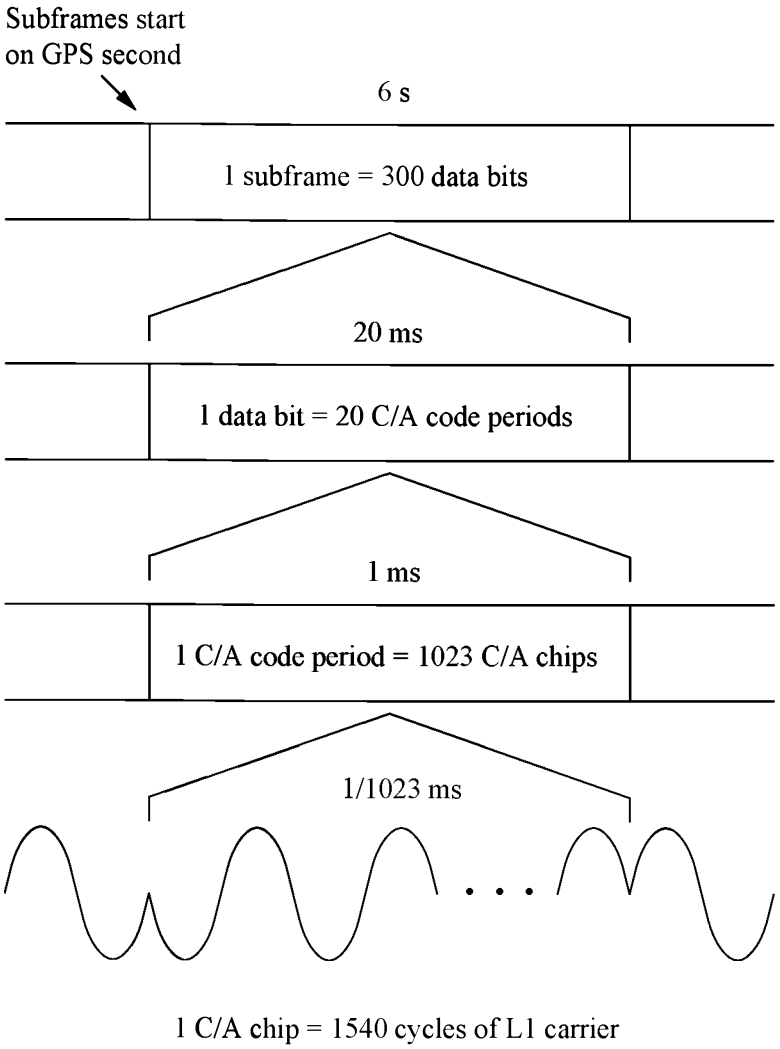

Figure 2.1: Sketch of GPS signal structure. This diagram is organized with the longest time scale structure of interest on top, proceeding downward through shorter time scale components until reaching the L1 carrier at a 1.57542 GHz rate. Additional levels of structure at longer time scales than the subframe exist (for example the frame, composed of 5 subframes) but are not shown in the diagram.

of importance to signal acquisition and tracking is the organization of the data bits into subframes of 300 bits. These subframes start exactly on the GPS second, as determined by the satellite's atomic clock, every six seconds. Additionally, part of the information contained in each subframe, the truncated Z-Count, tells the starting time of the next subframe. *Spilker* [1996*a*] and *Van Dierendonck* [1996] give further details of the navigation message which are not considered here.

2.3 Signal Acquisition

Normally, a single frequency receiver has 4–12 identical channels, each of which it dedicates to a single satellite. For example, the Plessey development system PC card, on which the Cornell scintillation monitor is based, has 12 channels. At the lowest level of GPS receiver operation lie two fundamental steps which each channel performs: acquisition and tracking. Once the channel acquires a signal and, by tracking, maintains it in lock, the receiver can proceed to higher level functions like decoding the navigation messages and solving for the receiver's position, velocity, etc. Most of the discussion in this section will be general, but when specifics must be introduced it will refer to the operation of the Plessey development system [*Plessey*, 1996]. *Van Dierendonck* [1996] has a similar discussion based on another model of receiver.

Figure 2.2 shows a simplified block diagram of one channel in a typical GPS receiver. Most modern receivers, including the Plessey development system, perform all the channel processing digitally. Consequently, $V(t)$ is in reality a sampled, quantized version of the signal (two bit representation in the Plessey receiver), after some steps of analog down conversion. Likewise, a digitally controlled oscillator (DCO) replaces

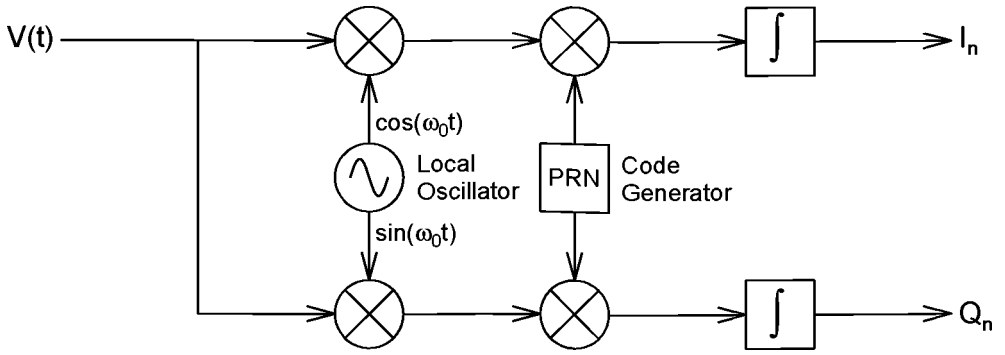

Figure 2.2: Simplified block diagram of one channel of a GPS receiver. The input signal $V(t)$ results from several steps of down conversion of the original RF signal. Note that timing logic (not shown) samples the outputs of the integrators every C/A code period ($\sim$1 ms, as determined by the code generator time base), producing the I_n and Q_n samples, and then resets the integrators.

the local oscillator, the mixers are actually digital multipliers and the integrators become accumulators. In the development system discussed here, the computer's program continually measures the in-phase and quadrature signals, I_n and Q_n, from the card and adjusts the DCO and code generator frequencies to acquire and track the satellite signals.

Acquisition consists of four steps, performed in the following order: code lock, carrier lock, bit lock and subframe lock. Note that code lock occurs before carrier lock because GPS is a spread spectrum system. There exists no strong frequency component to lock onto at the Doppler shifted L1 frequency. Instead, the receiver must look for strong code correlations first, before attempting to lock its frequency, and possibly its phase, to those of the underlying carrier.

2.3.1 Code Lock

The procedure for achieving code lock is fairly simple but may be achieved via two routes, depending on the state of receiver operation. If the receiver is already navigating using other satellites, or has a rough idea of its initial position and the satellite positions (for example, from an initial position guess and recent satellite almanacs), the receiver can make an informed estimate of the Doppler shift of the satellite signal and try to lock onto the code. Otherwise, the receiver must conduct a "brute force" search through all possible Doppler shifts, in relatively coarse 500 Hz steps, looking for a code correlation. The point is that, although the receiver performs code lock prior to carrier lock, the frequency of the DCO must be relatively close to the Doppler shifted, down converted signal before code lock may occur.

The receiver senses code lock by looking at the correlation power ${I_n}^2 + {Q_n}^2$, so called because multiplying the received signal samples by the locally generated PRN

code and summing over the code period forms a correlation operation. When the correlation power on a channel exceeds a certain threshold (defined for the Plessey receiver in *Plessey* [1996]), the software assumes code lock for that channel. Experience shows that the chosen threshold is set somewhat low, as indicated by the frequent declaration of code lock on channels assigned to satellites that have not yet risen. Nevertheless, the receiver quickly weeds out such false locks by the failure of that channel to achieve subsequent carrier, bit and subframe synchronization. So, one may regard the initial code lock as a provisional status.

Looking at the correlation process in more detail provides important definitions for later analysis. For simplicity, however, this section will only discuss the continuous time, nonquantized model shown in Figure 2.2. Some of the differences between the results for the present analog model and the true digital system will be considered later. Also, the article by *Van Dierendonck* [1996] contains more details of the digital system analysis.

First, we need some standardized symbology for the received signal resulting from the process of down conversion, $V(t)$. The signal resulting from one satellite is the following:

$$V(t) = ADC(t+\tau)\cos(\omega_D t - \phi) + n(t). \tag{2.3}$$

Now A is the *received* signal amplitude, assumed to remain constant during the integration period ($\sim$1 ms). We also assume that the navigation message data bit D (± 1) does not change over the integration period. The PRN code of the satellite in question is $C(t+\tau)$. In order to compare the received signal to the local oscillator and code generator, (2.3) incorporates a phase offset ϕ and a time offset τ, respectively. A natural goal for the tracking loops is then to drive ϕ and τ to zero. Finally, ω_D is the signal frequency after down conversion (in the neighborhood of 1.405 MHz

[*Plessey*, 1996]) and $n(t)$ is the thermal noise in the receiver. Technically, $n(t)$ also includes satellite signals with PRN codes different from the one in the channel under consideration.

Note that (2.3) slyly omits any change in code period resulting from Doppler shift. To see that this is not a gross approximation, consider the following. The range rate from a stationary user to a GPS satellite lies between zero, at zenith, and roughly ± 900 m/s (rising or setting). At the extremes, then, Doppler shift translates into ± 4800 Hz carrier deviation, or about 3% when mixed down to 1.405 MHz. Such a shift only alters the code bandwidth by $\pm 3 \times 10^{-4}\%$, however (a figure which down conversion does not affect). So the received code frequency does not change appreciably from 1.023 MBps. Of course, effects due to such small frequency deviations accumulate over time and the Doppler shifts change as the satellites move across the sky; thus, the receiver must perform code tracking after establishing code lock. Nevertheless, over short periods one may consider the code period to be essentially constant at 1 ms.

For now, we will neglect the contribution of noise. The in-phase and quadrature signals over a single period of the code are

$$I_n = AD \int_{-T_c/2}^{T_c/2} dt\ C(t)C(t+\tau)\ \cos(\omega_0 t)\cos(\omega_D t - \phi), \tag{2.4}$$

$$Q_n = AD \int_{-T_c/2}^{T_c/2} dt\ C(t)C(t+\tau)\ \sin(\omega_0 t)\cos(\omega_D t - \phi), \tag{2.5}$$

where T_c is the code period of approximately 1 ms, not the period of any of the sinusoids, and we assume AD to be constant over the interval. Following the usual practice of radio frequency analysis, the products of sinusoids yield sum and difference frequencies. Since the high frequency sinusoids at $\omega_0 + \omega_D$ vary rapidly over the code period, we neglect their contributions to the integrals on average. Thus, the

integrands simplify to the following:

$$I_n = \frac{AD}{2}\int_{-T_c/2}^{T_c/2} dt\ C(t)C(t+\tau)\ \cos(\Delta\omega t - \phi), \tag{2.6}$$

$$Q_n = -\frac{AD}{2}\int_{-T_c/2}^{T_c/2} dt\ C(t)C(t+\tau)\ \sin(\Delta\omega t - \phi), \tag{2.7}$$

where $\Delta\omega = \omega_D - \omega_0$.

Even neglecting the explicit noise terms, the presence of the $C(t)C(t+\tau)$ in the integrals makes I_n and Q_n random variables. After all, $C(t)$ is essentially random. Taking time averages with the expected value operator $\mathrm{E}\{\ldots\}$ yields

$$\mathrm{E}\{I_n\} = \frac{AD}{2}\int_{-T_c/2}^{T_c/2} dt\ \mathrm{E}\{C(t)C(t+\tau)\}\ \cos(\Delta\omega t - \phi), \tag{2.8}$$

$$\mathrm{E}\{Q_n\} = -\frac{AD}{2}\int_{-T_c/2}^{T_c/2} dt\ \mathrm{E}\{C(t)C(t+\tau)\}\ \sin(\Delta\omega t - \phi). \tag{2.9}$$

The value of $\mathrm{E}\{C(t)C(t+\tau)\}$ depends only on τ and can thus be pulled outside the integrals. Furthermore, $\mathrm{E}\{C(t)C(t+\tau)\}$ is the definition of the autocorrelation function $\mathrm{R}(\tau)$. Figure 2.3 sketches the autocorrelation function for the Coarse/Acquisition code. Since the C/A code is periodic, with period T_c, the autocorrelation function is also.

Introducing $\mathrm{R}(\tau)$ and evaluating the integrals gives

$$\mathrm{E}\{I_n\} = \frac{ADT_c}{2}\,\mathrm{R}(\tau)\,\mathrm{sinc}(\Delta\omega T_c/2)\cos(\phi), \tag{2.10}$$

$$\mathrm{E}\{Q_n\} = \frac{ADT_c}{2}\,\mathrm{R}(\tau)\,\mathrm{sinc}(\Delta\omega T_c/2)\sin(\phi), \tag{2.11}$$

letting $\mathrm{sinc}(x) = \sin(x)/x$ as usual. Equations (2.10) and (2.11) show explicitly that the receiver can achieve code lock with a frequency error $\Delta\omega$ since the sinc function has a rather broad maximum about zero. Given a frequency error of 250 Hz, for example, the correlation loss in ${I_n}^2 + {Q_n}^2$ comes to 0.9 dB [*Plessey*, 1996].

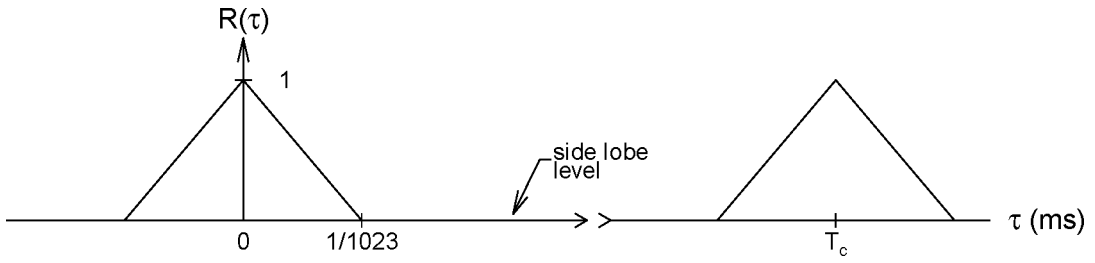

Figure 2.3: Autocorrelation function R(τ) of GPS Coarse/Acquisition code. The "side lobes" have magnitudes of the order of 10^{-3}, for these 1023 bit, maximal length codes [*Spilker*, 1996*b*] and show up as essentially zero on this linear scale. Also, R(τ) is periodic in τ, with period equal to the code period, T_c (1 ms), leading to a modulo 1 ms ambiguity in timing measurements based on the C/A code alone.

Of course, if the receiver maintains code lock, $\tau = 0$ and $C(t)C(t+\tau) \equiv 1$, remembering that $C(t) = \pm 1$. Specifically, under code lock I_n and Q_n are no longer random quantities (neglecting the receiver noise still), and the expectation operators in (2.10) and (2.11) can be eliminated after replacing R(τ) with 1. In other words, under code lock

$$I_n = \frac{ADT_c}{2} \operatorname{sinc}(\Delta\omega T_c/2)\cos(\phi), \tag{2.12}$$

$$Q_n = \frac{ADT_c}{2} \operatorname{sinc}(\Delta\omega T_c/2)\sin(\phi). \tag{2.13}$$

This "code lock" approximation will be useful when analyzing carrier lock in the next section.

Unfortunately, the unknown and variable signal strength A poses a problem for finding and maintaining code lock using the simple scheme outlined above. As stated before, the receiver searches for code lock by comparing the correlation power ${I_n}^2+{Q_n}^2$ against a threshold value to determine whether the local code nearly lines up with

the received code. Equations (2.10) and (2.11) suggest further that the receiver should try to make the correlation power reach maximum by adjusting τ. When $\tau = 0$, ${I_n}^2 + {Q_n}^2$ reaches a maximum, holding A, D and $\Delta\omega$ constant. The problem, of course, is knowing what that maximum correlation power should be since A is unknown (all other factors being of order unity).

One practical solution to the problem of having an unknown signal amplitude is to add an extra code correlation stage to the output of each of the in phase and quadrature mixers (Figure 2.4). A delay element makes the PRN code on the new correlators exactly one half chip later than the code fed into the original correlators. Thus, the literature refers to the outputs of the additional correlators as the "late" channel (sometimes, confusingly, the "prompt" channel), while the correlators without the delay in their codes become the "early" (or "tracking") channel. To conform to the notation of *Plessey* [1996], we will label the "late" channel outputs IP_n and QP_n, while the "early" channel outputs become IT_n and QT_n. We shall reserve the notations I_n and Q_n for the combinations $IP_n + IT_n$ and $QP_n + QT_n$, respectively.

Using the "early-late" correlation system, the receiver tries to drive the quantity

$$EML = ({IT_n}^2 + {QT_n}^2) - ({IP_n}^2 + {QP_n}^2) \tag{2.14}$$

to zero. When *EML* is zero, the two correlators exactly "straddle" the correlation peak; that is, the early channel is one quarter chip early while the late channel is one quarter chip late. Clearly, this measure of correlation lock is insensitive to the amplitude of the received signal for if the amplitude goes up or down, both the early and late correlation powers change together. If $EML < 0$, both copies of the code are too early, while if $EML > 0$ both copies of the code are too late. Also, the magnitude of *EML* varies proportionally to the timing error over a $\pm 1/4$ chip range. Hence,

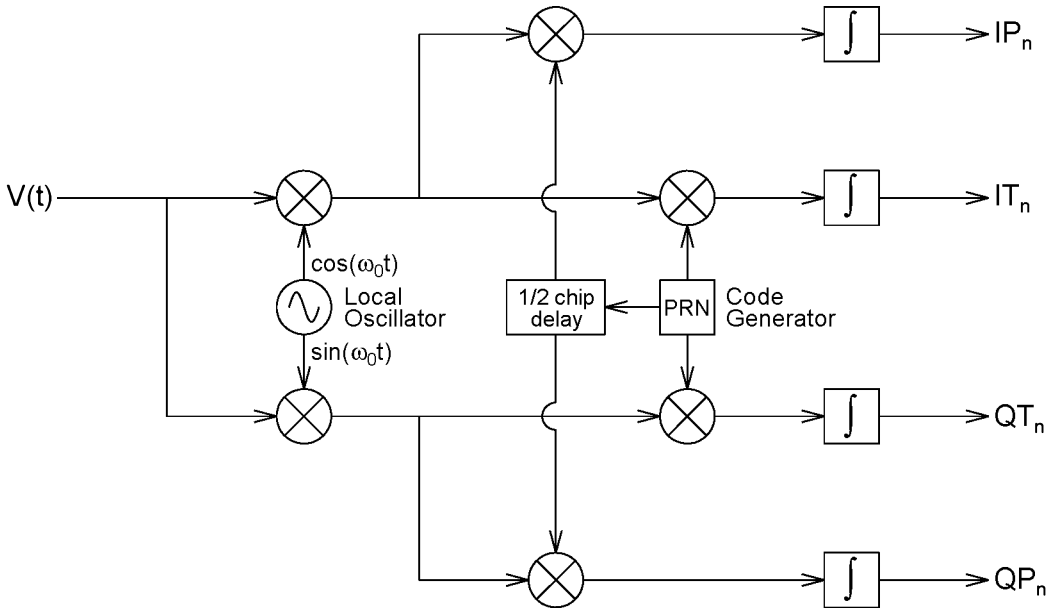

Figure 2.4: Block diagram of "early-late" correlation scheme. By adding a second set of correlators after the in phase and quadrature mixers, using a delayed PRN code, the receiver can seek and maintain code lock in a manner insensitive to signal amplitude.

using *EML* as an indicator of code lock tells the control loop which direction and by how much to steer the chipping rate of the locally generated PRN code.

Overall, then, the process of achieving and maintaining code lock in the Plessey receiver goes as follows. First, the receiver software selects a satellite to track on a given channel and presets the local oscillator based on the expected Doppler shift (either making an informed estimate or an outright guess, as discussed earlier). The program next sets the channel's code generator to the desired PRN code and the code rate to be slightly higher than the expected code rate, so that the local code drifts slowly relative to the received code. While the local code drifts through all possible correlation lags, the program monitors the correlation power ${I_n}^2 + {Q_n}^2$ for a significant value. If the software detects a possible lock, it starts up code tracking, using a delay locked loop (DLL) which monitors *EML* and adjusts the code frequency in response. By this process, the receiver maintains timing alignment between the local and received codes and can measure the time of signal transmission modulo 1 ms.

2.3.2 Carrier Lock

Following code lock and tracking, the receiver next seeks carrier lock. Carrier lock in the Plessey receiver consists only of adjusting the local oscillator to track the Doppler shifted frequency of the down converted signal. The receiver's tracking loop does not seek to match the phase of the received signal. Instead, it compensates for the residual phase error just before attempting to demodulate the 50 Bps navigation message. This "noncoherent" (frequency locked but not phase locked) design performs better under conditions of high receiver dynamics: high velocities, accelerations and jerks [*Cahn et al.*, 1977]. Of course, accommodating receiver dynamics is not a major concern

for stationary receivers like the Cornell scintillation monitor. Such a robust tracking scheme should, however, help the receiver to maintain lock under active scintillation conditions, with ionosphere induced phase and amplitude fluctuations in the signal.

To sense the frequency and phase error of the signal, the receiver looks at the (I_n, Q_n) vector. (Technically, the on time samples do not exist in early-late tracking, but the receiver may essentially recover them by summing the early and late samples.) This vector rotates from one code period to the next if there is a frequency error. For example, assume code lock and consider the I_n and Q_n samples defined earlier in (2.12) and (2.13). Integrating over the next code period, $T_c/2$ to $3T_c/2$, gives

$$I_{n+1} = \frac{ADT_c}{2} \operatorname{sinc}(\Delta\omega T_c/2) \cos(\phi - \Delta\omega T_c), \tag{2.15}$$

$$Q_{n+1} = \frac{ADT_c}{2} \operatorname{sinc}(\Delta\omega T_c/2) \sin(\phi - \Delta\omega T_c). \tag{2.16}$$

So, as Figure 2.5 illustrates, the I-Q vector rotates from one sample to the next for $\Delta\omega \neq 0$. The direction of rotation is clockwise for $\omega_0 < \omega_D$ and counterclockwise for $\omega_0 > \omega_D$. Further, the vector continues to rotate from sample to sample over subsequent code periods, provided that the frequency difference does not become zero.

Two levels of frequency control exist in the receiver's software: coarse and fine. At the coarse level, the frequency difference is still large, and the receiver employs a "four quadrant discriminator" method to correct the frequency error. Specifically, the receiver senses gross changes in I_n and Q_n from one correlation period to the next by taking account of sign changes in $\Delta I = I_n - I_{n-1}$ and $\Delta Q = Q_n - Q_{n-1}$. The corrections so gained reduce the frequency error from hundreds of Hertz to a few Hertz [*Plessey*, 1996]. After that, a frequency locked loop (FLL) takes over the fine carrier tracking.

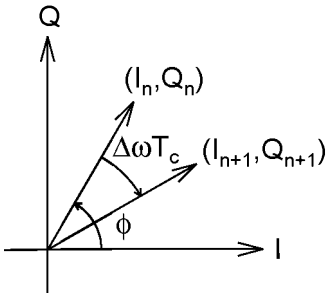

Figure 2.5: Rotation of (I_n, Q_n) vector between correlator output samples. This plot shows correlator samples plotted quadrature (Q) versus in phase (I) for two consecutive samples. The magnitude of phase rotation from one sample to the next is $|\Delta\omega T_c|$.

The FLL monitors frequency lock using the cross product

$$\begin{aligned} I_{n-1}Q_n - I_nQ_{n-1} &= \left[\frac{ADT_c}{2}\,\mathrm{sinc}(\Delta\omega T_c/2)\right]^2 \sin(\Delta\omega T_c) \\ &\approx \left(\frac{AT_c}{2}\right)^2 \Delta\omega T_c, \end{aligned} \tag{2.17}$$

for small $\Delta\omega$, assuming that signal amplitude A and the data bit D remain constant between samples. The important point is that the cross product is approximately proportional to $\Delta\omega$.

Finally, we need to consider the effect of the data bit D on carrier tracking. Clearly the value of D (± 1) does not affect code tracking because both of the monitored quantities, correlation power and the early-late difference *EML*, involve the squares of the correlator outputs. In the case of carrier lock and tracking, however, the data bit sign does affect the monitored quantity (I_n, Q_n). Specifically, changes in D abruptly change the angle of (I_n, Q_n) by 180° between samples.

In further detail, consider the following carrier lock scenario. The receiver has achieved code lock on a channel and has just begun to attempt carrier lock. Initially,

the I-Q vector rotates rapidly due to a large frequency error. Using the four quadrant frequency discriminator, the receiver rapidly slows the rotation, and hence the frequency error, to a few radians per second. Now, with only a small rotation from one sample to the next, the frequency locked loop can take over, gradually slowing the (I_n, Q_n) motion to a halt. Since the goal of the FLL is only to stop the rotation, however, the vector stops at an arbitrary angle, or phase error.

Now, the data bit changes sign. Between samples, the angle of (I_n, Q_n) suddenly changes by 180°. The FLL is insensitive to this abrupt change, however, since the cross product of the two successive samples on either side of the transition is still zero. So the vector stays in its new position for at least another 20 ms (the length of one data bit), prevented from rotating by the control of the FLL. At the next data bit transition, the vector flips back to its original position and the FLL again maintains lock. The resulting behavior of the I-Q vector is that it jumps back and forth between opposite positions, 180° apart along a line which is inclined at an arbitrary angle to the I axis, with the data bit transitions.

To eliminate the residual phase error ϕ in the I-Q vector, the receiver rotates the vector using the following relationship

$$\begin{bmatrix} I_{\text{new}} \\ Q_{\text{new}} \end{bmatrix} = \begin{bmatrix} \cos(\phi) & \sin(\phi) \\ -\sin(\phi) & \cos(\phi) \end{bmatrix} \begin{bmatrix} I_n \\ Q_n \end{bmatrix}. \tag{2.18}$$

Consequently, the $(I_{\text{new}}, Q_{\text{new}})$ vector lines up with the I axis. The bit transitions become transitions in sign of I_{new}. There remains ambiguity concerning whether $I_{\text{new}} > 0$ represents a data bit of +1 (corresponding to binary 1) or -1 (binary 0), however, because the receiver does not know whether the initial frequency lock occurred during a +1 or a -1. This ambiguity cannot be resolved until the receiver achieves subframe lock.

2.3.3 Bit and Subframe Lock

Once the channel achieves carrier lock on a signal, it must synchronize to the 20 ms data bit period so that the receiver may reliably decode the navigation message. To track bit transitions, the hardware for each channel in the Plessey receiver includes a 1 ms epoch counter which the local code generator drives. The counter increments from 0 to 19 with each code period. Whenever the counter resets to zero, it indicates to the receiver software that the GPS signal has reached a bit boundary, whether or not a bit transition actually occurs at that point.

To find the bit transitions initially and synchronize the 1 ms epoch counter to them, the receiver software keeps a "sliding window" sum of the sign of I_{new} over the current and previous 19 C/A code periods. If no bit transition occurs during the 20 ms of the sum, the sum will be either plus or minus 20. On the other hand, if the sign of I_{new} changes during the 20 ms, the absolute value of the sum will be less than 20. Of course, two data bits in succession can have the same value so that even if the 20 ms period does not line up with the data bit, the sum may be plus or minus 20.

For each channel, the software maintains 20 bins, grouped according to the value of the 1 ms epoch counter. Each bin contains a low pass filtered value reflecting the average of the absolute value of the sliding window sum for that 1 ms epoch (0–19). Only for the bin lined up with the bit transitions is the sliding window sum consistently at or near 20 in magnitude. Consequently, that bin should contain the largest value when averaged over time. If not already the case, the software slews the 1 ms epoch counter so that it is zero at the start of the data bits. For initial bit lock the software requires the maximum to remain in the same bin for 2 seconds (100 bits of the navigation message) [*Plessey*, 1996].

After bit lock, the receiver seeks the start of the subframe by collecting successive

data bits into two 30 bit words (GPS data words are 30 bits long). The first eight bits of every subframe start with the binary preamble 1000 1011, so the program searches for that bit combination first. Because of the possible ambiguity in the sign of I_{new} discussed earlier, the program also searches for the inverted version 0111 0100 and corrects the sign if necessary.

Naturally, the bit pattern of the preamble, normal or inverted, could appear elsewhere in the data stream by happenstance. So, once the program identifies a possible preamble, it immediately performs a consistency check based on the other contents of the data words. For example, the last 6 bits of each word form a parity code. If both words fails the parity check, the putative preamble does not mark the beginning of a subframe. Other items to check include the subframe ID (bits 20-22 of the second word), which should be in the range 1 to 5, and the mandatory zero bits (bits 29 and 30 of the second word) [*Plessey*, 1996]. A further possible check, although not performed by the Plessey software, takes the truncated Z-count from the second word (the hand over word), and verifies that it increments properly from one subframe to the next [*Van Dierendonck*, 1996].

After finding the subframe start for the channel, the receiver begins to decode the navigation data. Also, it sets another epoch counter, the 20 ms epoch counter, to zero at the start of the subframe. The 20 ms epoch counter counts up by one with each data bit and resets after 49. That is, this counter cycles every second, going through six cycles each subframe. With the setting of the 20 ms epoch counter, the receiver declares subframe lock on the channel in question.

Together, the 20 ms epoch counter and 1 ms epoch counter fix the time of broadcast to within one millisecond, modulo one second. Further timing information from the channel's code generator takes the resolution of the measurement of transmission

time down to a fraction of a chip, i.e., less than a microsecond. Knowing the transmission time of the signal from the C/A code and the reception time from the receiver's clock, the receiver can calculate the pseudorange to the satellite. By definition, the following equation gives the pseudorange ρ:

$$\rho = c\Delta t, \tag{2.19}$$

where c is the speed of light and Δt is reception time minus transmission time. Knowing the pseudorange and having decoded the navigation message for a given channel, the receiver may then add that satellite to its position solution.

2.4 Noise and Power Estimation

Several sources of noise exist in a GPS receiver. The most basic is thermal noise, as briefly mentioned earlier. Other sources of noise include quantization noise, uncorrelated GPS signals and multipath. The last two are perhaps more properly termed types of interference. Nevertheless, multipath and other GPS signals are unwanted sources of signal power that may mask the desired, directly received C/A code signal for a given channel.

The effects of thermal noise are the easiest to quantify. One may specify the receiver's noise temperature or noise figure, for example. We may also treat quantization effects as additional thermal noise. Quantization effectively decreases the signal to noise ratio (SNR) of the signal coming into the channel, since quantization error behaves in a roughly statistical manner like noise. For two bit quantization, the degradation in SNR amounts to 0.7 to 3.5 dB, depending on the receiver bandwidth and the quantization levels relative to the root mean square noise level [*Van Dierendonck*, 1996].

Technically, since GPS is a spread spectrum system, the quantity of interest is not the signal to noise ratio, but the carrier to noise ratio (C/N_0). The carrier to noise ratio is the ratio, expressed in dB, of received signal power, $S = A^2/2$, to noise power spectral density N_0 (W/Hz). The literature usually quotes the units of C/N_0 as dB-Hz as a reminder of the units inside the logarithm of the dB calculation. Having this definition in mind, we are ready to include the effects of thermal noise, along with quantization error, in the correlator outputs.

First, each of the in phase and quadrature samples now includes a noise term

$$I_n = \frac{ADT_c}{2} \mathrm{R}(\tau)\ \mathrm{sinc}(\Delta\omega T_c/2)\cos(\phi) + x_n, \tag{2.20}$$

$$Q_n = \frac{ADT_c}{2} \mathrm{R}(\tau)\ \mathrm{sinc}(\Delta\omega T_c/2)\sin(\phi) + y_n, \tag{2.21}$$

where x_n and y_n are independent, zero mean Gaussian random variables. These new noise terms each have a variance of $N_0T_c/4$, where N_0 is the one sided noise spectral density of the signal coming into the channel (see formulas of *Cahn et al.* [1977], modified to present notation and normalization).

One estimator of the signal plus noise power is the "wide band power"

$$\mathrm{WBP}_k = \left[\sum_{n=1}^{M} \left({I_n}^2 + {Q_n}^2\right)\right]_k, \tag{2.22}$$

where the sum covers the kth time interval of M samples, usually over one data bit so that $M = 20$ [*Van Dierendonck et al.*, 1993; *Van Dierendonck*, 1996]. The expected value of this estimator is

$$\mathrm{E}\{\mathrm{WBP}_k\} = M\left[\left(\frac{AT_c}{2}\mathrm{R}(\tau)\ \mathrm{sinc}(\Delta\omega T_c/2)\right)^2 + \frac{N_0T_c}{2}\right], \tag{2.23}$$

recalling that $D^2 \equiv 1$. For small code errors τ and frequency errors $\Delta\omega$, $\mathrm{R}(\tau) \approx 1$ and $\mathrm{sinc}(\Delta\omega T_c/2) \approx 1$. Both τ and $\Delta\omega$ should be small if the channel is tracking, so

the approximation

$$\mathrm{E}\{\mathrm{WBP}_k\} \approx \frac{MT_c}{2}(ST_c + N_0) \tag{2.24}$$

applies. We have assumed tacitly that the amplitude does not vary throughout the kth period so that S is fixed.

The variance of WBP_k is

$$\begin{aligned}
\mathrm{var}\{\mathrm{WBP}_k\} &= \mathrm{E}\left\{\mathrm{WBP}_k{}^2\right\} - (\mathrm{E}\{\mathrm{WBP}_k\})^2 \\
&= MN_0T_c\left[\left(\frac{AT_c}{2}\,\mathrm{R}(\tau)\,\mathrm{sinc}(\Delta\omega T_c/2)\right)^2 + \left(\frac{N_0T_c}{4}\right)\right] \\
&\approx \frac{MT_c{}^2}{4}(2SN_0T_c + N_0{}^2),
\end{aligned} \tag{2.25}$$

using the same tracking assumption as before. Equation (2.25) results from extensive, but fairly straightforward, algebra. For comparison, one may verify these formulas against Equations (110) and (112) of *Van Dierendonck* [1996], noting his use of a different normalization for the I_n and Q_n samples.

Rearranging (2.24) and (2.25) gives the following formulas explicitly in terms of S/N_0:

$$\mathrm{E}\{\mathrm{WBP}_k\} = \frac{MN_0T_c}{2}[1 + T_c(S/N_0)], \tag{2.26}$$

$$\mathrm{var}\{\mathrm{WBP}_k\} = \frac{MN_0{}^2T_c{}^2}{4}[1 + 2T_c(S/N_0)]. \tag{2.27}$$

Using these formulas, the normalized standard deviation of WBP_k is

$$\sigma = \frac{\sqrt{\mathrm{var}\{\mathrm{WBP}_k\}}}{\mathrm{E}\{\mathrm{WBP}_k\}} = \frac{1}{\sqrt{M}}\frac{\sqrt{1 + 2T_c(S/N_0)}}{1 + T_c(S/N_0)}. \tag{2.28}$$

For example, for a typical carrier to noise figure $C/N_0 = 35$ dB-Hz, $S/N_0 = 10^{3.5} = 3162$ s^{-1}. Since $M = 20$ (the receiver averages over one data bit to obtain WBP_k) and $T_c = 1$ ms, the normalized deviation of WBP_k is $\sigma = 0.14$ yielding about ± 0.6 dB deviation in the power estimate due to noise.

The effects of the two other noise sources discussed, multipath and uncorrelated PRN codes, are far more difficult to quantify because their parameters vary over a wide range depending on satellite positions, surrounding terrain, obstructions, etc. Multipath occurs when both direct and reflected signals reach the GPS antenna. If the time offset of the reflected signal relative to the direct signal is small, of the order of a fraction of a chip (corresponding to a path difference of less than 300 m), the reflected signal can significantly affect the correlation outputs. The next chapter will discuss multipath in more detail with an eye toward its effects on amplitude scintillation measurements.

Uncorrelated PRN codes might appear at first glance to be a wholly insignificant source of signal power. The C/A codes are fairly short codes, though, and the GPS designers made some compromises in their selection. As a result, the cross correlation between two different codes can occasionally rise to -21.6 dB rather than the expected -30 dB level [*Spilker*, 1996*b*]. For the most part, however, we will ignore the effects of uncorrelated codes.

2.5 Other Concerns

Finally, to round out this overview of GPS receiver design and operation, we briefly discuss some practical considerations. The first issue is the use of the automatic gain control (AGC) circuit in the Plessey receiver. For analog to digital (A/D) conversion with greater than one bit resolution, the receiver needs a way to control the gain of the radio frequency (RF) section automatically to compensate for variations in RF signal strength. Such variations could occur when using the same receiver with different antenna and cabling arrangements, for example. Also, strong interfering signals can

appear within the passband of the RF front end. Input signal strength variations can yield nonlinear distortion, e.g. clipping, in the digitized version of the signal.

As mentioned earlier, the Plessey receiver uses two bit quantization. The levels represented by this scheme are -3, -1, $+1$ and $+3$, in arbitrary units which depend on the channel gain. If the RF signal amplitudes are too small, always falling between the decision levels for -1 and $+1$, the digital representation will not change. (This problem does not occur for one bit quantization with a threshold set at zero volts. In the one bit case, if the RF gain is set too low, the signal still has zero crossings. Only the chance for spurious, noise induced sign changes increases with decreasing gain.) On the other hand, if the RF gain is too large, the signal crosses the ± 3 levels all the time. In this case, the digital signal becomes effectively a one bit representation, losing the signal to noise ratio advantage of having multiple bits.

The Plessey receiver has an AGC circuit to compensate for any variations in RF signal strength and take full advantage of the available two bits. This AGC circuit monitors the output of the A/D converter and adjusts the channel gain between the second and third stage of down conversion to compensate for any variations in average signal strength. It adjusts gain according to the following criterion: the digitized output should reach 3 in magnitude only 30% of the time [*Plessey*, 1996]. With the 0.1 μF capacitor used in the circuitry of the Plessey development system, the time constant of the AGC is about 2 ms (M. Lomer, private communication, 1996).

One should keep in mind that the signal which the RF chip digitizes is just the available signal in a ± 1.0 MHz band about the L1 frequency. This band contains both the C/A code and P (or Y) code broadcasts for all the visible GPS satellites, as well as any ambient signals or noise. Except in the presence of strong interfering signals, the

output of the A/D converter, to which the AGC circuit responds, appears essentially random due to the superposition of many spread spectrum signals. In contrast, some receivers use the correlator outputs, the power out of a channel "tuned" to a given C/A code signal, to adjust the AGC [*Van Dierendonck*, 1996].

Another practical consideration is the frequency error of the local oscillator. All timing in the Plessey hardware derives from a 10 MHz temperature compensated crystal oscillator. Frequency error in this oscillator yields two immediate consequences. First, each channel's local oscillator must tune to a higher or lower nominal frequency in order to match the Doppler offset. If the oscillator error is too great, the receiver may initially lock up slowly since the signals are out of the starting Doppler search bin. Second, larger frequency errors cause the receiver timing to slip relative to GPS system timing. The receiver does solve for the oscillator error as part of the navigation solution, and accounts for the error in its later Doppler bin searches. Nevertheless, some of the software's timing information derives from counters in hardware which "gain time" or "lose time" relative to GPS in the long run. The result is occasional lost data in the scintillation monitor, as will be discussed in the next chapter.

Chapter 3

Scintillation Monitor

3.1 Introduction

This chapter discusses the design and testing of the Cornell scintillation monitor in detail. The scintillation monitor is a modified Plessey GPS development system, specifically a version of the receiver with modified software. The primary goal of this modification was to provide power measurements of GPS L1 signals at a high rate. So, the bulk of this chapter will cover power measurements. First, though, we discuss more specifics of the Plessey receiver's operation and the nature of the modifications.

3.2 Plessey Overview

As stated above, the Plessey receiver used in the Cornell scintillation monitor is a development system. Specifically, the system consists of two parts: a card to be installed in an ISA slot on a PC and the software, including source code in C, required to run the card as a receiver. One of the two main integrated circuits on the card

performs the bulk of RF down conversion and then quantizes and samples the signal. The other half of the Plessey GPS chip set contains 12 sets of local oscillators, mixers and C/A code correlators to perform channel processing, where the control software typically assigns each channel to track one of the satellites in view. The PC performs all processing at the 1 kHz rate and slower, everything slower than the correlations with the 1.023 MHz pseudorandom noise code. In other words, the responsibility for achieving lock (code, carrier, bit and subframe) and maintaining tracking (code and carrier frequency) devolves on the computer.

The fact that the PC performs such low level operations makes the Plessey system, to our knowledge, unique. This involvement of the PC at such a fundamental stage of the GPS signal processing is precisely the characteristic that makes the Plessey development system so useful as a scintillation monitor. Indeed, the GPS chip sets from other manufacturers typically incorporate their own processors, responsible for locks and tracking as well as navigating. The Plessey chip set requires a separate, general purpose microprocessor and software to accomplish anything but the most rudimentary tasks. Which approach is better depends on the application. In the case of scintillation studies, however, the conventional sort of GPS chip set, where low level functions are buried in the imbedded controller, is particularly ill suited for the job.

The structure of the prototype software includes several layers. In general, the software must handle several tasks simultaneously, ranging from reading the correlations from the channel processing chip to computing the position of the receiver. A 505 μs periodic interrupt generated by the Plessey chip set drives the fast processing, such as reading the correlations and code and carrier tracking. Another interrupt called the TIC [*Plessey*, 1996], with a period of about 0.1 seconds, governs the slower

tasks like decoding the navigation message, selecting satellites to track, etc. Each of these timing signals also latches data in registers on the correlator chip.

Looking more closely at the activity upon the 505 μs interrupt, we now consider the fundamental operation of the Plessey receiver. Specifically, we note the large amount of data buffering and subsequent processing it performs. The timing of the fast interrupt is independent of any particular channel's timing: independent of its local oscillator and, especially, its code generator clock. The timing of the I_n and Q_n samples, however, exactly depends on the setting of the local code generator. Basically, at the end of each code period, the code generator sends a signal to clear the accumulator (integrator in the analog model), after latching its value in a register (sample and hold circuit in the analog version). If the code frequency drops, as when the receiver tracks a setting satellite, for example, the (I_n, Q_n) samples gain a spacing of slightly more than the nominal 1 ms.

Furthermore, the received satellite PRN codes all start at different times owing to differences in propagation delay. All of these variations among the channels in their timing, due to Doppler shifts and code offsets, mean that the in phase and quadrature correlation samples are generally asynchronous from channel to channel. What the 505 μs interrupt does, then, is to gain the attention of the processor at roughly twice the C/A code cycle rate. During this time, the processor polls the correlator chip for channels with available accumulation data, I_n and Q_n (actually early and late samples, IT_n and QT_n, IP_n and QP_n). It also updates the lock indications or tracking loops, as appropriate. Otherwise, the software's goal during these frequent interrupts is to read all the available data (e.g., epoch counts, code timing, carrier phase and data bits) and store them for future processing at a more leisurely pace.

During the TIC based portion of multitasking the receiver has two jobs to do

concurrently which directly relate to navigation. First, the receiver must decode the navigation message for each channel which has data in the "pipeline" that the fast interrupt driven routine feeds. The navigation message gives, among other things, ephemeris information so that the receiver may know the satellite's position. Then the receiver computes its position, time offset and velocity from the ephemerides plus the other information in the pipeline. The task "TPROCSBF" interprets the navigation messages while the task "Main" handles the actual navigation [*Plessey*, 1996]. The main task also performs various housekeeping functions such as assigning PRN numbers to unused channels when new satellites rise. Other, separate, tasks include updating the display on the PC's screen and processing incoming differential GPS data. (We have removed all tasks and functions related to differential GPS in the scintillation monitor version, however.)

In the Cornell scintillation monitor, the same hierarchy of tasks and interrupts applies. The modifications devoted to computing estimates of signal strength based on the correlator outputs reside in the fast interrupt portion of the program. The additions which allow the scintillation data to be logged, adding time stamps and so on, go in the TIC driven part of the code. Unfortunately, this approach allows some slippage between the timing of the signal strength measurements, as governed by the individual channel timing, and the TIC based time stamps in the event of modestly large oscillator errors.

For example, the current scintillation monitor software buffers five samples of WBP_k plus one other signal strength estimator to be saved to disk every TIC period, since each TIC period of 0.1 s contains five 20 ms long data bits. Occasionally, due to timing slippage, the data records contain duplicate sets of five samples of power data followed by the samples taken 0.2 s later, rather than three independent sets

of samples at 0.1 s intervals. An improved system of data buffering could alleviate the problem of skipped samples, but skipping happens only rarely unless the local oscillator frequency error is greater than about 0.5–0.8 ppm in magnitude.

3.3 Software Modifications

3.3.1 Overview

The specific software modifications required to make the Cornell scintillation monitor from the standard Plessey software fall into several categories. First, we eliminated all portions of the code pertaining to differential corrections, primarily to keep the program size and reserved array space to a minimum. We also added custom scintillation data logging capability, recording from all channels currently tracking satellites to the hard drive every 0.1 seconds (i.e., every TIC interval). Most of the logged data are already computed in the existing software, but we needed to add more detailed information on signal strength. The modified software also includes rudimentary automation so that the station can operate unattended over, say, a weekend and restart itself after power failures. Finally, the modified software incorporates many minor changes such as new displays to show the status of scintillation logging and new commands to set the header information for log files.

Table 3.1 lists the modified software modules of the Plessey source code, including brief synopses of the changes. (Appendix A provides more detailed discussion of the significant changes.) The table does not include changes to C header files. Most header file changes support the modifications already discussed: new or deleted global variables, constants, structures, function prototypes, etc. For example, the changes to the data structures are: (1) the addition to the channel control block of several items

Table 3.1: Modified source code modules.

Name	Description of Changes
ALLOCATE.C	Added allocation of "noise channel"
BUFFACC.C	Disabled changing local oscillator setting on "noise channel"
CMD.C	Deleted differential GPS commands; added misc. commands
DELAY.C	New module for rudimentary command automation
DISPFUN.C	Changed several display screens; added C/No to F3 display
DISPLAY.C	Modified display for top and bottom of all screens
GLOBALS.C	Deleted differential GPS variables; added new globals
INIT.C	Changed default track mode; added better startup diagnostics
IO.C	Deleted parts pertaining to differential GPS
MAIN.C	Removed option of serial data output
NAV.C	Added scintillation logging every TIC
PROCACC.C	Added update of new signal strength estimators; disabled code tracking on "noise channel"
RINEX2.C	Added modifiable header data and automatic file naming
RTCM.C	Deleted this differential GPS module
RTEXEC.C	Removed RTCM task; added DELAY task (module DELAY.C)
SAVEDATA.C	Removed serial data logging option
SCINT.C	New module with scintillation logging utilities
TAKEMEAS.C	Disallowed update of Doppler bin on "noise channel"

related to computing estimates of signal strength, and (2) the addition of header and record structures for scintillation logging files.

Also, Table 3.1 does not mention that the receiver excludes making RINEX observation files when RINEX logging is active. (The acronym RINEX means "Receiver INdependent EXchange format," a standard text format for GPS data exchange used by the surveying community. Two main file types exist: navigation files and observation files. Navigation files contain information from the navigation message: ephemeris, satellite clock models, satellite status, broadcast ionospheric model coefficients. Observation files contain measurements, such as pseudoranges, from all the tracked satellites. For format details see *Hofmann-Wellenhof et al.* [1994].) Unfortu-

nately, the portion of the code devoted to making RINEX observation files apparently has a subtle bug that causes program crashes once every day or so during continuous logging, giving generic floating point error messages. Frequent crashes are, naturally, highly undesirable for unattended station operation. By trial and error we discovered that these mysterious crashes disappear when RINEX observation data logging is bypassed.

The key parts of the modifications from the standpoint of monitoring scintillations are computing the signal strength estimates and saving them to disk. The program computes two quantities for each channel: (1) the aforementioned "wide band power"

$$\mathrm{WBP}_k = \left[\sum_{n=1}^{M} \left({I_n}^2 + {Q_n}^2\right)\right]_k, \tag{3.1}$$

and (2) the "narrow band power"

$$\mathrm{NBP}_k = \left(\sum_{n=1}^{M} I_n\right)_k^2 + \left(\sum_{n=1}^{M} Q_n\right)_k^2. \tag{3.2}$$

These definitions follow *Van Dierendonck et al.* [1993] and *Van Dierendonck* [1996]. In both cases, $M = 20$ and the summations cover the 20 code periods of the kth data bit. Essentially, $n - 1$ is the value of the 1 ms epoch counter (n runs from 1 to 20; the 1 ms epoch counter goes from 0 to 19). Also,

$$I_n = IT_n + IP_n, \tag{3.3}$$

$$Q_n = QT_n + QP_n. \tag{3.4}$$

When written to disk, the time tag takes the place of the index k.

Strictly speaking, the program computes $\sum I_n$, $\sum Q_n$ and $\sum \left({I_n}^2 + {Q_n}^2\right)$ for each data bit. Just before writing to disk, it uses the first two sums to compute NBP_k. The last sum is exactly WBP_k. Further, the program divides the saved NBP_k values

by M so that NBP_k and WBP_k values lie in the same range. This scaling is important to any data analysis which must combine the two estimators.

In addition to data from the channels tracking satellites, the scintillation monitor includes data from a channel which correlates the digitized output of the RF chip with an unused PRN code. This "noise channel" indicates variations in channel gain and is intended to provide information on the background noise power spectral density N_0. The receiver maintains this noise channel whenever the tracking mode is set to the new mode "NOISE_CHANNEL," now the default mode when the receiver software starts.

To allocate the noise channel, the receiver searches through the current satellite almanac to find the first PRN code, in ascending numerical order, which is presently unassigned to a satellite. Since only 24 satellites fly in the nominal GPS constellation, eight free codes typically exist at any given time. The receiver then reserves the highest available channel number to be the noise channel, using the unassigned PRN code and marking the channel with a special flag. The software permits no tracking on the noise channel; the code and carrier oscillators may not change from their default values, no matter how great or small the correlation power. Also, the 1 ms epoch counter and 20 ms epoch counter run freely from the channel's code generator, unsynchronized with any other timing reference. Nevertheless, the receiver records WBP_k and NBP_k for the noise channel using its free running epoch counters for timing.

In addition to WBP_k and NBP_k data at 20 ms intervals, the receiver saves other data into the scintillation logging file at 0.1 s intervals, the TIC rate. These data include pseudorange, as defined in the preceding chapter. The scintillation logging files also incorporate the following data: the integrated phase of the local oscillator,

range rates based on the current local oscillator setting (uncorrected for oscillator frequency error) and flags giving the state of tracking on the channel. On the noise channel, the receiver records zeros in the log file for all quantities except WBP_k and NBP_k samples.

3.3.2 File Format

The scintillation logging files are in FSL format ("fast scintillation logging"), a custom binary file format developed at Cornell. Since the FSL format depends on PC formatting of ANSI C data types, such as low byte before high byte order in integers, FSL files naturally do not transport directly to all other workstations. The use of a binary format saves considerable disk space, however. Even using the binary format, the data for a 12 hour period of scintillation logging amount to about 180 megabytes, varying with the average number of satellites in view.

The FSL format includes a header followed by an indefinite number of variable length records (Figure 3.1). The header essentially replicates the RINEX observation file format. Table 3.2 lists the contents of the header. Records consist of two parts, record headers and satellite entries. The record header contains a sync byte, a time stamp, a list of satellites in the record and a cyclic redundancy check (CRC) byte. Each satellite entry has the pseudorange, range rate, integrated carrier phase, NBP_k and WBP_k data for the listed satellite. Also, the satellite entry adds a simple checksum and a 20 ms epoch count, marking the start time of the first of the NBP_k and WBP_k samples. Including a 20 ms epoch count aids synchronization of data taking among nearby receivers.

In the record header, the TIC number encodes the universal time (UT) at which the receiver took the measurement. Since each TIC period is 0.1 seconds (actually

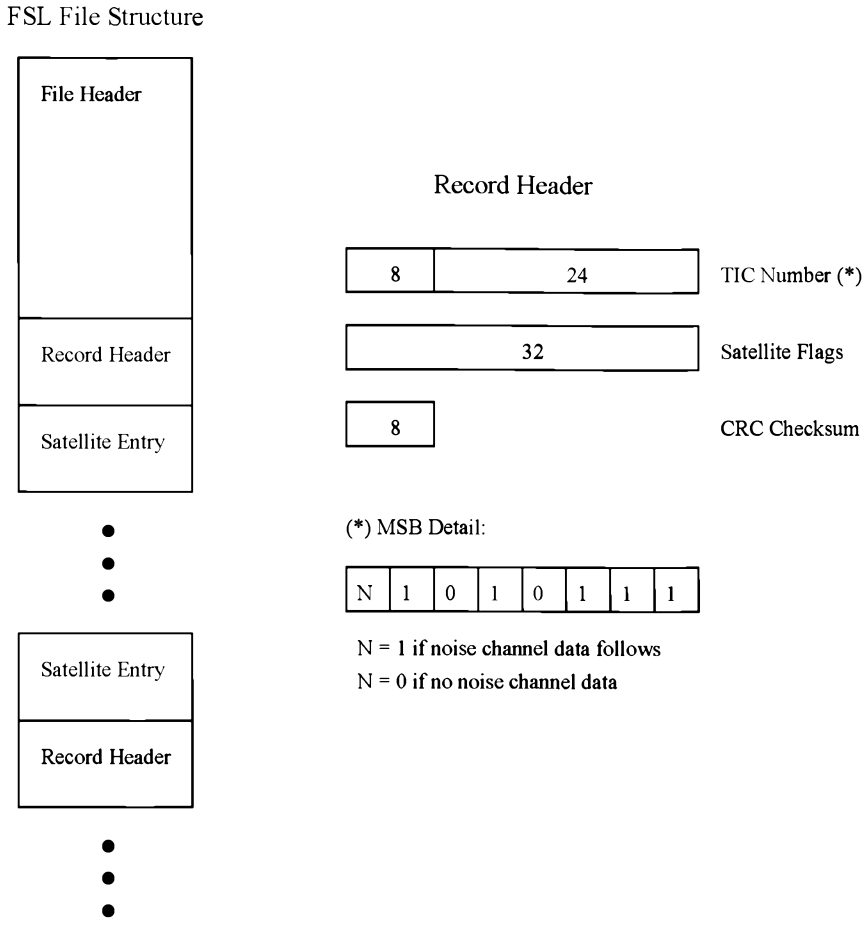

Figure 3.1: Structure of FSL files. The left side illustrates how an FSL file is organized: file header followed by records consisting of record headers and a variable number of satellite entries. The right side shows the details of the record header. Numbers inside the top three blocks represent number of bits. The most significant byte (MSB) of the TIC Number contains a noise channel flag and a fixed synchronization word. File headers and satellite entries are detailed later.

Table 3.2: FSL file header contents.

Field Name(s)	Type	Size	Description
FSLversion	int	—	Version of FSL format (currently 0)
pgm	char	21	Name of generating program
run_by	char	21	Name of agency running program
date	char	21	Date and time of program run
comment	char	61	User defined comment
marker_name	char	61	Name of site
observer, agency	char	21	Name of observer, observer's agency
rec_no	char	21	Receiver number
rec_type	char	21	Receiver type
rec_vers	char	21	Receiver version
ant_no, ant_type	char	21	Antenna number, antenna type
x, y, z	double	—	ECEF[1] xyz position of site (m)
delta_h	float	—	Antenna vertical offset from marker (m)
delta_e	float	—	Antenna east offset from marker (m)
delta_n	float	—	Antenna north offset from marker (m)
yy, mm, dd	int	—	Year, month and day of first observation
h, m	int	—	Hour and minute of first observation
s	double	—	Second of first observation

[1]Earth centered, earth fixed coordinate system.

0.0999999 s), the TIC number equals the number of seconds past midnight UT multiplied by 10. For example, the starting time in the FSL header should match the TIC number of the first record. If the time in the header is 22:30:45.3 UT, the first TIC in the file should be 810,453. At midnight, the TIC number rolls over from 863,999 to 0. Note that the FSL format itself does not require that the first TIC match the header time or that the TIC numbers increment from one record to the next (modulo 864,000). The intent of the receiver software, however, is that both of these conditions should apply and that any deviation from them indicates faulty operation of the receiver.

Together, the noise flag in the most significant bit of the TIC number and the satellite flags specify the entries which follow the record header. If the noise flag is set to 1, the noise channel entry immediately follows the header. Otherwise, one of the actual satellite entries follows the header. The satellite flags mark the presence of satellite entries according to PRN code. Bit 0 (the least significant bit) of the word indicates whether an entry for PRN 1 follows, and so on, up through bit 31 for PRN 32. The total number of bits set to 1 among the noise and satellite flags gives the total number of entries following the record header. After the noise channel entry, if present, the satellite entries come in ascending PRN order.

Because each record contains a variable number of entries, recovery in the event of disk reading errors becomes more difficult than recovery for fixed format files. Two features of the record header help the reading program to identify and skip bad header blocks. First, a CRC checksum attaches to each record header. (*Press et al.* [1992], for example, have a brief discussion of cyclic redundancy checks. The "primitive polynomial" used in our case is 1 0001 1101 in binary.) If the header fails the CRC check, the reader can skip to find the next good record. The upper byte of each TIC

number, less the noise flag, constitutes a synchronization word, 101 0111 in binary. To recover after a CRC error, then, the file reader can skip forward, byte by byte, until it finds the sync word in the lower 7 bits. After finding a sync word, the program may read up through the presumed CRC byte and see if the putative record header passes the check. Note, however, that this complicated scheme of error recovery seems to be rarely necessary in practice; our experience has shown disks and tapes to be generally reliable if they are readable at all.

Along these lines, another practical problem stems from variable record lengths. Variable record lengths make skipping ahead to a specified TIC number more difficult. Two potential solutions appear, although we have tried neither in practice. First, rather than read through all the records between the current TIC and the desired TIC, the reader can skip ahead in the file by an estimated byte offset based on an "average" record size, a quicker operation. Of course, the reader must resynchronize to the record headers after the skip and be prepared to scan backwards or forwards by a small amount to compensate for the error in the estimated offset. Alternatively, the reader could make a preliminary pass through the FSL file, storing the byte offsets of records with specified TICs, say every 10 minute mark, in an index file. Then, when the user requests that the file reader skip to a certain time, the program can skip rapidly to the nearest index point and scan from there.

Now all of this fancy file formatting is useless without discussing the data contents of the FSL file. The satellite entries are the real meat of each record. Table 3.3 lists satellite entry contents. The first three components, pseudorange, range rate and integrated local oscillator phase, are so called GPS observables, typically available from any receiver, albeit not generally at the rate of 10 samples per second. The NBP_k and WBP_k entries provide information on signal strength for amplitude scintillation

Table 3.3: FSL satellite entry contents.

Field Name(s)	Type	Size	Description
pseudorange	double	—	Code pseudorange (m)
range_rate	double	—	Doppler derived range rate[1] (m/s)
int_carrier_phase	double	—	Integrated phase of channel's local oscillator (cycles)
NBPk	unsigned int	5	Scaled narrow band power samples[2]
WBPk	unsigned int	5	Wide band power samples
epoch	unsigned int	—	Time of first power samples in entry
flags	unsigned int	—	Bit 0—carrier lock lost (if 1), Bit 1—code lock lost (if 1), Bit 2—lock lost (if 1), Bits 3–7—unassigned (reserved), Bits 8–15—checksum

[1]Uncorrected for receiver frequency error.
[2]That is, divided by 20.

studies and are only available in custom receivers, such as the Cornell scintillation monitor and possibly in the system described by *Van Dierendonck et al.* [1993] and *Klobuchar et al.* [1994].

The remaining data give channel status. The 20 ms epoch count, a multiple of 5 between 0 and 45, indicates the starting time of the narrow band and wide band power samples relative to the received subframe start times. (Recall that during subframe lock, the receiver synchronizes each channel's 20 ms epoch counter to the received signal so that the count is 0 at the start of a subframe and every second thereafter.) The epoch count helps to recover more precise timing information if the TIC counter slips relative to the received GPS signal's timing, as discussed earlier. Finally, the "flags" word divides into two bytes. The least significant byte contains a set of lost lock flags, only to three of which does the FSL version 0 format assign meaning (see Table 3.3). The most significant byte is a simple checksum of all the other bytes in

the satellite entry, the sum of those bytes modulo 256.

Appendix B lists prototype functions in C to read FSL files. This set of functions does not include recovery in the event of CRC errors in the record header or advanced search functions. Nevertheless it demonstrates the variable length record format and how to verify the CRC and checksum. More efficient CRC algorithms exist [*Press et al.*, 1992], but the direct approach used in these sample routines appears to be adequate.

3.4 Receiver Operation

For the most part, despite the modifications, the Cornell scintillation monitor functions like the original Plessey software. Upon startup, the receiver acquires and begins tracking as many satellite signals as it can. As soon as it tracks three or more satellites, and has acquired enough of the navigation message, it can begin computing solutions for the receiver position and the receiver's clock offset from GPS time (i.e., the receiver can begin navigating). The only active modification takes place in the background when the program updates the sums used to generate WBP_k and NBP_k while processing each incoming correlation sample. Even most of the function keys and commands operate normally at this stage.

The main difference occurs when the operator gives the command to start scintillation logging. First, the program waits until the receiver computes a navigation solution and the estimate of the local oscillator error stabilizes. It waits so that the time stamps it will write to the disk will be accurate. During the computation of the navigation solution, the receiver updates the local clock with the estimate of the clock offset. By the time the oscillator error estimate converges upon a stable value,

the local clock should be very close to GPS time.

Even with this applied clock offset, experience shows that two nearby receivers can still differ by ±1 TIC in their timing, as referenced to the 20 ms epoch count. Perhaps this "slippage" stems from different errors in the navigation solution between the receivers, for example. Whatever the cause, the postprocessing operation can correct the effects of slippage by using the 20 ms epoch count, as long as the receivers' clocks were sufficiently close to each other to begin with (within ±0.5 second). So, scintillation logging must wait until the local clock setting stabilizes.

After the local clock stabilizes, the program begins to generate the FSL file. First, it selects a new file name based on the GPS year, month and day that logging started, a station identification character and the files names already used for that starting day. After opening the file with the new name, the program writes an FSL header and then begins sending records to the disk in FSL format. Record writing continues at each TIC until the operator turns scintillation logging off.

During scintillation logging, the rate at which the program updates the navigation solution drops from once every 10 TICs (once per second) to once every 100 TICs (10 s), in an attempt to reduce processor loading. If the processor dwells too long on a single task without permitting a jump to the fast interrupt service routine, the receiver misses correlation samples, yielding data gaps. Even with the reduced rate of computing the navigation solution, missed accumulations still occur during scintillation logging. Usually, though, the culprit is another active program, such as a mouse driver, that generates its own interrupts.

Also, during scintillation logging the program closes and reopens the FSL file every two hours (part of the module DELAY.C). This action helps prevent data from being lost in the event of a power failure by flushing the disk write buffer and updating the

file pointers. If a power failure occurs between file closings, data in the write buffer will be lost. In this case, though, the data already written to disk can be read after updating the disk's file pointers with the DOS utility SCANDISK or another, similar utility. Without correcting the file pointers, the FSL file appears to be smaller than it actually is on disk.

Rather than start and stop logging by operator command, we usually set up the receiver to log data automatically. The software provides two means to do this. First, the program loads a file called CMD.INI at startup and executes the commands the file contains. By adding data logging commands at the end of CMD.INI, we can have the program begin RINEX navigation file logging and scintillation logging as soon as the software starts up. The other option is to use the "delayed execution" command. With this command, we tell the receiver to execute a command at a specified time. For example, suppose we wish to stop RINEX data logging at 1100 UT. In this case, we would enter the command DX 11:00 RN 0, where DX is the delayed execution command, 11:00 is the execution time and RN 0 tells the receiver to stop RINEX data logging.

Using these simple methods of automation, we can have the receiver start and stop data taking for several nights in succession, up to the limit of the computer's hard disk capacity. This procedure, automatically starting data logging on startup and entering delayed execution commands to stop logging later, also works in the event of power failure. Of course, for automatic startup in the event of a power failure, the AUTOEXEC.BAT file should include DOS commands to run the scintillation monitor program upon restart.

One problem with automating the current version of the scintillation receiver is the volume of storage space required for the raw data files. Scintillation log files typically

amount to 150–250 MB over a 14 hour period, depending on the total number of observations that they contain. Consequently, the common 1 GB hard drive holds at most four days of data, only enough for a long weekend. Presently, we back up the FSL files every couple of days during campaigns to a 4 mm DAT (digital audio tape) drive. The approximately 4 GB available on a 120 m long tape permit the storage of roughly three weeks of raw data files. After each campaign, we back up the data to CD-ROM discs for easier handling. Future versions of the scintillation monitor should include automatic backup of FSL files to tape, automatic erasure of backed up files and generation of summary files of scintillation parameters for remote download via modem.

3.5 Power Measurements

We now turn to more of the details of computing signal strength, the key new measurement that the scintillation monitor provides. Signal strength provides a direct indication of amplitude scintillations, fluctuations in signal intensity due to propagation through ionospheric irregularities. Older systems for scintillation measurements had satellites broadcast carrier waves on one or several frequencies; that is, they broadcast beacons. To measure amplitude scintillations was a simple matter. The receiving station needed an antenna and a radio receiver tuned to the desired beacon frequency. A strip chart then recorded the power output of the receiver, which usually included any noise in the system. Of course, the noise could be minimized by using low noise temperature receivers and antennas with high front to back gain ratios.

The direct analog of recording signal power on a strip chart is saving wide band

power samples to disk in the scintillation monitor. Recall that

$$\mathrm{WBP}_k = \left[\sum_{n=1}^{M}\left({I_n}^2 + {Q_n}^2\right)\right]_k, \tag{3.5}$$

where $M = 20$ is the number of I_n and Q_n samples per GPS data bit and k is the sample number. So WBP_k is simply an average of the signal plus noise power, scaled by the receiver gain, over a 20 ms period.

As derived in the last chapter, and repeated here in a slightly altered form for convenience, the expected value of wide band power is

$$\mathrm{E}\left\{\mathrm{WBP}_k\right\} = \frac{M{T_c}^2}{2}\left(S + \frac{N_0}{T_c}\right), \tag{3.6}$$

where S is signal strength, in arbitrary units because of the unknown gain, N_0 is the one sided noise power spectral density in the receiver bandwidth and $T_c \approx 1$ ms is the repetition period of the received Coarse/Acquisition PRN code of the satellite. In addition to contributing power to WBP_k, noise also causes measurement scatter. Repeated below, the standard deviation of WBP_k, normalized to $\mathrm{E}\left\{\mathrm{WBP}_k\right\}$, is

$$\sigma = \frac{1}{\sqrt{M}}\frac{\sqrt{1 + 2T_c(S/N_0)}}{1 + T_c(S/N_0)}. \tag{3.7}$$

Figure 3.2 shows how σ varies with the so called carrier to noise ratio, $C/N_0 = 10\log_{10}(S/N_0)$.

Clearly, above about 25 dB-Hz, C/N_0 strongly determines σ so that one may invert the problem reliably. Below this threshold, small errors in estimating σ give large errors in C/N_0. The inverse of (3.7) is

$$\frac{S}{N_0} = \frac{1}{T_c}\left(\frac{1 - M\sigma^2 + \sqrt{1 - M\sigma^2}}{M\sigma^2}\right). \tag{3.8}$$

So, in order to estimate the carrier to noise ratio, we only need to estimate σ from the WBP_k measurements.

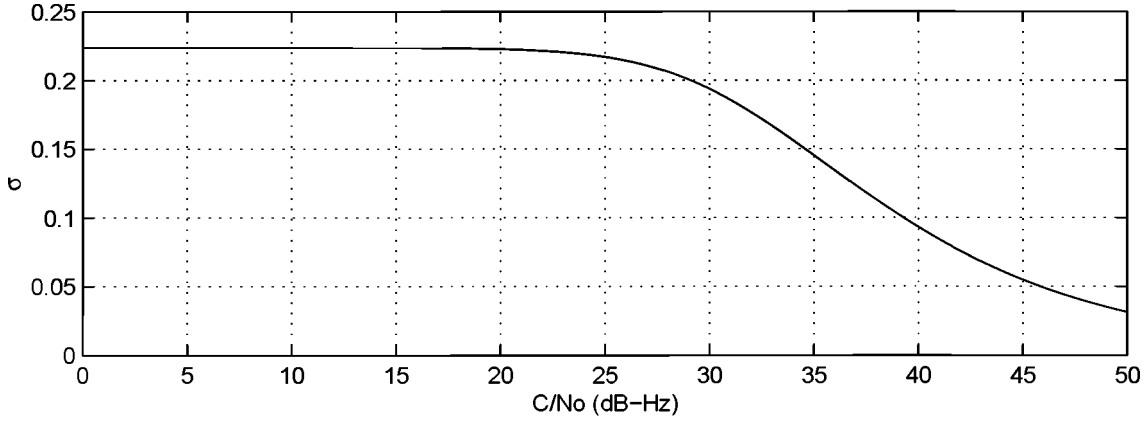

Figure 3.2: Normalized deviation of signal plus noise power, WBP_k, as a function of carrier to noise ratio.

For example, consider the test setups shown in Figure 3.3. We use a Northern Telecom STR2775 PC card single channel GPS simulator to provide a test signal. The 30 dB of attenuation between the simulator and the scintillation monitor sets the input signal level approximately to the signal level from an L1 GPS antenna with the Plessey-recommended 26 dB of preamplification. The two different arrangements used to provide 30 dB of attenuation allow us to set two different thermal noise levels for diagnostics.

In case (a), with a 50 dB attenuator followed by 20 dB of gain, the overall noise figure from output of the simulator onward is

$$NF = \frac{NF_{\mathrm{amp}}}{G_{\mathrm{att}}} + \frac{NF_{\mathrm{rcvr}} - 1}{G_1}, \tag{3.9}$$

where $G_{\mathrm{att}} = 10^{-5}$, the gain of the attenuator, and $G_1 = 10^{-3}$ is the overall gain between the simulator and the receiver. In contrast, the noise figure in case (b) is NF_{rcvr}/G_1. So with the low noise amplifier that we used, having $NF_{\mathrm{amp}} = 1.41$ in the worst case, the noise figure for case (a) is higher than case (b) by an added 1.41×10^5, *provided* that the receiver's noise figure does not change between the two

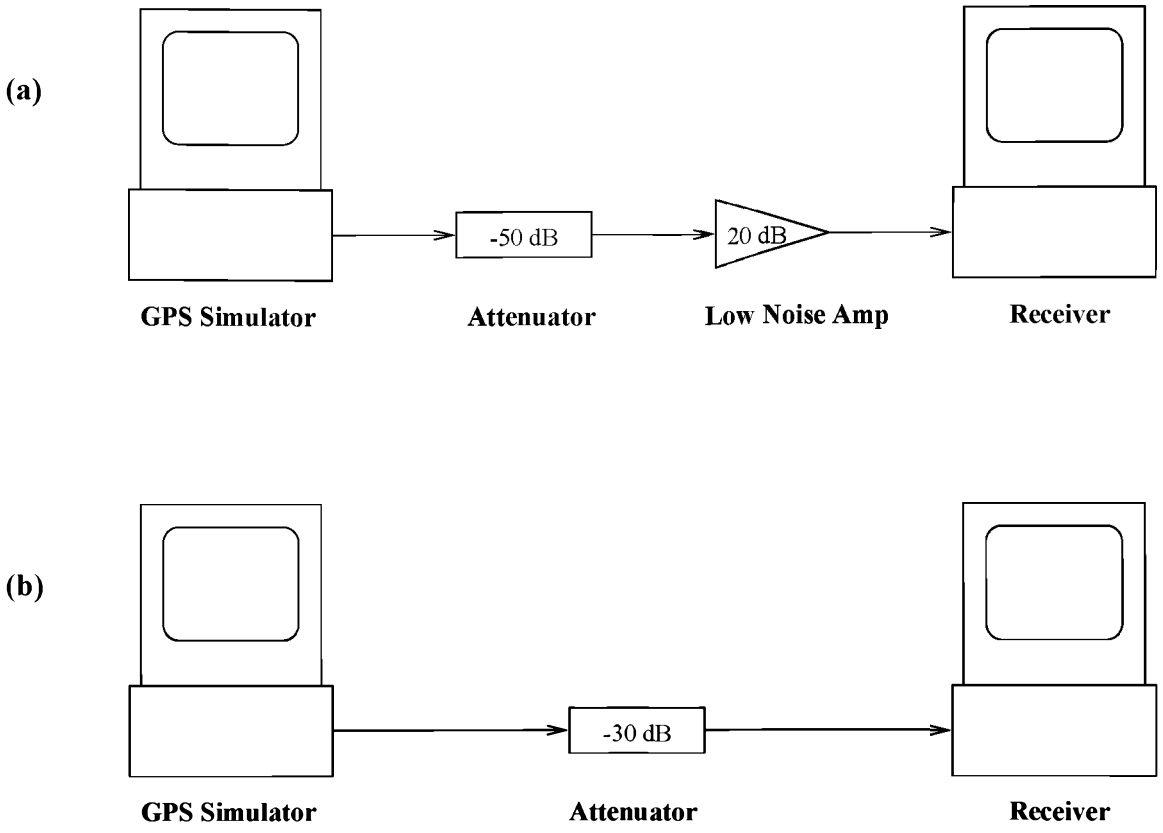

Figure 3.3: Setups used for laboratory testing of the scintillation monitor. Case (a) gives a higher thermal noise level than case (b). The simulator generates a single PRN code which modulates a 1.57542 GHz carrier (the GPS L1 frequency). The PC controlling the simulator can set the output signal amplitude over a ± 20 dB range and a simulated Doppler shift over a $\pm 15,000$ m/s range.

cases. Unfortunately, in the example below, the AGC responded to the difference in noise levels and the change in gain altered the receiver's noise figure so that this calculation does not strictly apply.

Figure 3.4 presents the results of two test cases using each of the setups shown in Figure 3.3. For tests with the simulator, we modified the scintillation monitor software slightly so that the receiver did not wait for a navigation solution, and the subsequent convergence of the oscillator error estimate, before starting scintillation data logging. (Having only one ranging signal does not permit a navigation solution.) In both cases, the simulator starts out with its signal level set to 0 dB. At the commencement of the test, the signal level goes to 10 dB for 10 s, providing a pulse to mark the start of the simulation. After the marker pulse, the simulation run continues at 5 dB for 30 s before the simulator turns off and the signal goes away.

Qualitatively, these simple tests verify that the variance of WBP_k does indeed increase with decreasing carrier to noise ratio, as expected, whether a decrease in signal strength or an increase in the noise level is the cause. Also, these tests demonstrate the automatic gain control circuit in action. The 10 dB setting on the simulator produces a roughly 3 dB higher value of WBP_k in the low noise case, case (b). This difference clearly does not result from the shift in the expected value of WBP_k due to noise (WBP_k goes up between the two tests although the noise level drops), and indicates that the AGC has changed the channel gain.

Quantitatively, the steps in WBP_k track the changes in signal strength almost exactly, the difference being the fixed contribution of noise. For example, in the low C/N_0 case, the mean of WBP_k drops by 4.5 dB between the 10 dB marker pulse and the 5 dB test signal. In the high C/N_0 case, the decrease is 4.6 dB. Using (3.8) and estimates of the mean and variance over the two segments, C/N_0 decreases from 47.9

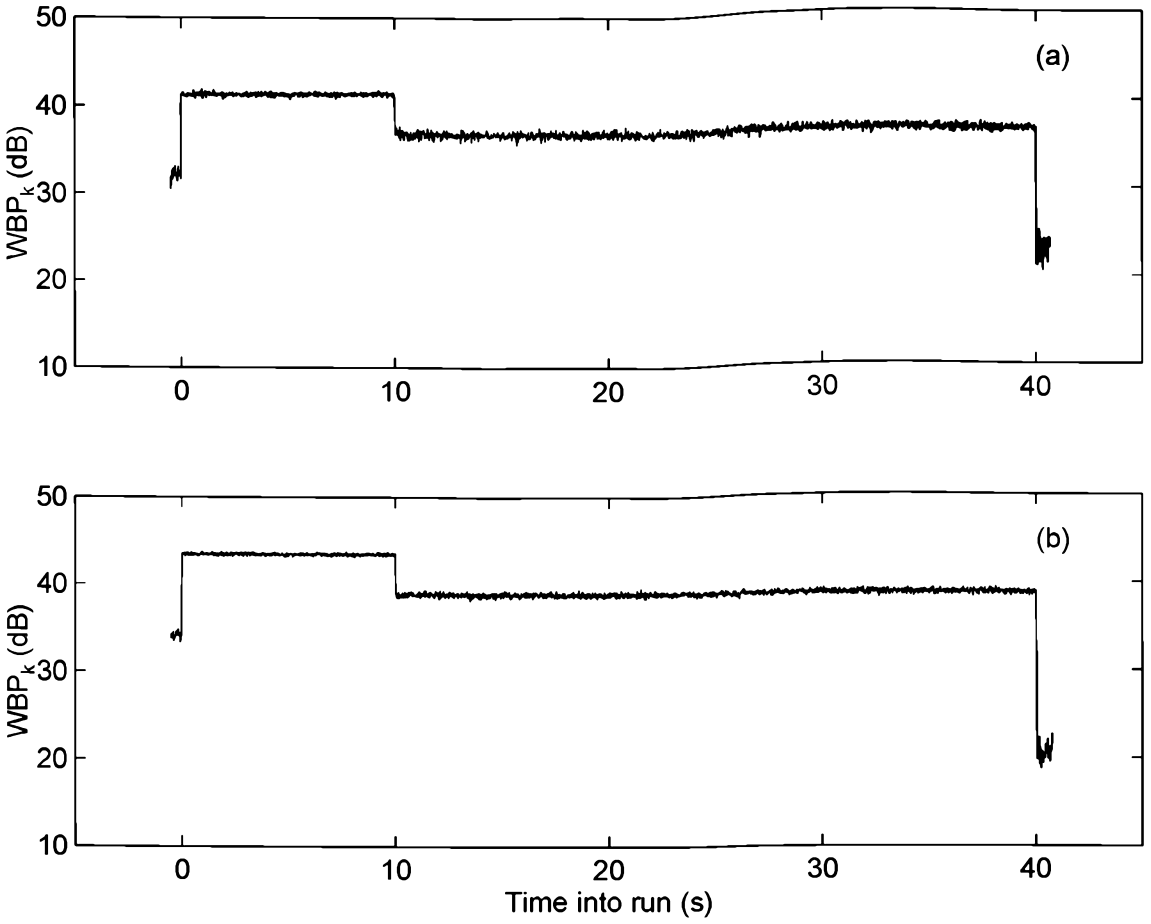

Figure 3.4: Simulation runs for simulator setups (a) and (b). In both cases the computer controlled simulator generates the same test pattern. The simulator idles at 0 dB until the operator starts the test. First the simulator sends out a 10 dB marker pulse for 10 s. The test continues at 5 dB for 30 s. Then the simulator shuts off.

to 43.7 dB-Hz in case (a) following the marker pulse, 52.7 to 47.6 dB-Hz in case (b). The latter is almost exactly the 5 dB by which the simulator's signal level changed.

Note that these estimates of C/N_0 using the mean and variance typically come out to be somewhat high compared another possible estimate. This second estimate employs the ratio of the wide band power at the 5 dB simulator setting to wide band power at the 10 dB setting:

$$\frac{\mathrm{E}\left\{\mathrm{WBP}_k\right\}_{5\mathrm{dB}}}{\mathrm{E}\left\{\mathrm{WBP}_k\right\}_{10\mathrm{dB}}} = \frac{10^{-0.5}S + N_0/T_c}{S + N_0/T_c}, \tag{3.10}$$

where S is the signal strength at the 10 dB setting, N_0 is the noise power spectral density (assumed to remain constant between settings) and T_c is the 1 ms C/A code period. Using the second estimate gives $C/N_0 = 43$ dB for the low noise setup and $C/N_0 = 42$ dB for the noisier setup, both at the 10 dB setting of the simulator. Errors in estimating the normalized variance perhaps cause this discrepancy. The latter, lower values are more consistent with typical values of carrier to noise ratio from field measurements calculated by using the noise channel measurements (see next section).

To test the frequency response of the scintillation monitor power measurements, we generated a frequency sweep ("chirp") on the simulator using the low C/N_0 test setup. Figure 3.5 shows the simulated signal and the receiver's response in one case. The chirp starts 20 seconds into the run, after a 10 dB marker pulse and an idling period at 5 dB. The chirp lasts for 100 seconds with a constant amplitude of 2 dB peak. Starting frequency is 0 Hz. Ending frequency is 25 Hz, the Nyquist frequency of the WBP_k measurement. The simulator updates its output amplitude during the chirp at a 50 Hz rate.

Clearly, the receiver has a slight dropoff in its amplitude response at high frequencies. This dropoff shows up to an extent in the spectrogram of WBP_k (Figure 3.6).

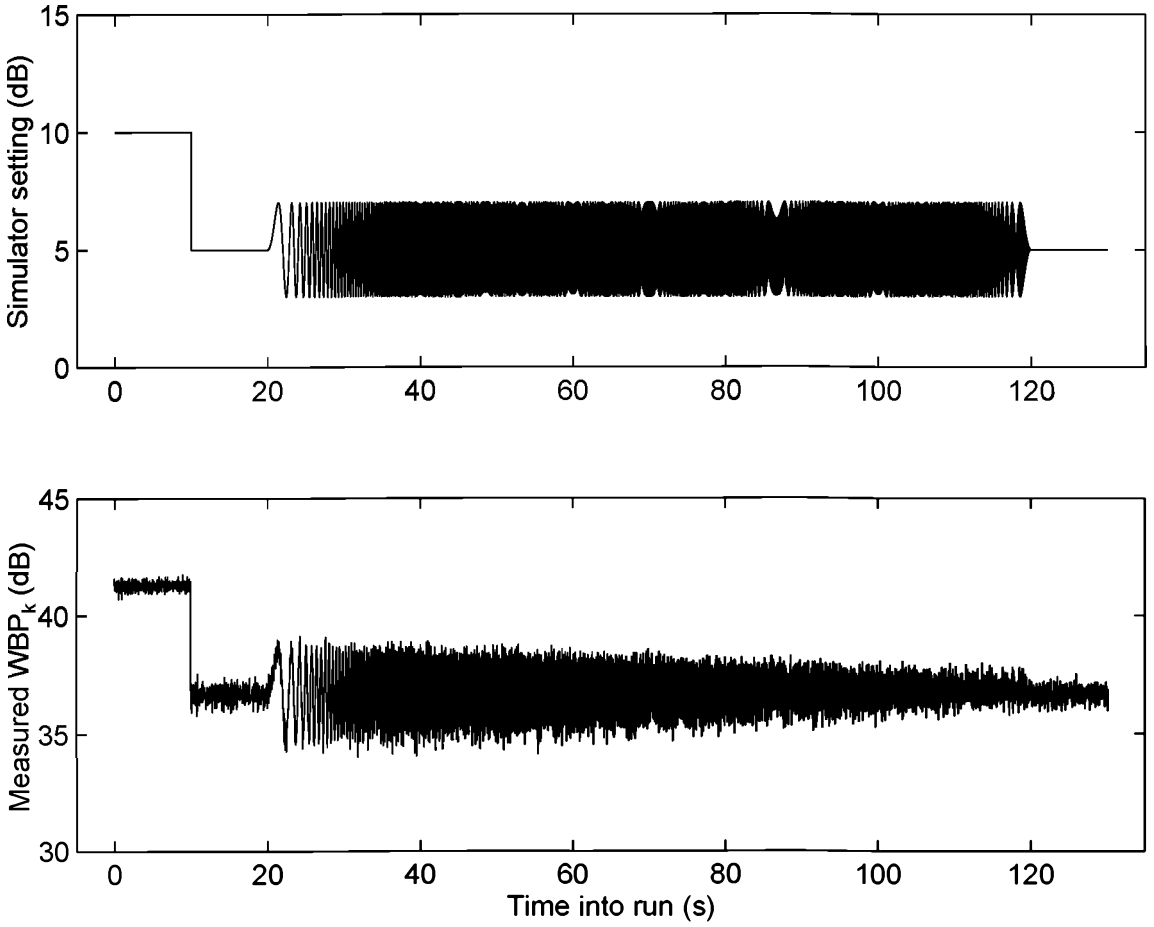

Figure 3.5: Sweep frequency, or "chirp," test of scintillation monitor. Top panel shows the amplitude setting on the simulator (in the low C/N_0 setup) as a function of time. The chirp begins 20 seconds into the run and lasts for 100 seconds. Bottom panel shows the GPS receiver response. The odd "envelopes" in the top panel (for example, near 70 and 85 seconds into the run) result from sampling effects.

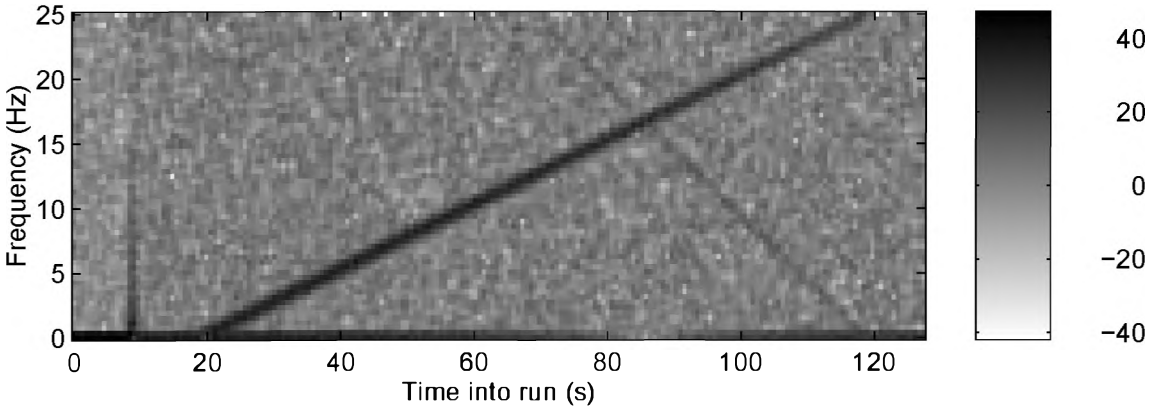

Figure 3.6: Spectrogram of receiver output during chirp test. Grayscale is in dB. The diagonal line slanted downwards is second harmonic power generated when the chirp signal changes frequency appreciably over the Fourier transform blocks.

More formally, Figure 3.7 plots the amplitude transfer function computed by dividing the Fourier transform of segments of the measured signal by those of the simulated signal and averaging to reduce the variance. Prior to computing the transfer function, we subtracted the mean from each of the signals to account for the unknown channel gain. This graph shows that the dropoff at the Nyquist frequency amounts to about 10 dB and that the 3 dB point lies roughly at 1 Hz.

Phase versus frequency (not shown) is predominantly linear and decreasing, indicating only a constant group delay. A quick estimate of the slope of phase versus frequency gives a 0.03 s group delay, some of which may be attributed to possible misalignment of the simulated signal relative to the measured signal. Misalignment by one sample would give 0.02 s delay, for example. At any rate, the group delay cannot be measured with assurance since we do not have absolute times recorded at the simulator setting changes in this case.

Overall, then, from simulator runs we see that wide band power gives a good indication of signal strength. Furthermore, the measured frequency response of the

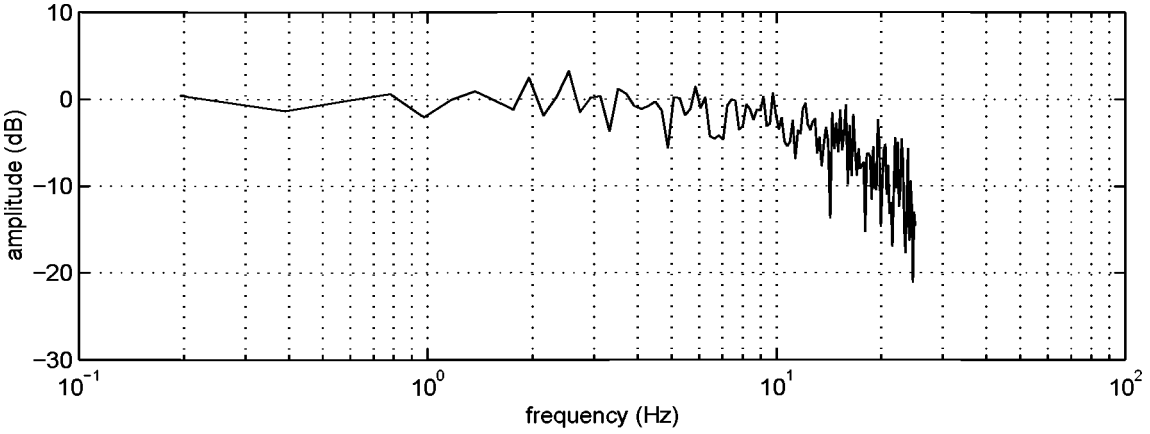

Figure 3.7: Amplitude of transfer function between simulated signal and scintillation monitor response. The phase (not shown) has a predominantly decreasing linear trend, indicating a constant group delay.

scintillation monitor shows that the receiver is capable of monitoring amplitude fluctuations at any rate, up to the Nyquist frequency of the WBP_k data. Generally, for convenience, we will assume that the fluctuations in WBP_k follow the fluctuations in signal; that is, a 5 dB change in signal gives a 5 dB change in WBP_k. Of course, this assumption is in error due to the constant (over fairly long periods) noise power included in WBP_k. If we require measurements of signal strength variations to be more accurate, we will subtract the noise power using the noise channel, as will be illustrated in the next section.

Note that we could use other estimators of signal strength. For example, NBP_k also tends to track power variations well. The quantity $\mathrm{NBP}_k - \mathrm{WBP}_k$, as suggested by *Van Dierendonck et al.* [1993] also works. These measures have larger scatter than WBP_k, however, owing to the larger deviation of NBP_k about its mean for a given carrier to noise ratio [*Van Dierendonck*, 1996]. Larger variance means more difficulty in identifying weaker amplitude scintillations.

Another benefit to using wide band power as the measurement of signal plus

noise power is that the estimate can be readily extended to longer blocks of time. For example, suppose that we wish to examine the signal plus noise power over one second intervals, rather than 20 ms intervals. All we need to do is add together the 50 samples of WBP_k that comprise each second to form a new wide band power estimate with $M = 1000$. Naturally, the normalized deviation of this new, long time scale, wide band power improves to $\sqrt{20/1000} = 0.14$ of the deviation of the 20 ms sums. One second wide band power sums provide useful reduced data sets for summary plots.

3.6 Measurement Examples

So far we have studied the response of the power measurement in the scintillation monitor in theory and in simulator tests. Now, we consider measurements from the field, some of which were taken under equatorial spread F conditions and contain amplitude scintillations. We acquired these data from two stations in South America during October 1996, concurrently with the NSF-sponsored MISETA III (Multi-Instrumented Study of Equatorial Thermospheric Aeronomy) campaign, and later during April 1997. One of the stations was located at Ancon, Peru, north of Lima and a few tens of kilometers away from the Jicamarca Radio Observatory. This first station actually had two GPS receivers, part of an experiment to measure east-west drifts. The other station was located at San Miguel de Tucuman, Argentina, in the northwestern part of the country. Magnetically, the Ancon station lies very near the dip equator; the Tucuman station lies just south of the southern equatorial anomaly.

3.6.1 Power Variations

Several factors affect received signal amplitude. At the longest time scale, the position of the satellite relative to the receiver sets the basic signal strength pattern. Rising and setting satellites are further away and thus have weaker signals than satellites near zenith. Overall, then, signal amplitude generally increases and then decreases over a period of 6–8 hours as a satellite moves across the sky. Spacecraft and receiver antenna patterns superimpose variations on this basic pattern at a somewhat faster rate. Multipath typically causes variations on shorter time scales yet. Scintillations produce amplitude fluctuations with periods of seconds. The fastest variations, from sample to sample, stem from the variance of the signal strength estimator due to measurement noise.

Out of all these variations, we are interested only in the scintillations. Fortunately, they may be identified by their time scale. Only multipath sometimes occurs on a similar time scale. Satellite motion and antenna pattern effects are slower; measurement variance is faster. Figure 3.8 illustrates all of these types of variations in signal strength for data from the Ancon east receiver on 6 and 7 October 1996, using one second averages of wide band power rather than 20 ms sums (indicated by WBP_{1s}). One of these days, 07 October, had amplitude scintillations from roughly 0215 to 0415 UT. Clearly, the general background trend repeats from day to day. Closer inspection reveals that the pattern actually occurs about four minutes earlier in UT on the 7th. This four minute shift gibes with the 12 *sidereal* hour orbits of the GPS satellites.

We can identify the various time scales of variability in these plots and their probable causes. The slow increase and then decrease over the nearly 9 hours of the plots shows the effect of the satellite rising and setting. The longer period "wiggles," such as the slight dip in power just after 0400 UT, probably stem from antenna pattern

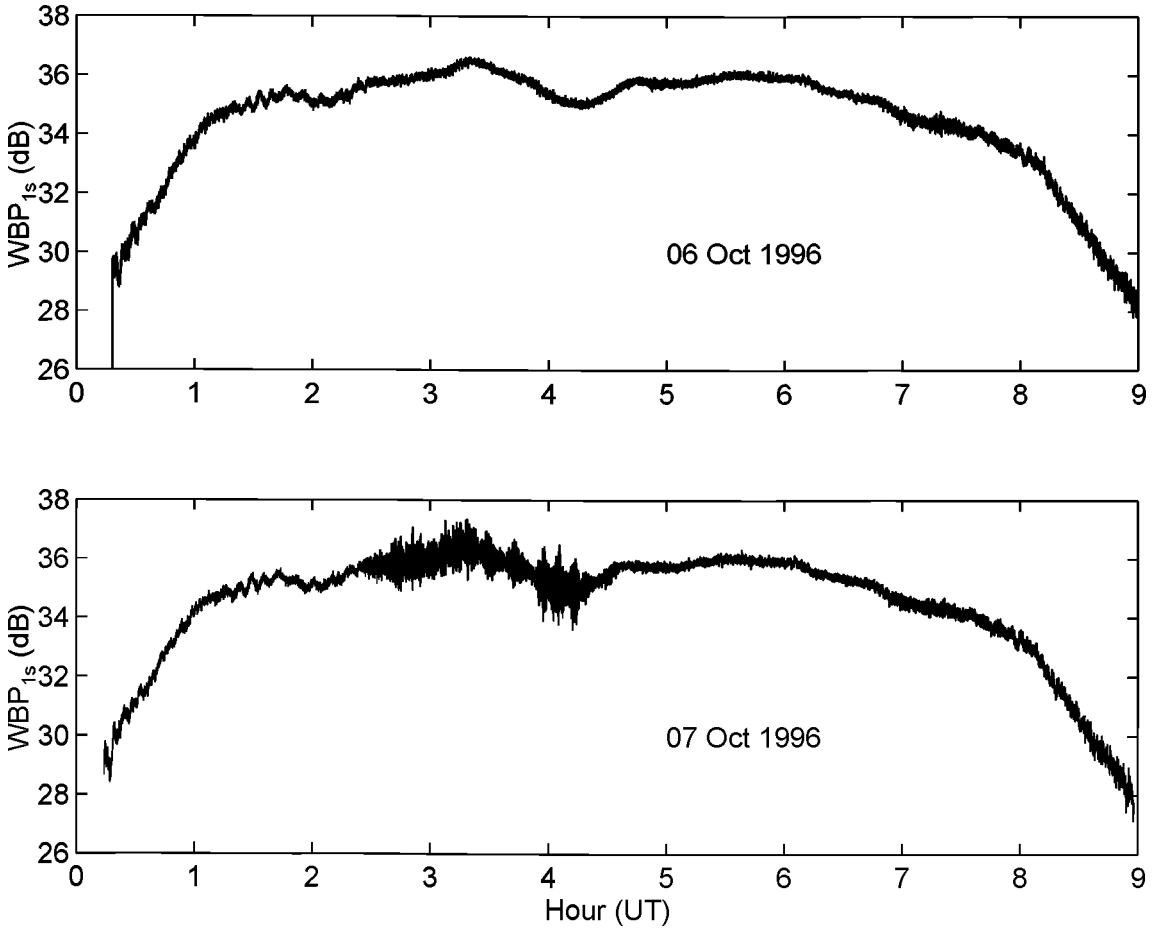

Figure 3.8: Comparison of power measurements on successive days for the Ancon east receiver. These data are one second averages, rather than 20 ms values, of wide band power measurements from PRN 14. Comparison of the two plots shows the repeatability of the background trend from day to day. Scintillations occurred between about 0215 and 0415 UT on 07 October (2115–2315 local on 06 October).

effects. Multipath effects generally appear as quasisinusoidal ripples with periods of several minutes, like those near 0130 UT and 0800 UT. Scintillations manifest as an irregular thickening of the trace with a time scale too short to be seen on a plot covering several hours. Measurement variance yields the normal thickening of the trace throughout the rest of the plot.

3.6.2 Multipath

Multipath deserves further discussion since it is the one form of signal strength variation most likely to be confused with scintillations. While multipath and scintillations may be readily separated in the 07 October 1996 data from PRN 14 at the Ancon east station, this easy identification is not always possible. For example, consider the power measurements from the Tucuman station for the same pair of dates and the same satellite (Figure 3.9). These data show much more variation, repeatable from day to day, due to multipath. Further, the repeatable variation sometimes occurs on a fine enough time scale to give nearly the appearance of weak scintillations, as between 0500 and 0700 UT in these plots. Closer inspection, however, reveals a similar pattern of quasiperiodic fluctuations with periods of tens of seconds from one day to the next (Figure 3.10). Such fine time scale repeatability is not visible in the Ancon east receiver data and indicates probable multipath effects. The difficulty these fine multipath variations pose is that they are almost at the same time scale as scintillations, particularly if the satellite motion happens to nearly match the drift of the ionospheric irregularities, slowing down the scintillation "fading rate."

Ideally, the best way to mitigate the effects of multipath is to install the antenna in a low multipath environment. Unfortunately such ideal locations are not always available. Our experience indicates that the best antenna placement for minimizing

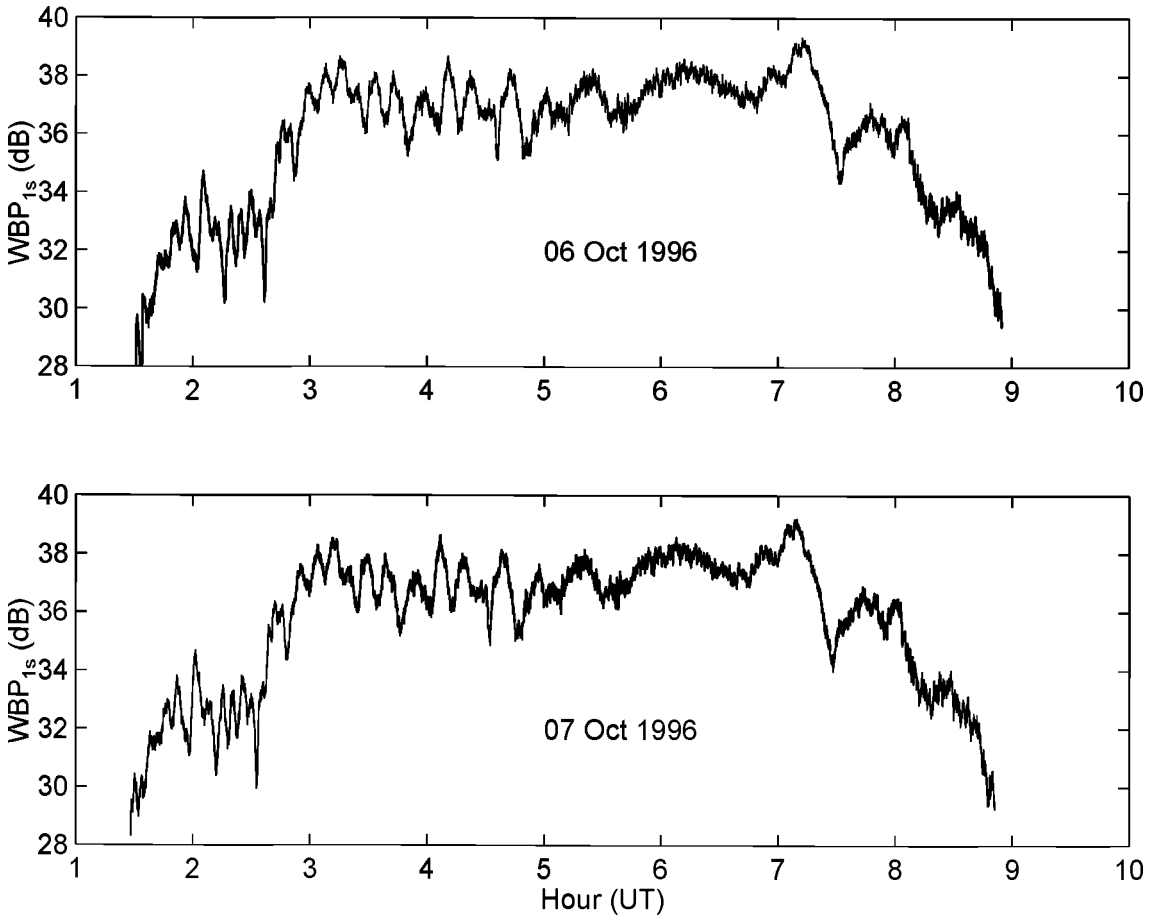

Figure 3.9: Comparison of power measurements on successive days for the Tucuman receiver. These data are again one second averages of wide band power measurements from PRN 14. This installation had much worse multipath than either Ancon receiver.

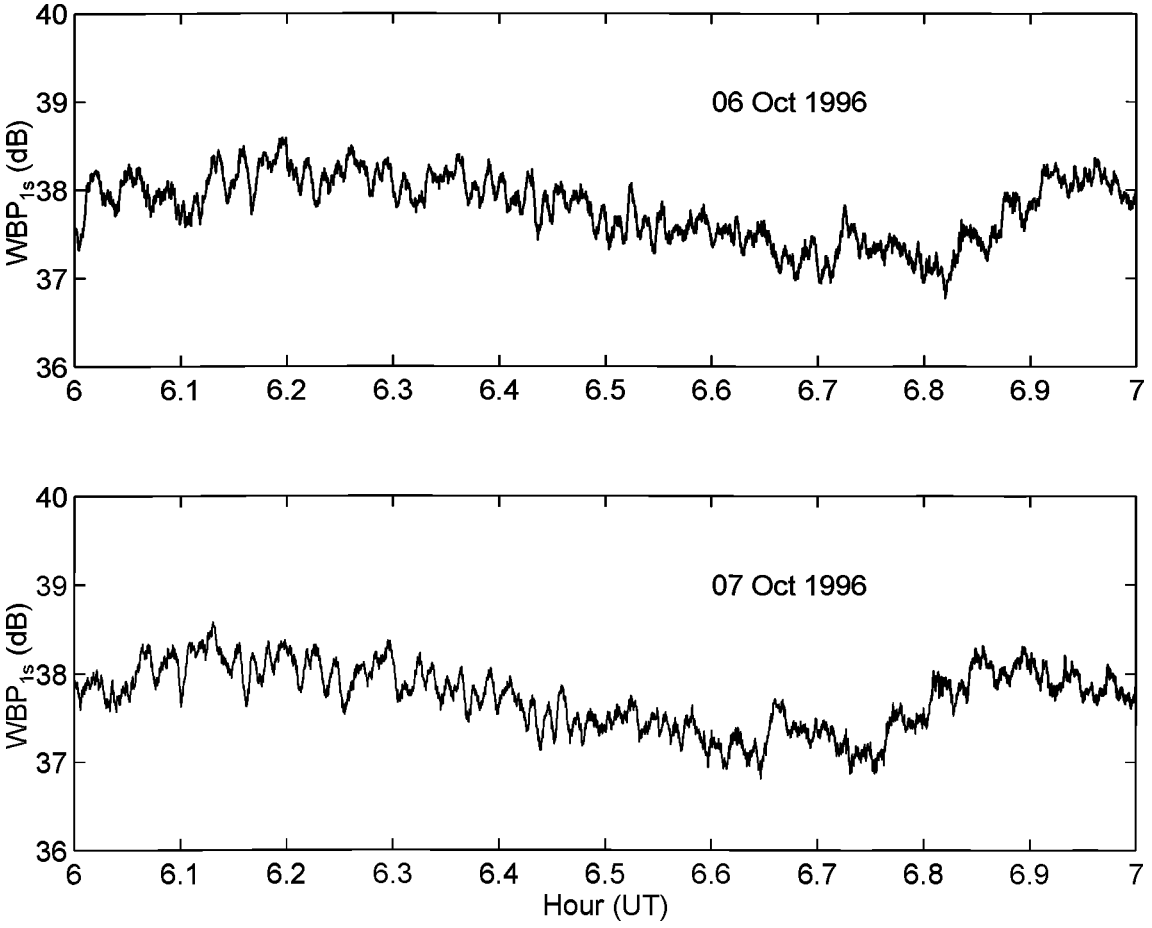

Figure 3.10: Fine time scale comparison of power measurements on successive days for the Tucuman receiver and PRN 14. Such day to day near repeatability at time scales of tens of seconds does not appear in the Ancon receiver data. Here also the sidereal shift of almost 4 minutes from one day to the next is clearly visible.

multipath is on a metal ground plane, on the ground, away from buildings, trees, hills, etc. At the Ancon site, for example, we had the luxury of a large, open desert field surrounding the operations building that housed the GPS receivers. We were able to place the eastern antenna on the ground far from most obstructions. To obtain sufficient east-west separation of the antennas to allow spaced receiver drift measurements, however, we located the western antenna in a less ideal spot, near some trees and buildings. Further, during the October 1996 campaign we placed the antenna on top of a wire spool about 1.5 meters high in an attempt to clear some obstructions. The result was greater multipath for the western antenna compared to the eastern one. In Tucuman we operated the receiver from a university campus with several multistory buildings. The only way to get adequate visibility of the sky was to place the antenna on the roof of the Physics building. This placement led to the terrible multipath problems visible in Figure 3.9.

One common myth about multipath is that it predominantly affects satellites near the horizon, with lines of sight that pass near to scattering objects on the ground. This bromide definitely holds for multipath effects on pseudorange. (See graphs of total electron content computed from pseudorange measurements in *Wanninger et al.* [1994], for example.) So we were surprised to discover significant fluctuations, apparently due to multipath, for satellites at high elevations. The problem seems to be diffraction of the GPS radio waves, which are reflected from below, around the edges of small ground planes.

Of course, each antenna should have a ground plane for several reasons. First, the antenna must be situated over a good conductor to establish the correct antenna impedance. Second, the ground plane prevents reflected waves from below the antenna from entering through back lobes. Last, the ground plane keeps the antenna from

seeing the bulk of the noise temperature of the ground. Apparently, however, we underestimated the ability of the 0.19 m wavelength L1 frequency waves to scatter efficiently from small objects. By unhappy coincidence, we also made the square ground planes for the October 1996 campaign very nearly 2.5 L1 wavelengths on a side. Consequently, we surmise that something like the situation sketched in Figure 3.11 occurred.

To fix this problem we tried two approaches for the April 1997 campaign which seemed to be helpful. In Ancon, we set the western antenna and its ground plane directly on the ground, rather than on a wire spool. In Tucuman, where buildings obstructed the view from the ground, we constructed a larger, 2 m square, ground plane out of wire mesh with a wood framework and placed it under the antenna and its small ground plane.

Power measurements are more sensitive to the effects of short distance multipath than pseudorange measurements. Because we overlooked this sensitivity and relied on conventional wisdom concerning multipath derived from experience with pseudoranges, we originally missed the potential for diffraction around the ground plane edges to influence the measurements. Multipath has two effects on the signal received by the antenna. First, the reflected signals add copies of the pseudorandom noise code with varying time delays to the original signal. Second, the reflected signals have longer phase paths, plus changes in phase due to the reflection process, and can partially interfere with the direct signal. The sensitivity of power measurements to short range multipath derives from partial constructive and destructive interference which alternate periodically as the reflected path length changes with satellite motion. In such case, naturally, the received signal strength changes over time.

On the other hand, the pseudorange measurements depend more on the shape

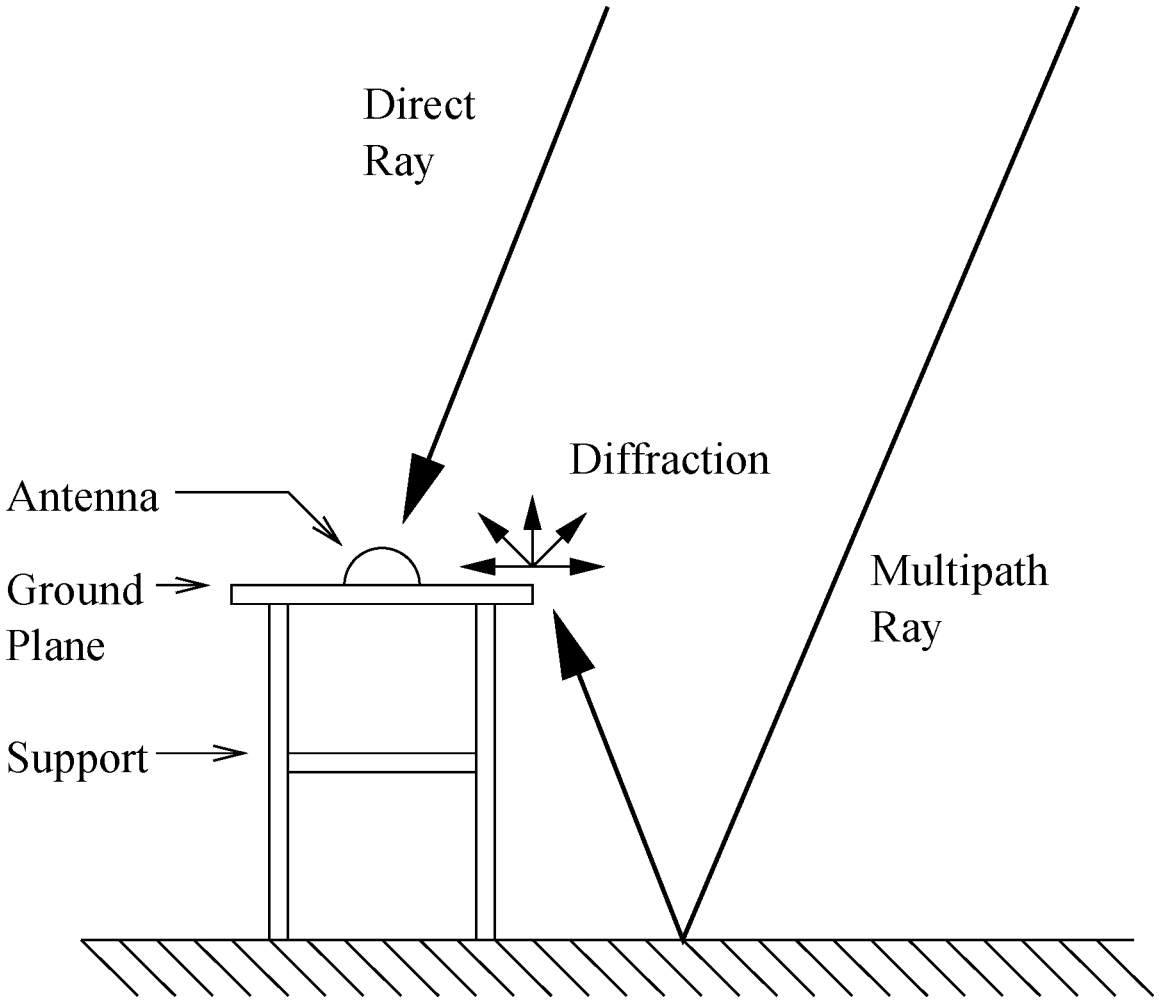

Figure 3.11: Sketch of hypothesized diffraction of multipath ray around the ground plane for a high elevation satellite and an elevated GPS antenna.

of the correlation peak and less on the absolute signal strength for the early-late correlation scheme. For long time delays, corresponding to path differences of the order of hundreds of meters, the reflected signal adds an extra, small correlation peak to the side of the main correlation peak at later lags. An altered shape for one side of the net correlation results. So, instead of straddling the main peak when the early-late correlation difference is zero, the correlators may be pulled off to one side, giving a timing error in the calculation of pseudorange. (This problem may be minimized by using a narrower correlator spacing than 1/2 chip [*Van Dierendonck*, 1996].)

For shorter time delays, corresponding to path differences between the direct and multipath signal of the order of meters, the distortion of the correlation peak is less; the added peak is displaced from main peak by only 1% of a chip or so. Consequently, the pseudorange error is small. When the signal amplitude changes due to interference effects, both early and late correlations change by the same amount, not affecting the early-late correlation difference or the timing error.

Since subtle multipath effects have a stronger influence on power measurements than conventional GPS measurements like pseudorange, one must expect to process data with multipath effects present. Even the best installations have some multipath; even satellites at higher elevations, above a selected mask angle, have signal strength variations due to the interference of direct and reflected signals. One way to reduce the effects of multipath capitalizes on its repeatability from one day to the next. One can detrend the power measurements on a day with suspected scintillation activity by using the previous day's power data, provided that the previous day was quiet and that the sidereal time shift is applied. A simpler, albeit somewhat *ad hoc*, approach that we have found to work is to filter the wide band power data with a high pass filter having a cutoff of 0.1 Hz and a gradual frequency rolloff below the cutoff. This

filtering also removes the other slow trends due to satellite motion.

3.6.3 Noise and Gain

Up to now, we have ignored the possibility of changes in wide band power due to changes in the receiver gain over time, particularly from AGC action. Also, we have not considered subtracting the noise power from the total power to examine signal strength alone. The noise channel measurement gives us the ability to estimate both of these effects simultaneously and to form carrier to noise, C/N_0, measurements directly.

The data that this section uses for illustration come from April 1997 measurements from the Ancon station. Earlier campaigns and other stations used an older version of the scintillation monitor software which had problems with the noise channel data. Specifically, the older versions allowed the local oscillator to change on the noise channel when no code lock attained, in a futile attempt to search a range of Doppler bin settings. Of course, the receiver never achieved code lock since the noise channel used an unassigned PRN code. These changes in the local oscillator setting caused spikes of power in the noise channel at semiregular intervals. While the data from the older software are probably usable with filtering to remove these spikes, we may use the data from the newer version of the software with more confidence.

Since, ideally, there is no correlation between the PRN code used in the noise channel and any of the PRN codes which may be observed, the expected value of WBP_k on the noise channel amounts to

$$\mathrm{E}\left\{\mathrm{WBP}_k\right\} = \frac{MT_c^{\,2}}{2}\left(\frac{N_0}{T_c}\right), \tag{3.11}$$

using (3.6). So to eliminate the effect of noise power in wide band power measure-

ments, we need only subtract the noise channel WBP_k from the desired satellite channel WBP_k to yield a measurement with the expected value

$$\mathrm{E}\left\{\mathrm{WBP}_k^{\mathrm{Channel}} - \mathrm{WBP}_k^{\mathrm{Noise}}\right\} = \frac{MT_c^{\,2}}{2}S. \tag{3.12}$$

Naturally, (3.12) still can vary with changes in gain since S can. Alternatively, we can estimate C/N_0 using the following formula

$$\widehat{C/N_0} = 10\log_{10}\left(\frac{1}{T_c}\frac{\mathrm{WBP}_k^{\mathrm{Channel}} - \mathrm{WBP}_k^{\mathrm{Noise}}}{\mathrm{WBP}_k^{\mathrm{Noise}}}\right), \tag{3.13}$$

since any changes in gain affect both channels equally (they process the raw signal from the RF chip, correlated with different PRN codes). To improve this estimate, we may average $\mathrm{WBP}_k^{\mathrm{Noise}}$ over a longer period since we do not expect much short term variation of the ambient noise level.

Figure 3.12 presents noise channel measurements from the Ancon east station for a portion of one night during the April 1997 campaign. The figure also includes a low pass filtered (1/400 Hz cutoff) version of the data showing that, although the noise channel $\mathrm{WBP}_{1\mathrm{s}}$ has a lot of measurement scatter, the mean value does not change much throughout this period. Figure 3.13 shows the results of using the filtered noise channel data to subtract the noise power from raw $\mathrm{WBP}_{1\mathrm{s}}$ measurements and to compute the C/N_0 estimate.

Of course, two parameters affect the noise channel measurements, the channel gain set by the AGC and the actual noise level. Both of these factors influence the satellite channel's wide band power too. Consequently, separating the two effects becomes difficult. If we subtract the noise channel power from the satellite channel, the resulting signal may still vary due to gain changes. If we eliminate the effects of the gain by forming the C/N_0 estimate, changes in noise level will change this value

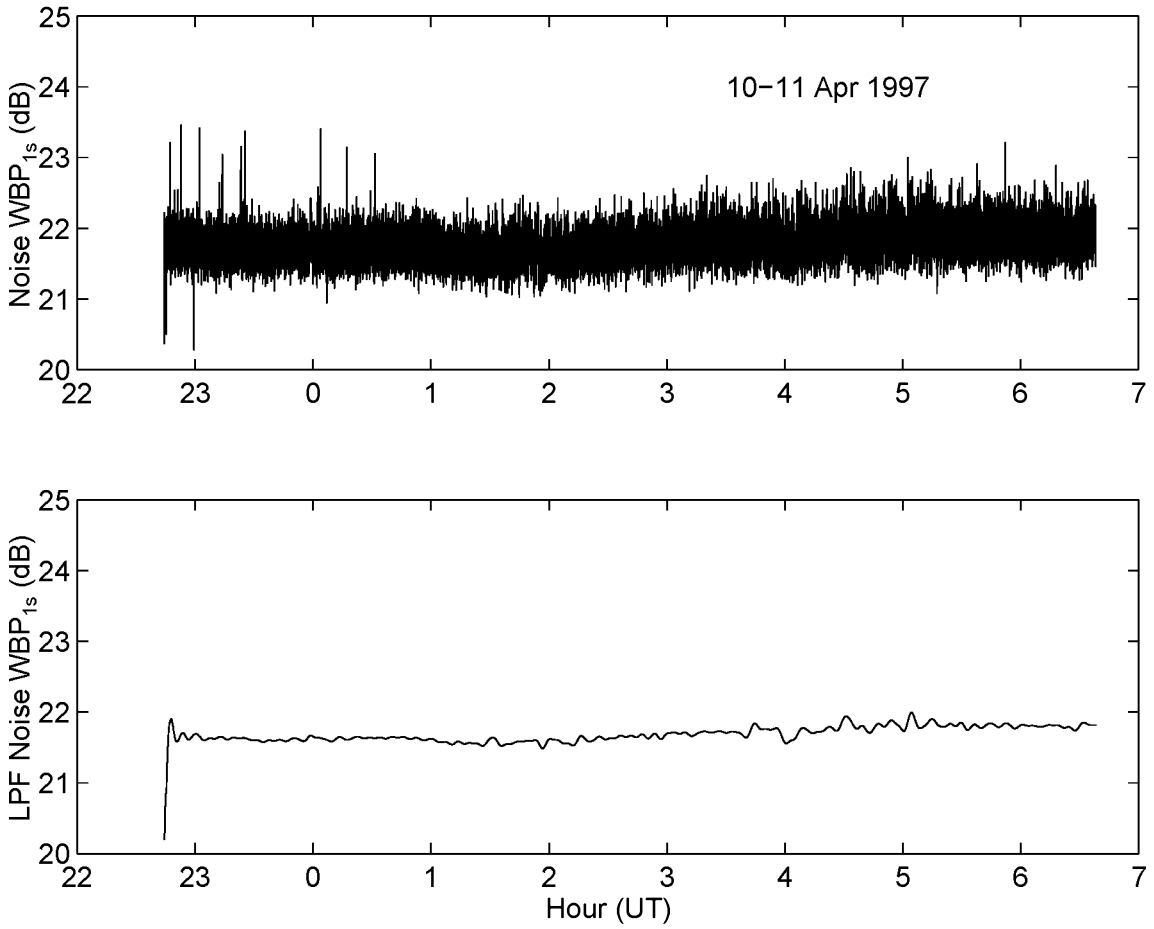

Figure 3.12: Noise channel measurements from Ancon east station for night of 10–11 April 1997. The top plot is raw wide band power, averaged over one second intervals ($\mathrm{WBP_{1s}}$). The bottom plot shows the average values of $\mathrm{WBP_{1s}}$ obtained by low pass filtering with a 1/400 Hz cutoff.

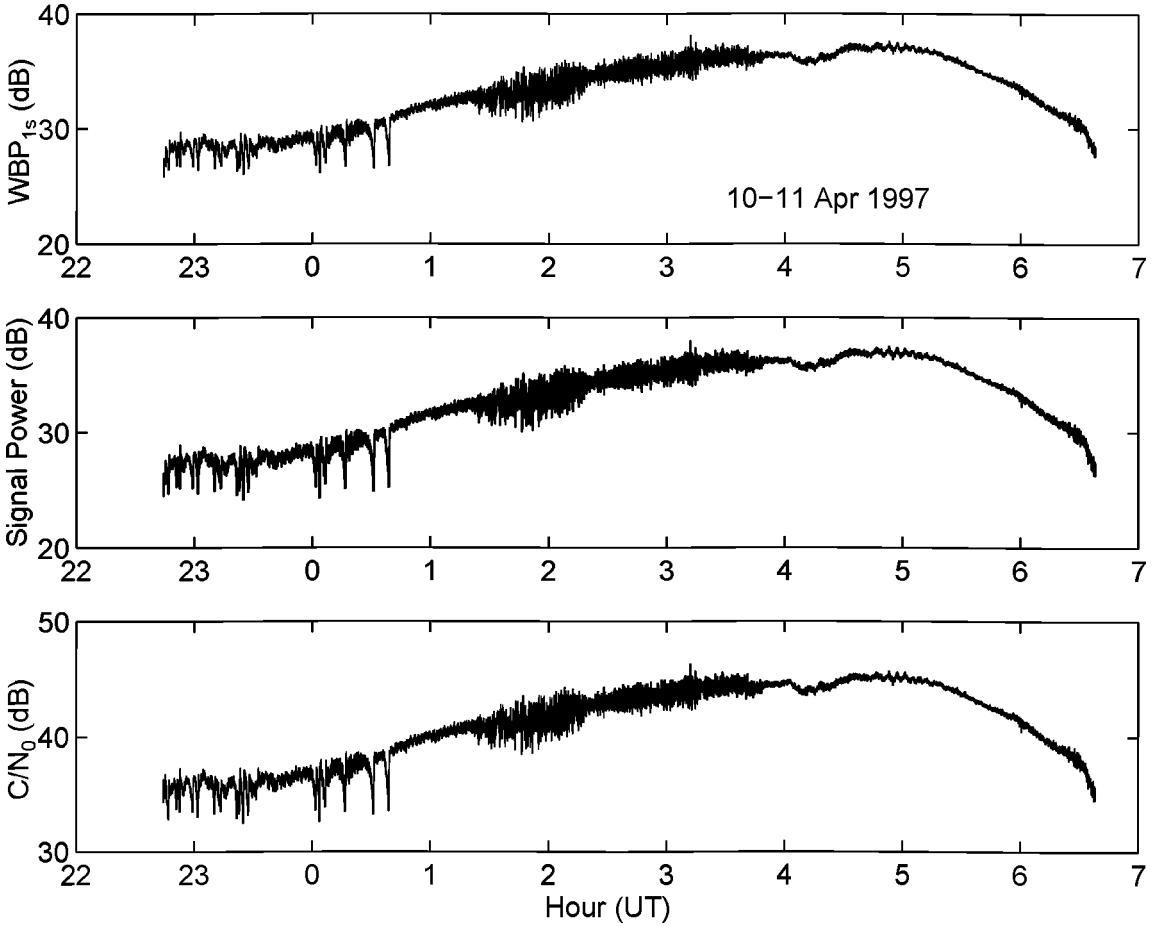

Figure 3.13: Measurements from the Ancon east station for PRN 9, processed using low pass filtered noise WBP_{1s}. These data are from the night of 10–11 April 1997. Top graph shows raw WBP_{1s} measurements. Scintillations occurred from about 0130–0400 UT during this night. The middle graph shows the effect of subtracting noise power. Bottom graph shows carrier to noise ratio estimates based on channel WBP_{1s} and filtered noise power.

even as the signal strength remains constant. (Noise levels can vary when sources of interference switch on and off, for example.)

Van Dierendonck et al. [1993] also make the latter point about using C/N_0 to monitor scintillations. Their receiver has the AGC disabled so that they do not have the former problem. They adopt another signal strength estimator based on WBP_k and NBP_k which supposedly minimizes the effect of noise variations. Unfortunately, the scatter in this measure is fairly large owing to its use of NBP_k. In our case, with a noise channel available, we note that the noise measurement fortunately does not vary much over the course of a day's measurements. Rather than adopt the approach of *Van Dierendonck et al.* [1993], then, we will continue to use raw wide band power measurements, or wide band power with the filtered noise channel power subtracted, for scintillation studies.

Chapter 4

Scintillations

4.1 Introduction

Nearly everyone has observed optical scintillation effects, disturbances in the propagation of light passing through an irregular medium. Common examples are the twinkling of stars caused by propagation through the turbulent atmosphere and the distortion seen through the unstable hot air above a candle flame. In general, passage through a medium with irregularities in refractive index modifies the amplitude and phase of electromagnetic waves, differently at different portions along the wave front. The effect on signal amplitude can be complicated since constructive and destructive interference occur as the wave propagates away from the medium.

We have already discussed amplitude scintillations of GPS signals from a phenomenological standpoint in Chapter 3. Now we turn to their origin in electromagnetic scattering from ionospheric electron density irregularities. Most of the material in this chapter is of a review nature. Nevertheless, it presents some new results for specific cases of the phase screen model.

Maxwell's equations form the starting point for our discussion of electromagnetic wave scattering. In our case, the necessary equations are

$$\nabla \cdot (\epsilon \boldsymbol{\mathcal{E}}) = 0, \tag{4.1}$$

$$\nabla \times \boldsymbol{\mathcal{E}} = -\mu_0 \frac{\partial \boldsymbol{\mathcal{H}}}{\partial t}, \tag{4.2}$$

$$\nabla \times \boldsymbol{\mathcal{H}} = \frac{\partial (\epsilon \boldsymbol{\mathcal{E}})}{\partial t}, \tag{4.3}$$

for propagation through a region with no free charges or current density and a permittivity $\epsilon = \epsilon(\boldsymbol{r}, t) = \epsilon_0 \langle \epsilon_r \rangle [1 + \epsilon_1(\boldsymbol{r}, t)]$, where ϵ_0 is the permittivity of free space, $\langle \epsilon_r \rangle$ is the average value of relative permittivity in the medium and ϵ_1 represents the fluctuations in permittivity. (Alternatively, ϵ may incorporate the effects of free charges and current densities.) Specifically, permittivity is a random function of position and time associated with electron density irregularities. Note that ϵ_1 need not be small, in general. The notation is merely a convenient way to break up the permittivity. Finally, $\boldsymbol{\mathcal{E}} = \boldsymbol{\mathcal{E}}(\boldsymbol{r}, t)$ and $\boldsymbol{\mathcal{H}} = \boldsymbol{\mathcal{H}}(\boldsymbol{r}, t)$ denote the electric and magnetic field intensities, respectively, while μ_0 is the permeability of free space.

From the first equation

$$\nabla \cdot \boldsymbol{\mathcal{E}} = -\boldsymbol{\mathcal{E}} \cdot \nabla \ln \epsilon, \tag{4.4}$$

replacing the normal free space relation that $\nabla \cdot \boldsymbol{\mathcal{E}} = 0$. Following the usual procedure to obtain a wave equation, we take the curl of the second Maxwell equation, yielding

$$\nabla \times (\nabla \times \boldsymbol{\mathcal{E}}) = \nabla(\nabla \cdot \boldsymbol{\mathcal{E}}) - \nabla^2 \boldsymbol{\mathcal{E}} = -\mu_0 \frac{\partial}{\partial t} (\nabla \times \boldsymbol{\mathcal{H}}), \tag{4.5}$$

in Cartesian coordinates. Finally, we substitute the third Maxwell equation for $\nabla \times \boldsymbol{\mathcal{H}}$ and the relation derived from the first Maxwell equation for $\nabla \cdot \boldsymbol{\mathcal{E}}$. The result is a wave equation,

$$\nabla^2 \boldsymbol{\mathcal{E}} - \frac{n^2}{c^2} \frac{\partial^2}{\partial t^2} \left[(1 + \epsilon_1) \boldsymbol{\mathcal{E}} \right] = -\nabla \left[\boldsymbol{\mathcal{E}} \cdot \nabla \ln(1 + \epsilon_1) \right], \tag{4.6}$$

where we have substituted the expression for ϵ and $n^2 = \langle \epsilon_r \rangle$ is the average refractive index. Clearly, if $\epsilon_1 \equiv 0$, as in a medium of constant refractive index, the homogeneous wave equation for the propagation of electromagnetic radiation results.

Following *Tatarskii* [1971], we let $\boldsymbol{\mathcal{E}} = \mathrm{Re}[\boldsymbol{E}(\boldsymbol{r},t)e^{-i\omega t}]$, where $\boldsymbol{E}$ is complex. Making this substitution and rearranging yields

$$\nabla^2 \boldsymbol{E} + k^2(1+\epsilon_1)\boldsymbol{E} = -\nabla\left[\boldsymbol{E}\cdot\nabla\ln(1+\epsilon_1)\right] - 2ik\eta\frac{\partial(\epsilon\boldsymbol{E})}{\partial t} + \frac{n\eta}{c}\frac{\partial^2(\epsilon\boldsymbol{E})}{\partial t^2}. \tag{4.7}$$

Here $k = n\omega/c$ is the wave number of the wave in a medium with uniform refractive index n and $\eta = (1/n)\sqrt{\mu_0/\epsilon_0}$. If ϵ_1 varies slowly enough in time, the last two terms on the right hand side may be neglected (see *Tatarskii* [1971] for a more detailed elaboration of the conditions required). If the scale lengths of variations in ϵ_1 are much greater than the wavelength $2\pi/k$, and if we consider only small angle forward scattering (more on this later), we may also neglect the first term on the right hand side [*Tatarskii*, 1971]. Thus, the resulting wave equation for propagation through a medium with refractive index irregularities is the vector Helmholtz equation

$$\nabla^2 \boldsymbol{E} + k^2(1+\epsilon_1)\boldsymbol{E} = 0. \tag{4.8}$$

For linear polarization, we may adopt coordinates such that only one electric field component is nonzero, giving a scalar equation. *Tatarskii* [1971] and *Born and Wolf* [1975] also show that for propagation through an optical system, in this case through the irregular medium, a complex scalar amplitude adequately represents the total electric field (or magnetic field) in a scalar Helmholtz equation. The scalar Helmholtz equation is

$$\nabla^2 \mathcal{A} + k^2(1+\epsilon_1)\mathcal{A} = 0, \tag{4.9}$$

where $\mathcal{A}$ is the complex amplitude of the electric field. The intensity, or power, in the electromagnetic wave is $\mathcal{I} \propto |\mathcal{A}|^2$. Often, we will take the proportionality constant to

be unity, which is equivalent to absorbing it into the definition of $\mathcal{A}$. At any rate, the scalar Helmholtz equation (4.9) is a typical starting point for scattering calculations for high frequency electromagnetic waves [*Lovelace*, 1970; *Tatarskii*, 1971; *Yeh and Liu*, 1982].

What have we lost in approximating (4.7) by the vector Helmholtz equation (4.8)? Certainly some nonlinear interaction in space and time between ϵ and $\boldsymbol{E}$ is missing. However, all of these interactions are small for high frequency wave propagation given the criteria listed earlier, particularly for small fluctuations in permittivity. Now the only time dependence of $\boldsymbol{E}$ derives from the variation of ϵ with time, a simple dependence since no derivatives of $\boldsymbol{E}$ with respect to time appear. If the wave's transit time through the medium is short compared to the fastest fluctuation time scale, and measurements are taken sufficiently close together in time, each measurement reflects a "snapshot" of the current propagation conditions.

By using the homogeneous Helmholtz equation we also lose coupling among the various Cartesian components of $\boldsymbol{E}$. For example, a wave linearly polarized in the x direction remains so throughout the medium. This amounts to an assumption of forward scattering or small angle scattering; that is, most of the scattered energy is in the direction parallel to the original direction of propagation for a transverse electromagnetic wave. To see that small angle scattering is not strictly the case, consider the field scattered from a single electron into angle θ as shown in Figure 4.1. In addition to an x component, the electric field acquires a z component in this example. The direction of energy flux in the far field, as given by the Poynting vector, depends on the angle back to the scatterer.

Nevertheless, as is clear from the radiation pattern of an elementary dipole, the scattered energy flux for this incident polarization diminishes as $\cos^2\theta$, going to zero

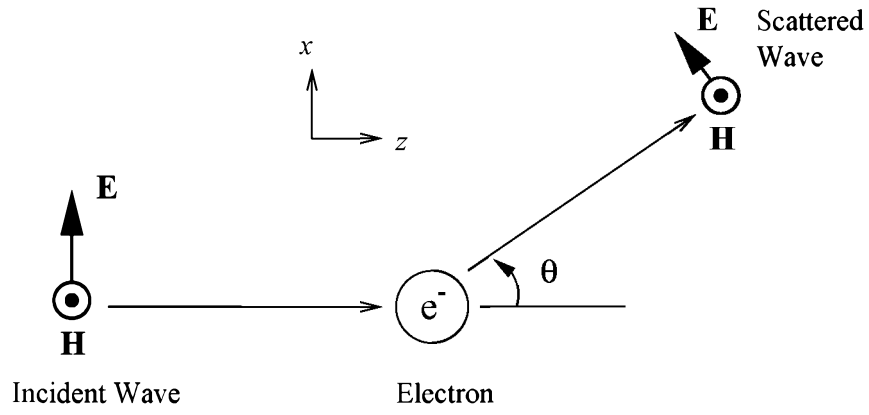

Figure 4.1: Scattering of an incident electromagnetic wave by a single electron.

for $|\theta| \rightarrow 90^\circ$ (perpendicular scattering out of the plane of the figure occurs, however). Also, the electron scatters very little of the original energy since its scattering cross section is small. Most of the incident wave's energy continues to propagate in its original direction. The region of irregularities must be sufficiently thin in the direction of propagation, however, so that the transverse deviations of the wave are small, for the Helmholtz equation (4.9) to be a good approximation [*Lovelace*, 1970]. How thin the layer must be depends on the strength of the scattering, of course.

To investigate the effects of the irregularities on the propagation of the radio wave, we follow *Tatarskii* [1971] and consider the scalar wave equation for a medium of uniform refractive index n:

$$\nabla^2 \mathcal{A} + k^2 \mathcal{A} = 0. \tag{4.10}$$

Now, the Green's function for the inhomogeneous version of this equation (source term of $\delta(\boldsymbol{r} - \boldsymbol{R})$) is

$$G_0(\boldsymbol{r} - \boldsymbol{R}) = -\frac{\exp(ik|\boldsymbol{r} - \boldsymbol{R}|)}{4\pi|\boldsymbol{r} - \boldsymbol{R}|}. \tag{4.11}$$

What we wish to find is the Green's function for (4.9) at a given time t (assuming that the irregularities vary much more slowly with time than the wave's transit through

the medium); that is, we want the solution to

$$\nabla^2 \mathcal{A} + k^2[1 + \epsilon_1(\boldsymbol{r})]\mathcal{A} = \delta(\boldsymbol{r} - \boldsymbol{R}). \tag{4.12}$$

Formally, we rearrange this equation so that the term including the permittivity variations appears as a source term

$$\nabla^2 \mathcal{A} + k^2 \mathcal{A} = \delta(\boldsymbol{r} - \boldsymbol{R}) - k^2 \epsilon_1(\boldsymbol{r})\mathcal{A}, \tag{4.13}$$

and convolve with the Green's function G_0 to get

$$\mathcal{A}(\boldsymbol{r}) = G_0(\boldsymbol{r} - \boldsymbol{R}) - k^2 \int d\boldsymbol{r}'\, G_0(\boldsymbol{r} - \boldsymbol{r}')\epsilon_1(\boldsymbol{r}')\mathcal{A}(\boldsymbol{r}'). \tag{4.14}$$

Of course, the problem is that the desired quantity $\mathcal{A}$ also appears on the right hand side, inside the integral.

Not to be daunted, we substitute (4.14) back into the integral and obtain

$$\begin{aligned}\mathcal{A}(\boldsymbol{r}) = {} & G_0(\boldsymbol{r} - \boldsymbol{R}) - k^2 \int d\boldsymbol{r}'\, G_0(\boldsymbol{r} - \boldsymbol{r}')\epsilon_1(\boldsymbol{r}')G_0(\boldsymbol{r}' - \boldsymbol{R}) \\ & + k^4 \iint d\boldsymbol{r}' d\boldsymbol{r}''\, G_0(\boldsymbol{r} - \boldsymbol{r}')\epsilon_1(\boldsymbol{r}')G_0(\boldsymbol{r}' - \boldsymbol{r}'')\epsilon_1(\boldsymbol{r}'')\mathcal{A}(\boldsymbol{r}'').\end{aligned} \tag{4.15}$$

We could now conceivably repeat the process and iterate *ad infinitum.* Naturally, the convergence of this process is not likely unless the variations in permittivity are small.

What do we gain by this exercise, where at each step $\mathcal{A}$ gets buried in successively more complicated integrals? Well, if we may justify truncating the series at some point by eliminating the last term containing $\mathcal{A}$, we come up with an approximation for the Green's function which represents propagation through the irregular medium. More importantly, each of the terms has simple physical significance in terms of scattering. The first term on the right hand side of (4.15) represents direct propagation through

the medium with no scattering; it is exactly the Green's function for a homogeneous medium. The second term represents the effect of waves propagating directly into the scattering volume, interacting with the fluctuation in ϵ at a single point and then propagating directly out, summed over all possible interaction points. Higher order terms in the continued series would represent multiple scatterings: two, three and so on.

Although *Tatarskii* [1971] does not explicitly mention it, the series gained by iterating (4.15) is essentially the Born series of quantum theory (for example, see *Ryder* [1985]). If the permittivity fluctuations are small enough that we may truncate (4.15) after the single scattering term, we get the "first Born approximation," also known as the single scatter approximation. Roughly put, this approximation states that, for weak fluctuations in refractive index, the incident wave passes through the medium essentially unchanged and that the scattering at each point reflects only scattering from the incident wave. Specifically, the contributions from the scattered fields of other points are negligible.

4.2 Scattering Example

To gain some geometrical insight into the scattering problem which will be useful later, we consider the following case. Again, much of this discussion parallels *Tatarskii* [1971]. Suppose we have a point source at $\boldsymbol{R}$ and a receiver at $\boldsymbol{r}$. Interposed between them, perpendicular to the line of sight, lies a thin medium of thickness L containing weak irregularities in permittivity. Figure 4.2 illustrates the geometry. Now, what we wish to do is to calculate the direct and singly scattered wave field at the receiver using the first two terms of (4.15). Note that the following "derivation" will be far

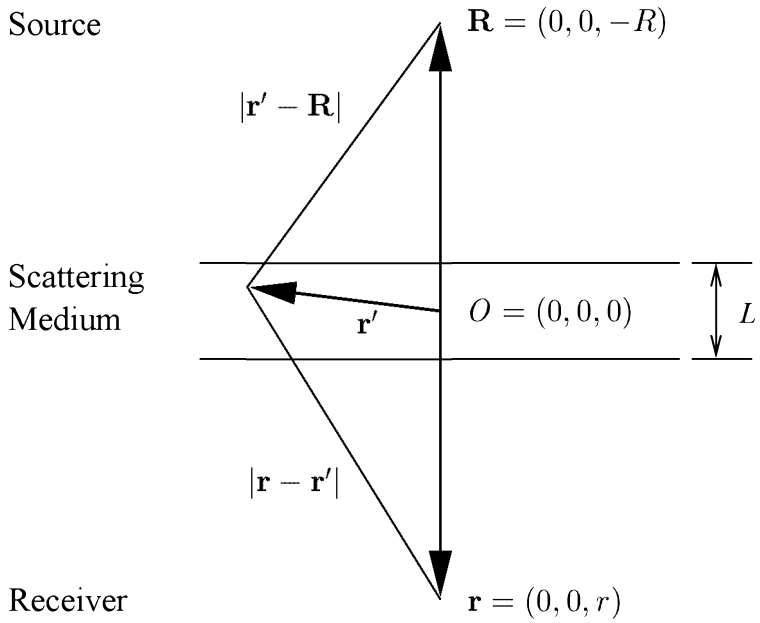

Figure 4.2: Scattering geometry for single scatter example. A slab containing weak irregularities lies perpendicular to the line of sight between a source and a receiver. The coordinate origin is in the middle of the slab, along the line of sight. The z axis points along the line of sight, toward the receiver.

from rigorous.

The scattering integral of interest is

$$\begin{aligned} I &= \int d\boldsymbol{r}'\, G_0(\boldsymbol{r} - \boldsymbol{r}')\epsilon_1(\boldsymbol{r}')G_0(\boldsymbol{r}' - \boldsymbol{R}) \\ &= \frac{1}{16\pi^2}\int d\boldsymbol{r}'\, \frac{\exp\left[ik\left(|\boldsymbol{r} - \boldsymbol{r}'| + |\boldsymbol{r}' - \boldsymbol{R}|\right)\right]}{|\boldsymbol{r} - \boldsymbol{r}'||\boldsymbol{r}' - \boldsymbol{R}|}\, \epsilon_1(\boldsymbol{r}'), \end{aligned} \tag{4.16}$$

substituting (4.11) for G_0. The phase term in the exponential is the crucial part. First, $|\boldsymbol{r} - \boldsymbol{r}'| + |\boldsymbol{r}' - \boldsymbol{R}|$ is simply the length of the piecewise straight line path from $\boldsymbol{R}$ to $\boldsymbol{r}'$ and then to $\boldsymbol{r}$. Now, we assume that the distances from the scattering medium to the source and the receiver are both much greater than the wavelength $\lambda = 2\pi/k$. When $\boldsymbol{r}'$ lies near the line of sight, the phase does not vary rapidly along this path with varying $|\boldsymbol{r}'|$. The larger $|\boldsymbol{r}'|$ becomes, however, the more rapidly the phase along the path varies. As the phase varies rapidly, the exponential term oscillates rapidly,

eventually faster than the fluctuations in ϵ_1 (assuming the variations in ϵ_1 to be bounded by an inner scale l_0, as is physically reasonable). Since the average of the exponential over a cycle is zero, the contributions to the integral for very large $|\boldsymbol{r}'|$ become negligible. Said the other way around, the bulk of the contribution to the integral comes from paths which are close in length to the line of sight path.

How close in length to the line of sight path must the paths be to contribute to the integral? As a first guess we estimate that the extra length should be no greater than $\lambda/2$ so that the phase factors of all these paths add constructively. This region of $\boldsymbol{r}'$ values is the "first Fresnel zone." (The region of $\boldsymbol{r}'$ values with extra path lengths in the range of $\lambda/2$ to λ is the second Fresnel zone, and so on. These zones become more and more closely spaced as $|\boldsymbol{r}'|$ gets larger.) What does the first Fresnel zone look like? The curve for which $|\boldsymbol{r}-\boldsymbol{r}'|+|\boldsymbol{r}'-\boldsymbol{R}| = |\boldsymbol{r}-\boldsymbol{R}|+\lambda/2$ marks its boundary. In other words, the boundary curve is the locus of all points $\boldsymbol{r}'$ such that the sum of the distance between $\boldsymbol{r}'$ and $\boldsymbol{R}$ and the distance between $\boldsymbol{r}'$ and $\boldsymbol{r}$ is a constant: an ellipsoid with foci at $\boldsymbol{R}$ and $\boldsymbol{r}$.

Assuming that the source and the receiver are far away from the scattering medium, the ellipsoid bounding the first Fresnel zone is very elongated along the line of sight. Since $\epsilon_1(\boldsymbol{r}') \equiv 0$ outside the scattering medium, the only contribution to the scattering integral I comes from the intersection of the ellipsoid and the scattering medium, hatched in Figure 4.3a. For a thin scattering layer, not too close to either focus, we may approximate the intersection as a cylinder. Figure 4.3b illustrates the geometry to be used to estimate the cylinder's radius r_F, called the Fresnel radius.

Mathematically, we want to find r_F so that $R_1 + r_1 = R + r + \lambda/2$. Since $R \gg r_F$ and $r \gg r_F$,

$$R_1 \approx R + \frac{1}{2}\frac{{r_F}^2}{R}, \tag{4.17}$$

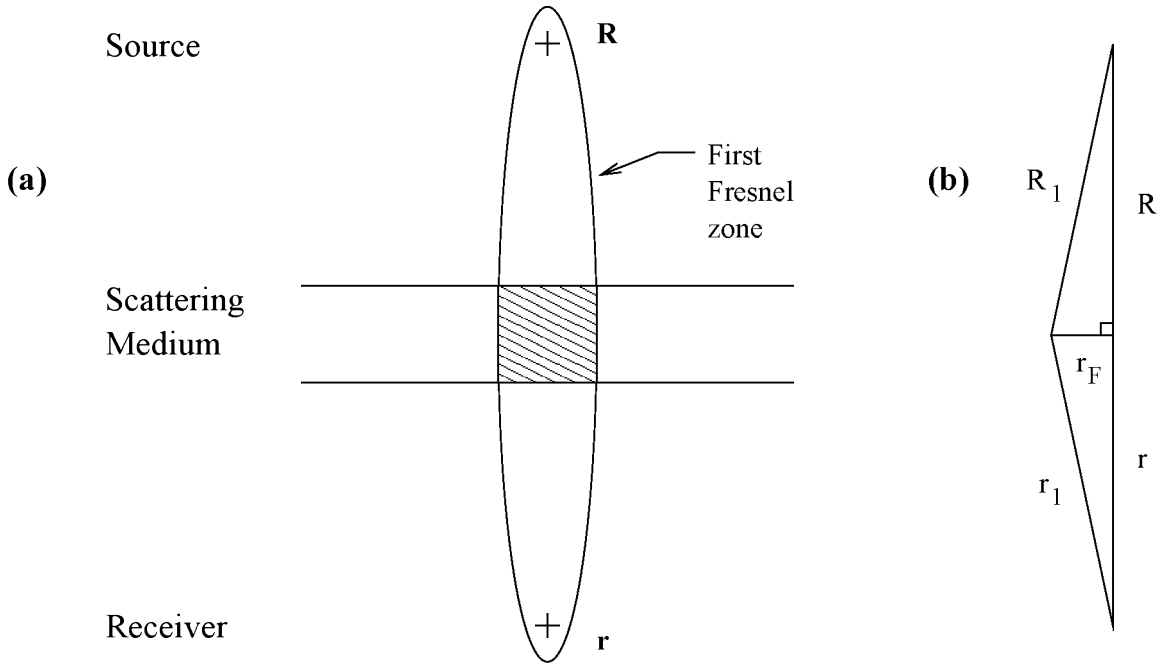

Figure 4.3: Sketch of Fresnel zone geometry. (a) Cross section of the ellipsoid that bounds the first Fresnel zone. The hatched area of intersection, approximately the cross section of a right circular cylinder, represents the key contribution to the scattering integral. (b) Geometry used to estimate the radius of the cylinder (r_F).

$$r_1 \approx r + \frac{1}{2}\frac{{r_F}^2}{r}. \tag{4.18}$$

Adding these expressions, setting the sum equal to $R + r + \lambda/2$ and solving for r_F yields

$$r_F = \sqrt{\lambda\left(\frac{rR}{r+R}\right)}. \tag{4.19}$$

When the source is so distant that the waves reaching the scattering layer are almost plane waves, $R \gg r$ and the Fresnel radius simplifies to $r_F = \sqrt{\lambda r}$.

Now we may approximate the scattering integral I. Assuming that the smallest scale size of the irregularities is much larger than the Fresnel radius ($l_0 \gg r_F$), ϵ_1 may be pulled out of the transverse (x' and y') integrals, allowing for possible variations along the line of sight (z' direction) and giving

$$I \approx \frac{1}{16\pi^2}\int_{-L/2}^{L/2} dz'\ \epsilon_1(0,0,z') \int_{-\infty}^{\infty}\int_{-\infty}^{\infty} dx'dy'\ \frac{\exp\left[ik\left(|\boldsymbol{r}-\boldsymbol{r}'| + |\boldsymbol{r}'-\boldsymbol{R}|\right)\right]}{|\boldsymbol{r}-\boldsymbol{r}'||\boldsymbol{r}'-\boldsymbol{R}|}. \tag{4.20}$$

Furthermore, we leave the limits of the x' and y' integrals as $\pm\infty$ without much error. The contribution of the remaining portion of the integral for $x'^2 + y'^2 > {r_F}^2$ is small thanks to the rapid oscillation of the exponential integrand.

Analogous to the approximations for R_1 and r_1 used to calculate the Fresnel radius,

$$|\boldsymbol{r}-\boldsymbol{r}'| \approx r - z' + \frac{1}{2}\frac{x'^2+y'^2}{r-z'}, \tag{4.21}$$

$$|\boldsymbol{r}'-\boldsymbol{R}| \approx R + z' + \frac{1}{2}\frac{x'^2+y'^2}{R+z'}, \tag{4.22}$$

within the scattering volume. Following usual practice, we approximate $|\boldsymbol{r}-\boldsymbol{r}'|$ with $r - z'$ in the denominator of the integrand, but retain the second order terms in the exponential. Treating $|\boldsymbol{r}'-\boldsymbol{R}|$ similarly gives

$$\begin{aligned} I &\approx \frac{e^{ik(r+R)}}{16\pi^2}\int_{-L/2}^{L/2} dz'\ \frac{\epsilon_1(0,0,z')}{(r-z')(R+z')}\iint dx'dy'\ \exp\left[\frac{ik}{2}\frac{(x'^2+y'^2)(r+R)}{(r-z')(R+z')}\right] \\ &= \frac{e^{ik(r+R)}}{16\pi^2}\int_{-L/2}^{L/2} dz'\ \frac{\epsilon_1(0,0,z')}{(r-z')(R+z')}\left[\frac{2\pi i}{k}\frac{(r-z')(R+z')}{r+R}\right], \end{aligned} \tag{4.23}$$

evaluating the Gaussian integral. Finally, simplifying,

$$I = \frac{ie^{ik(r+R)}}{8\pi k(r+R)} \int_{-L/2}^{L/2} dz' \; \epsilon_1(0,0,z'). \tag{4.24}$$

Now, we substitute our estimate for I back into the first Born approximation,

$$\mathcal{A}(\boldsymbol{r}) = G_0(\boldsymbol{r} - \boldsymbol{R}) - k^2 I, \tag{4.25}$$

and obtain,

$$\mathcal{A}(\boldsymbol{r}) = -\frac{e^{ik(r+R)}}{4\pi(r+R)} \left[1 + \frac{ik}{2} \int_{-L/2}^{L/2} dz' \; \epsilon_1(0,0,z')\right]. \tag{4.26}$$

Thus, the received amplitude appears as a wave which had propagated straight through a homogeneous medium with wave number k, multiplied by a correction factor that depends on the integrated irregularities along the line of sight.

What is the significance of the correction factor? Consider the accumulated phase along the line of sight (the "optical path" in the terminology of *Yeh and Liu* [1982]),

$$\Delta\phi = \int_{-R}^{r} dz' \; k\sqrt{1 + \epsilon_1(0,0,z')}. \tag{4.27}$$

For small fluctuations in ϵ we expand the square root and obtain

$$\Delta\phi = k(r+R) + \frac{k}{2} \int_{-L/2}^{L/2} dz' \; \epsilon_1(0,0,z'). \tag{4.28}$$

So the phase term in $\mathcal{A}(\boldsymbol{r})$ that one would estimate from the optical path amounts to

$$e^{i\Delta\phi} = e^{ik(r+R)} \exp\left[\frac{ik}{2} \int_{-L/2}^{L/2} dz' \; \epsilon_1(0,0,z')\right]. \tag{4.29}$$

If we further assume that the *integrated* permittivity fluctuations are small, we can expand the second exponential term on the right to give

$$1 + \frac{ik}{2} \int_{-L/2}^{L/2} dz' \; \epsilon_1(0,0,z'). \tag{4.30}$$

This expression is exactly the correction factor appearing in (4.26). (*Tatarskii* [1971] shows that assuming the integrated permittivity fluctuations are small is not strictly necessary. He obtains a power series expansion for the higher order scattering terms, under the assumption of straight line propagation, which sums exactly to the exponential of the phase from the integrated fluctuations.)

So, we have demonstrated the plausibility that propagation through an irregular medium may, under certain restrictive conditions, be regarded as if the primary effect of the medium were to alter the optical path length. To zeroth order, the effect of the irregularities, integrated along the line of sight, is to alter the phase of the received signal. The required conditions do not strictly hold for the propagation of GPS signals through ionospheric irregularities; for example, the Fresnel radius for the ionospheric F peak at the GPS wavelength (0.19 m in free space) is around 260 m and incoherent scatter radar observations tell us that 3 m irregularities exist in equatorial spread F. Nevertheless, the idea of collapsing the irregularities along the line of sight into a single phase term is a useful one and suggests immediately the "phase screen" model.

4.3 Phase Screen

Historically, the phase screen was among the first models used to study propagation through ionospheric irregularities [*Booker et al.*, 1950; *Hewish*, 1951]. The model is simple. One treats the random medium as if all its effects on the wave can be boiled down to abrupt changes in phase as the wave front crosses a plane between the source and the observer. (More generally, *Booker et al.* [1950] also considered changes in amplitude across that plane.) Otherwise, the wave propagates through a homogeneous medium, usually free space. Calculations are also relatively simple with

this model. The wave incident on the screen is usually a plane wave (occasionally a spherical wave). After the screen, the wave front generally has random phasing all across it and calculating the field seen by the observer becomes akin to an aperture antenna problem or a diffraction problem.

Figure 4.4 illustrates the geometry typically used for phase screen calculations. For now we assume normal plane wave incidence on the scattering layer and defer the complications of oblique incidence until later. From Huygens' principle, the random perturbations in phase immediately below the screen spread outward spherically and have complicated interactions. Not only does the received signal's phase change over the observation plane, but the amplitude varies as well, thanks to interference. If the phase pattern on the screen changes, evolving with time or merely drifting, a stationary receiver observes both phase and amplitude fluctuations: i.e., phase and amplitude scintillations.

Mathematically, we represent an incoming plane wave as $\mathcal{A}(x, y, z) = \exp(ikz)$, suppressing the $\exp(-i\omega t)$ time dependence and normalizing the amplitude. The field upon reaching the screen at $z = 0$ is then unity. Immediately below the screen the field becomes $\mathcal{A}^+(x, y) = \mathcal{A}(x, y, z = 0^+) = \exp[i\phi(x, y)]$, where $\phi(x, y)$ is the phase that the screen imparts. Further below the screen the field becomes more complicated (see *Yeh and Liu* [1982], for example):

$$\begin{aligned} \mathcal{A}(x, y, z) &= \frac{k}{2\pi z} \iint dx'dy' \; e^{i\phi(x', y')} \exp\left\{ \frac{ik}{2z} \left[(x - x')^2 + (y - y')^2 \right] \right\} \\ &= \frac{1}{{r_F}^2} \int d\boldsymbol{\rho}' \; \mathcal{A}^+(\boldsymbol{\rho}') \exp\left[i\pi \left(\frac{\boldsymbol{\rho} - \boldsymbol{\rho}'}{r_F} \right)^2 \right], \end{aligned} \tag{4.31}$$

where $\boldsymbol{\rho} = (x, y)$ and $\boldsymbol{\rho}' = (x', y')$. We have ignored all phase factors which multiply the integral (e.g., $\exp(ikz)$). Since the distance from the phase screen to the observation point is z and the incoming wave is a plane wave, the Fresnel radius becomes

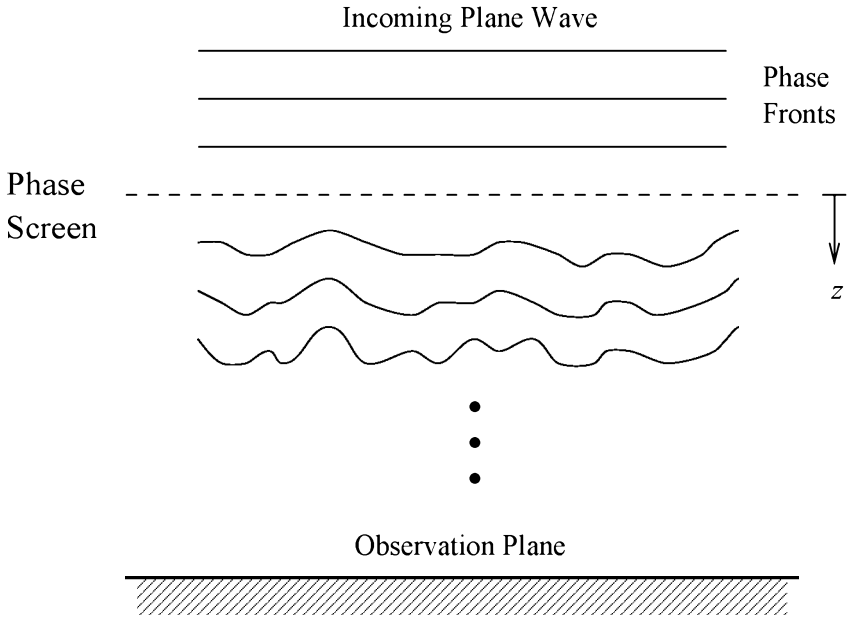

Figure 4.4: Phase screen model. The incoming plane wave experiences irregular perturbations in phase across its phase front upon encountering the phase screen. These irregularities then propagate to the ground, causing phase and amplitude variations across the observation plane. The phase screen sits at $z = 0$, while the observation plane lies at z.

$r_F = \sqrt{\lambda z}$.

In the case of the equatorial ionosphere, the irregularities are highly field aligned. Assuming the geometry of the ionospheric intersection is such that the equivalent phase screen has significant variation in only one direction, say the x direction, the propagation formula simplifies to [*Pidwerbetsky*, 1988]

$$\mathcal{A}(x,y,z) = \frac{1}{r_F}\int dx'\ \mathcal{A}^+(x')\exp\left[i\pi\left(\frac{x-x'}{r_F}\right)^2\right]. \tag{4.32}$$

The propagation formula (4.31) derives from Kirchhoff's diffraction theory as applied to the scalar Helmholtz equation (4.9) for the propagation below the screen [*Mercier*, 1962; *Born and Wolf*, 1975]. The approximations inherent to the formula result from stationary phase arguments, much like those made for the single scatter example of the previous section. One key condition for these approximations to be valid is that the distance from the phase screen to the observation plane (z) must be much greater than the wavelength (λ). This condition is easily met in practice. In fact, equation (4.32) is essentially the same formula used to derive the classical Fresnel diffraction pattern from the edge of an opaque half plane [*Born and Wolf*, 1975]. Alternatively, one may derive (4.31) from the "parabolic equation" approximation to the scalar Helmholtz equation [*Yeh and Liu*, 1982; *Pidwerbetsky*, 1988], an approach we shall not consider here.

The phase values to be used for the screen generally come from the optical path (4.27). Since the high frequency permittivity of the ionospheric plasma is $\epsilon = \epsilon_0\,(1 - \omega_p{}^2/\omega^2)$, where $\omega_p{}^2 = N_e e^2/(m\epsilon_0)$ (ω_p is the electron plasma frequency, N_e is the electron number density, e is electron charge and m is electron mass) and ω is the radio frequency, the phase along the optical path becomes

$$\phi(x,y) = \int dz\ k\ \sqrt{1 - \frac{[\omega_p(x,y,z)]^2}{\omega^2}}. \tag{4.33}$$

Here $k = \omega/c$. Because $\omega \gg \omega_p$, we may expand the square root to obtain

$$\begin{aligned} \phi(x,y) &\approx kz - \frac{k}{2\omega^2}\int dz\ [\omega_p(x,y,z)]^2 \\ &= kz - \frac{ke^2}{2m\epsilon_0\omega^2}\int dz\ N_e(x,y,z). \end{aligned} \tag{4.34}$$

The quantity $\int dz\ N_e(x,y,z)$ is the vertical total electron content (TEC) which is often given in TEC units (TECU), where 1 TECU = 10^{16} electrons per m^2. Since the phase velocity in the plasma is greater than the speed of light, the optical path of the wave shortens upon passing through the ionosphere, as compared to the free space optical path.

Of course, the phase screen model is an approximation. It relies on the assumptions of forward scattering and having a large distance from the irregularity region to the observer. Also, most direct justifications of its use rely on the presence of only weak irregularities (e.g., the previous section and *Lovelace* [1970]). Another requirement is that the medium be thin enough so that amplitude perturbations due to interference do not develop within the medium. Otherwise, the screen must include amplitude variations as well as phase variations.

Nevertheless, despite the model limitations, *Bramley* [1977] shows that typical statistical parameters deduced from a phase screen centrally located within an extended scattering medium fairly accurately reflect single scattering results, even if the medium extends all the way to the observation plane. *Booker et al.* [1985] expand upon these results to show that, somewhat remarkably, correspondence in scintillation statistics between the phase screen model and the extended medium often continues to hold even in the multiple scattering case. In these cases, however, one considers some sort of "equivalent screen" which may or may not bear a simple relationship to the TEC values or optical path.

In fact, as is clear from the principles of holography [*Born and Wolf*, 1975; *Fowles*, 1989], a thin screen having *both* amplitude and phase variations, as in the original formulation of *Booker et al.* [1950], can adequately reproduce the effects of any monochromatic wave front at the observation plane. Again, the relationship to line of sight TEC values is not necessarily direct in this case. The multiple phase screen model [*Lovelace*, 1970; *Uscinski*, 1993], uses several sequential phase screens to estimate the overall effect on a wave front passing through an extended medium. This model provides insight into what the equivalent single screen looks like, although it will not be covered here. For most work, however, the consensus of the literature is that the single phase screen model, where phase derives simply from TEC, usually applies to ionospheric propagation.

The beauty of the phase screen model is that results may be calculated in a computationally efficient manner. For a one dimensional phase screen, the integral (4.32) that gives the forward scattered field is a one dimensional convolution integral. Direct, accurate evaluation of the scattering integral is nigh impossible since convergence attains only through cancellation of adjacent Fresnel zones [*Buckley*, 1975]. Using the convolution theorem of Fourier transforms, however, we can replace the convolution operation by multiplication. Naturally, this substitution requires that we initially convert from the spatial domain to the Fourier domain, perform the complex multiplications, and convert back to the spatial domain to get our results. Nevertheless, this indirect path is highly computationally efficient, provided we can approximate the continuous Fourier transform by the discrete Fourier transform and compute it using fast Fourier transform (FFT) algorithms.

Several authors [*Buckley*, 1975; *Rino and Owen*, 1984; *Cordes et al.*, 1986; *Pidwerbetsky*, 1988] use techniques based on FFT algorithms to calculate the field below

a one dimensional phase screen. *Buckley* [1975] aptly terms such calculations "numerical experiments," although the generic term "simulations" will often appear in this dissertation. Keeping in mind the usual caveats about substituting the discrete Fourier transform for the continuous one (for example, considering the implied circular convolutions and remembering to maintain adequate frequency resolution), these simulations run very successfully. *Beach and Lovelace* [1997], for example, present a recent example of comparison between an analytical calculation for a deterministic, sinusoidal phase screen and the FFT based calculation. Appendix C lists the short MATLAB program they used for computing the field after propagation from the screen to the observation plane. The next section discusses more details of the sinusoidal phase screen example to illustrate the general properties of the one dimensional phase screen model.

4.4 Model Properties

The important characteristics of the phase screen model, or any scintillation model in general, are the variations in phase and amplitude of the signal across the observation plane. Of course, if the source is not coherent, e.g. a natural radio star source, then the amplitude pattern becomes the primary interest. In our case, we use artificial satellite sources so we may theoretically consider both quantities. Here also we will concentrate on equatorial ionospheric scintillations and, hence, the one dimensional phase screen model.

4.4.1 Amplitude Scintillations

We focus first on amplitude scintillations since they are easier to measure. The intensity or received signal power is $\mathcal{I}(x) = |\mathcal{A}(x)|^2 = \mathcal{A}(x)\mathcal{A}^*(x)$, where the asterisk denotes complex conjugation and we have taken the proportionality constant between $|\mathcal{A}(x)|^2$ and $\mathcal{I}(x)$ to be one. Also, for simplicity, the amplitude of the plane wave incident on the screen is normalized to unity. Substituting (4.32) for the field amplitude gives

$$\mathcal{I}(x) = \frac{1}{{r_F}^2} \iint dx'dx'' \exp\left\{ i\frac{\pi}{{r_F}^2}\left[(x-x')^2 - (x-x'')^2\right] + i[\phi(x') - \phi(x'')]\right\}, \quad (4.35)$$

where the limits of the integrals are $\pm\infty$ and $\mathcal{A}^+(x) = \exp[i\phi(x)]$ in equation (4.32). Already the analysis becomes complicated for a general $\phi(x)$. Further, we are interested in the variations of intensity across the screen, as measured by the autocorrelation function:

$$\begin{aligned} M^2(r) &= \langle [\mathcal{I}(x) - \langle\mathcal{I}\rangle]\,[\mathcal{I}(x+r) - \langle\mathcal{I}\rangle]\rangle \\ &= \langle \mathcal{I}(x)\mathcal{I}(x+r)\rangle - 1, \end{aligned} \quad (4.36)$$

where the angle brackets denote ensemble averages in the case of random $\phi(x)$. (Note that equation (4.35) gives $\langle\mathcal{I}\rangle = 1$, consistent with conservation of energy and the assumption of forward scattering [*Salpeter*, 1967].) The autocorrelation function is, of course, a second moment of the intensity (4.35) or a fourth moment of the amplitude (4.32).

What we would like to do is to relate the statistics of the intensity variations at the observing plane directly to the statistics of the phase variations at the screen. Unfortunately, such relationships do not exist except in a few limiting cases [*Mercier*, 1962; *Salpeter*, 1967]. We will describe these limits after first establishing some no-

tation for the stationary random quantity $\phi(x)$, generally following the notation of *Salpeter* [1967].

First of all, $\phi(x)$ is a Gaussian random variable in the case of propagation through ionospheric turbulence. The fact that $\phi(x)$ is Gaussian follows from the central limit theorem since the line of sight contains a large number of random fluctuations in refractive index; hence, $\phi(x)$ is the sum of a large number of random fluctuations in phase. We can always adjust $\phi(x)$ to be zero mean because intensity is insensitive to any constant phase offset in the screen. Finally, we denote the variance of $\phi(x)$ by ${\sigma_\phi}^2$.

Independently of the nature of the probability density function of phase at any given point along the screen, we define the correlation of phase between points separated by distance r by the normalized autocorrelation function $\rho(r)$ according to

$$ {\sigma_\phi}^2 \rho(r) = \langle \phi(x)\phi(x+r) \rangle \,. \tag{4.37} $$

Now the power spectral density, denoted by $\Phi_\phi(q)$ is the Fourier transform of the autocorrelation function. That is,

$$ \Phi_\phi(q) = \frac{{\sigma_\phi}^2}{2\pi} \int_{-\infty}^{\infty} dr \; e^{iqr} \rho(r), \tag{4.38} $$

where q denotes the horizontal wave number of the phase fluctuations across the screen (used to avoid confusion with the wave number k of the electromagnetic wave).

Often, in fact, the specification of the phase screen comes from the power spectrum of the irregularities. If the power spectrum of the (two dimensional) ionospheric electron density irregularities is $\Phi_{\Delta N}(q, s)$, letting s be the vertical wave number, the power spectrum of phase becomes

$$ \Phi_\phi(q) = 2\pi L \, (\lambda r_e)^2 \, \Phi_{\Delta N}(q, s = 0), \tag{4.39} $$

where L is the thickness of the ionosphere, λ is the free space wavelength of the electromagnetic wave and $r_e = 2.82 \times 10^{-15}$ m is the classical electron radius (see *Yeh and Liu* [1982], for example, for a more detailed discussion of the origin of this formula). This formula applies to normal incidence as shown in Figure 4.4.

In the case that the variance ${\sigma_\phi}^2$ of the phase is small, the power spectrum of the intensity takes on the simple form [*Salpeter*, 1967]

$$\Phi_{\mathcal{I}}(q) = 4\Phi_\phi(q) \sin^2\left(\frac{q^2 {r_F}^2}{4\pi}\right), \tag{4.40}$$

where $\Phi_{\mathcal{I}}$ is the Fourier transform of the intensity autocorrelation function $M^2(r)$. The literature refers to the $\sin^2$ term as the "Fresnel filter" function, a function which serves to de-emphasize sharply certain scale sizes of phase fluctuation in the intensity power spectrum, allowing the influence of other scale sizes to pass nearly unaltered.

The smallest q, hence the largest scale size, that the Fresnel filter passes without alteration occurs the first time that the $\sin^2$ term equals 1. This happens when the argument, $q^2 {r_F}^2/(4\pi)$, equals $\pi/2$. Accordingly, the desired horizontal wave number is $q = \sqrt{2}\pi/r_F$, corresponding to a scale size of $\sqrt{2}r_F$. Since the power spectrum of irregularities in the equatorial ionosphere decreases for increasing q, typically as a power law [*Basu and Basu*, 1993], the scale size most emphasized in weak equatorial scintillations is this first maximum of the Fresnel filter. One should keep in mind, however, that this maximum in the intensity spectrum is rather broad and also that this equation (4.40) applies only to weak scintillations.

The other limiting case which can be evaluated is when the observation plane lies a large distance from the phase screen [*Mercier*, 1962]. In this case, the spatial correlation function of intensity variations, rather than the power spectrum, more

conveniently represents the limiting form:

$$M^2(r) = e^{-2\sigma_\phi{}^2}\left[e^{2\sigma_\phi{}^2\rho(r)} - 1\right]. \tag{4.41}$$

Further, the deviation of intensity $m = M(0)$, called the "modulation index," is a key parameter of interest. For the case of strong fluctuations in phase, that is $\sigma_\phi{}^2 \gg 1$, equation (4.41) shows that m approaches 1. In other words, for strong fluctuations in phase and at distances far from the screen, the deviation of intensity equals the mean value of intensity.

The literature also calls the modulation index m the S_4 scintillation index after the terminology of *Briggs and Parkin* [1963]. In general, the modulation index measures the deviation of intensity from its mean, so that when the average intensity is not normalized to unity

$$m^2 = \frac{\langle \mathcal{I}^2 \rangle - \langle \mathcal{I} \rangle^2}{\langle \mathcal{I} \rangle^2}. \tag{4.42}$$

The modulation index starts at zero immediately below the phase screen since no interference occurs until the wave fronts propagate away from the screen. As the distance from the screen increases, fluctuations in intensity develop. In the case of a "deep" phase screen, where $\sigma_\phi{}^2 \gg 1$, m reaches a maximum when z equals the typical focal length from the various size refractive index irregularities acting as converging lenses [*Salpeter*, 1967]. Further away, the modulation index for the deep screen decreases and eventually reaches its limiting value of 1.

4.4.2 Sinusoidal Phase Screen

A useful pedagogic example which illustrates many of the properties of the phase screen model is the sinusoidal phase screen. In the sinusoidal phase screen, the variation of phase across the one dimensional screen is deterministic, not random.

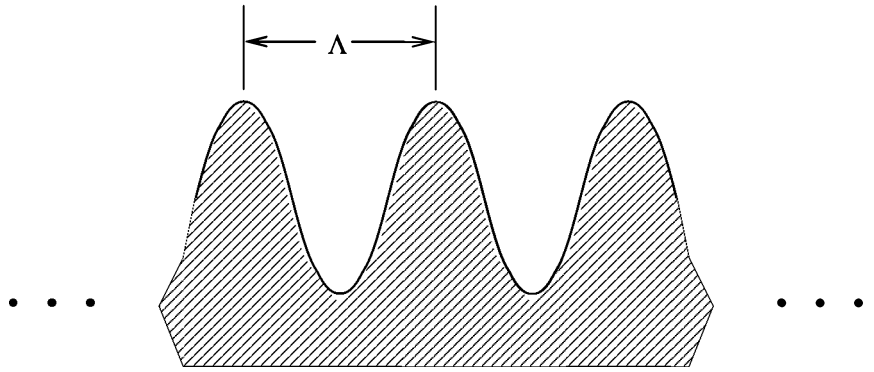

Figure 4.5: Cross section of sinusoidal profile lens, an example of where the sinusoidal phase screen model would apply.

Nevertheless, it illustrates much of the behavior discussed in the preceding section: development of intensity variation with increasing z, focusing effects in the case of large root mean square phase variations at the screen, etc.

Hewish [1951] first proposed the sinusoidal phase screen model as a starting point in the study of phase screens and their relationship to ionospheric scintillations. In this model, $\phi(x) = \phi_0 \sin(2\pi x/\Lambda)$, where Λ is much larger than the wavelength λ of the incident radiation, so the field just below the screen is

$$\mathcal{A}^+(x) = \exp\left[i\phi_0 \sin\left(\frac{2\pi}{\Lambda}x\right)\right]. \tag{4.43}$$

The sinusoidal phase screen model has been used as a test case for simulations from time to time; for example, *Buckley* [1975] used the sinusoidal phase screen as a test of his numerical experiments. Nevertheless, it appears that the intensity pattern below the screen was not derived until recently [*Beach and Lovelace*, 1997].

Practically speaking, the model remains largely a pedagogic tool. Nonetheless, some physical situations exist in which it applies. A simple example is a one dimensional lens with a sinusoidal cross section, as shown in Figure 4.5. Another is the diffraction of light by ultrasonic waves in liquid [*Born and Wolf*, 1975; *Mejias*, 1980].

In the latter case, the experimenter places a thin tank full of liquid transverse to the direction of illumination. Ultrasonic transducers along one end of the tank emit plane waves which propagate through the tank, perpendicular to the incident light and possibly forming standing waves upon reflection (depending on the "termination" of the tank at the other end). Since sound waves are compressional waves, the liquid's density alternately increases and decreases as the wave fronts pass. These slight variations in density translate into sinusoidal refractive index fluctuations, of the order of 10^{-4} of the refractive index of the undisturbed liquid [*Mejias*, 1980]. The result is essentially a phase screen with a one dimensional sinusoidal variation in phase.

To analyze the propagation, we follow *Hewish* [1989] and first consider the field just below the phase screen for a small peak phase variation ϕ_0. In that case, we can approximate the exponential by the first two terms of its Taylor series expansion, yielding

$$\mathcal{A}^+(x) \approx 1 + i\phi_0 \sin\left(\frac{2\pi}{\Lambda}x\right). \tag{4.44}$$

Now the second term on the right hand side is equivalent to

$$\frac{\phi_0}{2}\left[\exp\left(i\frac{2\pi}{\Lambda}x\right) - \exp\left(-i\frac{2\pi}{\Lambda}x\right)\right]. \tag{4.45}$$

For comparison, the field produced by two unit amplitude plane waves, with one particular set of phasings and traveling at angles $\pm\theta$ to the z direction, is

$$\begin{aligned} & e^{i(kx\sin\theta + kz\cos\theta)} - e^{i(-kx\sin\theta + kz\cos\theta)} \\ &= e^{ikz\cos\theta}\left(e^{ikx\sin\theta} - e^{-ikx\sin\theta}\right). \end{aligned} \tag{4.46}$$

So, at $z = 0$ this pair of plane waves looks exactly like the second term on the right hand side of (4.44), provided: (1) we make the plane waves at angles $\pm\theta$ have amplitudes $\phi_0/2$ instead of unit amplitude, and (2) we define θ so that $k\sin\theta = 2\pi/\Lambda$. The latter requirement demands that $\theta = \sin^{-1}(\lambda/\Lambda) \approx \lambda/\Lambda$ for $\lambda \ll \Lambda$.

What we have done is to reconstruct the field just below the phase screen in terms of a discrete "angular spectrum of plane waves" [*Booker et al.*, 1950]. These plane waves can then propagate freely below the screen to the observer. Specifically, in this case we have below the screen a direct wave of unit amplitude flanked by two weak side-scattered waves of amplitude $\phi_0/2$ at angles $\pm\lambda/\Lambda$. Note that all of the plane waves still have the same wave number k. The interference of these three waves produces amplitude scintillations as we move away from the screen. In this particular case, owing to the periodicity of the screen, there are also distances z where the intensity of the field returns to a uniform value just like it is at the screen [*Beach and Lovelace*, 1997].

Although the diagram of the sinusoidal lens suggests alternate converging and diverging lenses, not much focusing occurs for small ϕ_0. The radii of curvature of the lenses are very large, i.e. the lenses are almost flat, for fluctuations in phase less than 1 radian. Consequently, the scale size of the (modest) variations in intensity matches the scale size of phase fluctuations at the screen. As the lenses get thicker, however, significant focusing can happen. Also in this case, the case of large ϕ_0 where the two term approximation of the exponential does not apply, the angular spectrum of the wave becomes broader [*Hewish*, 1989]. In other words, additional plane waves appear at larger scattering angles up to about $\pm\phi_0(\lambda/\Lambda)$. Because of the broader plane wave spectrum, alternatively because of focusing, the intensity pattern on the ground develops finer scale variations than the screen. Certainly also, focusing produces larger intensity fluctuations, especially for z equal to the focal distance.

Figure 4.6 shows the effect of increasing distance from the screen on the intensity pattern for both "deep" ($\phi_0 > 1$) and "shallow" ($\phi_0 < 1$) sinusoidal phase screens. For the shallow screen with $\phi_0 = 0.5$, the intensity pattern develops slowly with increasing

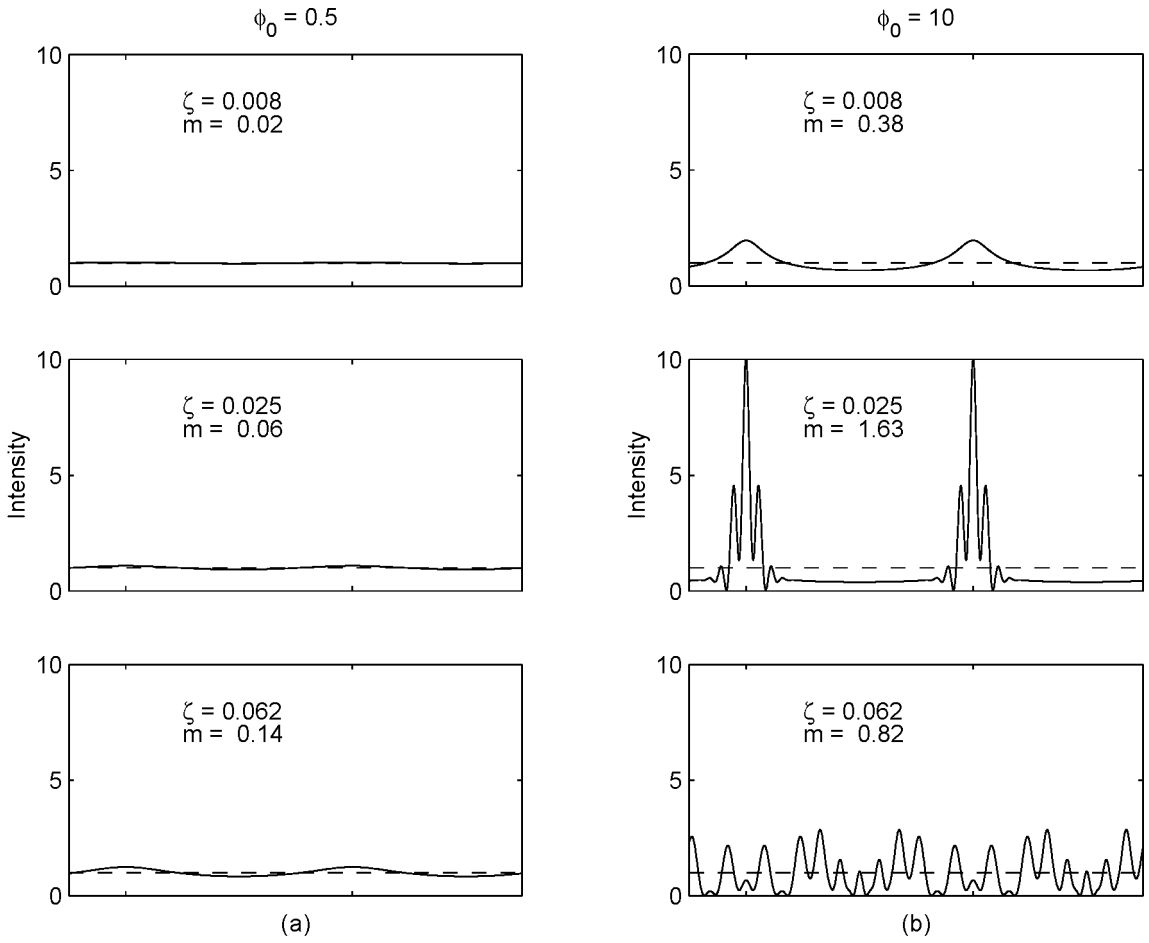

Figure 4.6: Development of intensity patterns below shallow and deep sinusoidal phase screens. Each sequence shows the effects of increasing observation distance, $\zeta = \lambda z/\Lambda^2$, on the intensity pattern below a shallow screen (a) and a deep screen (b). Distance increases from top to bottom in each sequence. The center plots are at the focal distance for the $\phi_0 = 10$ case. Dashed lines indicate unit intensity and the modulation index m labels each graph, along with ζ. Both sequences show two cycles of intensity variations out of a total of 128 cycles in the simulation ($\Lambda = 512$ grid spacings, $\lambda = 1$ grid spacing).

distance from the screen. Even at the greatest distance shown, for the shallow screen the intensity pattern is essentially sinusoidal about its mean of 1.

The deep screen with $\phi_0 = 10$ displays an entirely different set of characteristics. Near the screen, the pattern has already developed and is somewhat sinusoidal. The middle plot shows the pattern at the focal distance for the screen ($z \sim \Lambda^2/(4\lambda\phi_0)$). Further away from the screen, the intensity pattern is much less organized but it still displays fine scale variance. The behavior of the deep sinusoidal phase screen mirrors some of the behavior of the deep random phase screen as discussed by *Salpeter* [1967]. Specifically, it shows focusing at a particular z and the subsequent saturation of the modulation index near unity at larger distances from the phase screen.

Now we turn to the analytical details of the sinusoidal phase screen. First, the amplitude below the screen, for a unit amplitude incident plane wave and calculated using (4.32), is

$$\mathcal{A}(x) = e^{i\pi/4} \sum_{n=-\infty}^{\infty} J_n(\phi_0) e^{inq_0 x} e^{-i\pi n^2 \zeta}, \tag{4.47}$$

where J_n is the Bessel function of the first kind of order n, $q_0 = 2\pi/\Lambda$ and $\zeta = {r_F}^2/\Lambda^2 = \lambda z/\Lambda^2$ [*Beach and Lovelace*, 1997]. The expression for the corresponding intensity simplifies to a single summation, rather than an double sum, by the grace of a fortuitous Bessel function identity, giving [*Beach and Lovelace*, 1997]

$$\mathcal{I}(x) = \sum_{n=-\infty}^{\infty} J_n(w_n) e^{inq_0 x} \exp\left(in\chi_n - i\pi n^2 \zeta\right). \tag{4.48}$$

The w_n and χ_n derive from the following expressions used in Graf's addition theorem for Bessel functions [*Abramowitz and Stegun*, 1972, 9.1.79, p. 363]:

$$w_n = \phi_0 \sqrt{2(1 - \cos\alpha_n)}, \tag{4.49}$$

$$w_n \cos\chi_n = \phi_0 (1 - \cos\alpha_n), \tag{4.50}$$

$$w_n \sin\chi_n = \phi_0 \sin\alpha_n, \tag{4.51}$$

where $\alpha_n = -2n\pi\zeta$. The section in *Abramowitz and Stegun* [1972] also contains discussion of the appropriate branches to choose when computing the square root and the implicit trigonometric inverses above. Fortunately, we will have occasion to compute only w_n, and then only in a formula which is insensitive to whether w_n is positive or negative.

Equations (4.47) and (4.48) are explicitly in Fourier series form, making manifest the periodicity which we expect from the periodic nature of the phase screen. Further, we may readily calculate the discrete power spectrum of intensity, almost by inspection. Since $\mathcal{I}(x)$ is real, the Fourier coefficients for $\pm n$ are conjugate symmetric and the power spectrum becomes

$$S_n = \begin{cases} 1, & n = 0, \\ 2J_n^2\left(2\phi_0 \sin\left(n\pi\zeta\right)\right), & n > 0, \end{cases} \tag{4.52}$$

where S_n is the power in the nth harmonic component of (4.48) [*Beach and Lovelace*, 1997]. Equation (4.52) results from trigonometric identities, noting that $J_{-n}(x) = (-1)^n J_n(x)$ and recognizing that $J_n^2(x)$ is insensitive to the sign of its argument. Also, equation (4.52) explicitly demonstrates that the average value of intensity is unity, $\langle \mathcal{I}(x) \rangle = 1$, again verifying conservation of energy and the forward scattering assumption. (Now the angle brackets denote spatial averaging over a period Λ, rather than ensemble averages, for this deterministic and periodic screen.)

Applying Parseval's theorem permits us to calculate the modulation index m as well. Since

$$\left\langle \mathcal{I}^2(x) \right\rangle = \sum_{n=0}^{\infty} S_n, \tag{4.53}$$

we can subtract $S_0 = 1$ (the mean intensity) to obtain

$$m^2 = 2\sum_{n=1}^{\infty} J_n^2\left(2\phi_0 \sin\left(n\pi\zeta\right)\right). \tag{4.54}$$

Figure 4.7 graphs modulation index m, calculated using (4.54), versus normalized distance ζ for the deep and shallow sinusoidal phase screen examples considered earlier. The reflection symmetry, about $\zeta = 0.5$ for example, and periodicity of these plots stem from the sine term in the argument of the Bessel functions. Physically, they result from the phasing of the side scattered plane waves in the angular spectrum. At integer values of ζ, where the modulation index goes to zero, all the plane waves of the angular spectrum (at angles of $\pm n\lambda/\Lambda$ in the small angle scattering case) have traveled laterally an integer number of sinusoid periods, giving a symmetric pattern equivalent to that just below the phase screen. Hence, the intensity becomes uniform, just as it is at the phase screen.

Aside from the symmetries due to having a deterministic, periodic screen, Figure 4.7 illustrates what we noted earlier regarding the development of amplitude scintillations with distance. In the case of the shallow phase screen, the variations develop slowly as we move away from the screen. For the deep phase screen, the variance of intensity increases rapidly with increasing distance, reaching a sharp maximum at the focal distance and then dropping back to the neighborhood of unity as the interference becomes less organized.

Finally, we note that equations (4.47) and (4.48) are special cases of results for periodic screens, where the screens may alter both amplitude and phase in general. If the field below the screen is

$$\mathcal{A}^+(x) = \sum_{n=-\infty}^{\infty} c_n e^{inq_0 x}, \tag{4.55}$$

where the coefficients c_n may be complex, the amplitude at the observation plane from equation (4.32) is

$$\mathcal{A}(x) = e^{i\pi/4} \sum_{n=-\infty}^{\infty} c_n e^{inq_0 x} e^{-i\pi n^2 \zeta}. \tag{4.56}$$

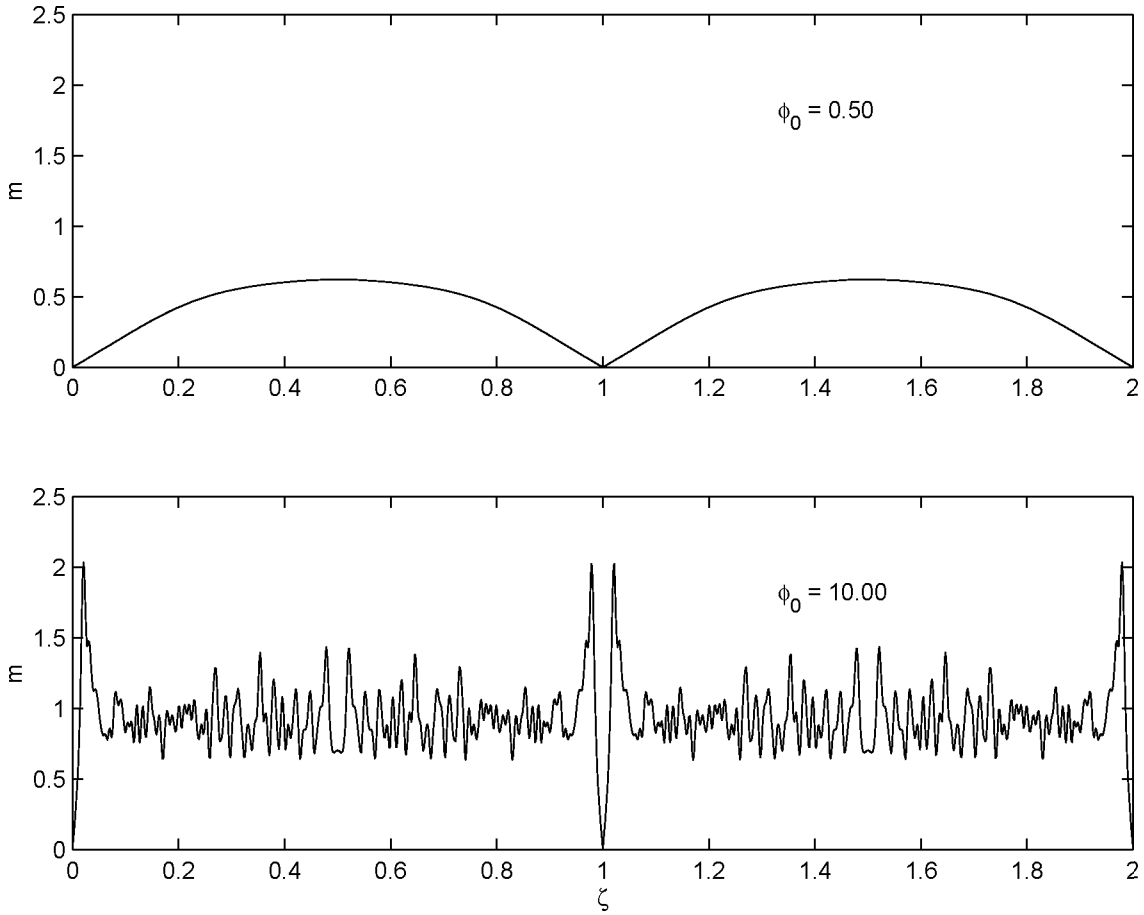

Figure 4.7: Modulation index as a function of normalized distance for deep and shallow sinusoidal phase screens. Here we have calculated modulation index m based on (4.54) for $\phi_0 = 0.5$ (shallow) and $\phi_0 = 10$ (deep) phase screens, where ϕ_0 is the peak phase deviation at the screen.

From the expression for the amplitude, the intensity at the observation plane becomes

$$\mathcal{I}(x) = \sum_{m=-\infty}^{\infty} e^{imq_0 x} e^{i\pi m^2 \zeta} \sum_{n=-\infty}^{\infty} c_n c_{n-m}^* e^{-2\pi i \zeta mn}. \tag{4.57}$$

Consequently, the power spectrum of intensity is

$$S_n = \begin{cases} \sum_r \sum_s c_r c_r^* c_s c_s^*, & n = 0, \\ 2 \sum_r \sum_s c_r c_{r-n}^* c_s c_{s-n}^* e^{-2\pi i \zeta n(r-s)}, & n > 0, \end{cases} \tag{4.58}$$

where the limits for the sums are $\pm\infty$.

Unfortunately, the general form above for periodic phase and amplitude changing screens does not appear to be too helpful. First, although the coefficient of the mth harmonic term in (4.57) is tantalizingly close to a convolution sum or a discrete Fourier transform, it does not appear to simplify except in special cases (such as the sinusoidal phase screen). Second, for phase screens, combining the effects of two arbitrary distributions of phase becomes quite difficult. For example, suppose we wish to determine the diffraction pattern from a screen composed of the sum of two sinusoidal variations, $\phi_1(x)$ and $\phi_2(x)$. The resulting field just below the screen is

$$\mathcal{A}^+(x) = e^{i[\phi_1(x)+\phi_2(x)]} = e^{i\phi_1(x)} e^{i\phi_2(x)}, \tag{4.59}$$

not a superposition at all! Further, even if $\mathcal{A}^+(x)$, and hence the field at the observing plane, were a simple superposition of functions, the intensity would not be.

In fact, the true nature of the composition of two phase distributions is the following. Repeating (4.32) for reference, the propagation integral below a one dimensional screen is

$$\mathcal{A}(x,z) = \frac{1}{r_F} \int dx' \; \mathcal{A}^+(x') \exp\left[i\pi \left(\frac{x-x'}{r_F} \right)^2 \right]. \tag{4.60}$$

As we noted earlier, the integral on the right is a one dimensional convolution, which we may evaluate in the Fourier domain. Letting $K(q,z) = \mathcal{F}\{\exp[i\pi(x/r_F)^2]\}$ and

$\mathcal{A}(q,z) = \mathcal{F}[\mathcal{A}(x,z)]$, respectively the Fourier transforms of the Gaussian kernel and the amplitude, the field at the observation plane is

$$\begin{aligned} \mathcal{A}(q,z) &= \mathcal{F}\left[e^{i\phi_1(x)}e^{i\phi_2(x)}\right] K(q,z) \\ &= \left\{\mathcal{F}\left[e^{i\phi_1(x)}\right] * \mathcal{F}\left[e^{i\phi_2(x)}\right]\right\} K(q,z), \end{aligned} \tag{4.61}$$

where the asterisk between the Fourier transforms denotes convolution in the wave number domain. Here we see a similar conundrum to that appearing in (4.57), a mixture of convolution and Fourier transforms in the same expression. Thus, the problem of analytically computing the amplitude or intensity below a general phase screen, even a deterministic one, appears to be beyond our grasp.

4.4.3 Phase Scintillations

To a first approximation, the phase variations imposed by the screen appear directly in the phase of the measured signal. This is especially true just below the phase screen, before the spreading wave fronts have had the opportunity to interact and develop intensity scintillations. For weak scintillations, Fresnel filtering effects further from the screen generate the following power spectrum

$$\Phi_S(q) = \Phi_\phi(q)\cos^2\left(\frac{q^2{r_F}^2}{4\pi}\right), \tag{4.62}$$

where S indicates the received phase [*Yeh and Liu*, 1982]. Unlike the case with amplitude scintillations, the Fresnel filtering effect here allows longer wavelength variations to pass. The first null in the phase Fresnel filter appears where there was a maximum in the Fresnel filtering function for intensity, at a scale size of $\sqrt{2}r_F$. In the case that the ionospheric thickness may not be considered negligible, the Fresnel filter minima are not so sharp, however [*Salpeter*, 1967; *Yeh and Liu*, 1982]. (The "smear-

ing" of the Fresnel filter minima for a thick ionosphere also holds for weak intensity scintillations.)

4.5 Time Variations

Up to this point we have discussed primarily the patterns of intensity and phase variations as functions of position in the observation plane for a given configuration of ionospheric irregularities. What is more realistic is to have a single, stationary receiver which monitors amplitude and phase as functions of time or perhaps to have a small array of these receivers. Time variations derive from several sources: (1) the drift of "frozen in" irregularities, (2) the evolution of the irregularities as they drift, and (3) satellite motion. From an observational standpoint, the latter are potentially most vexing because they contaminate the first two types of variations, the true objects under study.

For simplicity, we first consider the situation without satellite motion. Suppose also that we have the simplest possible viewing geometry, a geostationary satellite source at zenith and a one dimensional irregularity screen. A fixed pattern of ionospheric irregularities generates a fixed pattern of intensity (and phase) variations across the ground. If the irregularities drift, the corresponding intensity pattern moves also, causing time variations in the measured signal power at a stationary receiver. The temporal power spectrum relates to the spatial power spectrum of irregularities by the following:

$$\Phi_{\mathcal{I}}(\omega) = \Phi_{\mathcal{I}}(q = \omega/V), \tag{4.63}$$

where V is the drift velocity and, as before, q is the horizontal wave number of the irregularities. Under weak scattering, the Fresnel filtering effect serves to de-

emphasize some frequencies, in this case temporal frequencies, while allowing others to pass through virtually unchanged. For example, the first maximum of the spatial Fresnel filter function for intensity occurs at $q = \sqrt{2}\pi/r_F$, corresponding to an angular frequency $\omega = qV = \sqrt{2}\pi V/r_F$ or $f = V/(\sqrt{2}r_F)$ where $\omega = 2\pi f$. Analogous results hold for the power spectrum of phase $\Phi_S(\omega)$.

The next more complicated case is to consider measurements from two receivers separated by d meters in the direction of irregularity motion. Assuming uniform drift and no other time evolution of the drifting structure, the "downstream" receiver should see exactly the same pattern of intensity (or phase) variations as the "upstream" receiver but d/V seconds later. The cross correlation of intensity between the two receivers would be identical to the autocorrelation function at one receiver except that the correlation peak is displaced to a lag of plus or minus d/V seconds (sign depending on the direction of motion). Conversely, from the lag of the cross correlation peak the drift velocity may be inferred.

In practice, even barring instrument variations, perfect correlation does not occur between spaced receivers; the scintillation pattern evolves with time for several reasons. First, one may be taking the scintillation measurements as the irregularities develop or decay away. Also, the irregularities at different heights may drift with different velocities, causing the optical path through the ionosphere, and hence the intensity pattern, to change over time. Further, the bulk of the irregularities may in fact be at different heights at different times, altering the Fresnel radius. All of these effects cause the shape of the cross correlation to depart from the autocorrelation function at either station. If one knows a typical drift speed V and a typical correlation time τ of the irregularities in phase at a particular scale size, say at the first maximum of the Fresnel filter for intensity, one can space the receivers less than

$V\tau$ meters apart to measure drifts successfully.

Continuing to increasing complexity, suppose that the spaced receivers are not lined up with the motion of the ionospheric irregularities, but instead lie at an angle θ with respect to the motion of the phase fronts (Figure 4.8). In this case, as pointed out in an early paper by *Briggs et al.* [1950], the cross correlation lag between the receivers corresponds to an apparent drift of $V/\cos\theta$. This formula is easily verified at the extremes. For $\theta = 0°$ the observed drift should equal the actual drift speed; at $\theta = 90°$ the phase fronts appear simultaneously over both receivers, giving the appearance of infinite speed. On the other hand, to experience the minimum scintillation (or fading) rate, an observer moving along the line connecting the receivers must travel with the irregularity phase fronts at a speed $V\cos\theta$. Note the difference in the two formulas. That this difference exists is not immediately apparent without careful thought [*Briggs et al.*, 1950].

Now we tackle the more difficult question of satellite motion and its effect on the interpretation of scintillation time scales. Until the advent of GPS satellite measurements of scintillations in equatorial regions, this effect was easier to approximate away. In earlier days, scintillation measurements usually came from beacons on geostationary satellites or low earth orbit (LEO) satellites. The former case has minimal, ideally zero, satellite motion to contend with. Thus, all time variation stems from the ionosphere, not from satellite motion. In the LEO case, the line of sight from the observer to the satellite cuts through the ionosphere relatively swiftly. A crude approximation for LEO satellite beacon measurements is that the ionosphere is essentially stationary, over periods of perhaps the order of minutes, and that the observed time variations derive mostly from satellite motion.

For GPS satellites, in twelve hour circular orbits of roughly 26,600 km radius, we

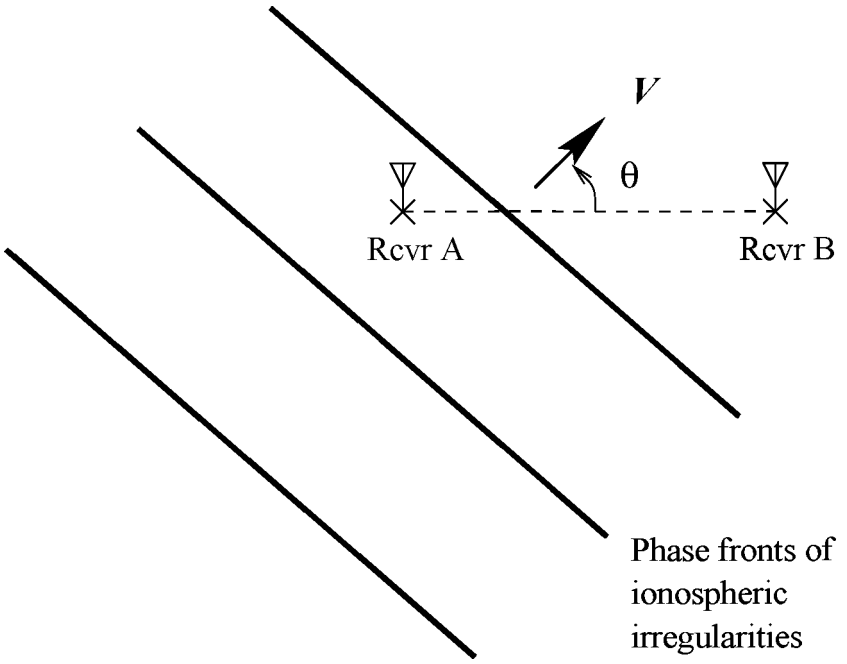

Figure 4.8: Top view of ionospheric irregularities passing over spaced receivers.

obtain slower cuts of the line of sight through the ionosphere. For example, consider the ionospheric penetration point velocity, defined as the horizontal velocity of the line of sight at a specific altitude in the ionosphere, often 350 km (i.e., the F peak). The ionospheric penetration point velocity can vary from 60 m/s near zenith to in excess of 400 m/s for low elevation satellites [*Bishop et al.*, 1994]. Typical post sunset ionospheric drifts near the dip equator are of the order of 100-200 m/s in the geomagnetic eastward direction [*Kelley*, 1989]. Since equatorial electron density irregularities typically form between sunset and local midnight near the F peak, GPS ionospheric penetration point velocities can match the horizontal drift of these irregularities, depending on the direction of motion of the satellite. Thus, neither of the previous approximations applies to GPS scintillation measurements in general.

To illustrate this point, we examine a snapshot of GPS ionospheric penetration point velocities from Ancon, Peru in October 1996. Figure 4.9 shows these velocities

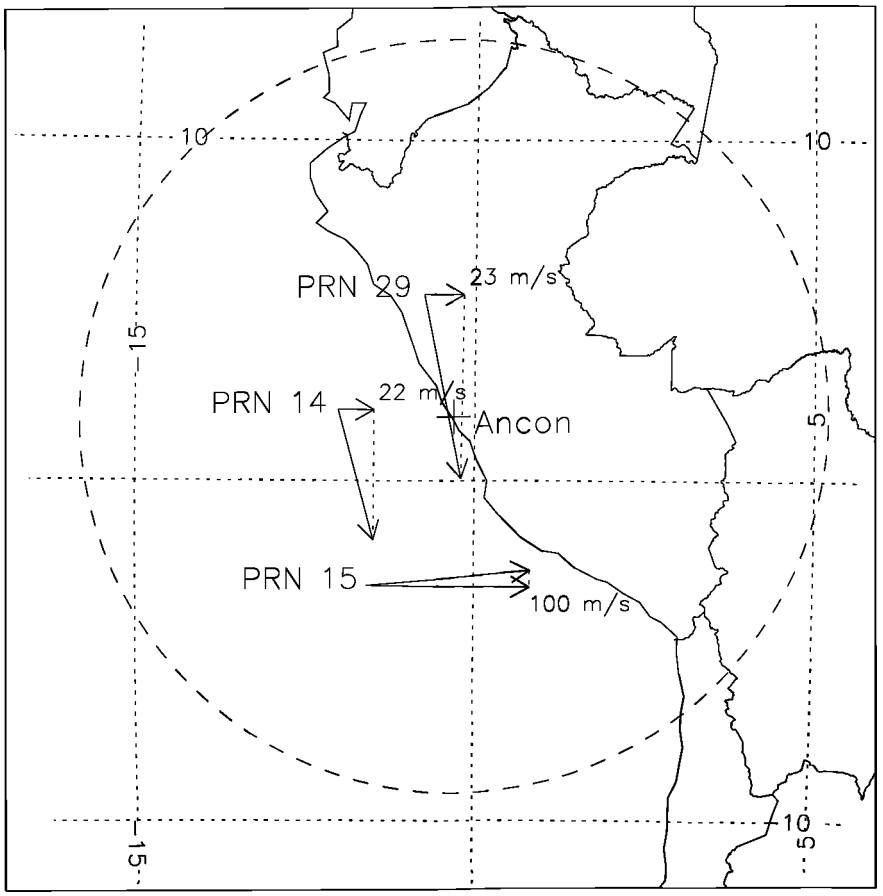

Figure 4.9: Ionospheric penetration point velocities at Ancon, Peru. These data are from 19 Oct 1996, 0115 UT. The arrows indicate the horizontal velocity of the line of sight at 350 km altitude where the geomagnetic eastward component of each is also plotted and labeled. The superimposed grid indicates geomagnetic latitude and longitude. The dashed circle denotes the limit of visibility at 10° satellite elevation. Geographic north is up in this figure.

over a map of the region with geomagnetic coordinates superimposed. Note that the magnetic declination of Peru is very slight (magnetic north lies about 1.6° east of true north at the time of the plot) and that Ancon lies just north of the dip equator. The main point of interest is the range of geomagnetic eastward components of penetration point velocity, the values labeled on the plot. This spread of tens of meters per second to 100 m/s is fairly typical of the Ancon station in our experience. Since the nighttime geomagnetic eastward drift of the ionosphere is of the order of 100 m/s, the potential for the penetration point motion of some of the GPS satellites to match the eastward drift of the irregularities and to cause long period scintillation fades is great.

Of course, the positions and motions of the GPS satellites are well known. Theoretically, then, the effects due to motion of the satellites may be accounted for. Several factors combine to complicate this task, however. First, the correct height to use is not always clear. We only estimate that most of the diffraction occurs near the F peak since that is where the bulk of the electron content lies. (Scintillations are sensitive to absolute, not relative, fluctuations in total electron content.) More seriously, for GPS lines of sight away from zenith, both vertical and horizontal irregularity drifts couple into the fading rate. Finally, from a practical standpoint, long fades become difficult to distinguish from multipath variations.

Now we turn generally to the problem of other than vertical incidence and its effects on scintillation measurements. Even for geostationary satellites the broadcast signal does not pass through the ionosphere above the observer from zenith unless the observer is situated at the geographic equator and at the same meridian as the satellite. For non-stationary satellites the difficulties compound since not only does the ionospheric penetration point move relative to the ionosphere, but the geometry of the line of sight's ionospheric incidence changes as well. Fortunately, the zenith angle

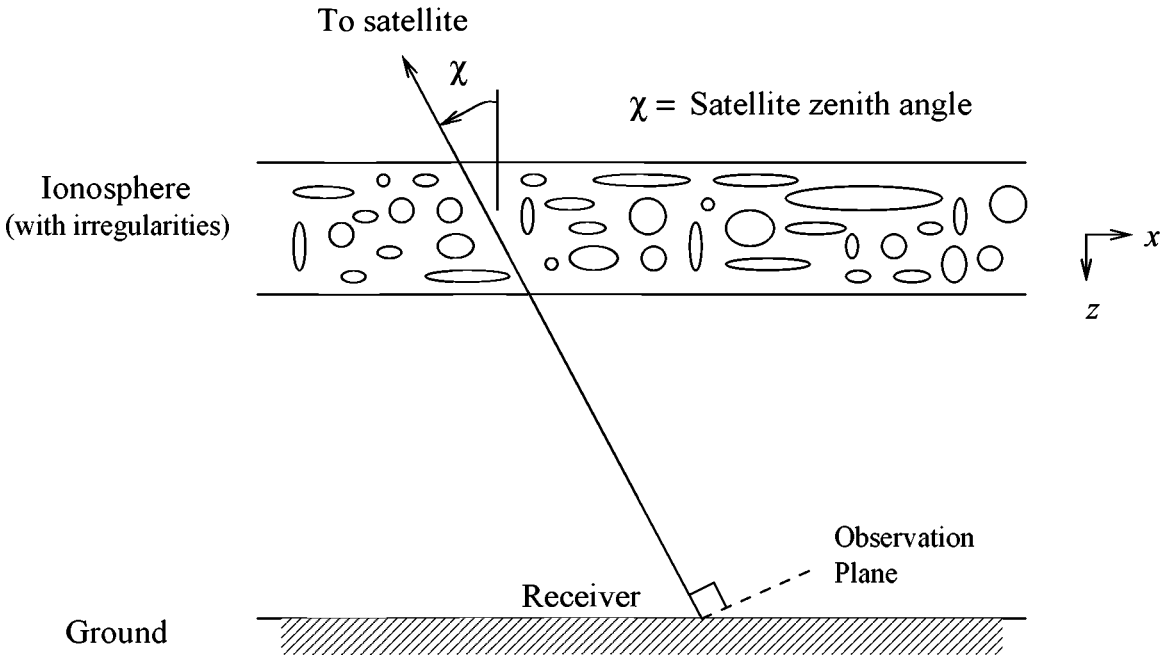

Figure 4.10: Simple ionospheric model for a non-zenith satellite. Note that the y axis (not shown) points out of the figure plane to complete a right handed coordinate system.

of the line of sight changes relatively slowly for GPS satellites. Over short periods of time, then, we may consider the line of sight to translate through the ionosphere without changing its geometry appreciably.

For a fixed viewing geometry and weak scintillations, we may consider the slant angle effects from a simple, intuitive viewpoint along the lines of that presented by *Briggs and Parkin* [1963]. Figure 4.10 illustrates a two dimensional model which we will use in the following discussion. For now, we assume that the ionospheric irregularities are isotropic even though they really extend along magnetic field lines.

In this simple model, we consider only weak scattering at high frequencies so that slant total electron content (TEC) adequately specifies the equivalent phase screen. Clearly, the TEC values which affect the intensity at the receiver are those measured in the observation plane near the receiver. In other words, the TEC along

the line of sight and adjacent TEC measurements along lines parallel to the line of sight, within a distance of a Fresnel radius or so, control the intensity at the receiver. Thus, the irregularity structure transverse to the line of sight generates the amplitude variations across the observation plane. Similarly, the net motion of the ionosphere (i.e., including effects of satellite motion) transverse to the line of sight governs the time scale of the scintillations.

More rigorous analysis of the single scatter case still shows these simple results to hold [*Rino and Fremouw*, 1977]. Moreover, the following modifications to the spatial power spectrum of optical path length variations across the ground (*not* across the observation plane) appear in this case,

$$\Phi_\phi(\mathbf{q}) = 2\pi L\,(\lambda r_e)^2\,\sec^2\chi\;\Phi_{\Delta N}(\mathbf{q}, s = -\tan\chi\;\hat{\mathbf{a}}_{k_T}\cdot\mathbf{q}), \tag{4.64}$$

also changing the previous weak scattering results for the power spectra of intensity and signal phase [*Rino and Fremouw*, 1977; *Rino*, 1979*a*]. Here, as in Figure 4.10, χ is the zenith angle at the point of ionospheric intersection. Additionally, $\hat{\mathbf{a}}_{k_T}$ is the unit vector along the projection of the radio wave propagation vector $\mathbf{k}$ onto the xy plane ($\hat{\mathbf{a}}_{k_T} = \hat{\mathbf{x}}$ in Figure 4.10). Most other factors are the same as before except that the transverse wave number $\mathbf{q}$ is a vector and now lies in the xy plane in general, rather than being restricted to the x direction. The $\sec^2$ term derives from the length of the slant path through the ionosphere. The term for the vertical wave number s comes from the height difference between the ground and the tilted observation plane at a given distance across the ground away from the receiver.

4.6 Concluding Remarks

We have discussed in this chapter the origin of scintillations and the phase screen model. The chapter includes heuristic applications of phase screen models to periodic screens, particularly the sinusoidal phase screen, to illustrate some of the behavior of the model both qualitatively and quantitatively. Additionally, we mentioned some of the relationships among the structure of fluctuations in electron density in the ionosphere and the structure of fluctuations in amplitude and phase in the received signal. There are important topics, however, which have not been mentioned. Among others, these topics include: (1) the actual power spectra of ionospheric irregularities, including the effects of magnetic field aligned anisotropy, and (2) the results of inhomogeneity in the ionospheric irregularities (e.g., transitions between irregular and "smooth" regions). We defer these topics until later chapters where they may be discussed in the context of specific measurements.

Chapter 5

Measurement Examples

5.1 Campaigns

This chapter presents results from field campaigns using the Cornell scintillation monitor. Already Chapter 3 showed a few examples in the section on power variations. Here we analyze these variations in more detail and also compare the Global Positioning System results to measurements from other instruments, including 630 nm airglow imagers and the Jicamarca radar, often operated in the coherent scatter JULIA mode (Jicamarca Unattended Long-term Investigations of the Ionosphere and Atmosphere).

All of the GPS data presented in this and subsequent chapters were taken in equatorial regions. The data come mostly from two campaigns. The first campaign occurred in October 1996, concurrently with part of the Multi-Instrumented Study of Equatorial Thermospheric Aeronomy (MISETA) campaign. The second, somewhat shorter campaign took place in April 1997. For both of these campaigns we have GPS scintillation data primarily from two stations in South America: Ancon, Peru

Table 5.1: Instruments for October 1996 campaign.

Location	Geographic Latitude	Geographic Longitude	Instrument(s)
Ancon, Peru	12° S	77° W	GPS scintillation monitors (2) VHF scintillation monitors Geostationary L band receiver
Arequipa, Peru	16° S	72° W	GPS TEC monitor[1] (low rate) 630 nm all sky airglow imager
Jicamarca, Peru	12° S	77° W	50 MHz radar Digisonde
Tucuman, Argentina	27° S	65° W	GPS scintillation monitor 630 nm all sky airglow imager

[1]Part of JPL/IGS network.

(11.77° S, 77.15° W, 1.5° dip) and Tucuman, Argentina (26.84° S, 65.22° W, −25.0° dip). The first station lies slightly north of the dip equator while the second sits near the southern equatorial anomaly. The Ancon station is at the Ancon Observatory, administered by the Instituto Geofísico del Perú (IGP, the Peruvian Geophysical Institute). The Tucuman station is on the campus of the Universidad Nacional de Tucumán (UNT, the National University of Tucuman).

Table 5.1 summarizes the instruments available during the October 1996 campaign. Table 5.2 lists instruments available for the April 1997 campaign. Two key differences exist between the campaigns. First, the airglow imager at Arequipa was at Boston University for repairs during the period of the April campaign (M. Colerico, private communication, 1997) and was therefore unavailable. Second, the April installation at Ancon included a third GPS receiver: a commercial dual frequency receiver for making total electron content (TEC) measurements. We also established the sta-

Table 5.2: Instruments for April 1997 campaign.

Location	Geographic Latitude	Geographic Longitude	Instrument(s)
Ancon, Peru	12° S	77° W	GPS scintillation monitors (2) GPS TEC monitor VHF scintillation monitors Geostationary L band receiver
Arequipa, Peru	16° S	72° W	GPS TEC monitor[1] (low rate)
Jicamarca, Peru	12° S	77° W	50 MHz radar Digisonde
Natal, Brazil	6° S	35° W	GPS scintillation monitor
Tucuman, Argentina	27° S	65° W	GPS scintillation monitor 630 nm all sky airglow imager

[1]Part of JPL/IGS network.

tion at Natal, Brazil between the two campaigns. The Natal station ran primarily for diagnostic purposes during April 1997, however, and most of its data were lost due to backup problems.

The multiple GPS receiver setup at Ancon requires elaboration. We used two scintillation monitors during both campaigns for the purpose of making ionospheric drift estimates. The antennas for these two monitors were spaced roughly 100 m apart in the geomagnetic east-west direction. Since the nighttime equatorial F region dynamo typically drives the plasma zonally from west to east with speeds of the order of 100 m/s [*Kelley*, 1989], the scintillation pattern should appear at the western antenna about one second prior to repeating itself at the eastern antenna (momentarily ignoring satellite motion).

Figure 5.1 shows a site sketch of the Ancon station. We changed the western

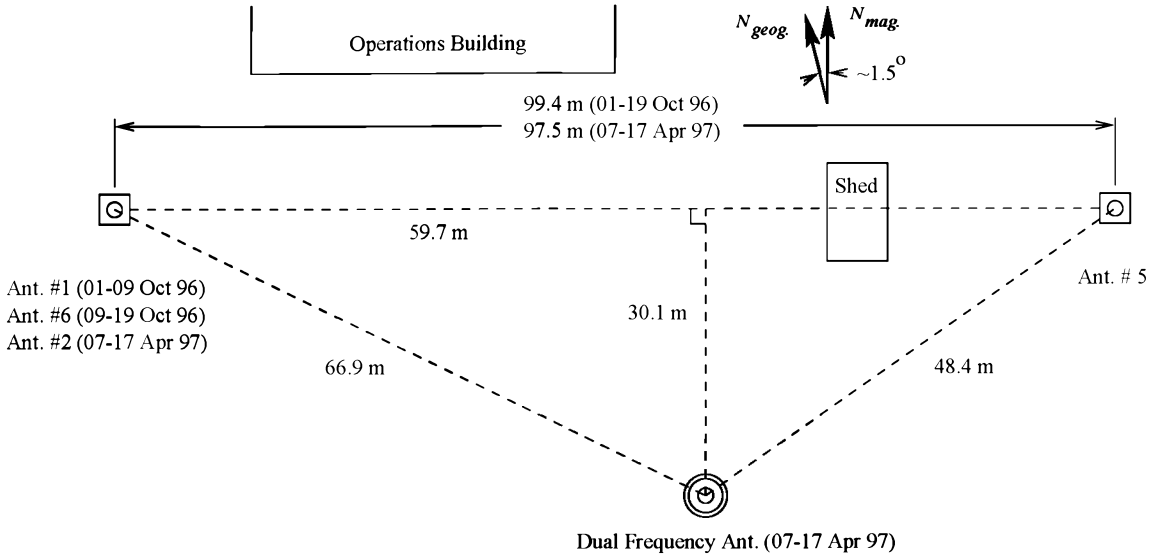

Figure 5.1: Site sketch of Ancon station (not to scale). All distances between antennas are measured; other distances are calculated. The numbered antennas are single frequency (L1) antennas. The dual frequency antenna was set up only for the April 1997 campaign.

antenna during the October 1996 campaign to isolate a problem that the associated receiver had with low signal strength. Antenna 6 remained at the Ancon Observatory after the October campaign for local studies. In April 1997, we used Antenna 2 for the western antenna, then, and left Antenna 6 where the Ancon personnel had located it.

Ideally, we would have liked to have placed the dual frequency antenna along the line connecting the other two antennas. Unfortunately, unless the dual frequency antenna were placed near one of the L1 antennas it would have its sky view partially obstructed by the Operations Building or the shed. So instead we placed the third antenna farther south than the first two, although in between the other two in the east-west direction.

A summary of the Ancon GPS data follows. During the October 1996 campaign

we collected 17 nights worth of data. (A power failure disrupted data logging early in the evening on 07 Oct 96 and the receiver software failed to restart properly due to an error in its setup.) Of those 17 nights, six (6) have definite GPS scintillation activity and two (2) more have possible scintillation activity. In April 1997 we logged 10 additional nights worth of data. Of those 10 nights, three (3) have definite GPS scintillation data. In addition, the receiver which remains at Ancon (associated with Antenna 6) recorded data from 04–06 Apr 97 under control of Ancon Observatory personnel. On one of those nights (04–05 Apr 97), then, we have GPS observations of scintillations by a single receiver, albeit from a different antenna location than those sketched in Figure 5.1.

The situation at Tucuman is more complicated. During the October 1996 campaign, the antenna was successively sited in four different locations in an attempt to mitigate the severe multipath effects that that station experienced. Data were collected from 03–18 Oct 96 for a total of 15 nights, including only 3 nights at the final site. In April 1997, the antenna remained at the final site of the previous campaign, but with an improved ground screen (as discussed in Chapter 3). Data were collected from 03–17 April, for a total of 14 nights. Additionally, the April data contained the first definite instance of GPS scintillation activity we identified in the Tucuman data, previous data having been heavily contaminated with multipath.

Finally, both the Ancon and Tucuman receivers operated some outside the campaign windows. The resident Ancon receiver operated from 04–18 Nov 96 while the Tucuman receiver ran from 06–16 Nov 96. In addition to the April dates prior to the full three receiver setup, the Ancon receiver also took data from 18 Apr through 05 May 97. Very few of these additional data have been examined and catalogued to date, however.

Table 5.3: Nights with Observed Scintillations at Ancon, Peru.

Night	Comments
03–04 Oct 96	Scintillations to east about 0100 UT
06–07 Oct 96	Started in west about 0300 UT and moved eastward
08–09 Oct 96	Scintillations to east starting around 0030 UT
09–10 Oct 96	Started in west and moved eastward, 0145–0430 UT
15–16 Oct 96	Scintillations from west to east, 0200–0400 UT
18–19 Oct 96	Scintillations from west to east, 0000–0800 UT
04–05 Apr 97	Single GPS scintillation monitor
08–09 Apr 97	Scintillations from west to east, 0145–0330 UT
10–11 Apr 97	Scintillations from mid-sky eastward, 0200–0400 UT. Also coronal mass ejection impact on magnetosphere on this night
16–17 Apr 97	Scintillations from west to east, 0200–0300 UT

Table 5.3 summarizes the nights on which definite scintillations were observed at the Ancon station for the two campaigns. The October 1996 data will be the primary focus of this chapter. In addition to the examination of individual scintillation measurements, this chapter will present a case study of airglow and JULIA coherent scatter radar measurements together with GPS scintillation measurements. We will discuss concurrent TEC and scintillation measurements from April 1997 in a later chapter.

5.2 Scintillation Index

The modulation or scintillation index m (or S_4) defined in Chapter 4 provides a convenient quantitative measure of the strength of intensity scintillations. Recall its definition as the normalized deviation of intensity:

$$m^2 = \frac{\langle \mathcal{I}^2 \rangle - \langle \mathcal{I} \rangle^2}{\langle \mathcal{I} \rangle^2}. \tag{5.1}$$

In the original definition, the angle brackets indicated ensemble averaging over many different phase screen realizations conforming to a given set of phase screen statistics (e.g., a given phase deviation σ_ϕ, etc.). Since the intensity data to be analyzed are actually time series, we shall reinterpret the angle brackets to denote time averaging over suitable periods. Changes in scintillation index with time then indicate some combination of spatial and temporal variations in ionospheric irregularities, depending on ionospheric drift and satellite motion as well as the actual development and distribution of the irregularities.

Computing the scintillation index from (5.1) would be relatively straightforward except for power variations due to multipath and due to measurement scatter in the power estimator (both discussed in some detail in Chapter 3). The other, longer scale power variations can easily be removed by low pass filtering or averaging. We can also eliminate some multipath variations by low pass filtering since typical multipath time scales are longer than scintillation time scales, but here two caveats apply. First, the antenna must be sited in a relatively benign multipath environment so that most of the multipath variations are slow. In a rooftop environment, for example, we have seen isolated incidents of patterns of power fluctuations with frequencies as high as 10 Hz that repeat from day to day with the four minute time shift characteristic of multipath. Second, the satellite's ionospheric puncture point must not move with the ionosphere. Otherwise, the scintillation fades lengthen and become comparable to ordinary multipath fluctuation rates.

Scatter in the power estimator contributes variance with fairly short time scales. Since the scatter variance is uncorrelated with variance from scintillations, the variances add. Thus, the modulation index calculated directly from the wide band power measurement comes out higher than its true value. This additional variance makes

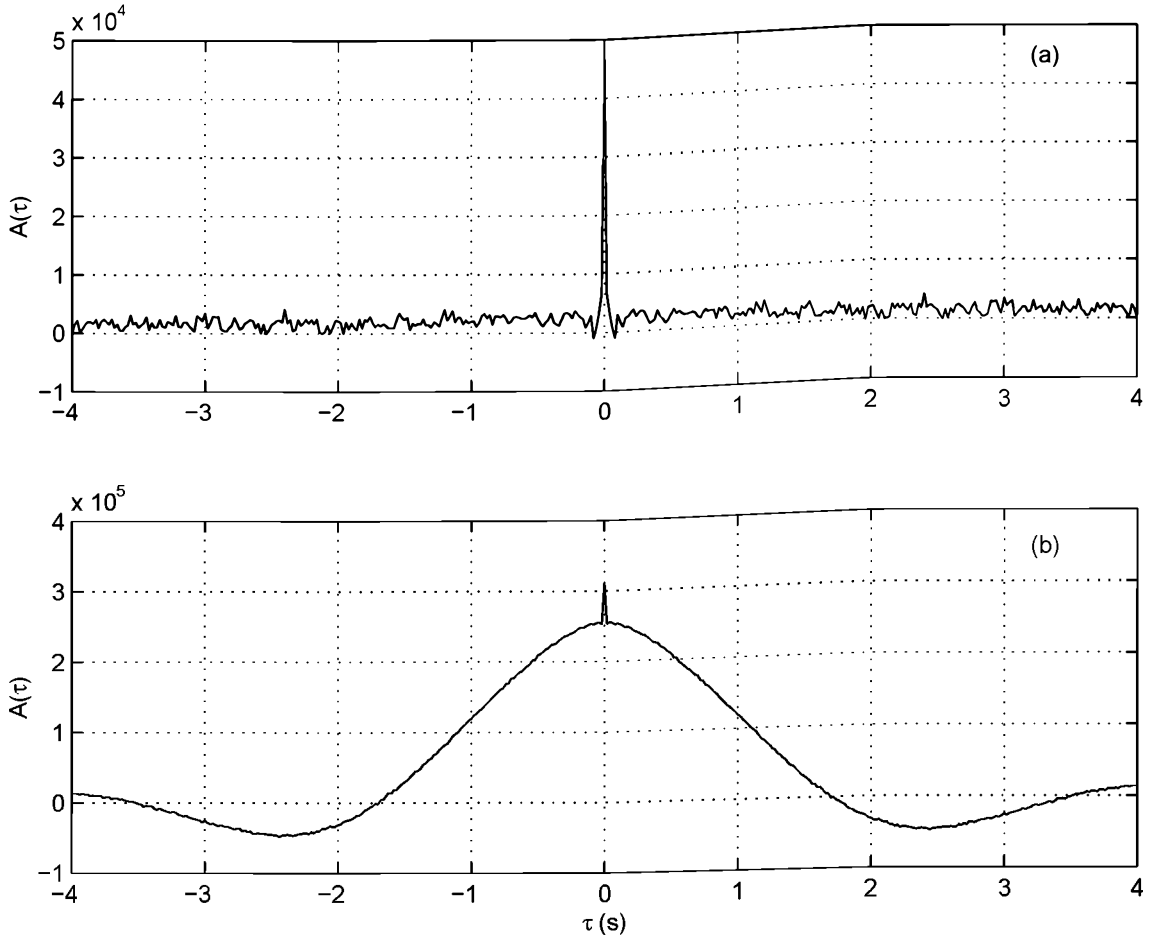

Figure 5.2: Example wide band power autocorrelation functions. These data are computed from one minute segments for PRN 29 at Ancon on 16 Oct 96 (UT). Cases: (a) no scintillation activity, (b) weak scintillations.

it difficult to identify weak scintillations or scintillations when the received signal strength is low (the latter because the estimator scatter increases with decreasing signal to noise ratio).

Fortunately, an examination of typical autocorrelation functions of wide band power data suggests a means to separate the measurement scatter from the signal variance (Figure 5.2). Usually, the autocorrelation functions exhibit a "nib" or spike at zero lag, particularly if the signal has little or no scintillation activity. These spikes

come from measurement scatter, which is largely uncorrelated from one sample to the next. To determine how the autocorrelation functions of the true wide band power $w(t)$ and measurement scatter $s(t)$ combine, we examine the autocorrelation function $A(\tau)$ in more detail:

$$A(\tau) = \langle [w(t) + s(t) - \langle w \rangle][w(t+\tau) + s(t+\tau) - \langle w \rangle] \rangle \,, \tag{5.2}$$

where the angle brackets indicate time averaging. It is straightforward to show that

$$A(\tau) = \langle w(t)w(t+\tau) \rangle + \langle s(t)s(t+\tau) \rangle - \langle w \rangle^2 \,, \tag{5.3}$$

assuming the measurement scatter to be uncorrelated with the scintillations. In other words the autocorrelation function of the scatter simply adds onto the true autocorrelation function of $w(t)$. Further, because the correlation time of the measurement scatter is very short, the predominant effect of the addition appears at zero lag as a spike.

So, to eliminate the spike and estimate the true scintillation variance we use the autocorrelation function and project the value at zero lag based on the neighboring values. Such projection can involve low pass filtering about the peak or parabolic fitting. In practice, using the autocorrelation value at a one sample lag (0.02 s) seems to be adequate and has the benefit of being less computationally intensive than computing several lags. If scintillations are present, the autocorrelation $A(\tau)$ will not drop by much at the 0.02 s lag since the minimum correlation time for the scintillations is typically two orders of magnitude larger. (The lower limit on the fluctuation period of weak scintillations is the order of $\sqrt{2}\, r_F/V$, where $r_F = \sqrt{\lambda z}$ is the Fresnel radius, λ is the free space wavelength of the radio wave, z is the ionospheric height and V is the ionospheric drift. Using $z = 350$ km and $V = 150$ m/s, along

with the GPS L1 wavelength $\lambda = 0.19$ m, gives a minimum scintillation period of roughly 2 seconds.)

The procedure to calculate the scintillation index may be summarized as follows. We use a low pass filter with a cutoff of 0.1 Hz to obtain the local mean values of the channel wide band power P_k and noise wide band power N_k, where k is the sample number. These filtered values are denoted $\langle P \rangle_k$ and $\langle N \rangle_k$, respectively. We estimate the true signal strength variance over a one minute period to be

$$\hat{\sigma}^2 = \frac{1}{M} \sum_{k=1}^{M} (P_k - \langle P \rangle_k)(P_{k-1} - \langle P \rangle_{k-1}), \tag{5.4}$$

where $M = 3000$ is the number of samples per minute while P_0 and $\langle P \rangle_0$ are defined to be the final power values of the previous one minute interval. Further, we calculate the mean power over the same period to be

$$\hat{S} = \frac{1}{M} \sum_{k=1}^{M} (\langle P \rangle_k - \langle N \rangle_k). \tag{5.5}$$

In this scheme the scintillation index becomes

$$m = \sqrt{\hat{\sigma}^2}/\hat{S}, \tag{5.6}$$

for the appropriate one minute interval. Note that this computation eliminates the gain setting of the receiver (common to all channels) provided the gain does not change significantly over the one minute averaging period.

Figure 5.3 compares wide band power data and the corresponding scintillation index over a six hour satellite pass. Generally, the index tracks the patches of scintillations well. Only when the satellite is near the horizon and has very low signal levels does the index respond much to measurement scatter. Also, quantitatively the computed scintillation index values agree favorably with the magnitude of the scintillations. For example, using the short equivalence chart of *Aarons* [1982], a value

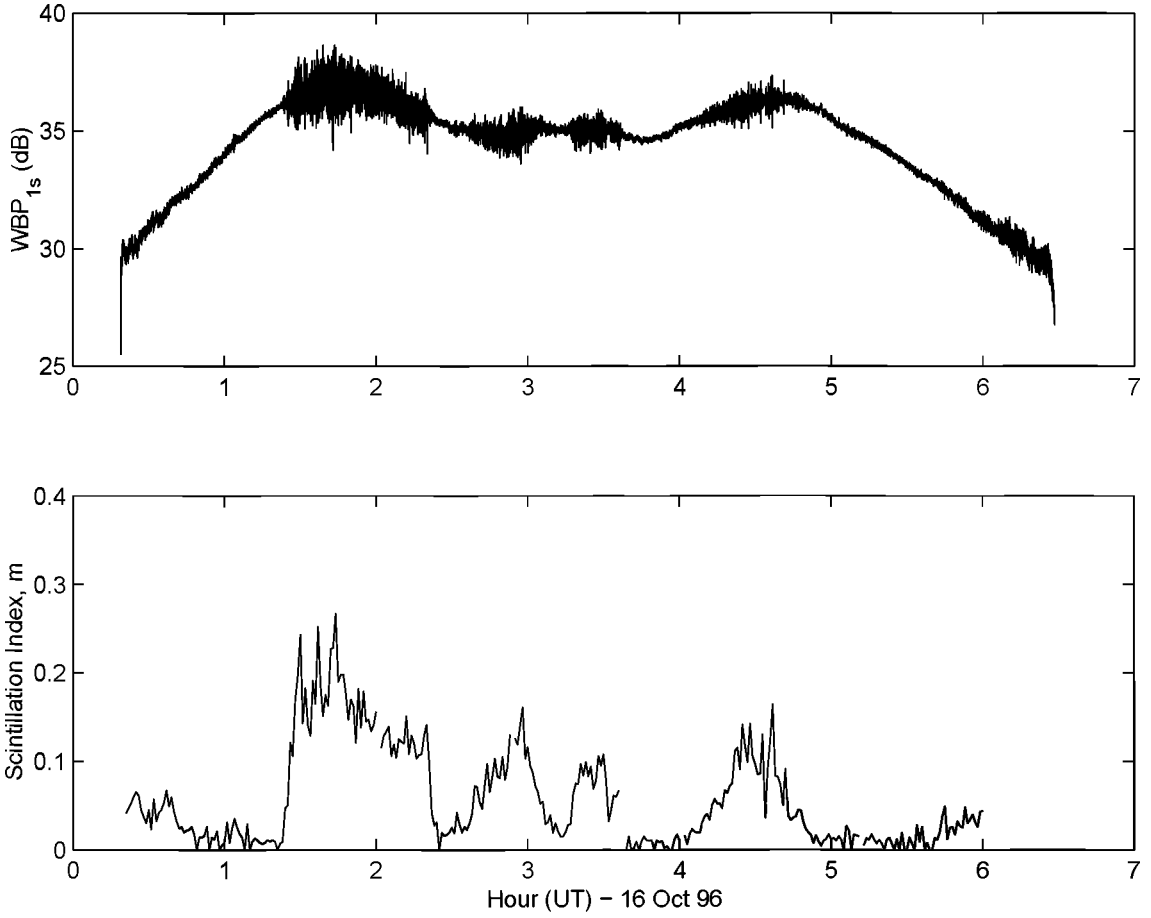

Figure 5.3: Comparison of wide band power measurements with scintillation index. These data are for PRN 29 from Ancon (east station) on 16 Oct 96. Note that the index m is more commonly called the S_4 index in the literature.

of 0.17 for the scintillation index corresponds to peak to peak fluctuations of 3 dB. These values attain in the early part of the scintillation patch that starts at 0130 UT.

We note two special cases that appear in Figure 5.3. First, if the one minute interval lacks even one set of wide band power samples from the satellite, the processing program puts a gap in the plot. Data gaps can occur when the receiver loses a satellite signal momentarily for any reason. In this case, since the wide band power data appear to be continuous, the gaps in scintillation index likely stem from repeated

sets of samples due to timing slippage (see discussion in Chapter 3). The second special case happens when the variance estimator $\hat{\sigma}^2$ ends up negative. This condition typically occurs when the only variance in wide band power is measurement scatter. Since the true variance can never be negative, the program assigns the value of zero to the scintillation index under these circumstances.

Finally, graphical displays of scintillation index provide a useful tool to examine the contents of scintillation data files. Figure 5.4 shows a screen shot of the output of the SCANFILE diagnostic program. This program plots the azimuth and elevation of all satellites in view as a "movie" while it scans through the data file. At each satellite's location the program indicates the magnitude of the scintillation index, which is calculated by a less sophisticated method than the one outlined above, with a circle of proportionate radius. Admittedly, this display is somewhat "dishonest" because doubling the radius causes the area to quadruple [*Huff*, 1954]. Nevertheless this simple technique crudely yields the true desired result: a line indicating the satellite's track whose thickness is determined by the scintillation index.

Not only does the SCANFILE animation provide the operator with the means to assess whether or not scintillations appear in a given file, it also gives a good sense of the dynamics of the irregularities in a way that is difficult to illustrate with static "snapshots" like Figure 5.4. Even sequences of snapshots often produce confusing results compared to "movies." In the animations, for example, it is easy to note the west to east drift of the scintillating patches or that two satellites on the same field line become "lit up" with scintillations simultaneously. Later in this chapter we shall grapple with trying to replicate in static form some of the sense of dynamics that SCANFILE gives.

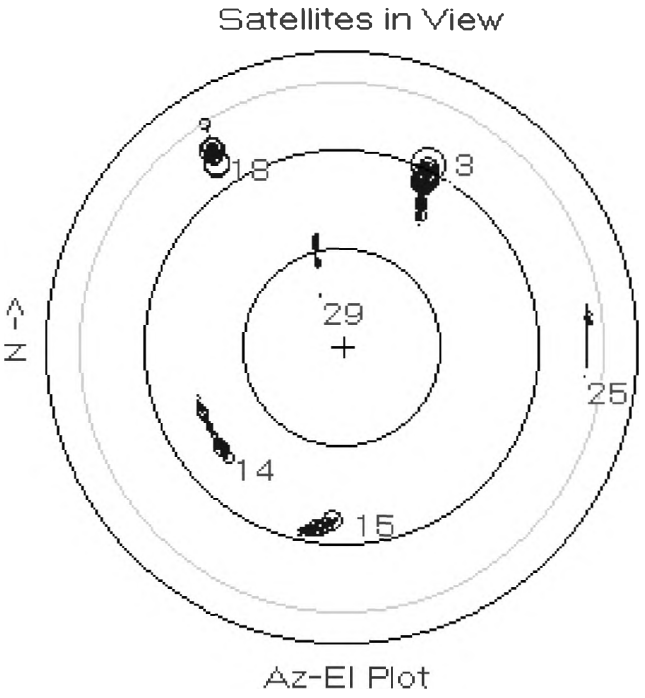

Figure 5.4: Example screen capture from SCANFILE diagnostic program. This is an azimuth-elevation plot of satellite sky position with signal strength indicated by line thickness (crudely plotted with circles of varying radius proportional to the scintillation index). The top of the plot is geographic north whereas the right side of the plot is east. A plus sign in the center represents zenith. Dark circles centered on zenith indicate elevation in 30° increments. These data are from the eastern station at Ancon at 0240 UT on 16 October 1996. Displayed trails cover 40 minutes' worth of data.

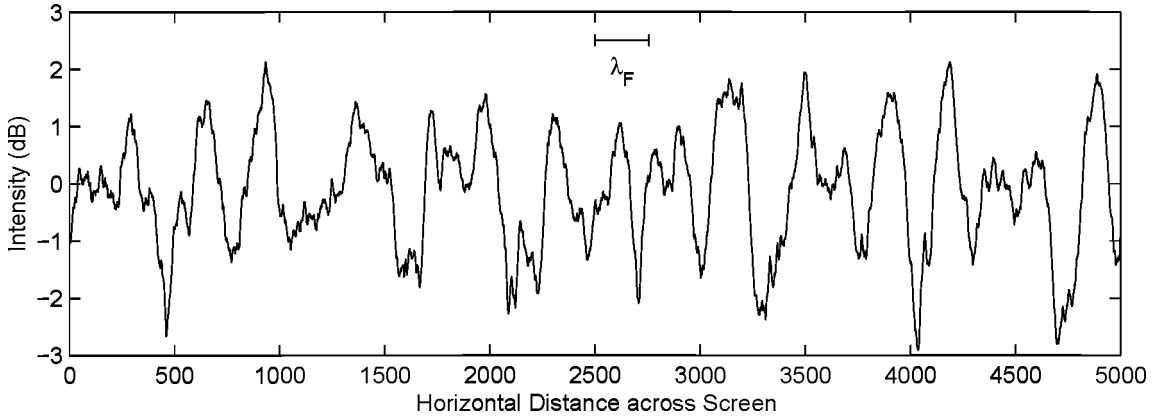

Figure 5.5: Phase screen numerical experiment to illustrate Fresnel filtering. Only 5000 points out of 65,536 are shown. The scintillation index of this particular power law phase screen realization is 0.23. The Fresnel filtering scale $\lambda_F = \sqrt{2}\, r_F$ governs the predominant scale size of the intensity fluctuations, although much spread about this width is visible.

5.3 Time Scales

Having parameterized the strength of amplitude scintillations, we turn to a discussion of their characteristic time scales. Again, these time scales usually reflect the spatial scale of the intensity pattern coupled with some characteristic velocity (composed of ionospheric drift and satellite motion). For weak scintillations, the predominant scale size in the intensity pattern is around $\lambda_F = \sqrt{2}\, r_F$, as determined by Fresnel filtering (see Chapter 4). This filtering effect is easy to demonstrate with numerical experiments. Figure 5.5 shows the intensity pattern developed below one realization of a random phase screen. This screen has Gaussian statistics with $\sigma_\phi = 3.53$ radians and a q^{-3} power spectral density having an outer scale cutoff at $q = 2\pi/8192$ grid spacings^{-1}.

Now assuming that the equivalent phase screen lies 350 km distant from the ground observer yields a Fresnel scale size $\lambda_F = 360$ m at the GPS L1 frequency. For a

stationary satellite directly overhead and 100 m/s ionospheric drift, the characteristic scintillation time scale is 3.6 seconds. This is approximately the case for the PRN 29 data that Figure 5.6 shows. Here the satellite is near zenith and has very little east-west velocity (see Figure 5.4). During 0210–0213 UT, the average geomagnetic eastward velocity of the 350 km ionospheric puncture point is 8 m/s. On the other hand, the average eastward puncture point velocity of PRN 15 is much larger, 72 m/s. Assuming that the ionosphere drifts at 100 m/s, the net drift of the irregularities relative to the line of sight reduces to 38 m/s in this case. The smaller relative drift gives longer fade times than those observed on PRN 29.

Figure 5.7 presents an interesting case where two satellites have nearly identical eastward motion, 28 m/s for PRN 3 and 26 m/s for PRN 14, but noticeably different fading rates. In this case, the satellites are likely in two different scintillating patches. For example, scintillations on PRN 29 stopped around 0220 UT on 16 October (Cf. Figure 5.3), indicating that the irregularities have drifted past the satellite toward the east, toward PRN 3. Meanwhile, scintillations start for PRN 14 to the west around 0130 and continue to 0330 UT without interruption. (The later case study of this chapter supports the assertion that PRNs 3 and 14 lie in separate patches at 0210–0213 UT.) So, if the two patches were to drift at different rates, different scintillation time scales would result. In this case, the patch appearing along the line of sight to PRN 14 is possibly drifting more slowly than the patch affecting PRN 3 to the east, thus giving longer period scintillations on PRN 14. The literature documents cases of differing scintillation drift measurements to the east and west for geostationary satellite beacons [*Basu et al.*, 1996].

We must keep in mind, however, that other factors influence the scintillation fading rate. For example, if the satellite appears at any elevation other than zenith, both

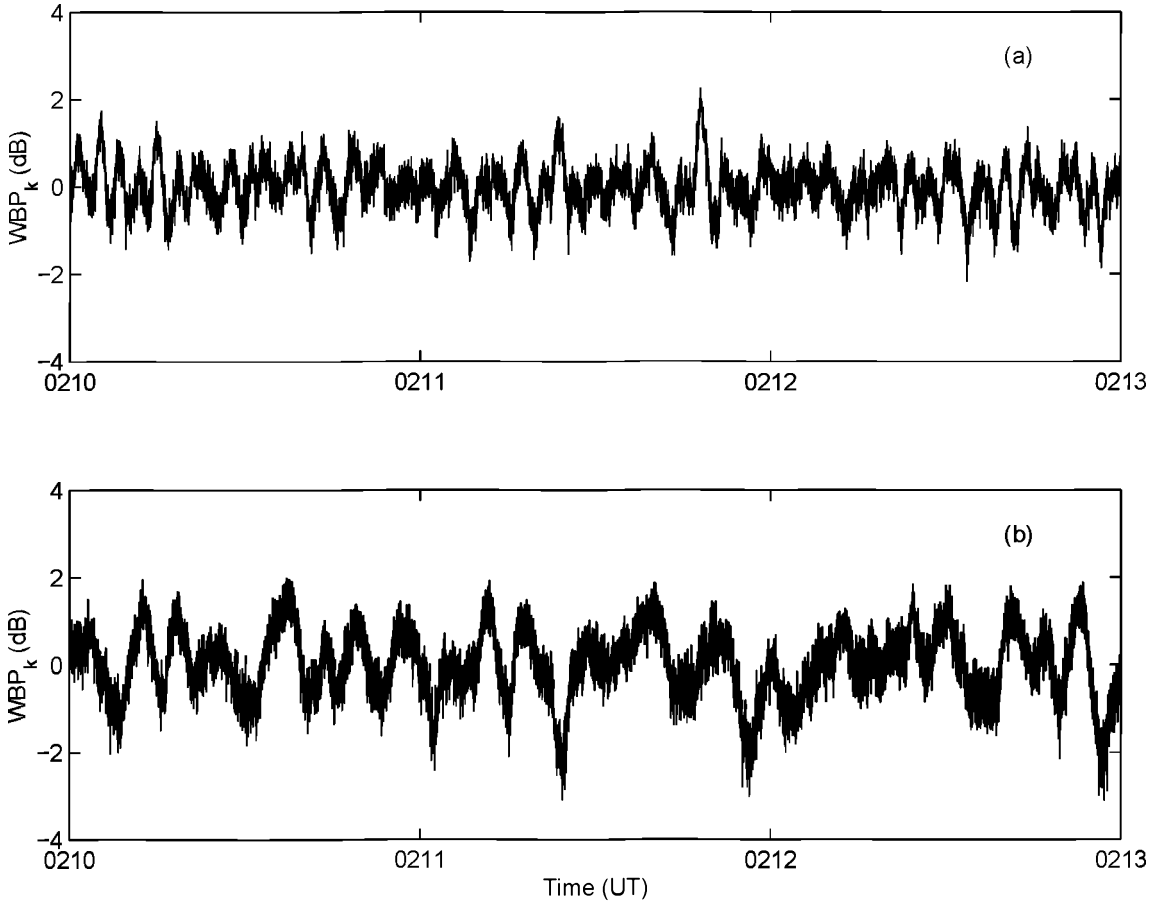

Figure 5.6: Comparison of scintillation fading rates from two satellites with different east-west puncture point velocities. These data are from Ancon on 16 October 1996. (a) Detrended wide band power data from PRN 29. (b) Data from PRN 15. PRN 15 had an eastward velocity component more closely matching the eastward drift of the ionosphere; consequently, PRN 15 experienced longer fades than PRN 29.

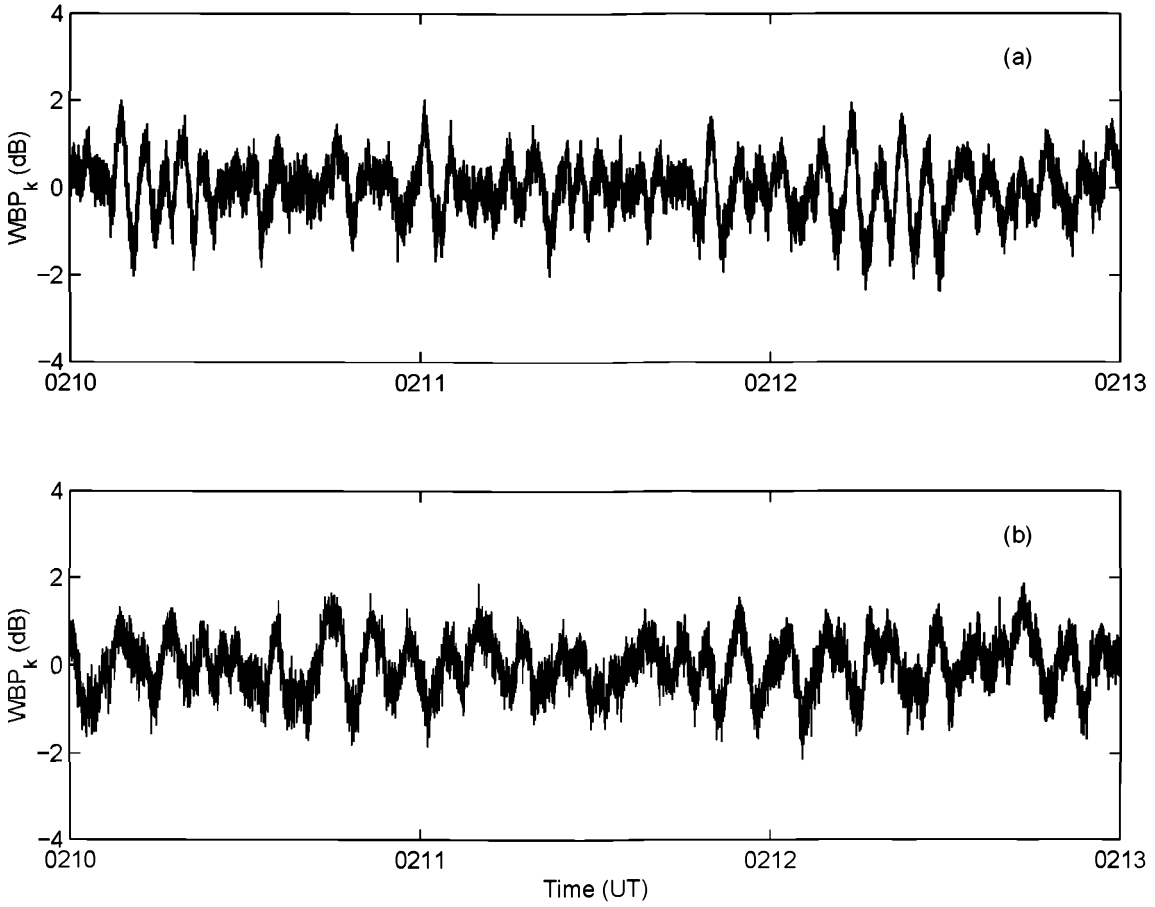

Figure 5.7: Comparison of scintillation fading rates from two satellites with the same east-west velocity. These data are again from Ancon on 16 October 1996. (a) Data from PRN 3. (b) Data from PRN 14. Even though both satellites' 350 km puncture points move in the geomagnetic eastward direction at almost the same speed, the data exhibit different fading rates for each satellite.

vertical and horizontal ionospheric drift affect the scintillation fading rate. Also, the distance to the equivalent phase screen increases for lines of sight away from zenith. Finally, the height of the F peak varies from the assumed 350 km.

Despite the complications listed above, we have independent means to ascertain the relative drift speed and to compare it to the scintillation fading rate. Recall that the Ancon station had spaced GPS scintillation monitors with their data collection independently synchronized to the GPS signal. Using these spaced receivers we can measure the effective west to east drift of the ionospheric irregularities (Figure 5.8).

Figure 5.9 shows a comparison of scintillation fading rates with the drift velocities measured by cross correlation for the night of 15–16 October 1996 at Ancon. This is similar to a study done by *Rino and Owen* [1980] with Wideband satellite data, except that they use drift velocities calculated from the satellite's motion, assuming the ionosphere to be stationary (an appropriate assumption for a satellite in a low altitude, high inclination orbit). We have normalized the fading rates by multiplying by r_F, the Fresnel radius (assuming 350 km altitude for the ionospheric intersection), to compensate for the varying distance to the F peak as the satellite moves. Each plus sign (+) represents the values of $r_F/\tau_{3\text{dB}}$ and v_{drift} computed for a one minute interval in which the satellite experienced scintillations. Here $\tau_{3\text{dB}}$ is the lag from the cross correlation peak to 50% correlation and v_{drift} comes from the time offset of the cross correlation peak from zero.

In some cases, especially for PRN 15 when it is rising in the west, $v_{\text{drift}} < 0$. In other words, the apparent ionospheric drift as computed by the cross correlation technique is westward. These negative drift values typically occur when the eastward motion of a satellite's ionospheric puncture point exceeds the actual ionospheric drift. In all cases the correlation between the period of the signal and the net drift is

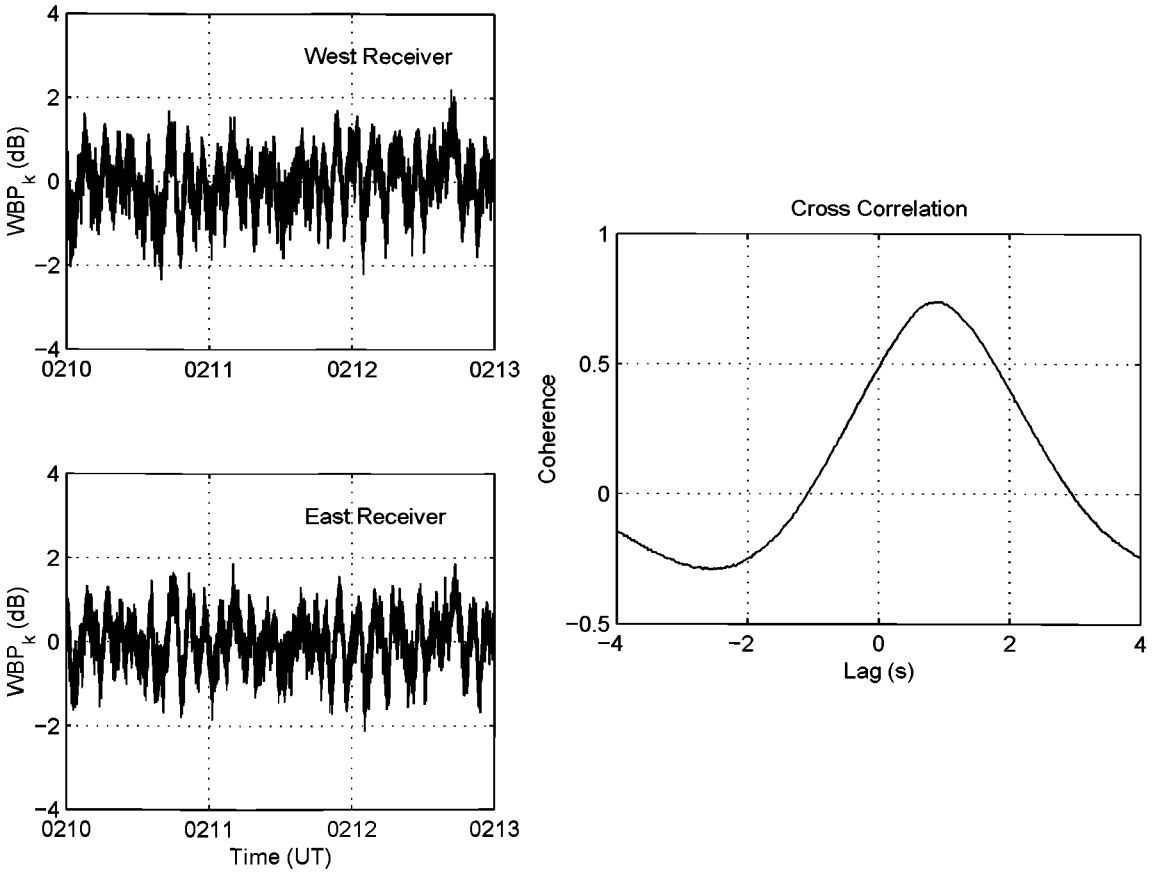

Figure 5.8: Example of spaced receiver drift measurements. These data are from Ancon for PRN 14 on 16 October 1996. The left hand side shows the comparison of detrended power data between the western and eastern receivers. The right hand side plots the cross correlation between the receivers. The cross correlation indicates that the scintillation pattern appeared at the western receiver about one second before repeating at the eastern receiver. This one second time delay amounts to 100 m/s of eastward ionospheric drift relative to the motion of the line of sight to PRN 14.

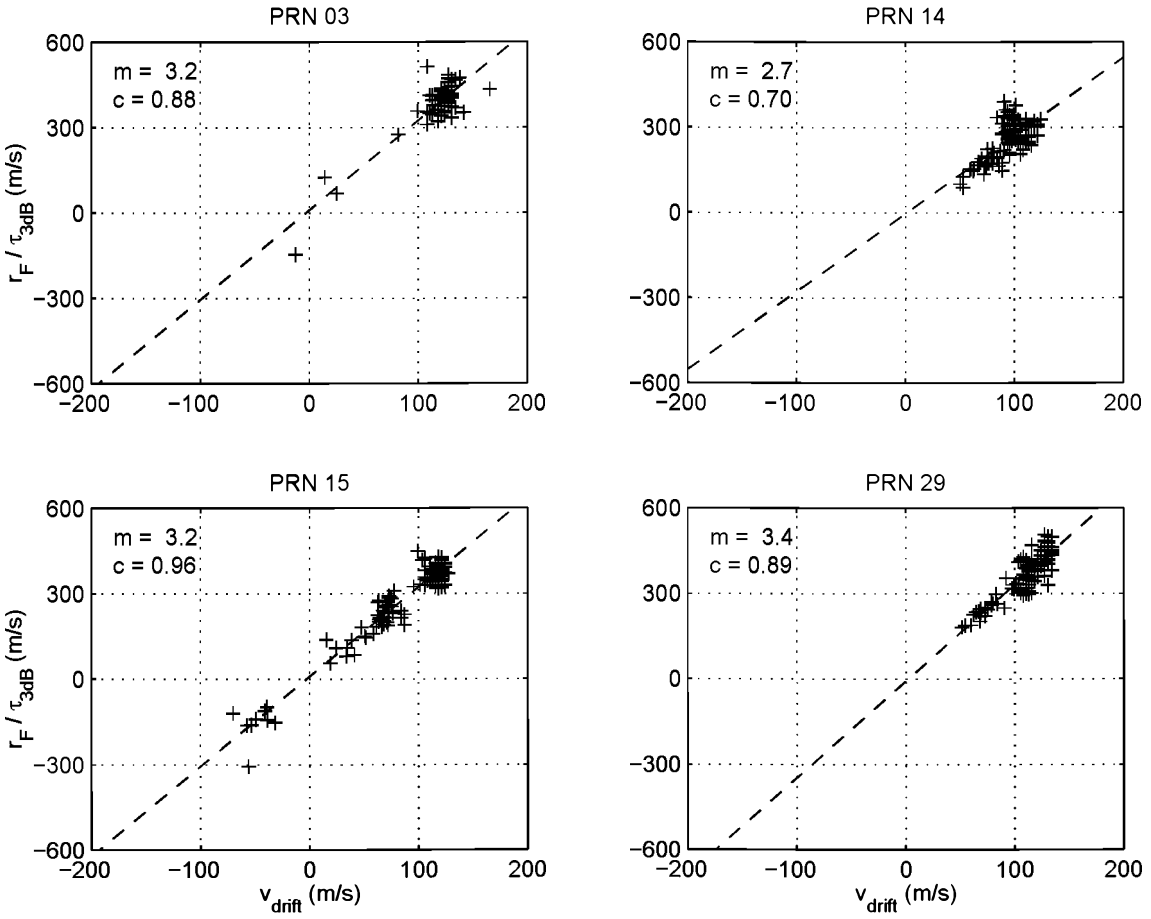

Figure 5.9: Comparison of spaced receiver drift measurements with scintillation period. For each satellite we have made scatter plots of $r_F/\tau_{3\text{dB}}$, where r_F is the Fresnel radius (for a 350 km altitude ionospheric puncture point) and $\tau_{3\text{dB}}$ is the half width of the cross correlation peak (i.e., lag from the correlation peak to 50% correlation), versus drift velocity v_{drift} computed from the peak's offset from zero lag. Note that we have made $\tau_{3\text{dB}}$ negative whenever $v_{\text{drift}} < 0$ in order to fit the lines. The dashed lines represent the least squares linear fit. The slope m and correlation coefficient c label each graph. These data are from 16 October 1996 at Ancon for times after 0100 UT.

quite good. This high correlation indicates that we observe essentially "frozen in" irregularities. That is, the irregularities do not change much with time in passing from one receiver to the next. Also, all the fitted lines pass very nearly through the origin with similar slopes for all the satellites, indicating a simple direct proportion.

We can estimate theoretically what the relationship between $r_F/\tau_{3\text{dB}}$ and v_{drift} should be by assuming a simple model. We assume that the intensity pattern across the ground is sinusoidal with a crest to crest distance of $\lambda_F = \sqrt{2}\, r_F$. (This crest to crest distance does not strictly apply for scintillations except when the satellite lies near zenith, however.) If the net horizontal drift of the ionosphere relative to the line of sight is v_{drift}, we expect the period observed at a stationary receiver to be $\lambda_F/v_{\text{drift}}$. For sinusoids, 50% correlation occurs at a lag equal to one sixth the period. Thus, $\tau_{3\text{dB}} = \lambda_F/(6v_{\text{drift}})$. Consequently, $r_F/\tau_{3\text{dB}} = 6v_{\text{drift}}/\sqrt{2}$. Specifically, $r_F/\tau_{3\text{dB}}$ is proportional to v_{drift} with a proportionality constant of approximately 4.2 in this model.

Now the measured slope in most cases of Figure 5.9 lies around 3.2. Many factors could contribute to the discrepancy between the measured slope and the slope derived from the simple model. For one, the true shape of the scintillation waveforms is not sinusoidal. Non-sinusoidal waveforms have different 50% correlation widths. If, for example, the waveforms were square waves (here meaning 50% duty cycle periodic pulses alternating between positive and negative intensities of equal magnitude), $\tau_{3\text{dB}}$ would become $\lambda_F/(4v_{\text{drift}})$ giving a slope of 2.8. Another simple factor which can affect the slope is the actual height of the F peak. The higher the F peak (i.e., the farther away the equivalent phase screen compared to our assumed 350 km altitude), the smaller the slope becomes. Notably, *Rino and Owen* [1980] attribute scatter from the theoretical curve in similar diagrams of theirs to "nonstationarities in the data

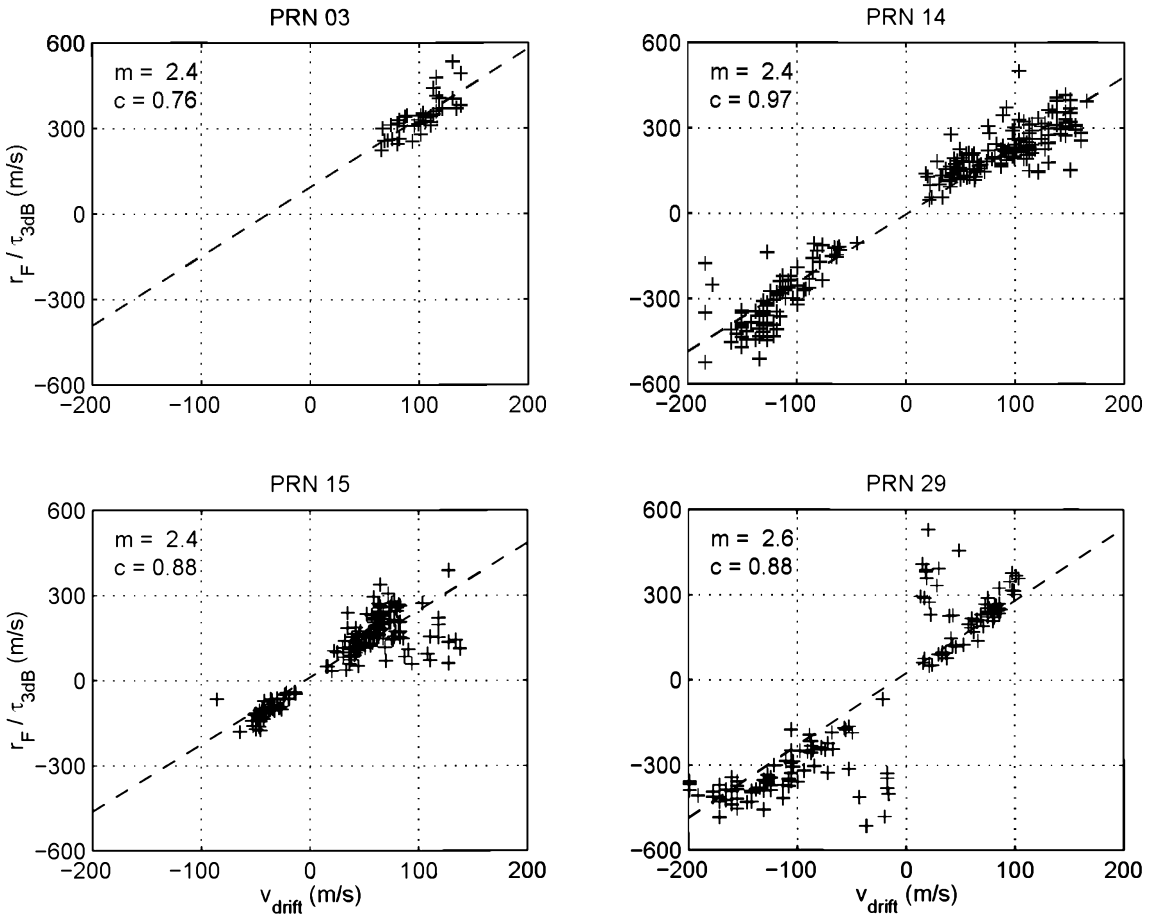

Figure 5.10: Comparison of spaced receiver drift measurements with scintillation period. Same as Figure 5.9 except for 19 October 1996 from 0000–0600 UT (after which the selected satellites showed little scintillation activity).

and/or effective height variations."

Figure 5.10 shows a similar plot for 19 October 1996. Here we observe several salient differences from the 16 October data. For one, the typical slope of the fitted lines is smaller, about 2.5 rather than 3.2. In one case (PRN 3) the y intercept is not zero. More cases with $v_{\mathrm{drift}} < 0$ appear. Also, there appear to be more clumps of data with different slopes than the predominant value. In the previous example of 16 October, only one satellite (PRN 14), notably the one with the exceptional value

of fitted slope, showed much variation from its fitted line.

Now, although the correlation coefficient is quite high, the positive and negative halves of the PRN 14 plot on 19 October appear to have different slopes. This difference suggests a time variation, for example in the height of the irregularities, since the negative net drifts occur later in the evening as the ionosphere slows down in its eastward drift and the satellites then outpace it. In order to test this hypothesis, we bin the scatter plots not by satellite but by time (Figure 5.11). We see that the negative net drifts do indeed appear at later times; around 0500 UT, or midnight local time, the preponderance of net drifts are negative. Further, the slope varies with time for all the satellites together.

Of course, we expect the slope of scintillation period versus drift velocity, as originally binned into observations from individual satellites, not to reflect the state of the ionosphere accurately. After all, the satellites cover different portions of the sky at different times and the ionosphere exhibits both temporal and spatial variations. In fact, we should marvel at the consistency that Figure 5.9 displays. Perhaps on that night, even though the ionosphere was disturbed, it was fairly uniform and relatively constant in altitude throughout the night.

Figure 5.11 suggests that the ionosphere, or at least the equivalent phase screen, did vary in height on 19 October, though. The selected satellites are mostly north and south of the receiver with a few degrees east-west separation during this time period. (Cf. Figure 5.4, recalling that the satellite pattern repeats from night to night.) Specifically, PRNs 14, 15 and 29 converge in longitude around 0300 UT and, somewhat remarkably, track across nearly the same field lines until almost 0600 UT while moving together to the east of Ancon. Around 0240 UT, PRN 3 is substantially farther to the east than the other three, but it soon sets and therefore does not factor

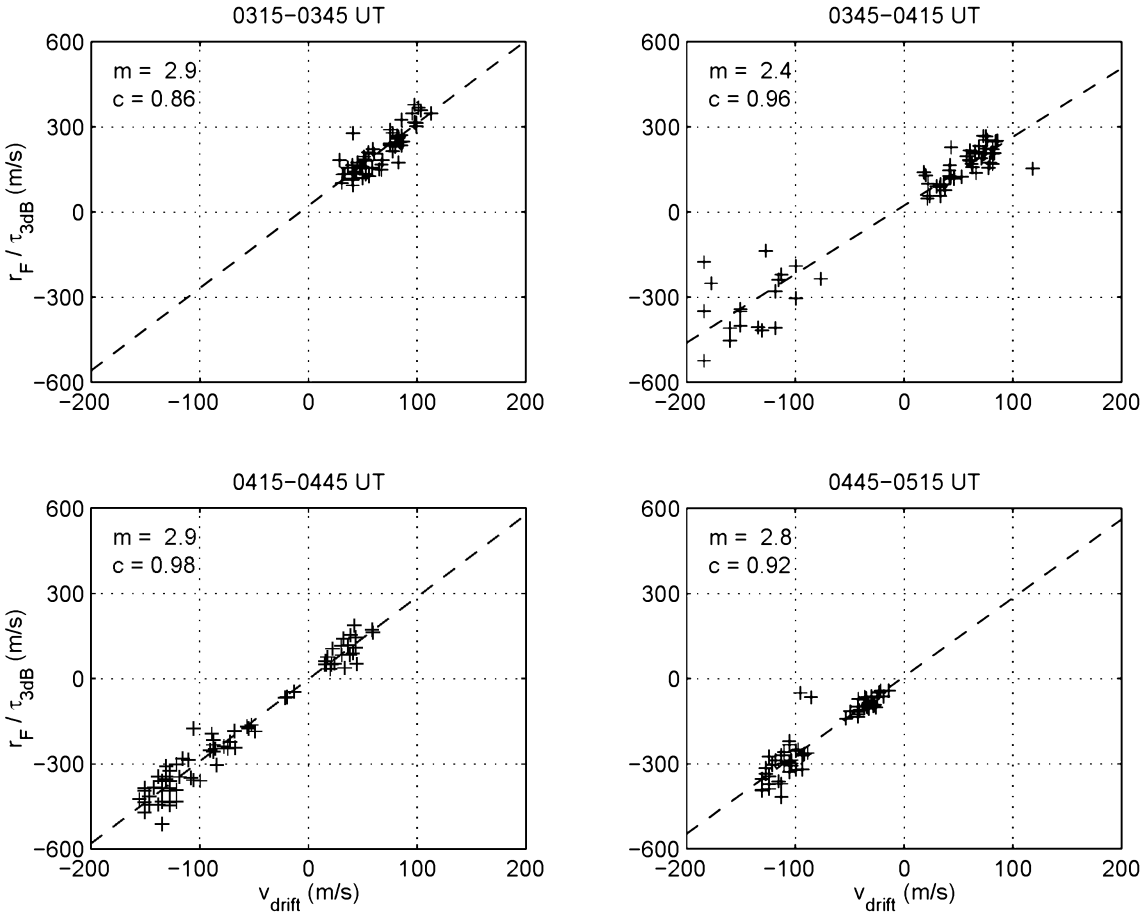

Figure 5.11: Comparison of spaced receiver drift measurements with scintillation period (binned by time). These plots combine satellite PRN 3, 14, 15 and 29 data for the stated time periods on 19 October 1996.

into the combined results at later times.

If necessary, we could further bin by geomagnetic longitude, but time dependence appears to cover the bulk of the variation in this example. Prior to the first time indicated in Figure 5.11, however, the correlation coefficients are rather low. The data at earlier times should probably be binned according to geomagnetic longitude because the selected satellites are not so close together.

If we examine the Jicamarca digisonde hmF2 data for the two nights considered thus far (Figure 5.12), we can see how closely our slope data from the scintillation frequency versus drift velocity scatter plots reflect the height of the F peak. The quick answer is that, while the relation between the hmF2 data and the slope is suggestive, there exist inconsistencies between our previous suppositions and the measured F peak height over Jicamarca. Generally, however, the height of the ionosphere varied only slowly (steadily decreasing from about 330 km at 0100 UT) on 16 October, consistent with the greater slope of the scatter plots on that date and the case made for less variation with time. On 19 October, the ionosphere experienced more rapid variations in height and had a greater average height, consistent with the demonstrable time variation and the lower slopes on average.

Nevertheless, looking at specifics reveals that there remains room for debate on the relationship of hmF2 at Jicamarca to the slopes of the fade rate versus drift velocity plots. First, consider the ratio of slopes between the two nights. During the time period covered by Figure 5.9, mean hmF2 = 300 km; for Figure 5.10, mean hmF2 = 330 km. A simple estimate then gives that the slope should decrease to $\sqrt{300/330} =$ 95% of its original value from the 16th to the 19th. This ratio holds between Figure 5.9 and specific periods in Figure 5.11, but not consistently, as Figure 5.10 indicates.

Second, the timing of the slope changes does not correspond well to the hmF2

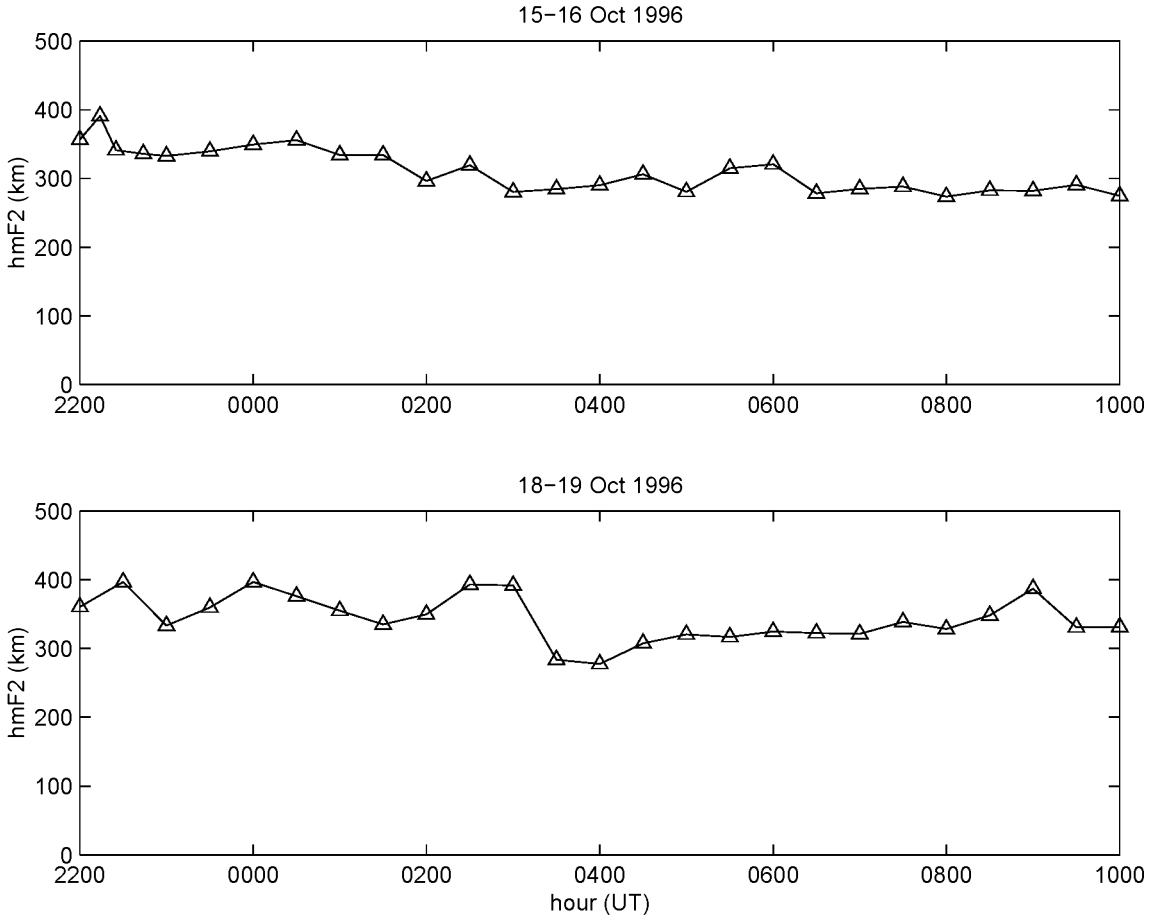

Figure 5.12: Height of the F layer as seen by the Jicamarca digisonde for the two nights studied in the text. These data are predominantly at 30 minute intervals. (Data courtesy J. Scali.)

changes. The ionospheric height drops below 300 km from 0330–0400 UT on 19 October, achieving its lowest values throughout the night. We would expect, then, the slope to become largest during this period. Instead, we get a low value of slope, $m = 2.4$, around 0400. A value so low, in fact, that the equivalent phase screen height would have to raise to 533 km to cause this change by itself. We cannot even plead time lag caused by zonal separation in this case (thinking of the more modest bump in F peak altitude at 0300 UT), because the scintillating satellites, PRNs 14 and 29, cross the Jicamarca field line around this time.

Looking at the range-time-intensity plot from the coherent scatter JULIA radar on 18–19 October (Figure 5.13) reveals that the details of the irregularities over Jicamarca exhibit greater correspondence with the slopes of the scatter plots between 0315 and 0415 UT than do the hmF2 plots. The 3 meter field aligned irregularities trace a relatively intense plume that erupted upwards between 0300 and 0330 UT (2200 and 2230 local). By 0400 UT, this plume had reached 500 km while the lower irregularities had descended and started to fade away. The presence of the bulk of the irregularities at high altitudes in the plume during this time period probably caused the slope of fade rate versus drift velocity to drop significantly between 0345 and 0415 UT, consistent with the 533 km phase screen distance estimated above. Soon thereafter, the only 3 meter irregularities exist around 350 km altitude, as the scatter plot slope increases to 2.8–2.9, indicating an equivalent phase screen height of 365–390 km.

(We note in passing that the character of the 3 meter irregularities as seen by JULIA on 15–16 October was quite different, as will be discussed in the next section. On 15–16 October, the plumes remained below 400 km altitude, again lending credence to the hypothesis that there were no dramatic changes in height of the phase

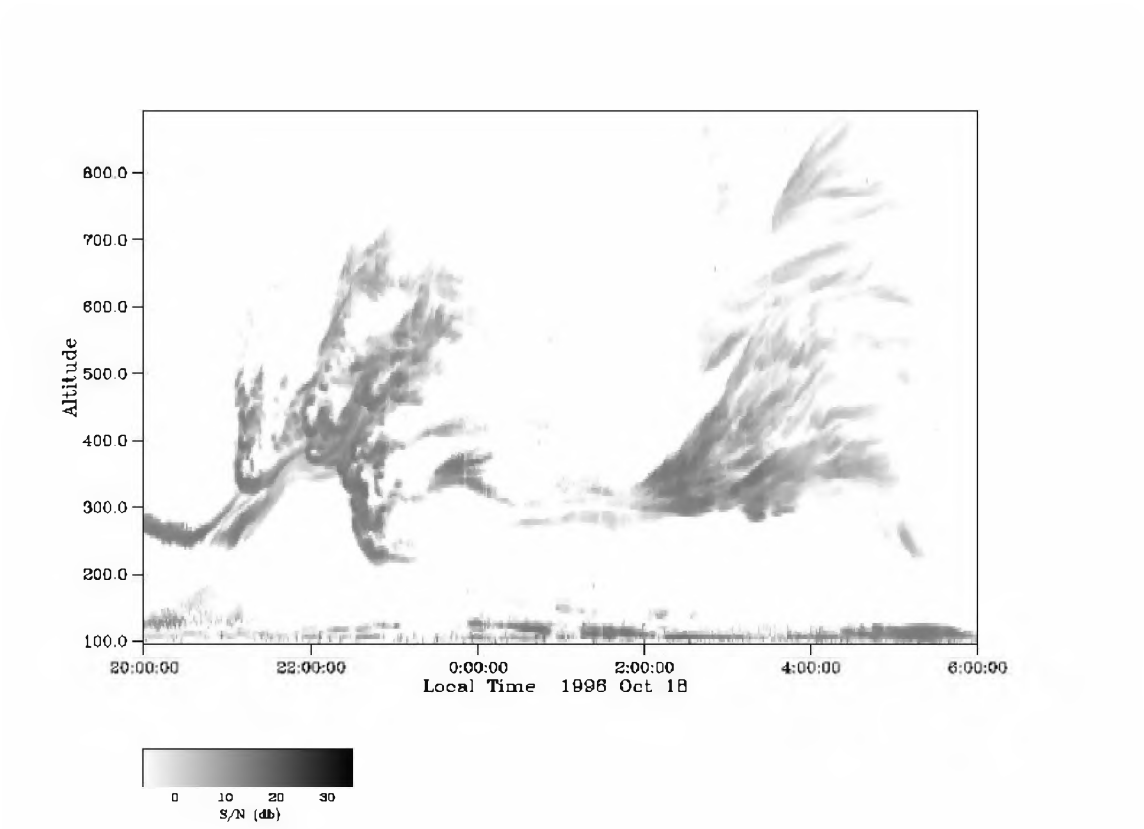

Figure 5.13: Range-time-intensity (RTI) plot from the JULIA radar at Jicamarca for the night of 18–19 October 1996. Local time is 5 hours behind UT, so that 2200 LT is 0300 UT on 16 October. (Courtesy D. Hysell.)

screen as a function of time or zonal distance from Jicamarca on that night. In fact, except for a brief period from 0130–0230 UT, most of the irregularities in the RTI plot lie between 220 and 300 km.)

To summarize, the relationship between fading rate and ionospheric drift relative to the GPS line of sight is definite and proportional, as expected for weak scintillations [*Rino and Owen*, 1980]. In estimating the proportionality constant, we must be careful to compare satellite observations where the height of the irregularities is similar, grouping them by time and geomagnetic longitude for example, but otherwise, the calculations are straightforward and yield convincing results. Conversely, the value of the proportionality constant gives information about the height of the equivalent phase screen, which does not always simply reflect the height of the F peak, as the example on 19 October shows.

5.4 Case Study

We now turn our attention to a study of the irregularities and GPS scintillations on the night of 15–16 October 1996, using some of the collection of multiple instruments available in the Peruvian sector at that time. On the night of 15–16 October, several GPS satellites experienced scintillations and both JULIA radar and Arequipa airglow data were available. Figure 5.14 shows the JULIA RTI plot for that night. Some 3 meter irregularities were already present when the radar switched on at 0100 UT (2000 LT). Around 0140 UT, some low altitude plumes appear. Most plumes are gone after 0300 UT (2200 LT), although some low altitude irregularities persist until about 0500 UT (0000 LT).

Figure 5.15 shows the amplitude scintillations experienced on the signal of PRN

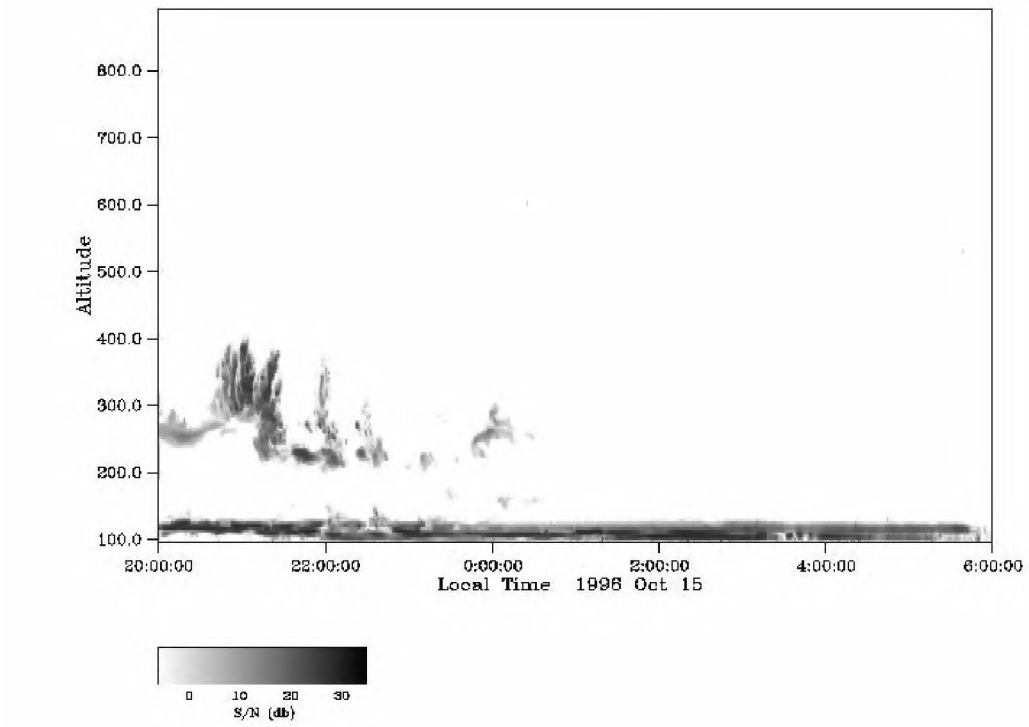

Figure 5.14: RTI plot from the JULIA radar for the night of 15–16 October 1996. Local time is UT − 5 hours. (Courtesy D. Hysell.)

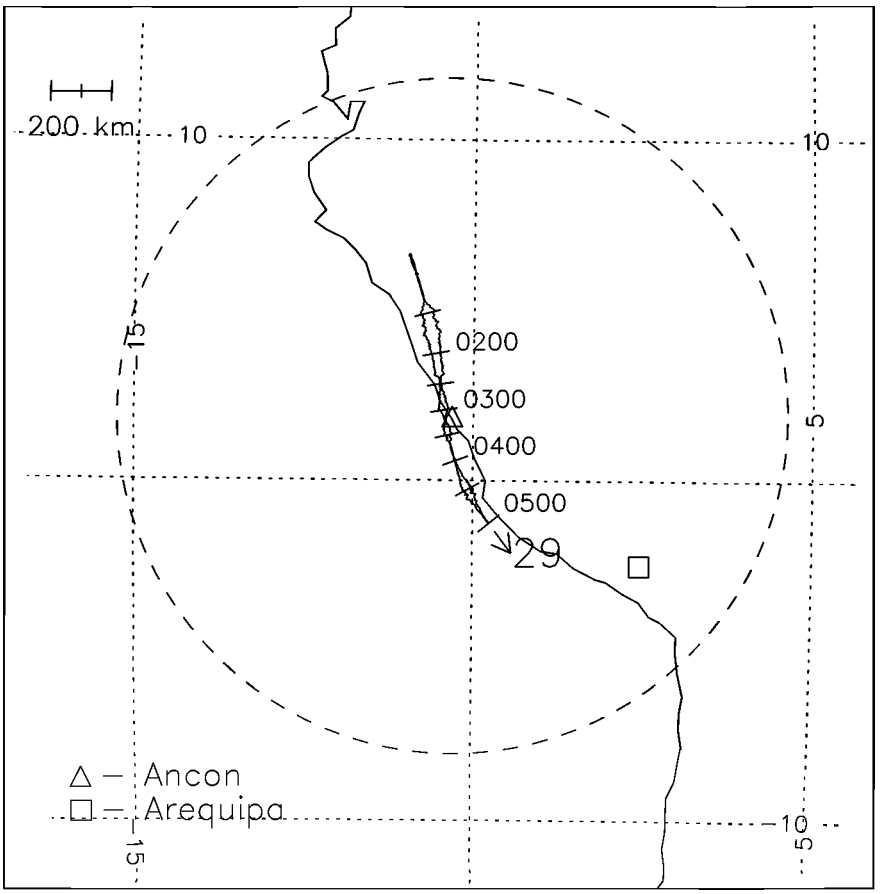

Figure 5.15: Map of scintillation activity from Ancon to PRN 29, 16 October 1996. The trail is the 300 km (mean hmF2 on this night) intersection of PRN 29's line of sight with the ionosphere. Overlaid coordinates are geomagnetic and the dashed circle represents the 10° elevation limit at 300 km altitude. The width of the trail is proportional to the scintillation index. Labeled times are UT. A time tick marks the trail every half hour. For reference, the width of a time tick corresponds to a scintillation index of 0.4.

29. This satellite moved north to south during the time period indicated, very nearly along the Ancon and Jicamarca field lines. The scintillation activity exhibits good correspondence with the plumes seen by the radar. First, the scintillations which start just before 0130 UT and end just prior to 0230 UT match up with the widest plume seen by the radar. The two periods of moderate scintillation activity around 0300 UT correspond to the low altitude (230 km) irregularities and associated plumes observed around 2200 and 2230 LT. Finally, the amplitude scintillations which occur from 0415–0445 UT appear to relate to the low altitude 3 m scale irregularities that the radar sees shortly after 2300 LT.

Note from the radar plot that the 3 m irregularities have mostly decayed away at 0400 UT but, apparently, the couple hundred meter scale irregularities which cause amplitude scintillations at the GPS L1 frequency persist. Such behavior is consistent with previous observations of VHF and UHF scintillations and concurrent 50 MHz radar observations [*Basu et al.*, 1980; *Basu et al.*, 1986]. Interestingly, the small plume that appears to the radar around 0000 local time does not trigger any further scintillations on the PRN 29 signal, for PRN 29 experiences no scintillations after 0445 UT.

Now we can use multiple satellite observations to survey some of the more detailed spatial and temporal behavior of the scintillations. Figure 5.16 shows several satellite trails between 0100 and 0200 UT on the 16th. First we note the near simultaneous, and relatively abrupt, commencement of scintillations on PRNs 14 and 29 around 0130 UT. Prior to 0100, neither satellite signal experienced significant scintillations. The radar suggests that both signal paths pass through the same plume structure, the mass of 3 m irregularities one hour in duration (approximately 350 km wide) which first appears over Jicamarca shortly after 0130 UT. In all likelihood, the hundred meter

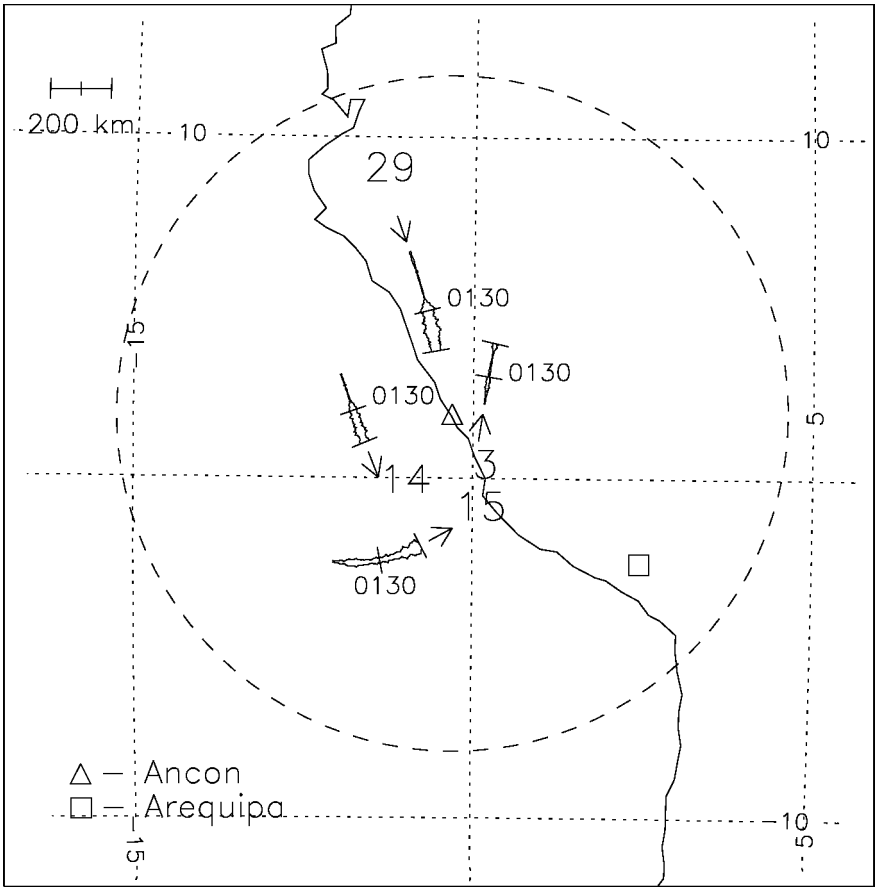

Figure 5.16: Scintillation map over Ancon for the period 0100–0200 UT on 16 October 1996. This map is similar in construction to the previous PRN 29 map, except that it shows all satellites signals with scintillations during a one hour time period. Only PRN 15 experienced minor scintillations prior to this time which ceased at 0040 UT about 90 km to the geomagnetic west of where PRN 14's track starts on this plot.

scale irregularities drifted into PRN 29's line of sight from the west. Nevertheless, they obviously developed between the puncture points, as the ionosphere drifted eastward, because PRN 14 shows no activity before PRN 29 does.

The commencement of scintillations on PRN 3 just prior to 0200 UT (seen better in the continuation plot) corresponds well to the irregularities drifting eastward from PRN 29 at 0130 UT. Judging by the JULIA RTI plot, the start of scintillations on PRN 29 marks the eastward edge of the largest plume structure. The half hour difference in scintillation onset from PRN 29 to PRN 3 fits well with the 200 km east-west separation between the points of onset and a 110 m/s eastward ionospheric drift.

On the other hand, we should examine data from PRN 15 more carefully. Two factors render its data characteristically different from those of the other satellites. First, PRN 15 lies at a lower elevation angle, meaning that small TEC fluctuations are magnified in effect (due to the slant factor) and that scatter in the power measurements increases (due to lower signal strength). Thus, we posit that the variance seen on PRN 15's signal between 0100 and 0140 UT stems from weak electron density fluctuations at best. Second, PRN 15's 300 km puncture point moves eastward at roughly 100 m/s during the time period shown. In fact, the few cases from 0100–0140 UT where scintillations are strong enough to make drift measurements show net westward drifts; i.e., the satellite "outruns" whatever weak irregularities it sees. Only around 0140 does the ionosphere "catch up" with the satellite track.

In fact, that PRN 15 "outruns" the ionosphere suggests that PRN 14's signal catches a plume in development rather than one that merely drifted into the line of sight. Otherwise, PRN 15 would have shown a much larger scintillation index when it passed through the region to the west of the field line where PRN 14 starts

scintillating. Instead, PRN 15 has a scintillation index of no more than 0.1 in this region, incommensurate with its lower elevation and the 0.15 modulation index that PRN 14 subsequently experiences if the "drifting in" versus "developing" hypothesis is to be believed.

Note that the "germ" of the PRN 14 scintillations at 0120 UT could stem from the arrival of the weakly scintillating patch that PRN 15 passed out of at 0040 (not shown, but mentioned in the caption of Figure 5.16). If this patch of scintillations is the one that affects PRN 14, it drifted approximately 150 km eastward in 40 minutes, a net speed of about 60 m/s. This drift speed is fairly low but it is not entirely inconsistent with scintillation drift measurements around 0120 UT (50 m/s relative drift on PRN 14 with 30 m/s eastward motion of the puncture point; -50 m/s relative drift on PRN 15 with 100 m/s eastward motion; both measured drifts ramping up in speed). Nonetheless, the scintillation index was still no more than 0.1 for PRN 15 even though it was at a lower elevation angle during the earlier scintillations. So, if the same patch of scintillations affected first PRN 15 and then PRN 14, irregularity growth definitely occurred between the two points.

After 0130 UT, PRN 15 shows steadily increasing scintillation strength, indicating perhaps that the irregularities first seen to the west on PRN 14 have caught up with its line of sight as PRN 15 turns northward. It is also possible, given that PRN 15's puncture point still has substantial eastward velocity, that the puncture point leads the main westward plume slightly and catches irregularities in development in advance of the patch affecting PRN 14. Without more detailed spatial and temporal knowledge of ionospheric drifts and irregularity regions, one may argue either case. At any rate, the presence of scintillations on both PRN 14 and PRN 29 at 0130 UT, whereas PRN 15 between them concurrently shows little activity, suggests that

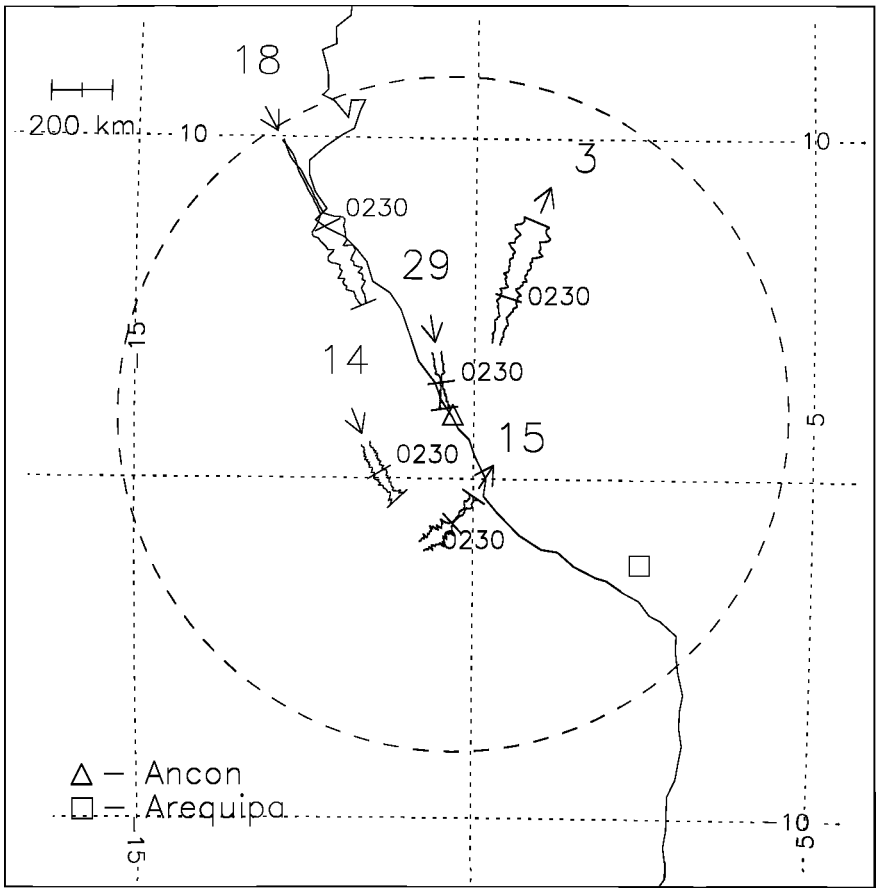

Figure 5.17: Scintillation map over Ancon for the period 0200–0300 UT on 16 October 1996 (same format as Figure 5.16 but covering the following hour).

initially the pattern of irregularities consisted of two scintillating regions with a gap in between. Eventually, that gap filled in so that scintillations remained continuous on PRN 29 until 0230 UT as the structures drifted eastward (Figure 5.17).

Turning to the time period 0200–0300 UT shown in Figure 5.17, we see clearly that the eastward edge of the first scintillating patch has now reached PRN 3 and that PRN 3 scintillates for a long time as the extended patch drifts past. Note the enhanced scintillation index on PRN 3 due to its low elevation at later times. Moving

westward in our summary, we observe that the first, wide patch apparently moves past PRNs 29 and 15 and the Jicamarca field line at 0230 UT (2130 LT). A second, narrow patch appears shortly thereafter, passing through PRN 29's and then PRN 15's lines of sight in succession. What has happened with PRN 14 is unclear, for it has scintillated continuously since 0120 UT. Certainly, it must now be in a different patch from PRN 3 because scintillations have ceased in between while PRNs 3 and 14 continuously scintillate.

Finally, yet another patch drifts through the PRN 18 line of sight to the west starting just before 0230 UT. With a 125 m/s drift, the patch that first affects PRN 18 could also be the one that restarts the scintillations on PRN 14 following the brief lull at 0250. This patch must be relatively narrow, around 130 km wide (assuming 125 m/s ionospheric drift with a calculated 65 m/s eastward motion of the puncture point), because the scintillations cease shortly after 0300 UT. Again, PRN 18 illustrates the enhancement of amplitude scintillations at low elevation angles.

Figure 5.18 shows the next one hour snapshot of scintillation activity. Working from east to west again, scintillation activity decreases on PRN 3 at 0305, possibly marking the end of the first, large scintillating patch. The next patch following behind it appears to pass PRN 15 at 0300. Then, PRN 15 sees a small, weak patch that appears to have just passed PRN 29. When that patch appears on PRN 29, how it relates to scintillations seen earlier on PRN 14 is not straightforward since PRN 14 saw one continuous patch from 0120 to 0250 UT. However, the patch that moves out of the line of sight of PRN 14 at 0330 UT probably appears on PRN 29 as weak scintillations between 0400–0500 (Figure 5.15).

In all likelihood, we witness the decay of the hundred meter scale irregularities between plumes as they drift eastward between PRN 14 and PRN 29. Certainly, from

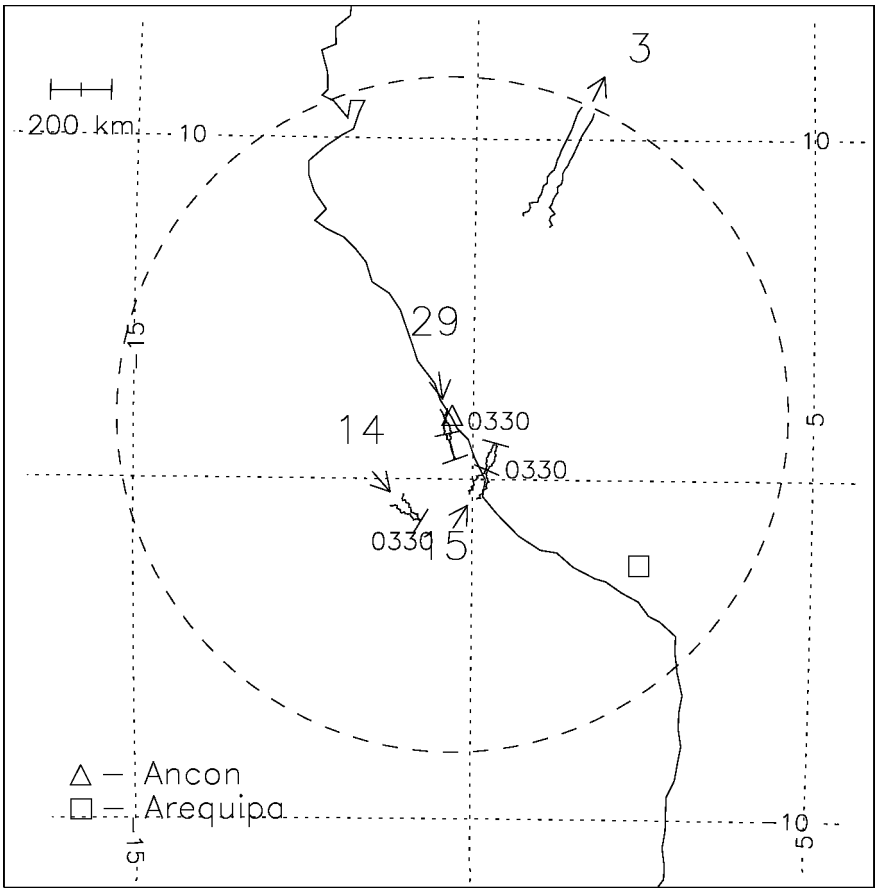

Figure 5.18: Scintillation map over Ancon for the period 0300–0400 UT on 16 October 1996 (same format as previous plots). Shortly after 0300, scintillations cease on PRN 18, so it is not shown to continue from the previous plot. After 0330, PRN 14 has no scintillations either, so its track does not continue past then. Finally, at 0325, PRN 3 sets below the 10° horizon mask.

the earlier comparison with the radar plot, the scintillations on PRN 29 correlate well with the plumes, or vestigial plumes, of 3 meter irregularities. It is possible that these later plumes, which appear "faded" in the RTI diagram, were once connected to each other further west, somewhat in the manner of the mass of plumes that appears over Jicamarca at 0130 UT (2030 LT). Thus, PRN 14 scintillates continuously earlier but PRN 29 observes smaller patches. The breaking up of large, scintillating patches into smaller ones within a half hour's to an hour's drift has been observed for VHF scintillations [*Aarons et al.*, 1980].

To summarize the scintillation and radar results, a first, relatively strongly scintillating plume developed somewhere between the puncture points for PRNs 14 and 29 prior to 0130 UT. This scintillating patch drifted though the PRN 29 line of sight and the JULIA radar beam for approximately an hour, then continued to affect PRN 3 to the east until at least 0300 UT.

Scintillation activity started on PRN 14 just before 0130 UT also, possibly indicating the growth of a weakly scintillating patch seen earlier to the west on PRN 15. The patch affecting PRN 14 could represent the formation of the westward end of the large plume structure seen by the radar from 0130–0230 UT. Whatever the case, PRN 14 experienced scintillations without interruption until 0250, indicating a continuous patch of irregularities not seen later by the radar or PRN 29. By the time these irregularities reach the Jicamarca field line, they have resolved themselves into discrete plumes and scintillation patches which progressively fade in intensity.

Finally, a later, relatively strong and narrow patch of scintillations appears to the west, first impacting PRN 18's signal at 0230 UT. These irregularities, too, weaken progressively as they move eastward. They appear to be the source of the last, mild scintillations observed by PRN 29 between 0400 and 0500 UT. No further GPS

scintillation activity is observed to the west or to the east.

Now we turn to maps of airglow depletions to corroborate the GPS scintillation observations. Figure 5.19 shows some of the airglow activity observed at Arequipa, Peru by the Boston University imager on 16 October 1996. These long (15 s) exposure images capture the development of depletions to the east of Ancon from 0000–0200 UT. Notably, they display a pair of depletions developing and moving eastward, one of which crosses the Arequipa field line at 01:16:34 UT. Unfortunately, no GPS satellites were observed to be affected by irregularities associated with the depletions shown in this montage.

Later images from Arequipa show depletions which do appear to affect some of the GPS lines of sight at Ancon. Figure 5.20 presents an image from 0242 UT which has been mapped onto geographic coordinates. The contrast is very low, but there are depletions during this time period which show up more clearly in the raw, unmapped images (M. Mendillo, private communication, 1998). To highlight the locations of the depletions, the Boston University imaging team has marked their approximate centers with white lines and annotated them with numerical indices above the image. Also, the 300 km puncture points for PRNs 14, 15 and 29 as seen from Ancon at this time are indicated.

Referring to Figure 5.20, the depletions marked 1 and 2 could relate to earlier scintillation activity seen at Ancon. Although its east-west extent is not clear, depletion 2 may be responsible for the scintillations on PRN 3 (puncture point not shown) during the time of the image. The depletion marked 3 has recently passed PRN 15 and may relate to the recurrence of scintillations there around 0245 UT. Note that in subsequent plots that the depletion labeled 3 will show up as three closely spaced, narrow depletions. From a time sequence of the raw images, including short (6 s)

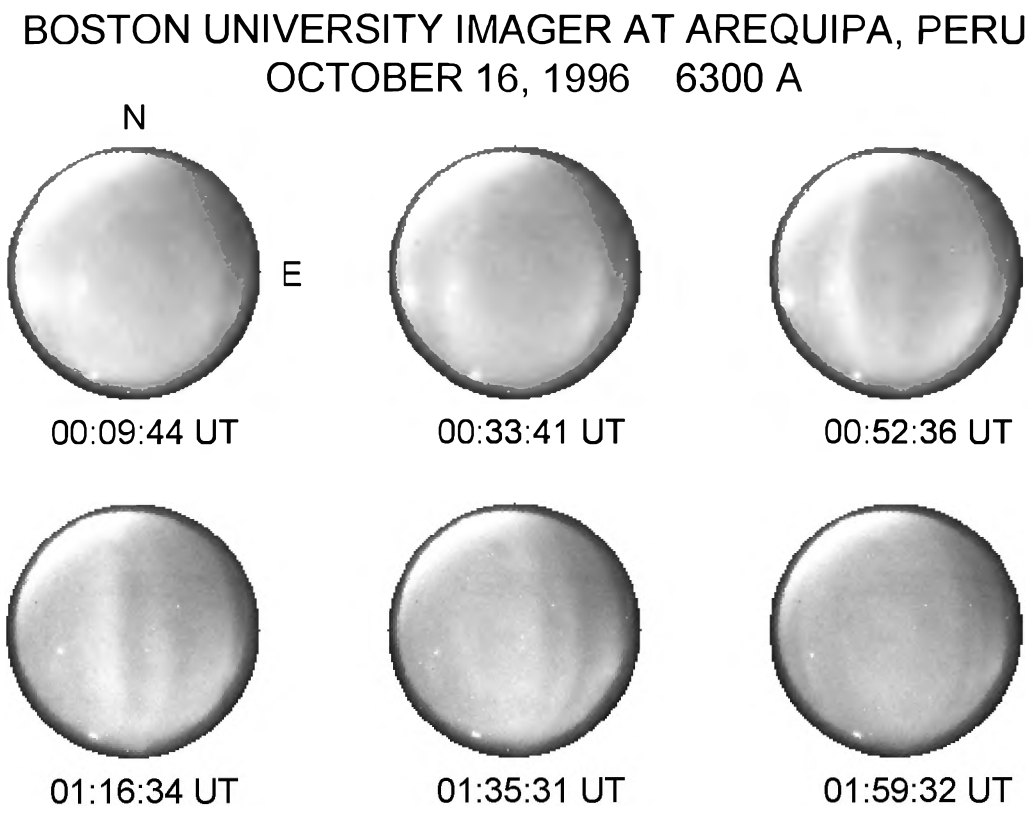

Figure 5.19: Sequence of 630 nm airglow images from Arequipa on 16 October 1996. The lights of the city of Arequipa produce the bright region on the image to the northwest. (Images courtesy M. Colerico, Boston University.)

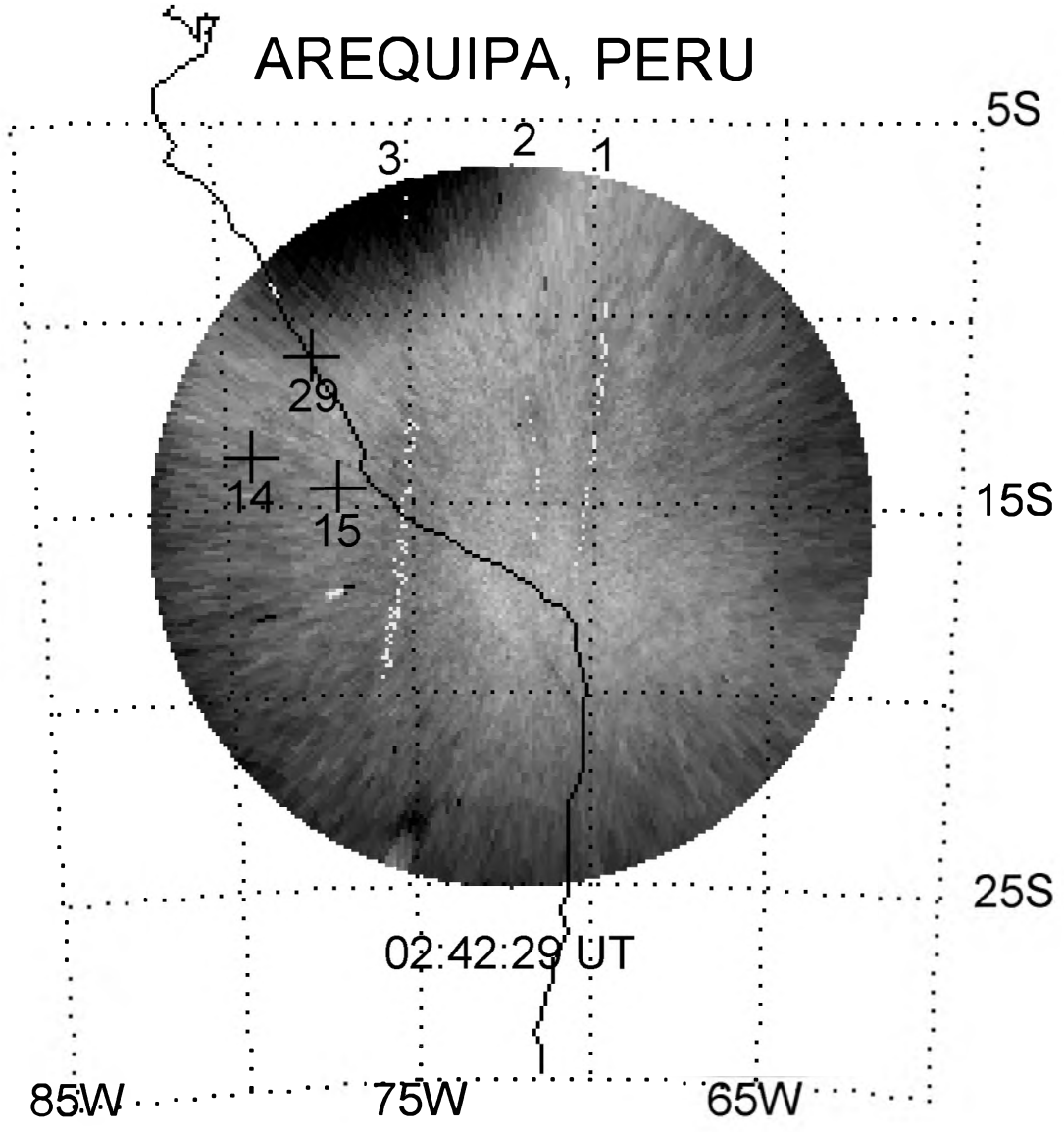

Figure 5.20: Unwarped 630 nm airglow image from Arequipa for 0242 UT on 16 October 1996. Indicated coordinates are geographic and white lines mark the approximate centers of the depletions. The crosses represent the 300 km ionospheric puncture points of PRNs 14, 15 and 29 as seen from Ancon. The elevation limit of the unwarping process is 22° and the altitude used for unwarping was 300 km. (Courtesy J. Wroten, Boston University.)

exposures which are not shown, it appears that the subsequent three depletions all come from the area marked 3 in the present image (J. Wroten, private communication, 1998). Distortion by the imager's lens may be the cause of the earlier, apparent merger but it is possible that the spaces between the three small depletions were also depleted in the earlier image.

Figure 5.21 presents the next image in the sequence, now at 0301 UT. Here we see the full extent of depletion 3 as it has resolved itself into three depletions (3a, 3b and 3c). Translating backwards in time, we find that the narrow depletions could be responsible for the cessation and almost immediate restarting of scintillations as observed on PRNs 14 and 29 around 0250 and 0230, respectively. A new depletion, depletion 4, comes in from the west and passes PRN 15. Depletion 4 also marks the patch whose passage causes scintillations to stop on PRN 29 around 0310 UT, perhaps. None of the marked depletions appears to be responsible for the scintillations that persist on PRN 14 until 0330.

The last image in the sequence, Figure 5.22, shows that the eastward drift of depletion number 4 has slowed. In the same 24 minutes between Figure 5.21 and Figure 5.22, depletion 3c has moved about 4° eastward in geographic longitude while depletion 4 has moved only 1.5°. If the depletion 4 irregularities were to have "pinched off" into two scintillating patches, the trailing patch would account for the short period of scintillations on PRN 29 between 0310 and 0340 and the similar behavior on PRN 15 from 0330 to 0400 UT. Finally, a hypothesized structure to the west of depletion 4, which may be the remnants of the scintillating patch that affected PRN 18 between 0230 and 0300, drifted past PRN 14 at 0330 (trailing edge) and on to PRN 29 with (leading edge) by 0415 UT.

Overall, the structures of airglow depletions and patterns of GPS scintillations

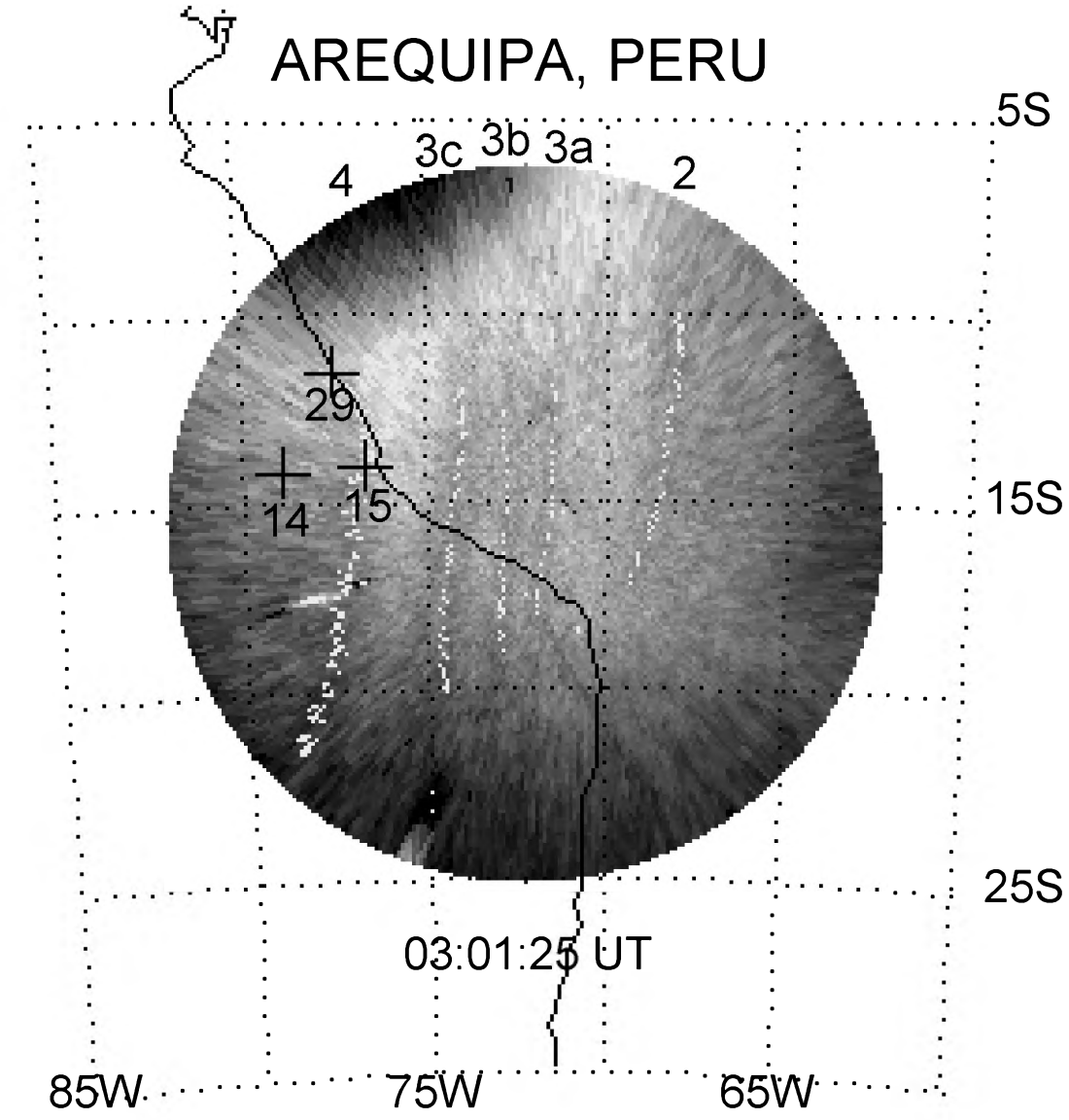

Figure 5.21: Unwarped 630 nm airglow image from Arequipa for 0301 UT on 16 October 1996. Same format as previous figure. (Courtesy J. Wroten, Boston University.)

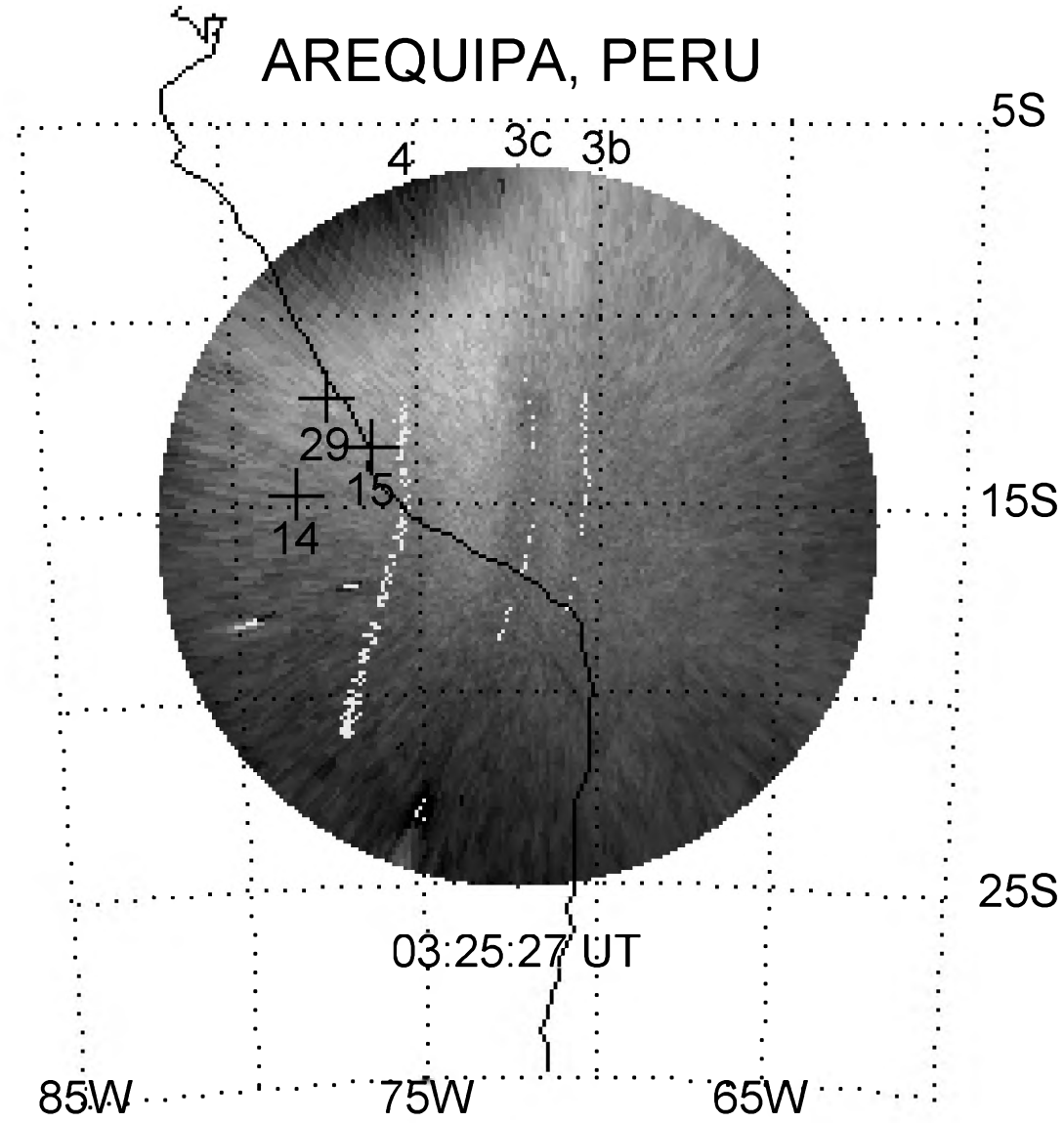

Figure 5.22: Unwarped 630 nm airglow image from Arequipa for 0325 UT on 16 October 1996. Same format as previous two figures. (Courtesy J. Wroten, Boston University.)

show a fairly good correspondence. Of course, the low contrast of the later images hampers the interpretation of the airglow results. For example, resolving whether a given GPS line of sight lies within a particular depletion is essentially impossible. Still, the airglow depletions generally show the structures inferred from the scintillation observations. The correspondence would undoubtedly be better if it were possible to have airglow observations from a nearby site, but the weather in the vicinity of Lima (where Ancon and Jicamarca are located) is invariably cloudy. Also, the GPS satellites with scintillations happened to be relatively close together during the time period under investigation, so that they only covered a small percentage of the overlap between the Ancon and Arequipa fields of view.

Together, the airglow images and GPS scintillation measurements show some of the dynamic detail of equatorial irregularities that the radar, with its fixed, narrow view, cannot capture. The coverage of an imager is unmatched, but it is limited in observation times by the lunar cycle and local weather. In contrast, although GPS satellite coverage can be spotty, visibility conditions do not limit these observations. Furthermore, GPS observations reveal fine scale structural detail not visible in the larger scale structures that the imager shows, at least not at the low contrast levels of the later structures in this case study. For example, the GPS observations indicate that the structure within depletion 4 actually separated into two scintillating patches.

5.5 Summary

We have demonstrated some of the new potential of GPS scintillation observations in two areas: (1) studies of scintillation drifts by spaced receivers and (2) regional studies tracing the development and decay of scintillating patches. The former shows

promise for diagnosing the height of the equivalent phase screen via the comparison of spaced receiver drift measurements (by cross correlation of signal strength data) with the width of the cross correlation peak. The latter provides a picture of the L band scintillation activity within the field of view of a single receiver, at least on a case by case basis. In addition to these relatively novel features, the GPS scintillation monitors can also provide traditional information, such as values of the scintillation index m (S_4) for statistical studies.

Chapter 6

Edge Diffraction

6.1 Background

Up to this point we have primarily considered the characteristics of homogeneously scintillating media with only cursory mention of the fact that these ionospheric irregularities are localized in space and in time. Clearly, as the examples in the preceding chapter illustrate, GPS scintillations often appear in patches, sometimes abruptly switching on and off and sometimes gradually fading in or fading out. In this chapter, we explore some of the transient behavior possible when the radio line of sight passes from a region of undisturbed ionosphere into an equatorial depletion, or vice versa.

The original motivation for these studies consisted of occasional observations of faint V shapes ("spectral Vs") in the spectrograms of 50 sample per second GPS amplitude scintillation data. As subsequent sections will demonstrate, these spectral Vs are not instrumentation anomalies, nor do they likely stem from conventional multipath. In fact, the evidence suggests that spectral Vs are probably of ionospheric

origin and we hypothesize that they are associated with sharp gradients in electron density in equatorial spread F depletions or, possibly, sporadic E layers. Sharp gradients in total electron content (TEC) lead to diffraction phenomena similar to the classical Fresnel knife edge diffraction pattern. We postulate that relative motion of the line of sight through such gradients generates the spectral Vs.

Observations of diffraction patterns in amplitude scintillation data are not new. Apparent instances of edge diffraction from TEC gradients have long appeared in observations from middle latitudes and higher [*Ireland and Preddey*, 1967; *Basu and Das Gupta*, 1969; *Slack*, 1972; *Davies and Whitehead*, 1977]. Most of these earlier observations were associated with sporadic E layers. *Hajkowicz* [1977] includes a review of the subject and in this historical context such diffraction patterns are termed quasiperiodic scintillations. Some observations in equatorial regions also exist [*Kelleher and Martin*, 1975; *Franke et al.*, 1984; *Basu et al.*, 1986], where the various authors infer that the patterns are generated by diffraction from sporadic E layers [*Kelleher and Martin*, 1975], or from depletions associated with equatorial spread F [*Franke et al.*, 1984]. Most of the earlier observations, at all latitudes, came from VHF satellite beacons of 40 to 260 MHz (wavelengths of 7.5 to 1.2 m), although frequencies as low as 20 MHz [*Ireland and Preddey*, 1967; *Slack*, 1972] and as high as 360 MHz [*Davies and Whitehead*, 1977] were used.

Given that observations of patterns of amplitude scintillations similar to diffraction patterns are not new, what is unique about the recent observations? First, most of the earlier observations were in the VHF band. *Franke et al.* [1984] had L band (1.5 GHz) and C band (3.9 GHz) measurements, for example, but apparently only saw quasiperiodic scintillation activity on the 258 MHz link in their experiment. Second, most authors examined the older data by using time series plots rather than

spectrograms. Although *Franke et al.* [1984] do allude to frequency sweeps in passing, referring to the form of the VHF time series data, they do not present spectrograms, nor do they demonstrate L band observations of frequency sweeps.

Unfortunately, the utility of spectral V observations may be minimal. Careful dissection of any observation based on quantities integrated along the line of sight, especially where the ionosphere is highly disturbed and quite inhomogeneous, is challenging enough. In the case of spectral Vs, for example, a coincidence of the motions of several depletion bubbles passing through the line of sight, rather than the edge of a single plume, could supply the postulated sudden change in TEC. Also, spectral V measurements do not supply much quantitative information regarding the magnitude of TEC changes. The amplitudes of the intensity fluctuations that comprise the spectral Vs are low, near the noise level, and the frequency structure does not change with the magnitude of the step in TEC. Still, GPS observations of quasiperiodic scintillations, if confirmed to be generated by diffraction from TEC gradients, constrain the gradient scale sizes of steepened ionospheric structures to be smaller than the VHF observations of *Franke et al.* [1984] and *Basu et al.* [1986] indicate.

6.2 Observations

Figure 6.1 illustrates the first spectral V observation in L1 wide band power (WBP_k) measurements that came to our attention. These data were collected by the eastern GPS scintillation monitor at Ancon, at 50 samples per second from PRN 29 on 16 October 1996, a few minutes prior to the onset of scintillations around 0120 UT (see case study in Chapter 5). The diagram shows a spectrogram composed of 128 point FFTs, giving frequency bins roughly 0.4 Hz wide. The FFTs overlap each other by

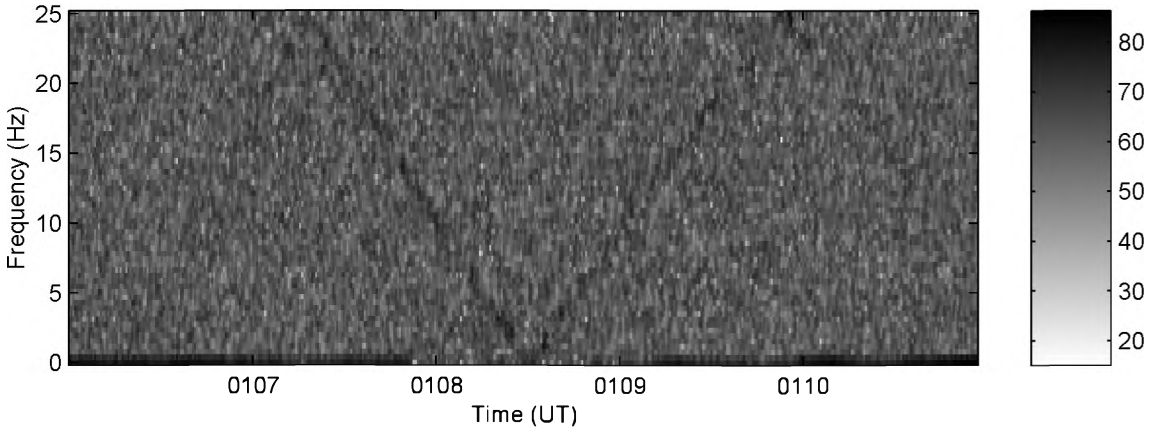

Figure 6.1: "Spectral V" in spectrogram of PRN 29 intensity data on 16 October 1996 from Ancon. The grayscale on the right indicates fluctuation power in dB.

96 samples to increase the time resolution. The V-shaped spectral feature centered on 1:08:30 is faint and broken, but sits 10–15 dB above the background noise level. Also, the variations apparently continue to increase in frequency past 25 Hz on the right hand side of the V, producing an aliased signal around 0110 UT.

As will be shown shortly, the slope of the V is roughly 0.28 Hz/s in magnitude on either side. Thus, the frequency of amplitude fluctuations changes by 0.72 Hz over the period of each FFT making up the spectrogram, almost two bin widths. Note that the "chirp test" of the scintillation monitor with a GPS signal simulator in Chapter 3 demonstrates that the scintillation monitors can track frequency variations all the way up to the Nyquist frequency of 25 Hz. In fact, the chirp test was a frequency sweep of 0.25 Hz/s and the spectrogram plotted in the Chapter 3 discussion of that test used exactly the same FFT length and overlap as the present figure.

At first, we suspected that the V might be an instrumentation anomaly. Yet further examination suggested that its origin was in the propagation of the GPS signals and it was probably an ionospheric effect. After presenting a few more examples

of spectral V observations, this section will outline arguments concerning why Vs likely do not stem from non-ionospheric sources. Critical discussion is vital because many interference phenomena can generate frequency sweeps; for example, interference between two satellite signals was determined to be the source of certain, early quasiperiodic scintillation observations [*Hajkowicz*, 1974; *Hajkowicz*, 1977]. Subsequent sections cover the proposed ionospheric model, diffraction from phase discontinuities on an equivalent phase screen, and its refinements. Finally, we examine *in situ* plasma density data from the Atmospheric Explorer E (AE-E) satellite to ascertain whether steep enough gradients exist in equatorial spread F depletions to account for the observed diffraction patterns.

The following line of evidence suggests that the spectral Vs originate in radio propagation and not in the instrument or interference. First, a few other events of this nature appear in the data records of the October 1996 and April 1997 campaigns. Although we have not examined enough data records to verify conclusively a high correlation between the spectral Vs and scintillations, we observe that such spectral features typically appear prior to or during scintillations. Second, the CDMA (code division multiple access) spread spectrum nature of the GPS signals all but rules out interfering radio transmissions or radio frequency (RF) noise as the source of the Vs. Although it is possible for signals without the GPS PRN code modulation to produce observable correlator output power [*Van Dierendonck*, 1996], the chances of this interference behaving a highly structured fashion for several seconds, on more than one occasion, are slim. Finally, similar spectral Vs appear within seconds of each other on both receivers at Ancon (Figure 6.2), eliminating anomalies associated with a specific receiver as a possible cause.

It would be useful to know whether the Vs were exactly concurrent for later,

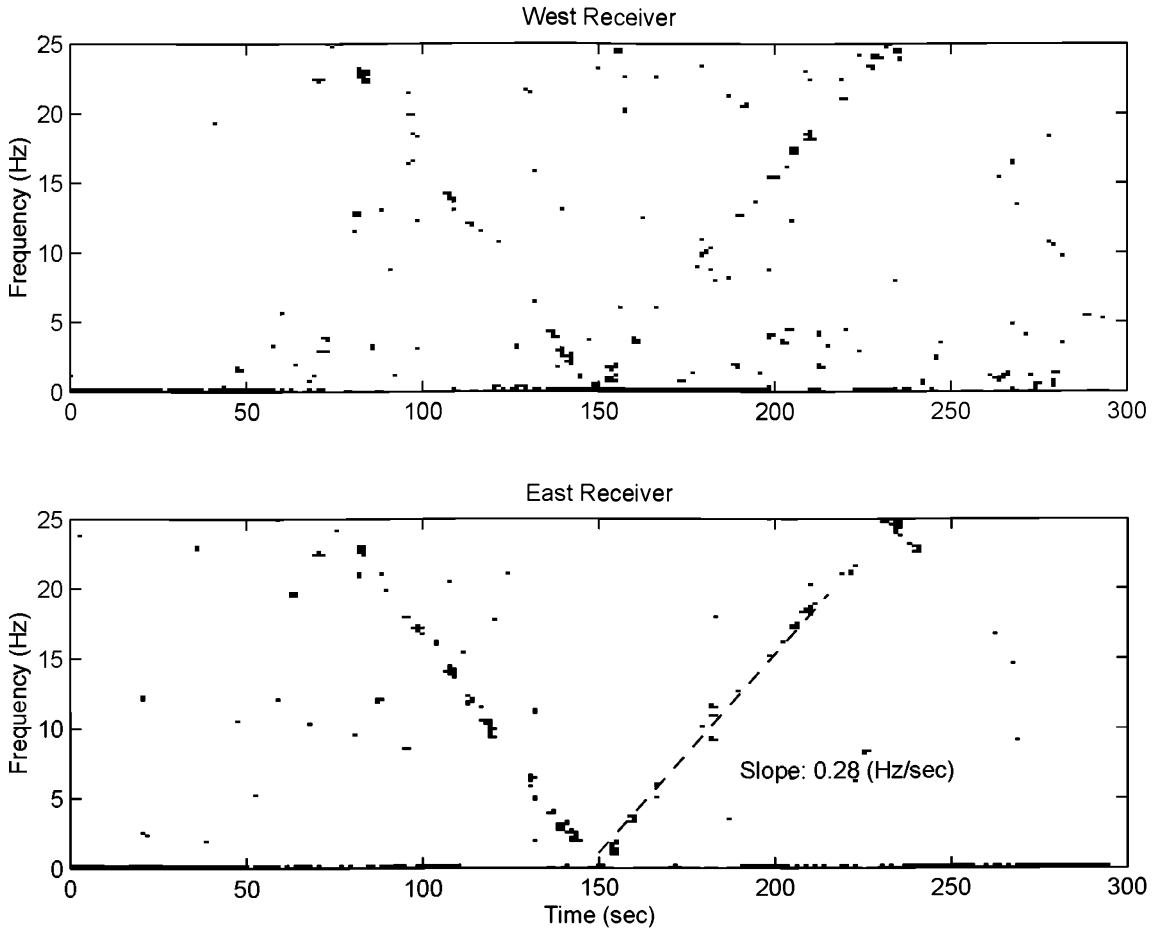

Figure 6.2: Concurrent spectral Vs observed on PRN 29 signal at western and eastern stations (Ancon, Peru on 16 October 1996). Start time is 0106 UT. Here we present "clipped" versions of 256 point FFT spectrograms, based on the mean and standard deviation of fluctuation power. Only points with power greater than the mean background power plus four times its standard deviation are shown. The magnitude of the slope of the fitted line is representative of both halves of the Vs for both receivers.

critical discussion of models leading to their formation. Also, correlation drift measurements between the two, spaced receivers would help to determine what velocity to use for later height estimates. Unfortunately, the intensity fluctuations associated with the Vs in Figure 6.2 are small and do not correlate well. From the spectrograms, all that we can infer, because of constraints imposed by frequency versus time resolution tradeoffs, is that the Vs form within seconds of each other. With 256 point FFTs, each time step covers approximately 5 seconds and adjacent spectra also overlap by about 4 seconds.

Figure 6.3 shows another example, a pair of Vs observed by both stations during the April 1997 campaign. These events occurred during weak scintillations on PRN 26 with a scintillation index of 0.1. For future reference, the relative drift velocity during this period, as measured by cross correlation of the amplitude scintillations between spaced receivers, was 95 m/s. The trajectory of PRN 26 took it from south to north near the Ancon field line during this time, similar to PRN 29's path on 16 October 1996 but in the opposite direction. (In this case, as in the 16 October 1996 example, the Vs on the western receiver are clearly weaker. For both campaigns, however, the western receiver consistently experienced lower signal to noise ratios and, therefore, increased measurement scatter in wide band power WBP_k with respect to its mean.)

Having narrowed the probable source of the spectral Vs to propagation phenomena, we must consider carefully the possibility that multipath could cause the Vs. We may regard multipath as another type of RF interference, only now the interference comes from reflected copies of the GPS signals themselves. Since the reflected signals carry the same PRN code modulation as the direct signal, we cannot immediately conclude that this RF interference does not produce significant correlator outputs for the duration of the spectral V structures. Indeed, as mentioned in Chapter 5, we

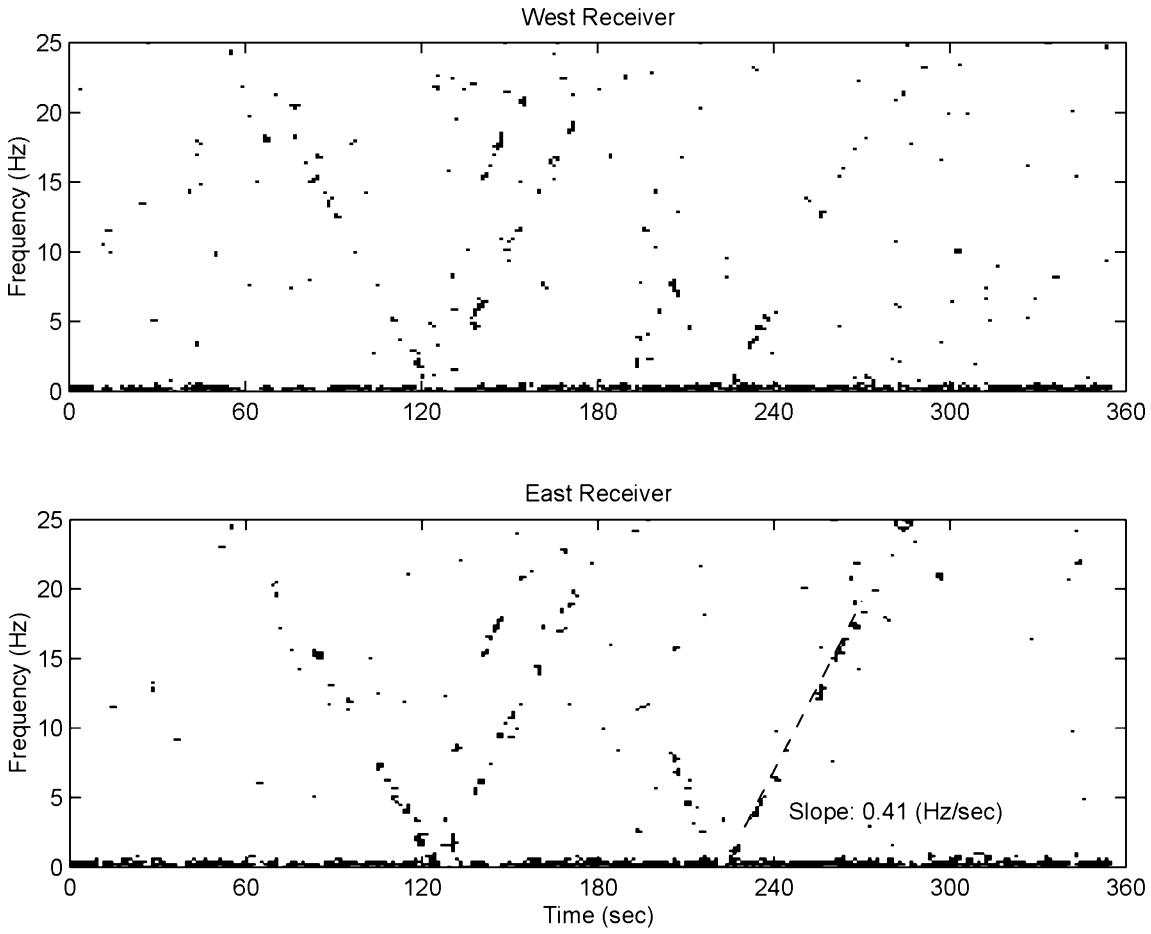

Figure 6.3: Pair of spectral Vs observed on PRN 26 signal at western and eastern stations (Ancon, Peru on 10 April 1997). Start time is 0233 UT. Same "clipped" format as before. The continuous low frequency power in the 0–0.25 Hz range results from scintillations.

have seen isolated incidents of multipath produced amplitude fluctuations with frequencies as high as 10–15 Hz. These fluctuations probably resulted from reflections from nearby metal structures in a rooftop environment and could be identified as multipath by the near repetition of the frequency pattern from day to day for the same satellite (with the appropriate time shift).

Even though the atypical, multipath induced, high frequency amplitude fluctuations behave in a structured fashion, several factors rule out scattered signals from nearby, stationary objects as the source of the Ancon spectral Vs. For one, we have not observed V shapes in the spectrograms of the high frequency multipath observations. Rather, each contains a monochromatic spectral component that meanders in frequency over time in a more complicated fashion. Furthermore, the local multipath environments for the two antennas at Ancon were arguably quite different, yet both receivers saw identical spectral V patterns on more than one occasion. (The western antenna sat nearer to a 9 m dish antenna used for receiving GOES-8 signals, for example.) Finally, and critically, the Ancon spectral Vs do not repeat from night to night; e.g., the Vs appearing on 16 October 1996 do not appear four minutes earlier in UT on the 17th.

Multipath from moving, more distant scattering objects is more difficult to eliminate as the source of the Vs, however, especially since Ancon is near the approach to the airport in Lima. Disregarding the specifics of the scattering process for the moment, consider a scattering body moving perpendicular to the GPS line of sight (Figure 6.4a). For $vt \ll r_1$, the excess path of the scattered signal is

$$r_2 - r_1 \approx \frac{(vt)^2}{2r_1}. \tag{6.1}$$

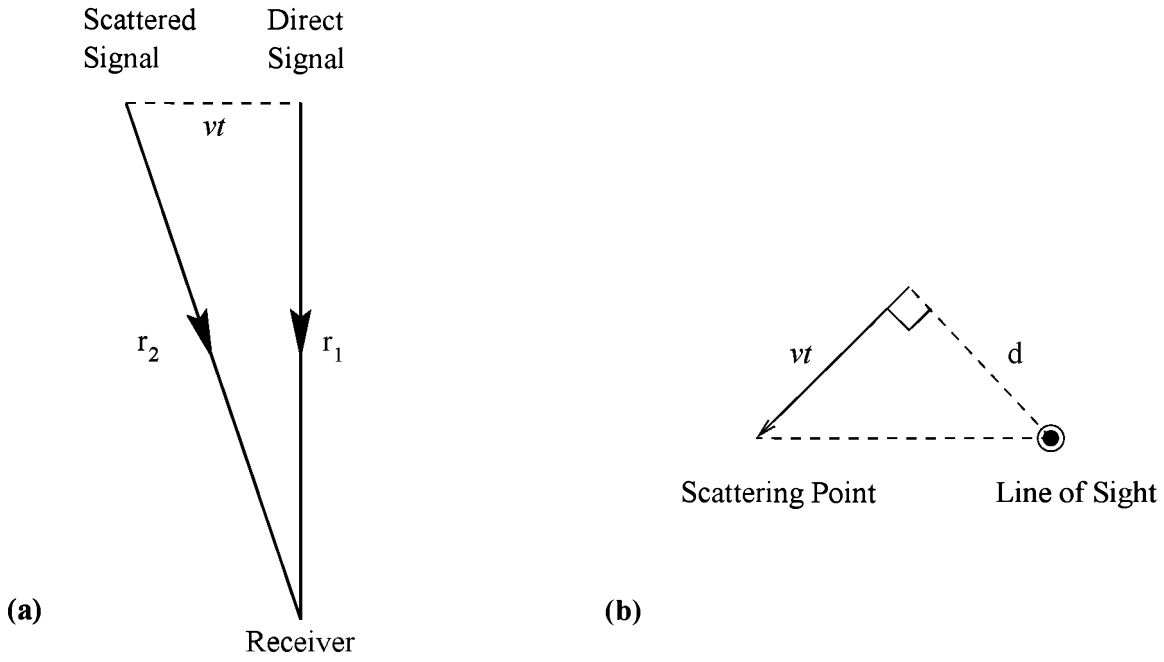

Figure 6.4: Possible multipath models for spectral Vs. (a) An incoming plane wave scatters from a point moving toward the line of sight path with velocity v. The direct and scattered signals interfere at the receiver to produce a time varying intensity. (b) The scatterer now moves in the plane perpendicular to the line of sight with velocity v and distance of closest approach d. The distance from the receiver to the plane containing the scatterer's trajectory is r_1 (not shown in this view).

Translating the excess path into a phase difference ϕ gives

$$\phi = \frac{2\pi}{\lambda}\frac{(vt)^2}{2r_1}, \tag{6.2}$$

which yields a frequency of

$$f = \frac{1}{2\pi}\left|\frac{d\phi}{dt}\right| = \frac{v^2|t|}{\lambda r_1}, \tag{6.3}$$

taking f to be always a positive quantity. This frequency versus time characteristic is exactly a spectral V.

The rate of change of frequency with respect to time is

$$\left|\frac{df}{dt}\right| = \frac{1}{2\pi}\frac{d^2\phi}{dt^2} = \frac{v^2}{\lambda r_1}. \tag{6.4}$$

Using (6.4) we can evaluate the hypothesis that scattering from, say, aircraft is responsible for spectral Vs. We take the altitude range to be 100–10,000 m. The distance to the aircraft should not more than triple in magnitude for elevation angles down to 20°. So the distance r_1 ranges from about 100–30,000 m. For the narrower of the two spectral V examples, $|df/dt| = 0.41$ Hz/s. The corresponding velocity range goes from 2.8–48 m/s or 10–174 km/h (these would be slightly lower for a wider V). The lower speed lies well below stall speed for most planes, a significant practical problem since it corresponds to 100 m altitude. The upper value is very slow for a jet at cruising altitude. These low velocities could, however, apply to other types of aircraft such as helicopters.

Of course, the scatterer need not fly directly through the GPS line of sight to cause a frequency sweep. What matters is the rate of change of distance to the line of sight with respect to time. For example, suppose that an aircraft flies in the plane perpendicular to the line of sight at velocity v with $d \ll r_1$ its distance of closest approach to the line (Figure 6.4b). Then, for times near its closest approach,

$$\phi \approx \frac{2\pi}{\lambda}\frac{d^2 + (vt)^2}{2r_1}. \tag{6.5}$$

The addition of the constant d^2 in the numerator does not change frequency $f(t)$ or the rate of frequency sweep. (Naturally, when $d \sim r_1$, approximation (6.5) is not valid and the rate of sweep decreases for increasing d, as expected.) If we further allow the aircraft to have a velocity component along the line of sight, the aircraft can have a higher overall speed, one more consistent with airplane speeds, for example. Velocities toward or away from the observer do not affect the phase significantly, as long as the airplane's distance from the line of sight is much less than the distance from the aircraft to the receiver.

Nevertheless, other arguments do not favor the aircraft theory of spectral V formation. Primarily, the aircraft theory does not explain how spectral Vs only appear to be seen during times of ionospheric irregularities (although this correlation is not yet solidly confirmed). Also, in order for the Vs to appear within seconds of each other at two stations, the aircraft would have to reach its closest point of approach to both lines of sight at the same time or nearly the same time, which it can only do for limited flight directions (less limited near the high end of aircraft speeds estimated above, though). Although it is not impossible that the required speed and velocity conditions are met, the likelihood of V formation by aircraft on several occasions decreases as the conditions become more stringent. Even more troublesome, the observation of two Vs spaced less than 120 seconds apart (Figure 6.3) requires two aircraft to be uncomfortably close.

Overall, then, we argue that the characteristics of the most likely non-geophysical source of spectral Vs, multipath from aircraft, are not fully consistent with the observations. In place of the non-geophysical models, we propose a simple model based on ionospheric scattering in the next section that appears better to fit the observations. Of course, only further and more systematic observations of spectral Vs, particularly

with multiple receivers, can determine their source with more certainty. One decisive experiment would be to place receivers farther apart, maybe as little as 1 km, along the same field line. If the source were aircraft multipath, the chance of forming Vs at nearly the same time on both receivers would be low. On the other hand, since the ionosphere's irregularity structures are greatly elongated along the field lines, both receivers would see similar ionospheric effects. As a side benefit, spaced receivers in the geomagnetic north-south direction could potentially monitor vertical drifts at the equator if some lines of sight were to pass near the footprints of the equatorial field lines (since vertical motion of field aligned irregularities at the dip equator translates into horizontal motion near the field line footprints).

6.3 Phase Screen Model

Figure 6.5 shows the well known intensity pattern of diffraction seen below the edge of a perfectly conducting half plane. The pattern immediately suggests a spatial frequency sweep. The "ringing" around unit intensity on the illuminated side starts out slowly, then gradually increases in frequency (while decreasing in amplitude) as the distance from the edge increases. If the edge were to move through the line of sight between a satellite and a stationary observer, the observer would first see constant signal strength from the satellite. As the edge approached, the observer would note a rapid variation in signal power whose rate of fluctuation decreased with time. A spectrogram of these intensity measurements would show the rate of frequency decrease to be roughly constant until reaching zero frequency; the scattered wave from the moving knife edge is essentially the problem treated in the preceding section. Of course, as the half plane interposed itself between the satellite and the

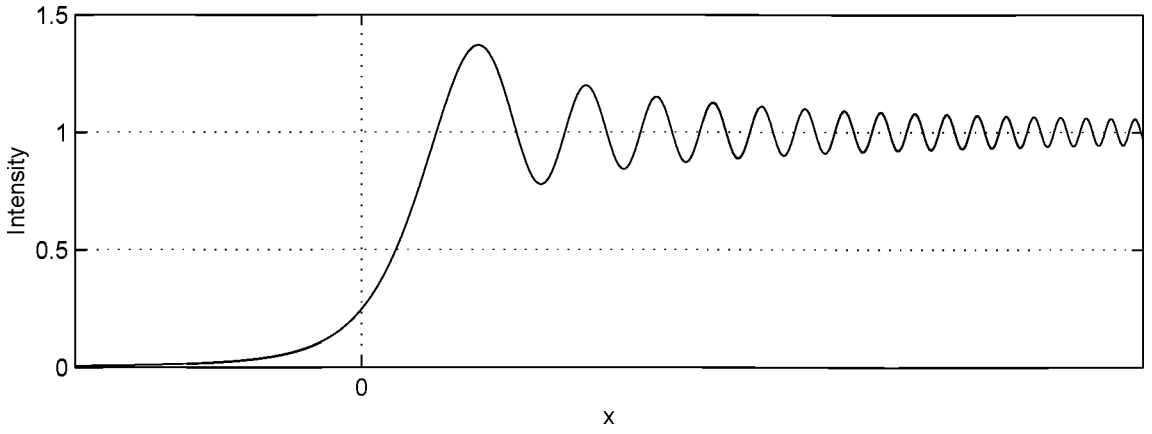

Figure 6.5: Plot of normalized field intensity observed below the boundary at $x = 0$ between a perfectly conducting half plane (on the left) and free space. The illumination source is a plane wave.

observer, the signal intensity would rapidly decrease to zero in the shadow. Thus, diffraction from a moving knife edge would not produce a symmetric V shape.

Creating a V shaped spectrogram requires some sort of "symmetric edge" to scatter from, an edge with transmission on both sides. Since we require transmission on both sides of the discontinuity, the discontinuity must be in phase, not in amplitude. Figure 6.6 shows the intensity pattern generated near a discontinuity in phase in a one dimensional phase screen, as calculated by the Fourier transform method of Chapter 4. Here, the spatial frequency of the amplitude fluctuations increases in either direction away from the phase discontinuity at $x = 0$. Consequently, if such a discontinuity were to drift through the line of sight between a satellite and an observer, the observer would see a V shape in an intensity spectrogram. This simplified model represents what we hypothesize to occur in the equatorial spectral V observations. In the case of the observed spectral Vs, the phase discontinuity could come from the steep edges of equatorial F region depletions or sporadic E.

Fortunately, the intensity pattern below a one dimensional phase screen with a

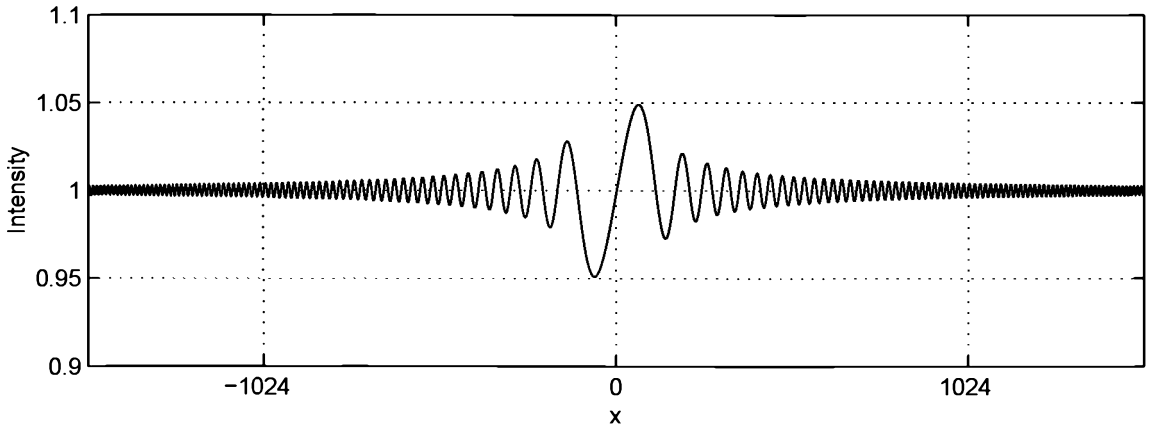

Figure 6.6: The diffraction pattern observed below a phase screen with a discontinuity in phase at $x = 0$ as calculated by the one dimensional phase screen code of Chapter 4. The parameters used to produce the plot include a phase step $\Delta\phi = 0.1$ radians and a Fresnel radius of 128 wavelengths. Horizontal distance is also expressed in terms of wavelengths of the incident plane wave.

step in phase at $x = 0$ may be readily derived from the standard half plane diffraction formula. We assume a one dimensional phase screen model since the ionospheric structures are greatly elongated along the magnetic field lines. Rigorous Huygens-Fresnel diffraction theory, as justified by Kirchhoff's integral theorem, gives the scattering integral of Chapter 4,

$$\mathcal{A}(x) = \frac{1}{r_F} \int_{-\infty}^{\infty} dx' \; \mathcal{A}^+(x') \; \exp\left[i\pi \left(\frac{x - x'}{r_F} \right)^2 \right], \tag{6.6}$$

where x is the horizontal distance along the screen, $r_F = \sqrt{\lambda z}$ is the Fresnel radius (λ is the free space wavelength of the incident plane wave and z is the height of the phase screen), $\mathcal{A}^+(x)$ is the wave amplitude immediately after the wave emerges from the screen and $\mathcal{A}(x)$ is the wave amplitude in the observation plane. Note that the amplitudes $\mathcal{A}^+(x)$ and $\mathcal{A}(x)$ are complex, including both magnitude and phase information, and $\exp(-i\omega t)$ time dependence is implied. Also, the incoming wave is plane with a propagation vector perpendicular to the screen. We defer the discussion

of zenith angle effects.

Since the scattering integral is a linear operator on $\mathcal{A}^+(x)$, superposition holds. Specifically, for a step in phase at $x = 0$, $\mathcal{A}^+(x)$ can be decomposed into two parts (normalizing the magnitude of the wave incident upon the screen to unity),

$$\mathcal{A}^+(x) = e^{i\phi_1}U(-x) + e^{i\phi_2}U(x), \tag{6.7}$$

where ϕ_1 is the phase screen's phase when $x < 0$, ϕ_2 is the phase screen's phase for $x > 0$ and $U(x)$ is the unit step or Heaviside function,

$$U(x) = \begin{cases} 0, & x < 0, \\ 1, & x > 0. \end{cases} \tag{6.8}$$

Each of the terms in (6.7) produces a classical edge diffraction pattern in amplitude at the observation plane [*Born and Wolf*, 1975]. The two patterns may be superimposed to yield a back to back diffraction pattern centered on $x = 0$.

Of course intensity, $\mathcal{I}(x) = |\mathcal{A}(x)|^2 = \mathcal{A}(x)\mathcal{A}^*(x)$ (where the asterisk denotes complex conjugation), is a nonlinear function of amplitude, so intensity patterns cannot be superimposed. Nevertheless, the intensity calculation is relatively simple for a discontinuity in phase. Denoting the amplitude at the observation plane due to the first term in (6.7) by $\mathcal{A}_1(x)$ and the amplitude due to the second by $\mathcal{A}_2(x)$,

$$\mathcal{A}_1(x) = \frac{e^{i\phi_1}}{\sqrt{2}}\left[\left(\frac{1}{2} - C\left(\frac{\sqrt{2}}{r_F}x\right)\right) + i\left(\frac{1}{2} - S\left(\frac{\sqrt{2}}{r_F}x\right)\right)\right], \tag{6.9}$$

$$\mathcal{A}_2(x) = \frac{e^{i\phi_2}}{\sqrt{2}}\left[\left(\frac{1}{2} + C\left(\frac{\sqrt{2}}{r_F}x\right)\right) + i\left(\frac{1}{2} + S\left(\frac{\sqrt{2}}{r_F}x\right)\right)\right], \tag{6.10}$$

where $C(w) = \int_0^w du\ \cos(\pi u^2/2)$ and $S(w) = \int_0^w du\ \sin(\pi u^2/2)$ are the Fresnel functions. After some mathematical manipulations,

$$\mathcal{I}(x) = |\mathcal{A}_1(x)|^2 + |\mathcal{A}_2(x)|^2 + 2\mathrm{Re}[\mathcal{A}_1(x)\mathcal{A}_2^*(x)]$$

$$= \cos^2\left(\frac{\Delta\phi}{2}\right) + 2\sin^2\left(\frac{\Delta\phi}{2}\right)\left[(C(w))^2 + (S(w))^2\right] + \sin(\Delta\phi)\left[C(w) - S(w)\right], \quad (6.11)$$

letting $\Delta\phi = \phi_2 - \phi_1$ and $w = \sqrt{2}\,x/r_F$ for notational convenience. Clearly, intensity becomes uniform (and unity) when $\Delta\phi = 0$, as expected.

Equation (6.11) points out some of the difficulties in trying to determine $\Delta\phi$ from the amplitude pattern. First, if $\Delta\phi$ is small, the fluctuations are very small. As $\Delta\phi$ increases to π, the maximum intensity fluctuation rises to the vicinity of 80% (Figure 6.7), but such large fluctuations quickly decay away as the horizontal distance from $x = 0$ increases (see, e.g., Figure 6.6). Also, equation (6.11) explicitly exhibits the ambiguity that would be expected in terms of adding an integer number of cycles of phase advance to ϕ_1 or ϕ_2. (One cycle of L1 phase corresponds to 1.173 TECU, where 1 TECU = 10^{16} electrons per m^2, of total electron content, giving a ΔN_e of 1.173×10^{11} m^{-3} throughout a 100 km thick ionosphere.) Finally, ambiguity due to the reflection symmetry about $\Delta\phi = \pi$ also exists.

That the Fresnel functions in (6.11) generate frequency sweeps may be crudely demonstrated by considering the Cornu spiral in Figure 6.8. The spiral represents $C(w)$ and $S(w)$ as, respectively, the horizontal and vertical coordinate values at a distance w traveled along the curve from the origin [*Born and Wolf*, 1975]. (Physically, $w = \sqrt{2}\,x/r_F$ represents the normalized horizontal distance.) First, the $(C(w))^2 + (S(w))^2$ term is the square of the distance from the origin to the spiral, which clearly oscillates with decreasing amplitude as the spiral becomes tighter and tighter, reaching an asymptotic value of 1/2. Moreover, the rate of oscillation of $(C(w))^2 + (S(w))^2$ increases with arc length $w > 0$ traveled along the spiral because the diameter of the spiral, hence the distance required to complete an approximate circuit, becomes

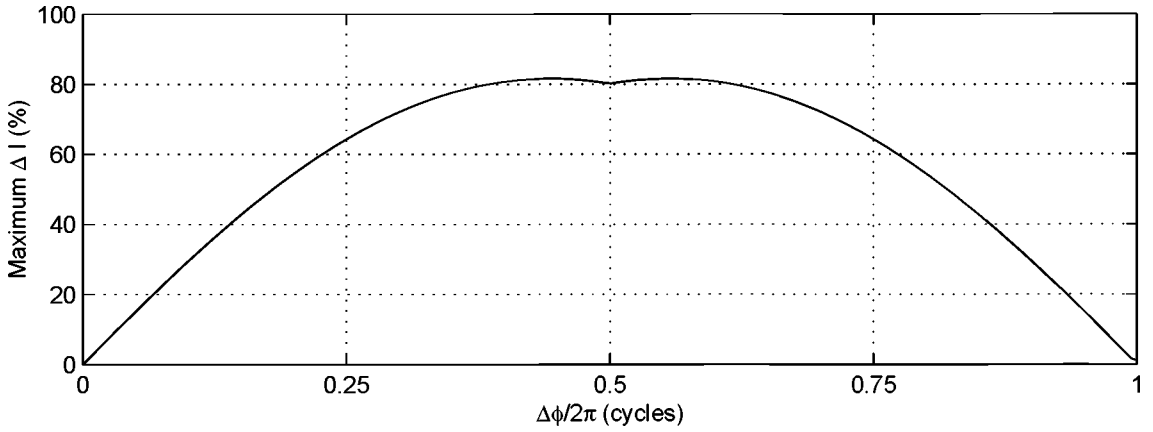

Figure 6.7: Maximum percentage fluctuation in intensity for a step phase screen as a function of $\Delta\phi$. The plotted values come from the first maximum in intensity as computed numerically by the Fourier transform method. This maximum intensity fluctuation is not representative, however, since the intensity fluctuations decrease rapidly in magnitude away from the edge (see Figure 6.6).

progressively smaller. Also, for the $C(w)$ and $S(w)$ functions individually, we can find the distance between successive maxima and minima and estimate the rate of change of frequency.

The angle θ of the tangent to the Cornu spiral is simply $\theta = \pi w^2/2$ [*Born and Wolf*, 1975]. The maxima and minima of $C(w)$, for $w > 0$, occur for $\theta = (4n+1)\pi/2$ and $\theta = (4n+3)\pi/2$, respectively (where $n = 0, 1, 2, \ldots$). Similarly, the maxima and minima of $S(w)$, for $w > 0$, occur for $\theta = (2n+1)\pi$ and $\theta = 2n\pi$, respectively (where $n = 0, 1, 2, \ldots$). So the difference $w_{\text{max}}^2 - w_{\text{min}}^2$, where w_{min} is the location of a minimum for $C(w)$ and w_{max} is the very next maximum, varies as

$$\frac{\pi}{2}\left(w_{\text{max}}^2 - w_{\text{min}}^2\right) = \pi, \tag{6.12}$$

with the same result holding for $S(w)$.

Now the main item of interest is the average rate of change of "phase" θ with w

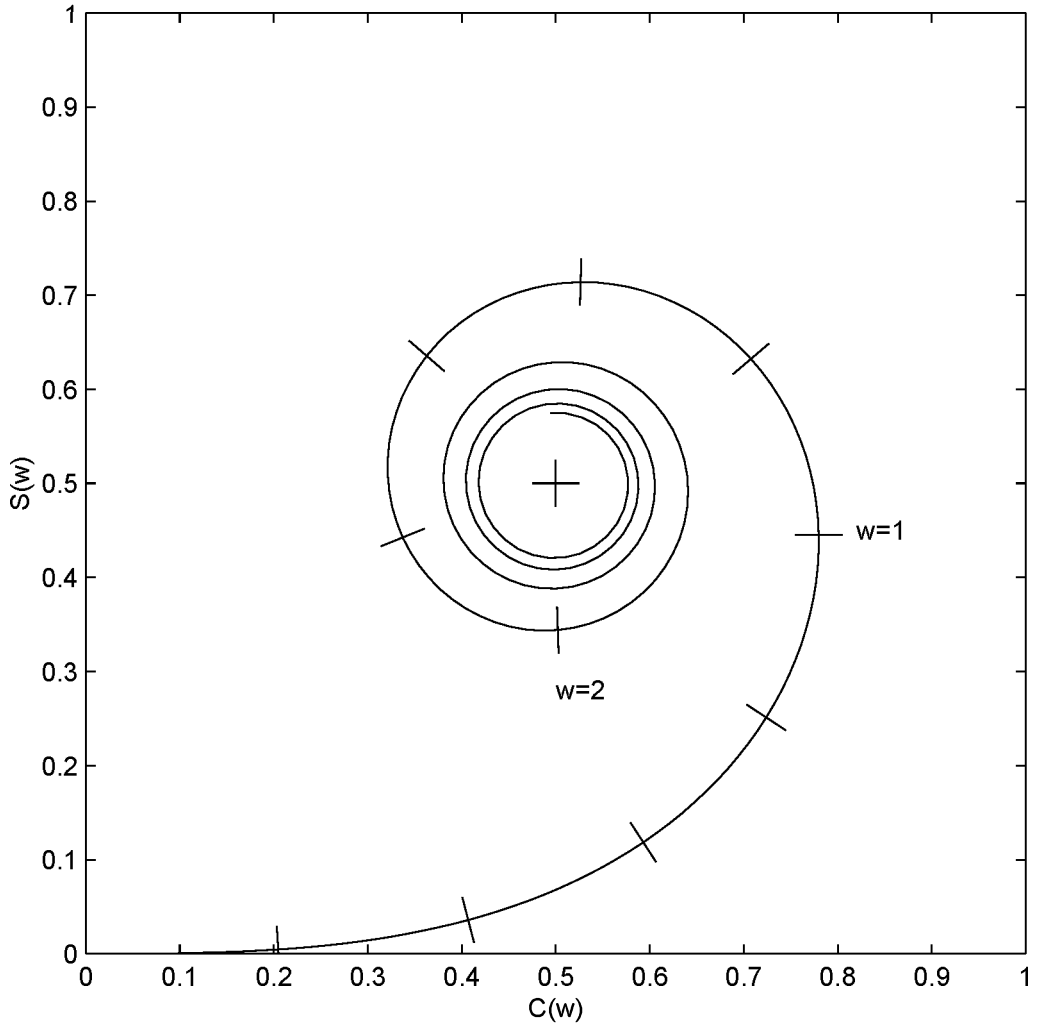

Figure 6.8: Cornu spiral used to characterize the behavior of the Fresnel functions. The arc length along the spiral, as measured from the origin is w, where the tics indicate steps in w of 0.2. The abscissa of the curve at a given w is $C(w)$; the ordinate is $S(w)$. Both $C(w)$ and $S(w)$ reach asymptotic values of $1/2$ as w becomes unbounded. (For the definitions of $C(w)$ and $S(w)$, see text.)

over this "half cycle" of variation. The average $d\theta/dw$ is

$$\Omega = \frac{\pi}{\Delta w} = \pi \overline{w}, \tag{6.13}$$

where $\Delta w = w_{\max} - w_{\min}$ and $\overline{w} = (w_{\max} + w_{\min})/2$. Specifically, the "angular frequency" Ω varies linearly with $\overline{w}$, increasing for $w > 0$, which is exactly the $x > 0$ side of a spectral V (in terms of spatial, not temporal, frequency). Similar results hold for the $w < 0$ branch of the Cornu spiral (not shown).

Slightly more rigorously, one functional representation of the Fresnel functions has both $C(w)$ and $S(w)$ made up of $\cos(\pi w^2/2)$ and $\sin(\pi w^2/2)$ terms, each multiplied by certain "envelope functions" [*Abramowitz and Stegun*, 1972, 7.3.12 and 7.3.14, p. 301]. This functional form immediately suggests that $C(w)$ and $S(w)$ contain harmonic components that linearly increase in frequency with increasing w (for $w > 0$). Nevertheless, the properties of the envelope functions are not as transparent as the properties of the Cornu spiral.

Taking the Fresnel functions to be composed of $\cos(\pi w^2/2)$ and $\sin(\pi w^2/2)$ terms with relatively slowly varying envelopes, we may determine the rate of change of spatial frequency with respect to distance on a somewhat more rigorous basis. Differentiating the arguments of these sinusoidal "chirps" with respect to x, recalling that $w = \sqrt{2}x/r_F$, one finds that the horizontal wavenumber $q(x) = 2\pi x/{r_F}^2$. More importantly, the angular frequency of intensity fluctuations seen by a stationary observer, as the phase discontinuity drifts overhead at velocity v, is $\omega(t) = 2\pi v^2 t/{r_F}^2$. In Hertz per second, the slope of frequency versus time is then

$$\left|\frac{df}{dt}\right| = \frac{v^2}{{r_F}^2} = \frac{v^2}{\lambda z}, \tag{6.14}$$

exactly the same result as the problem treated earlier of the generic scatterer moving with speed v toward the line of sight. This correspondence is to be expected since

the phase discontinuity constitutes a scattering object with a fairly broad scattering "beam width."

To determine how well these rough theoretical considerations fit the numerical model, we take the previously calculated intensity pattern, of which Figure 6.6 shows an enlargement, and assume that it drifts to the right past a receiver located at $x = 0$ at a constant rate of $v = 50$ radio wavelengths per second. In this example, the screen is at $z = 2^{14}$ wavelengths away, so the predicted $|df/dt| = 50^2/2^{14} = 0.15$ Hz/s. Figure 6.9 gives the spectrogram of intensity for the previous numerical example (after the mean intensity of 1 is subtracted). The slope through the middle of the frequency structure in the V shape on either side is 0.15 in magnitude, as predicted.

Figure 6.9 does illustrate one drawback to the phase step model, though: namely, that the intensity fluctuations quickly become reduced in amplitude away from the scattering edge. Only when the line of sight is nearest the discontinuity in phase are the fluctuations relatively strong. If we judge by the shaded portion of the spectrogram, for example, the region of strong fluctuations extends about 250 wavelengths on either side of the discontinuity (50 s times the 50 wavelengths per second drift). Since $r_F = 128$ wavelengths in this example, we estimate that the strongest fluctuations in intensity occur within $\pm 2\, r_F$ of the step in phase screen phase. Given an ionospheric Fresnel radius $r_F = 300$ m and a 100 m/s drift, for example, this estimate suggests that the Vs should endure for no more than 12 seconds, a value which is an order of magnitude less than the duration of the observed Vs.

The exact sensitivity of the scintillation monitor is unknown, though. We have seen examples where the scintillation spectrum covered at least four orders of magnitude in power spectral density before reaching the noise floor. If the power threshold for detection were lowered by 10 dB, for example, the V would persist approximately

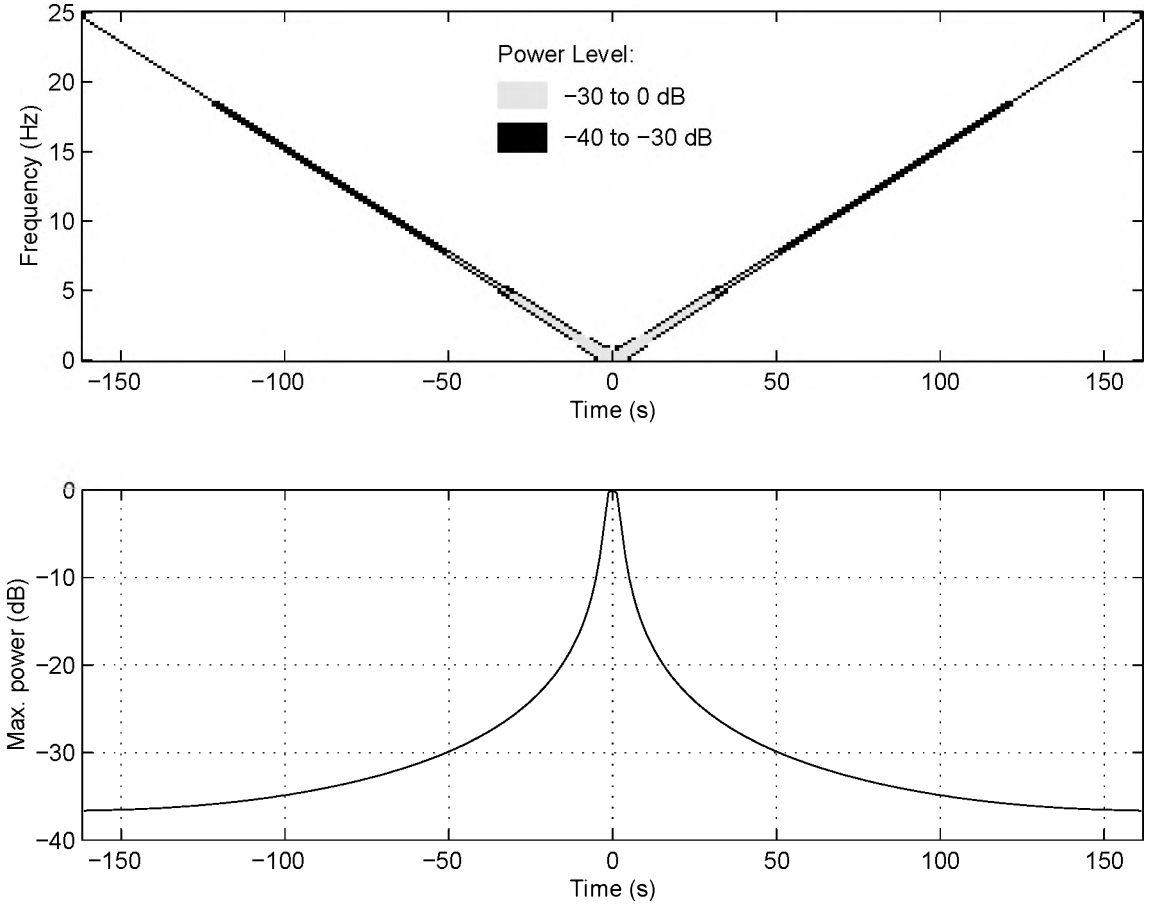

Figure 6.9: Spectrogram of intensity for numerical example of a phase screen with a $\Delta\phi = 0.1$ rad step in the middle (otherwise uniform). The phase screen drifts from left to right at a constant speed of $v = 50$ wavelengths of the incident radio wave per second and the middle of the screen is directly overhead at $t = 0$. The bottom plot shows the maximum power level in the spectrum at each time. Note that most of the fluctuations for $|t| > 50$ s are 30–40 dB in power below the largest fluctuations in the diffraction pattern. Also, -40 dB refers to the relative power level of the intensity *fluctuations*; i.e., -40 dB corresponds to 0.01 times the maximum intensity deviation level.

three times longer than the above estimate (Cf. Figure 6.9), not a full order of magnitude, but certainly helpful. So, it is plausible that Vs resulting from diffraction by a phase discontinuity could persist long enough to account for the observations. In any case, the qualitative features of this numerical experiment definitely correspond to the spectral V observations.

A quantitative plausibility check involves the verification that the expected relative drift velocities and phase screen distances conform to the observed slopes of Vs according to relation (6.14). Since the governing relationship is the same, this check is essentially that performed in the preceding section to evaluate the aircraft multipath hypothesis, except with different altitude and velocity ranges. At that point, we did not have a diffractive scattering model for the ionosphere in mind and so we did not explore higher altitude ranges.

Recall that the GPS L1 wavelength $\lambda = 0.19$ m. For the V observed on PRN 29's signal on 16 October 1996 with slopes of 0.28 Hz/s in magnitude, we initially assume a phase screen distance of 300 km (the average hmF2 at nearby Jicamarca from the Chapter 5 discussion). This assumption implies a drift velocity of 126 m/s, a reasonable value of F region ionospheric drift. Actually, PRN 29 is not at zenith during the time of the V observation; the slant distance to the F peak at this time is 576 km. Using the slant distance instead of the F peak altitude yields a 175 m/s drift, high but not out of the question. From the opposite tack, during the initial period of scintillations on PRN 29, about 15 minutes after the spectral V observation, the net eastward drifts were typically 100–130 m/s, as measured by spaced receivers. These velocities would give 190–320 km slant ranges, or 95–160 km altitudes at the time of the V. In either case, the drifts and altitudes are compatible with ionospheric generation of the Vs, although the latter figures suggest E region generation of the

Vs (perhaps by diffraction from the edge of sporadic E layers).

The Vs observed on PRN 26's signal on 10 April 1997 occurred during regular scintillations, permitting an estimate of the ionospheric drift from spaced scintillation monitors. As quoted in the preceding section, the estimated relative ionospheric drift during the time that the Vs occurred (0234–0238 UT) was 95 m/s. That drift speed, coupled with slopes of the Vs of 0.41 Hz/s, gives a slant distance of 116 km. At 0235 UT on 10 April, 116 km slant range corresponds to 98 km altitude for PRN 26. If, however, the observed diffraction were actually to come from E region altitudes, the drift velocity of the postulated electron density gradient would not necessarily match that derived from scintillation drift measurements, since the latter velocity undoubtedly derives from the drift of F region irregularities.

Overall, ionospheric drift velocities and heights are consistent with the slopes of the observed Vs for the two cases presented earlier. If the lower drift velocities are to be believed, the altitudes may correspond to the E region rather than the F region, as we had initially supposed. Nevertheless, they still lie in the ionosphere. Altitudes lower than the F peak are not inconsistent with some previous observations of VHF quasiperiodic scintillations near the dip equator and in the northern and southern equatorial anomaly regions [*Kelleher and Martin*, 1975]. Other VHF observations of quasiperiodic scintillations, matched with AE-E satellite *in situ* plasma density data from 370 km altitude, have implicated F peak structure as their source [*Franke et al.*, 1984]. At any rate, the slopes of the spectral Vs are are more sensitive to drift velocity estimates than to equivalent phase screen distance. To maintain a given slope, for example, a 41% increase in velocity requires that the distance doubles.

6.4 Model Refinements

Up to now, the model has centered on a very abrupt transition in phase in the equivalent phase screen, a step with a width of one radio wavelength or less. Forming a diffraction pattern with 20% or more variation in intensity in the first extremum past the phase step requires a phase difference $\Delta\phi$ of at least $\pi/6$ radians across the discontinuity (Figure 6.7). This $\Delta\phi$ at the GPS L1 frequency implies a change in electron density ΔN_e of 9.8×10^9 m^{-3} within a horizontal scale length of 0.19 m or less, assuming a 100 km thick slab ionosphere. One may legitimately question whether such steep gradients can persist for the time period of several minutes required to account for the GPS spectral V observations. In reality, the transition is probably more gradual.

Viewing geometry is another factor that can make the transition in phase in the equivalent phase screen less sharp, even if the depletion boundary itself is sharp. Figure 6.10 illustrates one simple case in schematic form, where the line of sight to a slowly moving or stationary satellite slants to the geomagnetic west of zenith. Probably the simplest viewpoint is to consider the total electron content. Before the depletion passes through the line of sight, TEC derives from the normal ionospheric plasma density and is relatively high. As the depletion boundary crosses the line of sight, TEC decreases until it reaches a minimum when the line of sight lies wholly within the electron density depletion. In terms of the ionospheric phase advance throughout the entire process described above, the phase starts out at a relatively high value, decreases as more and more of the line of sight passes through the depletion boundary and reaches a minimum inside the depletion.

This time sequence of phase values essentially mirrors the spatial distribution of

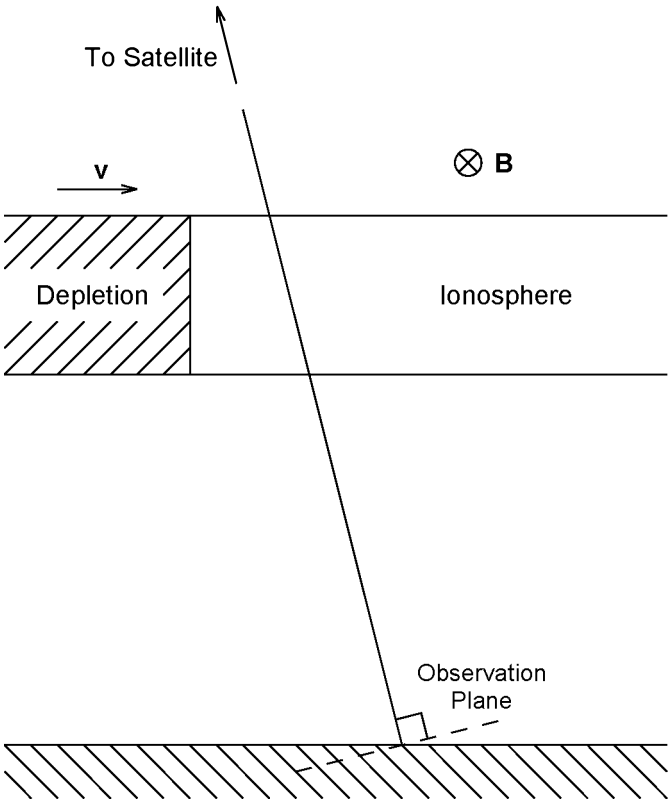

Figure 6.10: Slab model to illustrate how slanted ray paths through a depletion can generate a graded transition in phase.

phase for parallel ray paths across the observation plane. That is to say, at a given instant, the paths on the western side of the depletion boundary have a low value of phase advance while those on the eastern side have a high value of phase advance. In between lies a transition region. Thus, the equivalent phase screen contains a graded transition in phase. Note that the phase screen is still effectively one dimensional in this geometry because the depletion extends north and south along the field line for a large number of Fresnel radii.

A simple one dimensional phase screen model of a graded transition incorporates a linear transition between ϕ_1 and ϕ_2 so that now

$$\begin{aligned} \mathcal{A}^+(x) &= e^{i\phi_1}U(-x-\delta/2) + e^{i\phi_2}U(x-\delta/2) \\ &+ \exp\left\{i\left[\phi_1 + \Delta\phi\left(\frac{x+\delta/2}{\delta}\right)\right]\right\} P_\delta(x), \end{aligned} \tag{6.15}$$

where $P_\delta(x)$ is a unit amplitude pulse of width δ centered about $x = 0$ and $\Delta\phi = \phi_2 - \phi_1$ as before. The resulting amplitude pattern at the ground may be calculated and gives

$$\mathcal{A}(x) = \mathcal{A}_1(x+\delta/2) + \mathcal{A}_2(x-\delta/2) + \mathcal{A}_3(x), \tag{6.16}$$

where $\mathcal{A}_1(x)$ and $\mathcal{A}_2(x)$ are given by (6.9) and (6.10), respectively, and

$$\mathcal{A}_3(x) = \frac{e^{i[(\Delta\phi/\delta)x + \overline{\phi} - \xi^2]}}{\sqrt{2}}\left[(C(w_2) - C(w_1)) + i(S(w_2) - S(w_1))\right], \tag{6.17}$$

letting $\overline{\phi} = (\phi_1 + \phi_2)/2$, $\xi = \Delta\phi\, r_F/(2\delta\sqrt{\pi})$ and

$$w_{1,2} = \sqrt{2}\left(\frac{x}{r_F} \mp \frac{\delta}{2r_F} - \frac{\Delta\phi}{2\pi}\frac{r_F}{\delta}\right), \tag{6.18}$$

where the notation indicates that w_1 goes with the upper $(-)$ sign and w_2 goes with the lower $(+)$ sign.

Now from the amplitude $\mathcal{A}(x)$, we could calculate the intensity pattern across the observation plane,

$$\mathcal{I}(x) = |\mathcal{A}_1|^2 + |\mathcal{A}_2|^2 + |\mathcal{A}_3|^2 + 2\mathrm{Re}(\mathcal{A}_1\mathcal{A}_2^*) + 2\mathrm{Re}(\mathcal{A}_1\mathcal{A}_3^*) + 2\mathrm{Re}(\mathcal{A}_2\mathcal{A}_3^*). \quad (6.19)$$

Rather than immediately tackle the computation of $\mathcal{I}(x)$ by such a "brute force" approach, let us first consider what information we would like to obtain from the graded step phase screen model. Two important questions are: (1) does the more gradual transition still produce spectral V features? and (2) what is the minimum rate of change of phase required to produce a noticeable diffraction pattern? Existence questions are easy to approach by setting up a numerical experiment. Numerical experiments may also provide guidance concerning ranges of parameter values required to generate an observable frequency sweep.

Figure 6.11 shows some sample intensity plots as would be observed below a phase screen with the linear transition modeled above. We observe that some intensity modulation is present for transition widths $\delta \geq r_F$, but that the strength of the fluctuations diminishes rapidly for wide transitions. Within the visible patterns of fluctuations, the frequency of the fluctuations increases with increasing distance from the screen's center, as before. Thus, we expect to observe V shapes in the spectrograms of signal power with the graded phase transition also.

That the strength of the intensity fluctuations dies off with increasing width of the transition region is to be expected. If the transition becomes much wider than a few Fresnel zones, it looks like an infinitely wide screen of the form $\mathcal{A}^+(x) = \exp(i\alpha x)$, a screen whose phase increases linearly with distance at the constant rate α. In that case, the field amplitude at the observation plane becomes

$$\mathcal{A}(x) = \exp\left[i\left(\alpha x - \frac{\alpha^2 {r_F}^2}{4\pi} + \frac{\pi}{4}\right)\right], \quad (6.20)$$

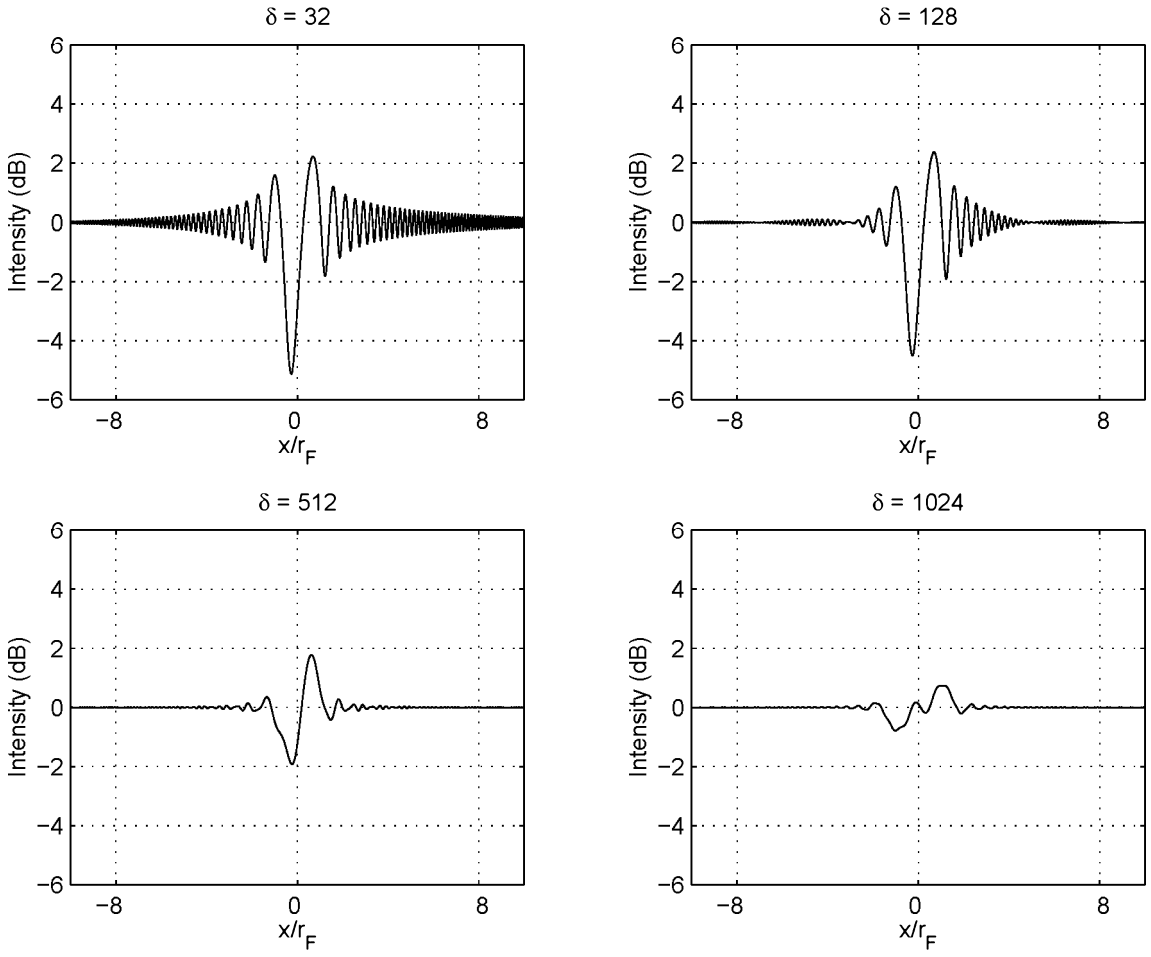

Figure 6.11: Intensity patterns observed below a phase screen with a linear transition in phase at $x = 0$ of width δ, for various values of δ (expressed in grid spacings) with $\Delta\phi = \pi/2$. For this example, $r_F = 512$ (grid spacings, also wavelengths of the incident plane wave). All calculations come from the numerical phase screen code of Chapter 4.

a result that may be readily derived from the general formula listed earlier for the linear transition region of phase by replacing $\Delta\phi/\delta$ with α, letting $\overline{\phi} = 0$ and taking the limit as $\delta \rightarrow \infty$. Thus, for an infinite screen with a linearly increasing phase, the intensity $\mathcal{I}(x) = |\mathcal{A}(x)|^2$ becomes uniform and unity. Consequently, as the transition grows wider in the graded transition model, the intensity should become more and more uniform (except near the discontinuity in slope on either side of the transition region).

The effect of the parameter $\Delta\phi$, the total phase change across the transition region, is more difficult to constrain theoretically. Clearly, with the graded transition, the effects of $\Delta\phi = \pi$ become distinct from $\Delta\phi = 3\pi$, for example, because the slope of the transition region triples in magnitude. (In the phase step model, values of $\Delta\phi$ separated by integer multiples of 2π produce identical results.) As $\Delta\phi$ grows indefinitely, a situation which is physically unlikely in the ionosphere, one of two scenarios occurs. If $\delta \ll r_F$ (i.e., the transition region is narrow), the graded transition begins to appear like a step in phase in its effects. On the other hand, if $\delta \gg r_F$, the diffraction effects only become profound near the edges of the transition region, where the rate of change of phase screen phase is discontinuous.

The intermediate case, with $\delta \sim r_F$, is more complex. Figure 6.12 illustrates some of the intensity patterns observed below a screen with a graded transition of width $\delta = r_F/4$ as $\Delta\phi$ increases. The peak intensity fluctuations move out away from the center of the screen to one side at large $\Delta\phi$ values. Also, for particular combinations of δ and $\Delta\phi$, the intensity pattern becomes quite "bursty." For example, the cases in Figure 6.12, particularly where $\Delta\phi = 2\pi$ and $\Delta\phi = 5\pi/2$, illustrate some of the intermittent fluctuation patterns that can be observed. "Bursty" and "asymmetric" more accurately characterize real spectral V observations as well, lending credence to

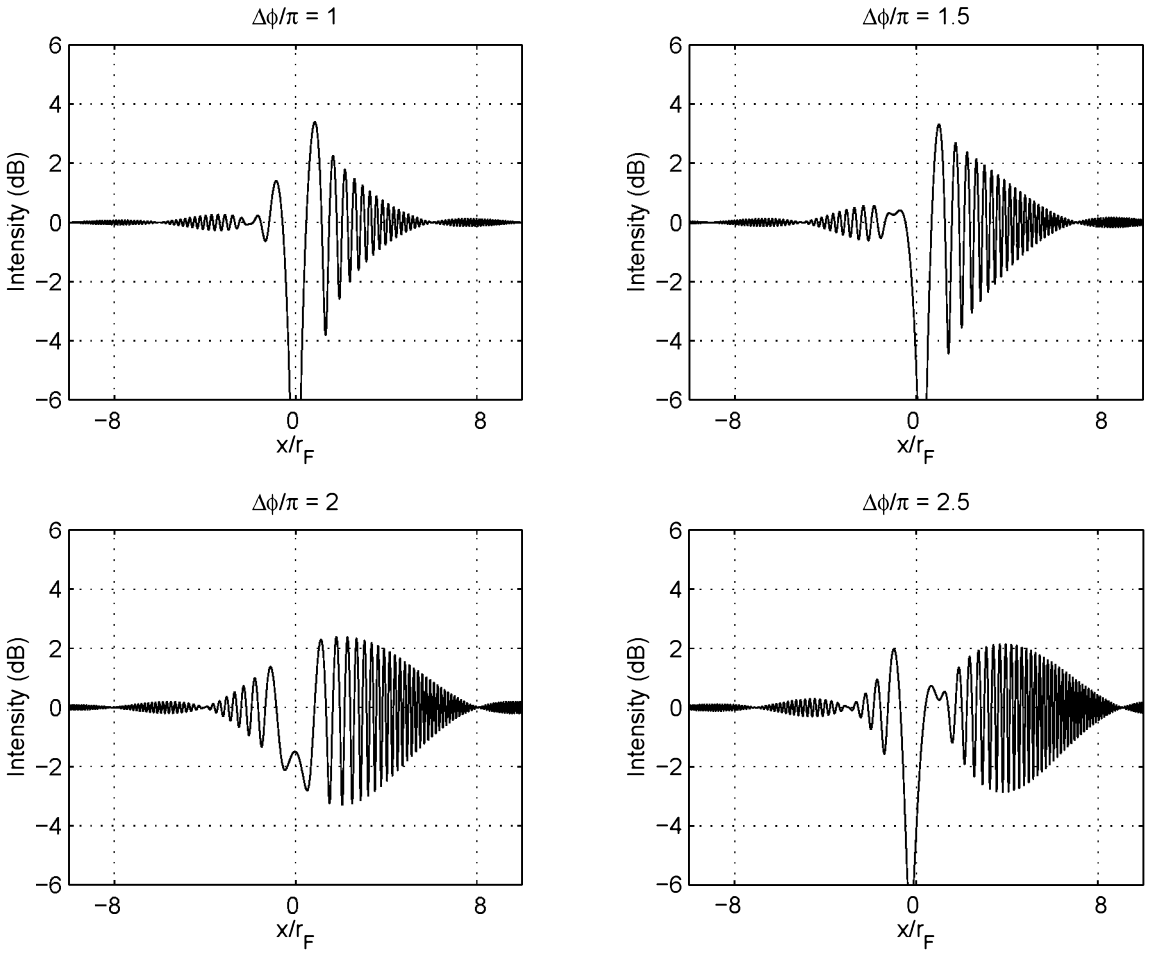

Figure 6.12: Intensity patterns observed below a graded phase screen with a transition of width $\delta = r_F/4$ for increasing $\Delta\phi$. Again, these results come from the numerical phase screen code of Chapter 4 with $r_F = 512$ (grid spacings and wavelengths of the incident plane wave).

the graded transition phase screen model.

Exploring the δ versus $\Delta\phi$ parameter space in more detail, Figure 6.13 illustrates how the maximum modulation index $m_{\max}$ behaves over a small portion of that space for simulations with $r_F = 512$ radio wavelengths. When $\delta \to 0$, $m_{\max}$ becomes periodic in $\Delta\phi$ with period 2π, as expected from the phase step model. As δ increases, however, $m_{\max}$ becomes a much more complicated function of $\Delta\phi$. Finally, at very large values of δ, $m_{\max}$ decreases in accordance with the argument outlined above.

Of even greater interest is the width of the portion of the intensity pattern with significant fluctuations in intensity. Figure 6.14 displays the results for the same portion of parameter space previously used to graph $m_{\max}$. Now the quantity of interest is W, the total width of significant fluctuations in intensity, defined as the distance between the farthest separated points where $m = 0.1\, m_{\max}$. The dominant areas of significant intensity pattern width occur for small values of δ ($\approx r_F/16$) and near $\Delta\phi = 2n\pi$ ($n = 1, 2, 3, \ldots$). Notably, these values of $\Delta\phi$ would give no intensity fluctuations below a screen with a phase step (a transition region of zero width).

Figure 6.15 compares the widths of two intensity patterns having $\Delta\phi = 2.2\pi$. The pattern with $\delta = 0$ is much more narrow than the pattern with $\delta = r_F/16$. Vertical lines in the figure indicate the width between the farthest points with $m = 0.1\, m_{\max}$, where modulation index m is computed over segments of width $r_F/4$ as before. In fact, observable fluctuations exist out to about $45\, r_F$ in the positive x direction and $-25\, r_F$ in the opposite direction for the transition of finite width. In contrast, visible fluctuations die out after approximately $20\, r_F$ in either direction for $\delta = 0$. So, this example illustrates how a finite but narrow transition in phase can broaden the pattern of intensity fluctuations for a given phase change $\Delta\phi$.

Before discussing the implications for possible observations of edge diffraction in

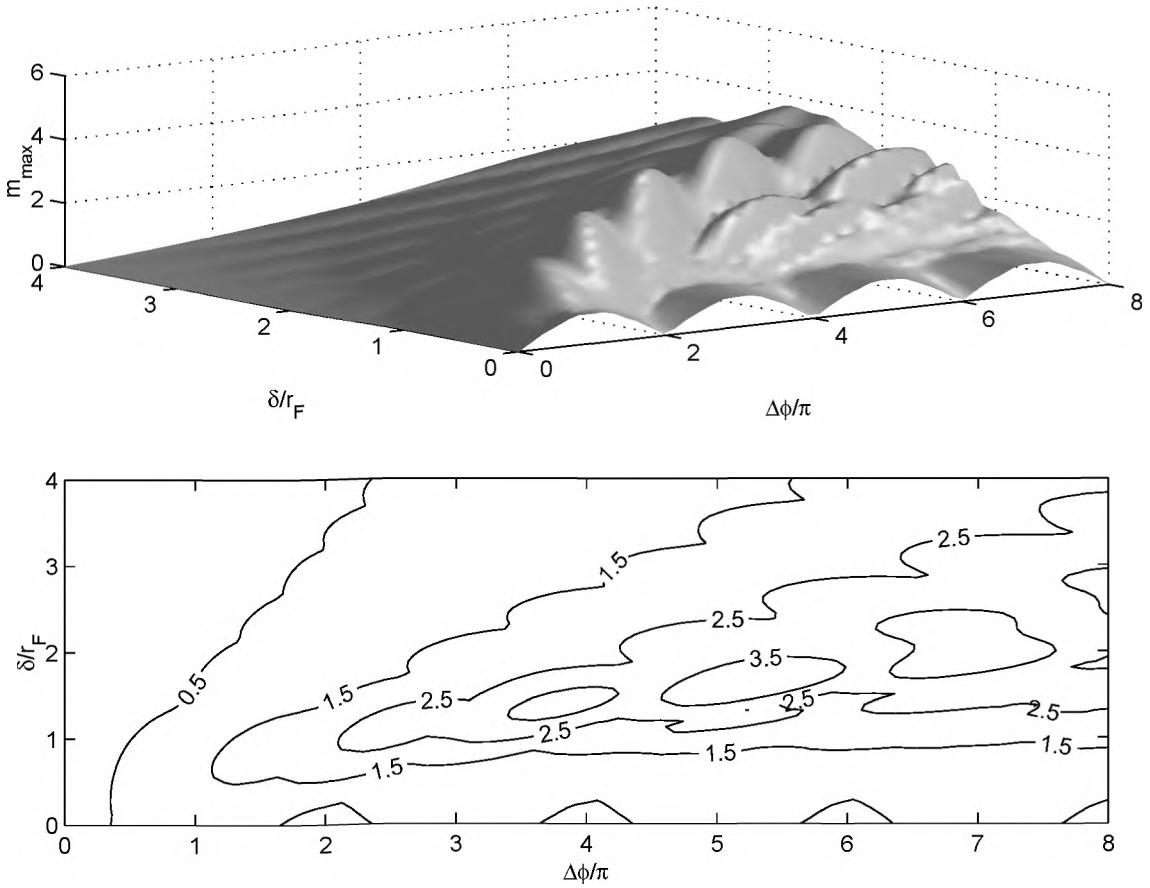

Figure 6.13: Maximum modulation index $m_{\max}$ as a function of $\Delta\phi$ and δ for a phase screen with a finite, linear transition in phase and $r_F = 512$ wavelengths of the illuminating plane wave. The surface plot and contour plot display the same results. These results were calculated from the numerical phase screen code of Chapter 4 with a 2^{17} point screen (radio wavelength $\lambda = 1$ grid spacing). The resolution of parameter space sampling is 0.16π in $\Delta\phi$ and $r_F/16$ in δ. Modulation index values are computed over intervals of width $r_F/4$ on the observation plane for each realization.

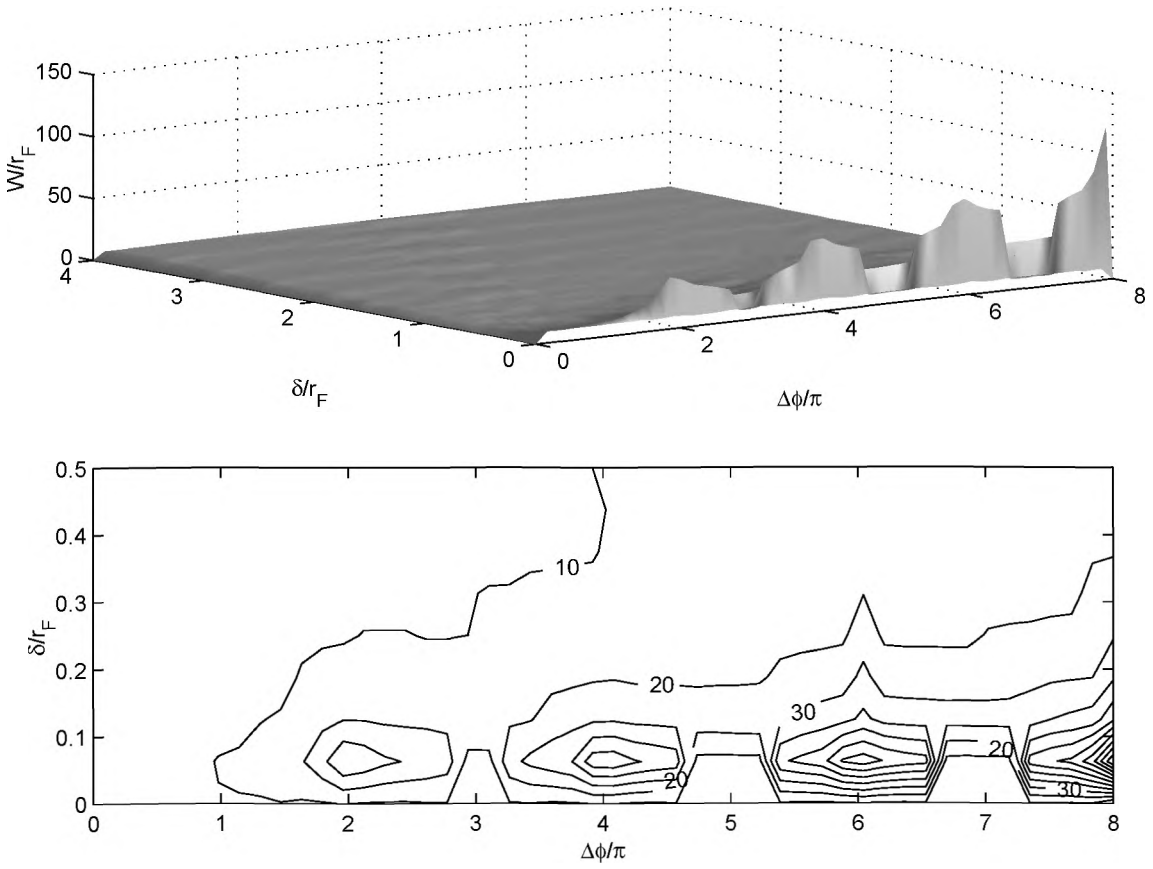

Figure 6.14: Intensity pattern width W over the parameter space explored in Figure 6.13 for the graded transition model. The width is defined as the horizontal distance between the farthest points for which $m = 0.1\, m_{\max}$. The contour plot shows only a portion of the surface plot, specifically the portion where the greatest values of W are observed. Contour lines are separated by $10\, r_F$.

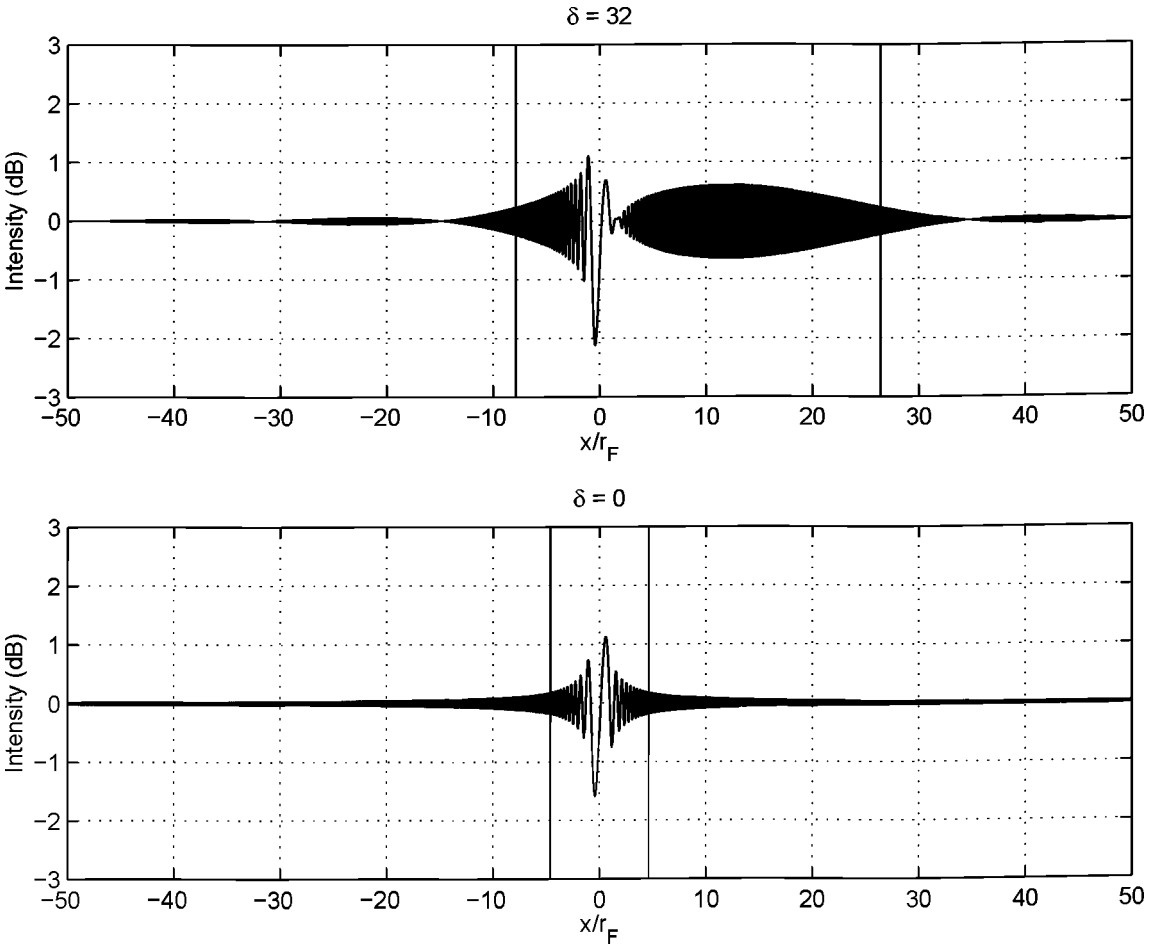

Figure 6.15: Comparison of the widths of two intensity pattern for $\Delta\phi = 2.2\pi$. The top plot is for a phase screen with a linear transition in phase of width $\delta = r_F/16$ ($r_F = 512$ wavelengths); the bottom plot is for a phase step ($\delta = 0$). Vertical lines mark the points farthest from $x = 0$ where the modulation index m falls below $0.1\, m_{\max}$. Modulation index is computed over segments of width $r_F/4$.

the ionosphere, it is important to consider whether the results of Figures 6.13 and 6.14 are universal; i.e., do they apply to any Fresnel radius r_F? Certainly, so long as we define horizontal distance x and transition width δ in terms of multiples of the Fresnel radius, $\mathcal{A}_1(x + \delta/2)$ and $\mathcal{A}_2(x - \delta/2)$ are unaffected by changes in r_F (see (6.9) and (6.10)). Similarly, r_F scales nearly all of the terms of (6.17) which contain x and δ. The only term in which r_F does not scale x or δ appears in the exponential function: $\exp[i\Delta\phi(x/\delta) + \ldots]$. In this case, only the ratio of x to δ matters and it is immaterial whether we express both in terms of multiples of r_F or in some other unit. Consequently, the surfaces generated always apply if x and δ are normalized by r_F.

(Incidentally, it is the $\exp[i\Delta\phi(x/\delta) + \ldots]$ term that generates "bursty" behavior. Its effect shows up in the "cross terms," $\mathrm{Re}(\mathcal{A}_1\mathcal{A}_3^*)$ and $\mathrm{Re}(\mathcal{A}_2\mathcal{A}_3^*)$, of the intensity pattern. After taking the real parts of the products, terms like $\sin(\Delta\phi(x/\delta) + A)$ and $\cos(\Delta\phi(x/\delta) + A)$, where A is a constant depending on $\overline{\phi}$, ξ^2, and ϕ_1 or ϕ_2, multiply the Fresnel functions. The result is a periodic modulation of the intensity pattern generated by the Fresnel function terms.)

Given that the observations of the spectral Vs last for several minutes, they probably represent values of δ and $\Delta\phi$ near the peaks of the surface shown in Figure 6.14. In that case, the width δ of the transition region lies around $r_F/16$ while the phase difference is near $\Delta\phi = 2n\pi$ $(n = 1, 2, 3, ...)$. For F peak altitudes with a zenith look direction, $r_F = 260$ m at the GPS L1 frequency. For E region altitudes, $r_F = 150$ m. Thus, the width of the transition would be 16 m for F region generation of the Vs and 9 m for E region generation. To estimate the difference in electron density required to generate 2π of phase difference at L1, we recall that one cycle of phase advance corresponds to a TEC of 1.173×10^{16} m^{-2}. Crudely modeling the F region as a 100

km thick slab implies a difference in electron density across the transition region of 1.2×10^{11} m^{-3} (alternatively, 1.2×10^5 electrons per cubic centimeter). For a 10 km thick sporadic E layer, the required density change is one order of magnitude greater, 1.2×10^{12} m^{-3}. Thus, the required electron density gradients are about 7.5×10^9 m^{-3} per meter for F region generation and 1.3×10^{11} m^{-3} per meter for E region generation, each within a narrow transition region with phase relatively constant on both sides.

With the linear transition model we can also examine diffraction behavior at other frequencies with an eye toward understanding why L band observations are less likely for a given set of ionospheric conditions. First, the Fresnel radius scales the diffraction pattern width. At lower frequencies, r_F is larger (for a fixed phase screen height) and, thus, the diffraction pattern becomes broader. This effect may be observed in the simultaneous 140 and 360 MHz measurements of *Davies and Whitehead* [1977]. Pattern width is proportional to $f^{-0.5}$, where f is the radio frequency. A narrow diffraction pattern at L band may attract less attention to itself.

Probably of greater importance, diffraction features at higher frequencies require steeper gradients in total electron content. If the required $\Delta\phi$ is fixed (e.g., at 2π), $\Delta\text{TEC} \propto f^2\Delta\phi$ must increase at higher frequencies. Also, for a fixed value of δ/r_F (e.g., 1/16) and phase screen altitude z, $\delta \propto f^{-0.5}$ must decrease at higher frequencies. Overall, then, the ratio $\Delta\text{TEC}/\delta \propto f^{2.5}$ increases with increasing frequency and it is more difficult to meet the required conditions for spectral V formation at greater radio frequencies. For a tangible example, the difference between achieving a certain $\Delta\phi$ and δ/r_F at 250 MHz and 1.6 GHz is an increase of two orders of magnitude in $\Delta\text{TEC}/\delta$ in the latter case.

6.5 AE-E Data

The generation of spectral Vs at L band requires fairly steep gradients in electron density with narrow widths, according to the linear transition phase screen model. This section assesses the plausibility of observing such gradients based on *in situ* measurements of plasma density in the F region. For this study, we use data from the Atmospheric Explorer E (AE-E) satellite because of its low altitude, low inclination orbit and the availability of high resolution plasma density measurements from its retarding potential analyzers (RPAs) operating in "duct mode" [*Hanson et al.*, 1973; *Basu et al.*, 1980]. Unfortunately, the ~ 35 m resolution of the AE-E duct mode measurements cannot detect the 16 m required for a transition which is $r_F/16$ wide at the GPS L1 frequency and 350 km in altitude at zenith. Nevertheless, we shall find examples of fairly steep gradients in electron density with relatively narrow widths (of the order of $r_F/3$ to $2\,r_F/3$).

Ideally, we would like to have AE-E observations made near solar minimum to match the point in the solar cycle when the GPS measurements that exhibited spectral Vs were taken. Unfortunately, the AE-E satellite orbited below 300 km altitude until mid-1978, well into the period around solar maximum. At that point, the satellite was boosted to an orbit above 400 km where it remained until reentering the atmosphere in 1981. We selected the higher altitude measurements to ensure that we were seeing topside spread F activity, indicative of the plume structures generally required to produce L band scintillations.

Figure 6.16 illustrates some AE-E observations of steep electron density gradients that approximate steps in density with linear transitions. Table 6.1 lists some auxiliary information such as the satellite's altitude and the angle of its velocity vector

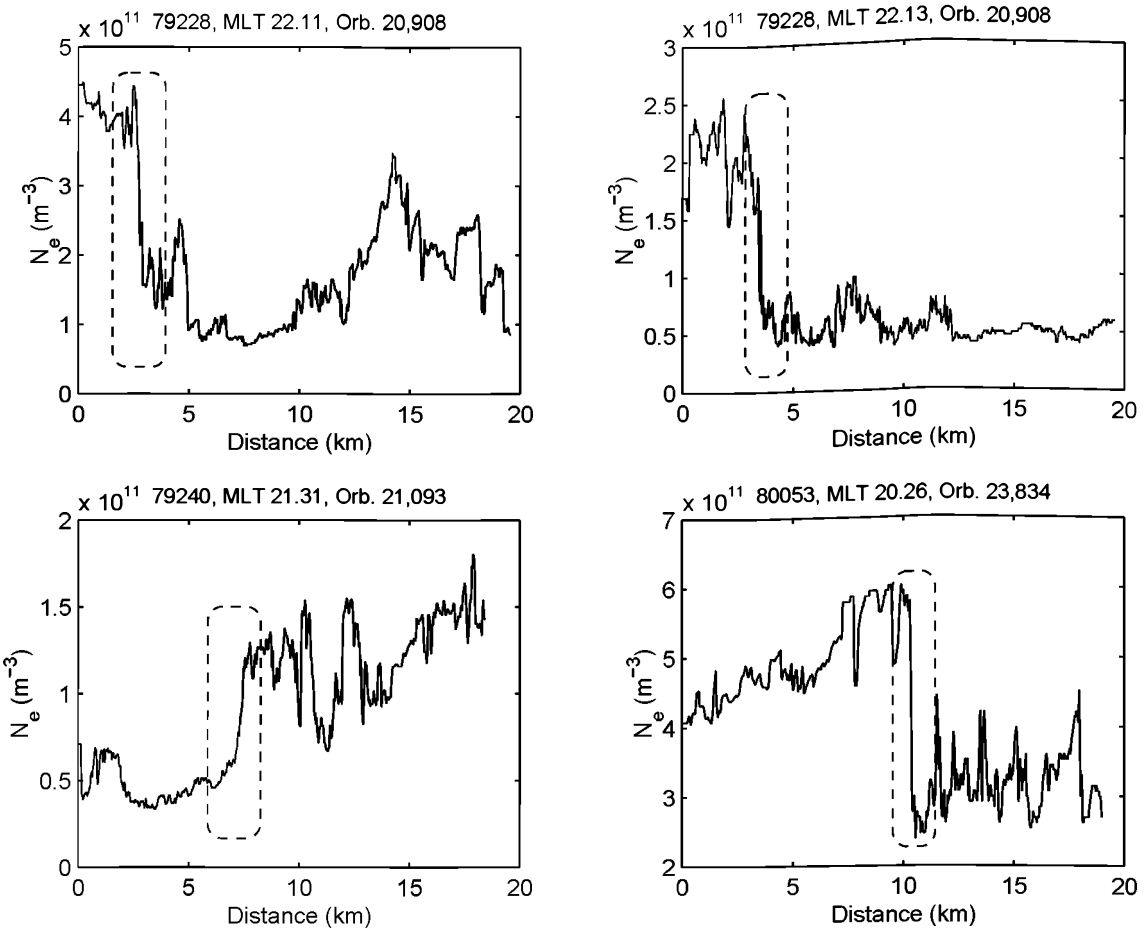

Figure 6.16: Examples of sharp gradients in *in situ* electron density from AE-E RPA duct mode measurements. Each graph is labeled with the date in *YYDDD* format, the magnetic local time (MLT) of the observation and the orbit number. These data represent 3 s duration snapshots of plasma density sampled every 4.45 ms for approximately 35 m resolution. Dashed ovals mark the gradients of interest and Table 6.1 lists some additional parameters not shown in the plots. (Data courtesy H. Kil, UT Dallas.)

Table 6.1: Auxiliary data for Figure 6.16 observations.

Date (*DD MMM YY*)	Date (*YYDDD*)	MLT (hr)	Dip	Alt (km)	Angle to **B**	Est. Width (m)
16 Aug 79	79228	22.11	0.48°	444	84°	374
16 Aug 79	79228	22.13	0.66°	444	84°	204
28 Aug 79	79240	21.31	25.56°	445	110°	480
22 Feb 80	80053	20.26	11.48°	423	99°	99

with respect to the magnetic field. The table also includes an estimate of the width of each transition region in the direction perpendicular to the magnetic field for comparison with the Fresnel radius. All of these transitions consist of a change in N_e of the order of 10^{11} m^{-3}, corresponding to about 1 TECU, if the density change were assumed to persist throughout a 100 km thick slab ionosphere. Since one cycle of phase advance at L1 corresponds approximately to 1 TECU of total electron content, these transitions are about the right magnitude to cause $\Delta\phi \sim 2\pi$, the condition stipulated in the last section to be near one of the "islands" of significant spectral V width for a finite width linear transition in phase. Again, of course, these estimates of $\Delta\phi$ assume that the observed plasma density depletion structures persist throughout a significant altitude range.

All of the gradients in these examples range from $0.4\,r_F$ to $1.8\,r_F$ in width, if we use the zenith value $r_F = 260$ m for a 350 km altitude equivalent phase screen. Consequently, we would not expect to observe very wide spectral Vs if, indeed, they were to form at all. If we were to allow slanted ray paths, however, the Fresnel radius would increase. For example, suppose that these electron density gradients occurred on 16 Oct 96 between the receiver at Ancon and PRN 29 around 0108 UT. In that case, the satellite would lie to the geomagnetic north and the Fresnel radius would increase to over 650 m (if the equivalent phase screen remained at 350 km altitude).

Then, the narrowest gradient, of approximately 99 m width, would fall below $0.15\,r_F$ and approach the transition widths which form spectral Vs of significant extent. Furthermore, at lower elevation angles, total electron content viewed through a given electron density structure increases over that observed at zenith because of the longer signal path through the ionosphere. Thus, the magnitude of the phase step increases, also improving the chance of forming broader spectral V structures.

In order to examine what type of diffraction pattern the *in situ* variations might generate, we examine the two cases with the most narrow gradients from Figure 6.16: namely, 22.13 MLT on 79228 and 20.26 MLT on 80053. First, we consider the density data in the context of the entire nighttime portion of the AE-E orbit for each case. Figure 6.17 shows the averages of RPA duct mode measurements for orbit 20,908 on 79228. The measurements indicate the presence of several depleted regions that the AE-E satellite flies through. The observations at 22.13 MLT lie within the deepest electron density depletion observed. Similarly, Figure 6.18 shows the averages of RPA duct mode density on 80053 (orbit 23,834). The 20.26 MLT observations appear to the east of the first deep depletion at 2000 MLT.

Now, the two selected examples of 3 second RPA duct mode snapshots may be used to generate equivalent phase screens for the numerical phase screen code. In this crude model, we assume a slab ionosphere 100 km thick and that the irregularities observed by the AE-E satellite extend throughout this slab. This simplistic model of vertically extended irregularities is similar to the earlier approach of *Wernik et al.* [1980], except that they treat the ionosphere as a thick medium rather than a phase screen. After computing the phase at the screen, also adding smooth transition zones on both ends to minimize wraparound edge effects in the discrete Fourier transform computations, the program propagates the wavefront to the ground using the formulas

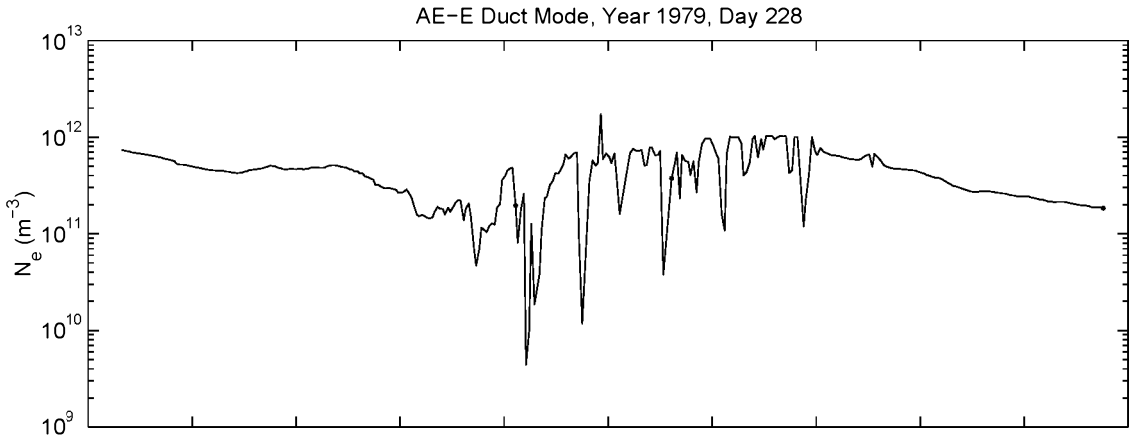

MLT (hr)	1900	2100	2300	0100	0300
GLON (deg)	−47.0	−19.0	8.0	36.0	64.0
GLAT (deg)	−7.2	3.3	12.8	18.6	19.5
DIP (deg)	3.0	−3.8	7.6	21.9	25.2
ALT (km)	447.0	445.0	444.0	445.0	446.0
UT (s)	80031	80525	81009	81468	81910

Figure 6.17: Averaged AE-E RPA duct mode density data for orbit 20,908 on 16 Aug 1979. (Data courtesy H. Kil, UT Dallas.)

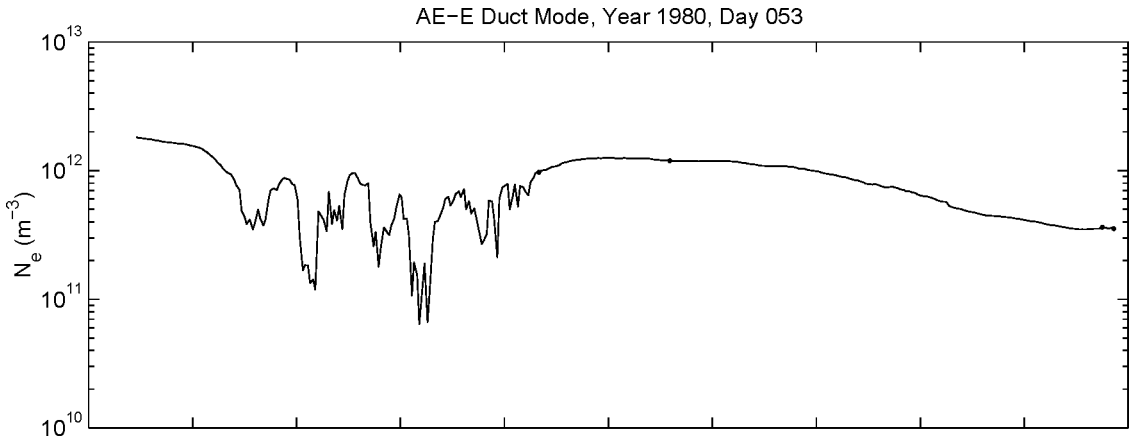

MLT (hr)	1900	2100	2300	0100	0300
GLON (deg)	171.7	−159.5	−131.0	−103.0	−75.0
GLAT (deg)	12.5	3.0	−7.6	−15.8	−19.6
DIP (deg)	15.6	7.0	−8.2	−16.4	−12.7
ALT (km)	422.0	424.0	427.0	430.0	431.0
UT (s)	27915	28398	28891	29362	29809

Figure 6.18: Averaged AE-E RPA duct mode density data for orbit 23,834 on 22 Feb 1980. (Data courtesy H. Kil, UT Dallas.)

of Chapter 4.

The simulations utilize the following parameters. The grid spacing represents one wavelength of the GPS L1 carrier or 0.19 m. Since the AE-E duct mode plasma density measurements are 35 m apart, we interpolate the data smoothly, using a cubic spline method, to fill out the phase screen grid without introducing any unnecessary discontinuities. The phase screen is 350 km away at zenith (or 1.84×10^6 grid spacings) and contains 2^{17} points for an effective width of almost 25 km. Thus, since the Fresnel radius is 260 m (1.37×10^3 grid spacings), the screen is of the order of 100 Fresnel radii wide.

Figure 6.19 shows the equivalent phase screen constructed for the 1979, day 228 data. Subsequent distances x refer to Figure 6.19, not Figure 6.16, since the features have been shifted and the pattern truncated. The phase screen is inverted from the density data because increasing TEC corresponds to a decreasing phase. Below the screen, the spatial pattern of intensity is plotted. The intensity pattern does not appear to contain any quasiperiodic scintillations corresponding directly to the abrupt change in phase highlighted in Figure 6.16 (and now placed in the center of the phase screen). Instead, some quasiperiodic scintillations occur to the left, around $6 < x < 9$ km, and seem to be associated with the step in phase at $x \approx 9$ km.

The step in phase at $x \approx 9$ km turns out to be fairly narrow: approximately 60 m. Also, across the transition $\Delta\phi = -4.4$ rad. Evidently, the relatively abrupt change in phase is sufficient to generate a quasiperiodic scintillation pattern of about 3 km width ($\sim 12 r_F$). It appears also that fairly smoothly varying phase is required on either side of the phase transition to allow quasiperiodic scintillations to develop. In the case illustrated in Figure 6.19, for example, the quasiperiodic scintillations are only visible for $x < 9$ km, where the phase variations are artificially smoothed

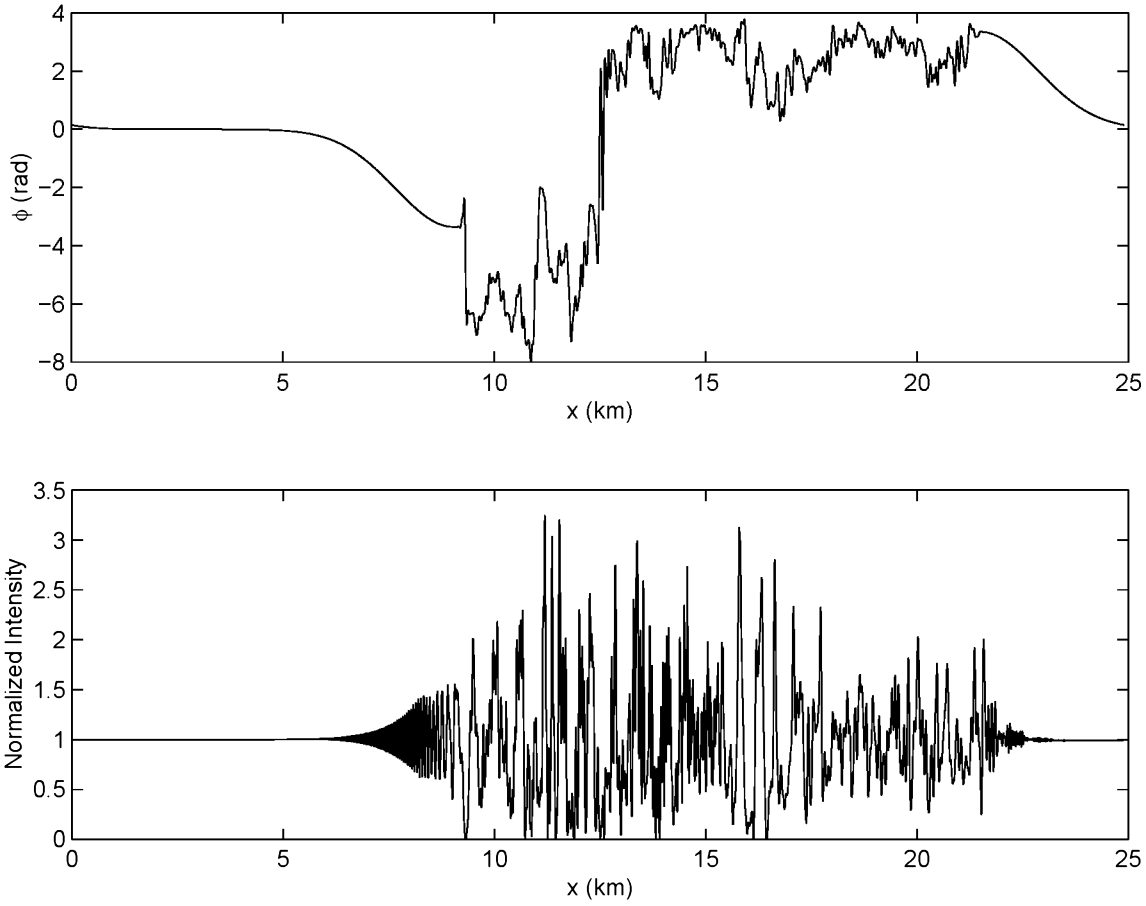

Figure 6.19: Equivalent phase screen and calculated intensity pattern for 22.13 MLT on 79228 (orbit 20,908).

by adding a Gaussian taper. The side with $x > 9$ km, where the more irregular phase variations derive from measured electron density variations, does not exhibit any prominent quasiperiodic scintillations. Furthermore, the large phase transition that was the original target of this investigation does not generate any noticeable quasiperiodic scintillation behavior. So, apparently, having phase fluctuations on either side tends to obscure quasiperiodic scintillations.

The situation does not improve for the narrower structure observed on 1980, day 053. Figure 6.20 shows the equivalent phase screen phase and the intensity pattern developed below it at a distance of 350 km. Again, no prominent quasiperiodic scintillation pattern appears, even though the large gradient in phase only extends 99 m in width. Instead, the intensity pattern has the aspect of normal, moderately strong, random scintillations. We conclude that any potential quasiperiodic scintillations were disrupted by the high degree of irregularity in the phase screen on both sides of the narrow transition region in the center of the screen.

In sum, the AE-E *in situ* data show that there potentially exist steep enough, and narrow enough, gradients in topside electron density depletions in the F region to account for GPS observations of quasiperiodic scintillation patterns. The likelihood of generating quasiperiodic scintillations (or "spectral Vs") depends on how smooth the surrounding ionosphere is, however. In the examples presented of phase screen simulations based on AE-E measurements, the one unambiguous case of quasiperiodic scintillations was one in which the approximate step in phase lay close to the artificially smooth background added for "FFT padding."

Of course, the slab model used to generate the phase screen from the *in situ* data is simplistic. The actual vertical variation in electron density may act to smooth out some of the "roughness" we see in the model phase screens which obtains when as-

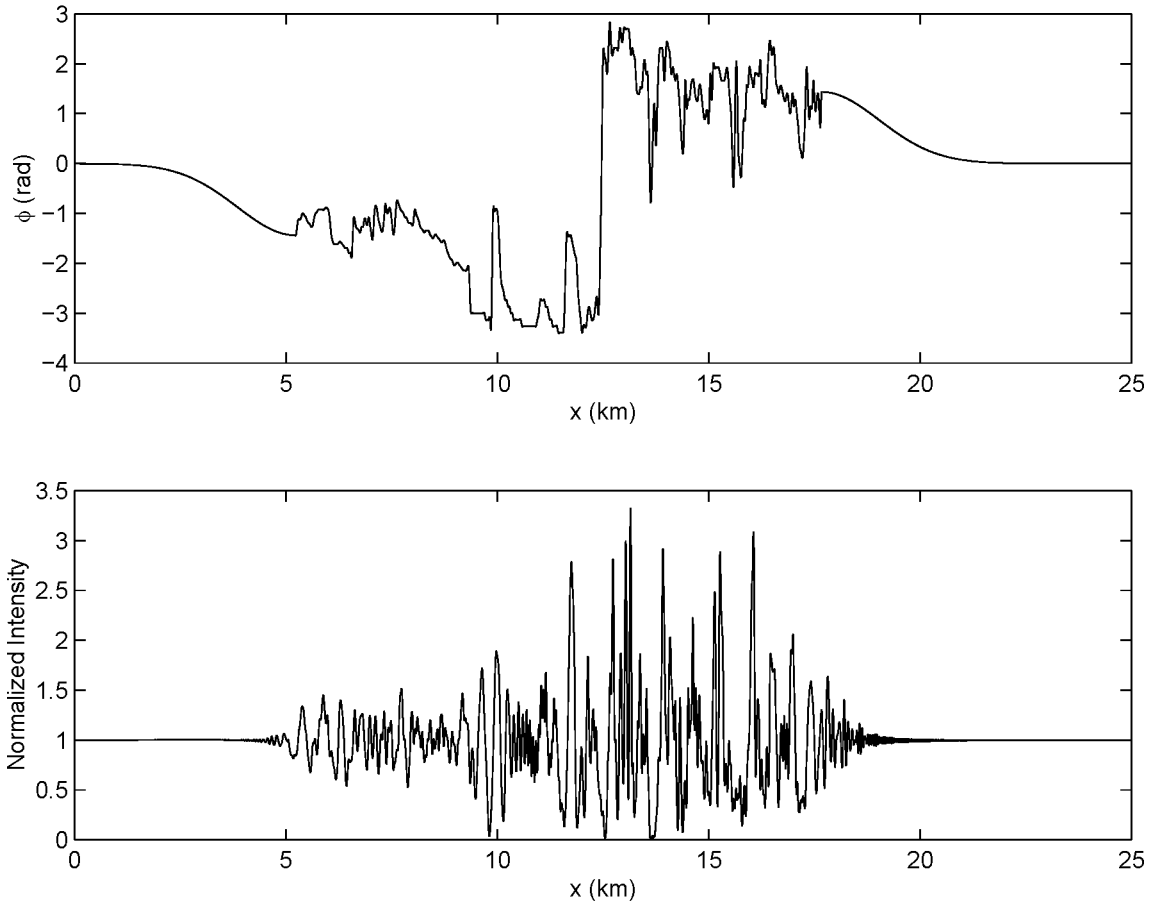

Figure 6.20: Equivalent phase screen and calculated intensity pattern for 20.26 MLT on 80053 (orbit 23,834).

suming that even the smallest scale structures extend through the whole ionosphere. For example, the slab model assumptions contravene the picture of small scale perturbations developing on the boundaries of large scale depletions that characterizes the formation of actual equatorial spread F [*Kelley*, 1989].

6.6 Summary

We have presented observations of unusual, structured features in the spectrograms of GPS amplitude scintillation patterns. These patterns, which we term "spectral Vs" because of their shape, appear on both receivers at Ancon within seconds of each other for a given satellite. The evidence points to propagation phenomena in the generation of the Vs and scattering from a moving object is a plausible model. Based on the slopes of the Vs (the rate of change of frequency with respect to time), low altitude objects such as aircraft are unlikely to generate the Vs. Instead, the slopes suggest that ionospheric generation is more likely. Depending on the value of drift velocity used, we estimate that the altitudes of the scatterers forming the Vs lie in the range 95–350 km, although E region or lower F region generation may be slightly favored.

A probable source of the scattering in the ionosphere is diffraction from sharp electron density gradients. We demonstrate that diffraction from a phase screen with a step in phase generates a spectral V, where the phase screen model represents an abrupt change in electron density such as may be observed in the walls of equatorial spread F depletions (or sporadic E). In a more realistic model, we find that adding a finite width linear transition region between the high and low values of phase screen phase can create much more pronounced diffraction patterns than the simple step in

phase can. The broadest diffraction patterns form when the width of the transition region is the order of one tenth the Fresnel radius r_F and the phase difference across the transition is an integer number of cycles of the incident wave.

Spectral V observations are similar to earlier observations of so-called "quasiperiodic" scintillations, except that in our case the bulk of the intensity fluctuations are small, near the noise level of the WBP_k measurements, and do not really stand out except in the spectrograms. As with spectral Vs, quasiperiodic scintillations are thought to be associated with diffraction from gradients in ionospheric electron density. The current observations differ from the documented quasiperiodic scintillation cases in that the radio frequency is higher, implying narrower transition regions between the high and low electron density regions. For example, the Fresnel radius at 350 km for a 250 MHz VHF satellite signal (the highest frequency commonly used in quasiperiodic scintillation observations) is 650 m. At the GPS L1 frequency, $r_F = 260$ m for the same altitude. Since the transition width required to produce an observable diffraction pattern is proportional to r_F, the GPS observations imply that horizontal gradients exist which are 40% narrower than those required for VHF quasiperiodic scintillations. Furthermore, the change in electron density must be much greater (by a factor of $(1575/250)^2$) to produce the same phase difference at the higher frequency.

Nevertheless, AE-E *in situ* electron density data suggest, even within their resolution limitations, that steep enough, and sufficiently narrow, gradients exist in equatorial spread F depletions to account for GPS observations of spectral Vs. Phase screen simulations based on AE-E plasma density measurements show that the phase values on either side of the transition region must be relatively smooth for diffraction patterns to appear, however. We have not attempted to perform a comparable study of sporadic E gradients in the case that the diffraction occurs at those altitudes.

A few outstanding issues need to be resolved concerning spectral V observations. One major question is whether the source of the Vs lies within the *E* region or the lower *F* region or near the *F* peak. The slope measurements of the Vs are not definitive because the drift speeds of the diffraction patterns are not known to sufficient precision. Earlier VHF observations of quasiperiodic scintillations by equatorial stations indicate cases of possible generation in each of the three ionospheric regions listed above. Correlation studies of the Vs together with other ionospheric phenomena may be required. Along those lines, the apparent correlation of spectral Vs with regular (random) scintillations should be corroborated. The handful of examples that we have encountered seem to bear this assertion out, but we have not conducted a systematic survey of spectral V occurrences.

Chapter 7

TEC Fluctuations

7.1 Introduction

Recently, as we shall summarize in this chapter, several research groups have begun to use total electron content (TEC) fluctuation measurements from Global Positioning System receivers to study the morphology of ionospheric electron density irregularities. The availability of networks of dual frequency GPS receivers established for geodesy or survey work allows these studies to cover various geographic scales, ranging from the field of view of a single receiver to global scales. Although several researchers [*Aarons et al.*, 1996; *Pi et al.*, 1997] are careful to distinguish between "phase fluctuations" (fluctuations in TEC derived from dual frequency phase measurements) and scintillations in their publications, invariably such carefully drawn distinctions become blurred in less formal discourse. Phase fluctuations are not phase scintillations, primarily because of the inability to resolve Fresnel scale structure at the low sample rates available. Still, phase fluctuations relate to the low frequency portion of the phase scintillation spectrum.

The relationship of phase fluctuations to amplitude scintillations is less clear, but inquiry into that relationship is of great practical significance and, indeed, is the focus of this chapter. Ideally, we should like to employ TEC fluctuations as a proxy for amplitude scintillations so that, if we observe TEC fluctuations of a specific magnitude on a global or regional network, we can estimate the likelihood of severe amplitude scintillations in the covered area, for example. Certainly, there exists some relationship between phase scintillations and amplitude scintillations via the power spectrum of ionospheric electron density irregularities (manifest in the power spectrum of the equivalent phase screen), as discussed in Chapter 4 for the case of weak scintillations. Experimentally, where phase measurements are taken, concurrent phase and amplitude scintillations are common in the ionosphere [*Fremouw et al.*, 1977; *Rino*, 1979*a*; *Basu et al.*, 1993]. Yet, there are also times when phase scintillations appear without amplitude scintillations [*Fremouw et al.*, 1977].

This chapter presents some case studies of concurrent TEC and amplitude scintillation measurements from the April 1997 campaign at Ancon. Chapter 5 already discussed the experimental setup, particularly the antenna arrangement at Ancon and the campaign dates. Here, after a summary of TEC measurement techniques using GPS and a literature survey of TEC fluctuation studies, we examine data from the campaign to investigate the relationship between TEC fluctuations and amplitude scintillations. Although the sample set is small, it does show enough variety to illustrate important points concerning that relationship. Following the case studies from the April campaign, we then consider the theoretical relationship of weak phase fluctuations to amplitude scintillations by using a simplified, one dimensional phase screen model. The theoretical discussion will emphasize the important role of the outer scale cutoff of the ionospheric irregularities, whether real or one imposed

by measurement limitations, on the measured root-mean-square deviation of phase [*Rino*, 1979*a*].

7.2 TEC Measurements

7.2.1 Available Data

The ability to use GPS observations from data sets not originally intended for ionospheric studies makes GPS measurements a unique ionospheric research tool. Every day, users record dual frequency GPS measurements for surveys or solid earth geophysics studies. One of the primary resources for measurements is the International GPS service for Geodynamics (IGS), a worldwide network of stations taking dual frequency GPS measurements for continental drift studies. The Jet Propulsion Laboratory (JPL) collects and archives the IGS data daily. The data are easy to obtain on line via ftp services and are stored in a standardized ASCII format, the RINEX format (see *Hofmann-Wellenhof et al.* [1994] for further details of the format). *Doherty et al.* [1994] and *Aarons et al.* [1996] credit *Wanninger* [1993] with first demonstrating the potential of the IGS data base for morphological studies of ionospheric irregularities.

The mere fact that TEC data from stations around the globe, along multiple lines of sight at each station, are available on a regular basis recommends that they ought to be used. Nevertheless, understanding the limitations of the IGS data and other "data sets of opportunity" is critical. If we wish to estimate the magnitude of amplitude scintillations based on the level of TEC fluctuations, for example, the sampling rate and how the receiver averages or filters its data internally affect that relationship. Although nearly all of the discussion in this chapter focuses on the IGS data base, many of the considerations apply to GPS data from other sources.

Perhaps the chief limitation of the IGS data set for long term morphological studies is the current lack of coverage of many regions. From a recent map of the system [*Pi et al.*, 1997], coverage is, predictably, most dense over Europe, North America and Southeast Asia. Stations in these regions often overlap each other's field of view. On the other hand, Africa, Australia, Central Asia, the Middle East and all oceans are very sparsely populated by IGS GPS receivers. If we wished to study the equatorial ionosphere using the IGS network, for example, we would be severely limited in the longitude sectors we could cover. Even South America, one of the more densely instrumented regions in the network near the geomagnetic equator, has very little overlap among its stations' sky views.

Other limitations, applicable to most available dual frequency GPS data sets, stem from the measurement rate and the data format. Stations in the IGS chain typically record data at 30 second intervals. Survey receivers and other GPS networks have comparable rates, usually no faster than one sample every 15 seconds. These data rates are not sufficient to capture ionospheric fluctuations in great detail. Worse, averaging of carrier phase measurements inside the IGS receivers over the 30 second intervals uses only 10 seconds' worth of data [*Aarons et al.*, 1997; *Pi et al.*, 1997]. Thus, some aliasing of phase fluctuation spectra inevitably occurs. Finally, the RINEX format does not include sufficient information on signal strength to monitor amplitude scintillations, even if a high data rate were available.

Again, we emphasize that the data from the IGS network and similar sources are important despite their limitations. We have discussed the limitations primarily because some of them affect how we need to treat the data for our case studies. For example, in the April 1997 campaign we collected relatively high time resolution GPS TEC data (one sample per second) specifically for the purpose of ionospheric studies.

In order to compare our TEC fluctuation measurements with the IGS data we must account for the reduced sample rate in a realistic fashion.

7.2.2 Measurement Techniques

The predominant ionospheric quantity of interest that dual frequency receivers can measure is total electron content (TEC) along satellite lines of sight, calculated from the ionosphere's dispersion of GPS signals. Total electron content is simply the integral of electron density along the ionospheric line of sight L,

$$\text{TEC} = \int_L ds\ N_e(s). \tag{7.1}$$

This definition generalizes that of Chapter 4 to slanted propagation paths. Given that the GPS frequencies are typically much, much higher than all the plasma frequencies and gyrofrequencies in the ionosphere along the ray path, the ionospheric refractive index $n(s)$ becomes

$$\begin{aligned} n(s) &= \sqrt{1 - {\omega_p}^2(s)/\omega^2} \\ &\approx 1 - \frac{{\omega_p}^2(s)}{2\omega^2}, \end{aligned} \tag{7.2}$$

where $\omega_p(s)$ is the local plasma frequency and ω is the signal frequency. Since ${\omega_p}^2(s)$ is proportional to the local electron density $N_e(s)$,

$${\omega_p}^2(s) = \frac{e^2 N_e(s)}{\epsilon_0 m}, \tag{7.3}$$

where e and m are the electron charge and mass and ϵ_0 is the permittivity of free space, the ionospheric group delay or phase advance relates directly to TEC. Specifically, the ionospheric ranging error ΔR_{iono} in meters is

$$\Delta R_{iono} = \frac{40.296}{f^2} \int_L ds\ N_e(s), \tag{7.4}$$

where f is the signal frequency in Hertz and $N_e(s)$ is expressed in terms of electrons per cubic meter. Equation (7.4) also describes the phase advance in meters, which may be converted to radians by multiplying by $2\pi/\lambda$, $\lambda = c/f$.

Now the GPS satellites broadcast on two frequencies, L1 at 1.57542 GHz and L2 at 1.2276 GHz, specifically to allow users to estimate the ionospheric ranging error. So far we have primarily discussed the L1 frequency because that is the only signal which bears the civilian Coarse/Acquisition (C/A) code. Civilian users cannot use the military Y code (the encrypted Precise (P) code), except under extraordinary circumstances. Therefore, civil receivers cannot directly make ranging estimates on both GPS frequencies, nor can they lock onto the L2 carrier in a straightforward fashion. Nonetheless, through clever signal processing, which exploits the fact that the Y code is the same on both L1 and L2, or the Y code's relationship to the unclassified P code, civil receivers can make range estimates and carrier phase measurements on L2 [*Hofmann-Wellenhof et al.*, 1994]. The penalties that the user must pay are reduced receiver performance, compared to the direct correlation process we analyzed earlier, and noisier measurements.

Without belaboring the details, dual frequency GPS receivers provide two types of measurements on each of the GPS frequencies: pseudorange and carrier phase. We defined pseudorange ρ in Chapter 2,

$$\rho = c\Delta t, \tag{7.5}$$

where Δt is the measured difference between transmission time and reception time. (Note that "measured" here means clock difference; i.e., it is entirely possible to have the signal transmitted at 0120 UT by the satellite's clock and received at 0119 UT, according to an inaccurate receiver clock, giving a negative pseudorange.) Pseudo-

range relates to the true range R according to

$$\rho = R + \Delta R_{iono} + \Delta R_{other}. \tag{7.6}$$

The extra error term, ΔR_{other} incorporates all other sources of ranging error: tropospheric propagation delay, multipath induced timing errors, incorrect clock settings, hardware time delays, etc. Only ionospheric delay changes with frequency; R and ΔR_{other} are common to both channels (ignoring differential errors in timing between the L1 and L2 transmitting or receiving hardware channels, which can be substantial [*Snow et al.*, 1994]). So, if we subtract the L1 and L2 pseudoranges, we obtain a compound ionospheric error term that is proportional to TEC.

Unfortunately, pseudorange measurements are relatively noisy, especially in civilian dual frequency receivers when Anti-Spoofing is activated (i.e., when GPS uses the Y code instead of the P code) [*Snow et al.*, 1994]. Consequently, the resulting TEC estimates include relatively large measurement uncertainties. Phase measurements are much less noisy and therefore yield better TEC estimates. The tradeoff is that phase measurements intrinsically have integer ambiguities. Thus, we lose absolute TEC information unless we perform additional processing to recover the integer ambiguities.

For phase measurements, the receiver usually records the number of cycles of the carrier observed since the receiver locked onto the signal, including fractional cycles, with an accuracy of 0.01 cycles or better [*Hofmann-Wellenhof et al.*, 1994]. Denoting cycles of L1 by ϕ_1 and cycles of L2 by ϕ_2, relative TEC becomes

$$\text{TEC} = 1.17\ (\beta_1\phi_1 + \beta_2\phi_2), \tag{7.7}$$

in TEC units (TECU; 1 TECU = 10^{16} electrons per m^2), where

$$\beta_1 \;=\; -\frac{f_1^2}{f_1^2 - f_2^2}, \tag{7.8}$$

$$\beta_2 = \frac{f_1 f_2}{f_1^2 - f_2^2}, \tag{7.9}$$

and f_1 and f_2 are the L1 and L2 carrier frequencies [*Musman et al.*, 1997]. The literature uses the term "relative" TEC to distinguish these measurements from the "absolute" TEC measurements that pseudorange measurements provide. Plotting relative and absolute TEC on the same graph would show the former data displaced up or down from the latter by a fixed amount. If any cycle slips occur, periods in which the receiver loses lock on L1 or L2 briefly and following which it acquires new integer ambiguities, the portion of the graph following the cycle slip becomes shifted to a new offset unless corrections are applied through further processing.

With work, one may reconstruct absolute TEC along slanted paths by combining phase TEC measurements with the more noisy pseudorange TEC measurements and correcting for cycle slips and timing differences between channels. With some assumptions, one may also convert the slant TEC to zenith TEC over a single GPS station or network of stations [*Mannucci et al.*, 1993; *Schaer et al.*, 1996]. Some of those assumptions are dubious, however, particularly the assumption of insignificant horizontal ionospheric electron density gradients implicit in most slant to vertical TEC conversions [*Vladimer et al.*, 1997]. Focusing on the accuracy of these absolute, vertical TEC measurements will not be the major thrust of this chapter, though. Instead, we concentrate on the relationship of TEC fluctuations to ionospheric electron density irregularities and associated amplitude scintillations.

7.2.3 Fluctuation Studies

Clearly, except perhaps in cases of unusual line of sight geometry, ionospheric electron density fluctuations will produce TEC fluctuations. Although we are interested in the

geophysics behind the irregularities, we concentrate on the effects of TEC fluctuations in this chapter, particularly amplitude scintillations. Usually, TEC fluctuation studies in the literature focus more on occurrence patterns in equatorial or auroral regions and on using the fluctuations to map the associated geophysical phenomena (of types which are already known to exist and whose presence may be inferred from the TEC fluctuations). Nevertheless, we include these studies in the present discussion since they provide examples of how researchers process GPS data and what quantitative indicators of TEC fluctuation strength they use.

Most researchers who study ionospheric irregularities use TEC derived from phase measurements since it has inherently less measurement scatter than pseudorange derived values. Often, they leave results in terms of relative TEC, but occasionally they convert those values to absolute TEC by identifying the integer ambiguities [*Aarons et al.*, 1996]. A survey of recent examples of TEC irregularity studies follows.

Doherty et al. [1994] studied statistics of TEC fluctuations in auroral regions using IGS stations. *Coker et al.* [1995] determined part of the auroral oval boundary using high pass filtered TEC measurements derived from Alaska GPS phase data. In equatorial regions, *Kelley et al.* [1996] demonstrated qualitative correlation between spread F plume structures, seen by the Altair scanning radar, and relative TEC fluctuations from a survey receiver on the island of Kwajalein. *Weber et al.* [1996] show correlation of GPS amplitude scintillations with TEC and airglow observations of depletions near the southern equatorial anomaly in Chile.

More quantitatively, for equatorial studies, *Aarons et al.* [1996] compare absolute values of TEC rates of change with Jicamarca back scatter maps and airglow measurements from Arequipa. *Aarons et al.* [1997] present a longer term study of equatorial irregularities in the South American sector using IGS data (while *Aarons*

[1997] gives a similar study at high latitudes). *Musman et al.* [1997] employ an ionospheric "roughness" measure related to the rate of change of TEC to study equatorial spread F together with portable 50 MHz radar observations in Brazil. Finally, *Pi et al.* [1997] generate global maps of irregularities, employing IGS data and yet another derivative based measure of TEC fluctuations.

Generally, the trend is to use some measure of the rate of change of TEC with respect to time to indicate the strength of TEC fluctuations. This method has some good points to recommend it. First, it eliminates any effects of unknown TEC offsets so that we may use the more easily generated relative TEC measurements directly. The rate of change of TEC is itself relatively simple to calculate. Furthermore, this measure is intuitively satisfying since we expect TEC to be a less smoothly varying function when irregularities are present. On the other hand, using a derivative based measure has some drawbacks. Differentiation amplifies the effects of measurement noise. Judging by published graphs of $d\text{TEC}/dt$ [*Aarons et al.*, 1996], however, measurement scatter causes very little trouble in practice (for the 30 second sampling period IGS data). Taking the derivative also exacerbates the effects of any sudden jumps in phase due to cycle slips.

Recent publications employ three basic variations on the derivative measure. *Aarons et al.* [1996] take the direct approach of computing $d\text{TEC}/dt$ in TECU/min and high pass filtering the results to eliminate 25 minute or longer fluctuations. The absolute value of filtered $d\text{TEC}/dt$ then indicates the strength of the irregularities. *Pi et al.* [1997] perform essentially the same analysis and then find the standard deviation of $d\text{TEC}/dt$ over 5 minute intervals to give a value they call ROTI (rate of TEC index). *Musman et al.* [1997] define a statistical parameter related to the deviation of the slope of detrended TEC data over 7.5 minute intervals called "roughness."

The root-mean-square deviation of TEC (σ_{TEC}) should also be a useful measure of the strength of ionospheric irregularities, just as the deviation of intensity provides a measure of amplitude scintillations. In favor of σ_{TEC}, its value should relate to the phase screen scintillation parameter σ_ϕ, depending on sampling rate, the spectral form of the electron density irregularities and the cutoff frequency of any detrending performed. One problem with σ_{TEC} lies, as we shall see, in its response to very low frequency changes in TEC, however. Whereas weak amplitude scintillations only respond to a particular range of irregularity scale sizes because of Fresnel filtering, TEC fluctuations (and phase scintillations) potentially reflect scales all the way up to the outer scale of the irregularities.

In practice, stationary GPS receivers do not observe electron density irregularities at the largest scales because the changing elevation of the line of sight dominates the low frequency fluctuations of TEC. Consequently, common practice is to detrend phase TEC measurements by high pass filtering, inevitably reducing σ_{TEC}. Additionally, irregularities evolve as they pass through the line of sight, and longer scale irregularities take more time to drift by than the shorter scales. In such a statistically non-stationary environment, time averages cannot replace spatial averages. So the detrending process also eliminates geophysical TEC variance of questionable importance.

Perhaps because of the somewhat arbitrary nature of the detrending cutoff (made even more arbitrary because it is a time scale cutoff and irregularity drift velocities vary) GPS researchers do not commonly use σ_{TEC} as a TEC fluctuation measure. Derivative based measures inherently eliminate low frequency power, although their low frequency cutoff is typically not as sharp as that of a high pass filter used for detrending. On the other hand, derivative based fluctuation indices have problems

at high end of the spectrum, as we shall see presently.

In order to quantify the strength of TEC fluctuations for our case studies we need to adopt a TEC fluctuation index. In fact, we shall adopt two: (1) the rate of TEC index (ROTI) of *Pi et al.* [1997], and (2) the deviation of TEC (σ_{TEC}). The former, a derivative based measure, allows for comparison of our results with published accounts. We select the latter because of its relationship to the phase scintillation parameter σ_ϕ. In both cases, selecting a root-mean-square type measure permits more ready comparison with theory.

7.3 Comparison of Fluctuation Measures

In addition to the scintillation monitors, Cornell fielded a dual frequency receiver at Ancon in April 1997. This receiver was an Allen Osborne ICS-4000Z receiver, a version of their TurboRogue receiver adapted to log pseudorange TEC and phase TEC directly. The IGS network also uses TurboRogues at many sites, although in other software and hardware configurations. In the presence of Anti-Spoofing, the TurboRogues cross correlate the Y code on L1 and L2 to measure the difference in group delay between the signals and to obtain phase measurements on L2.

During the April 1997 campaign, we usually collected data on the Allen Osborne receiver at one second intervals (exception: over the weekend of 11–14 April 1997, data were collected at 5 second intervals to allow continuous, unattended logging). Consequently, additional post processing must be performed to emulate the IGS measurements at 30 seconds per sample. For now, we consider examples using the higher data rate.

Figure 7.1 shows one example of simultaneous amplitude and TEC measurements

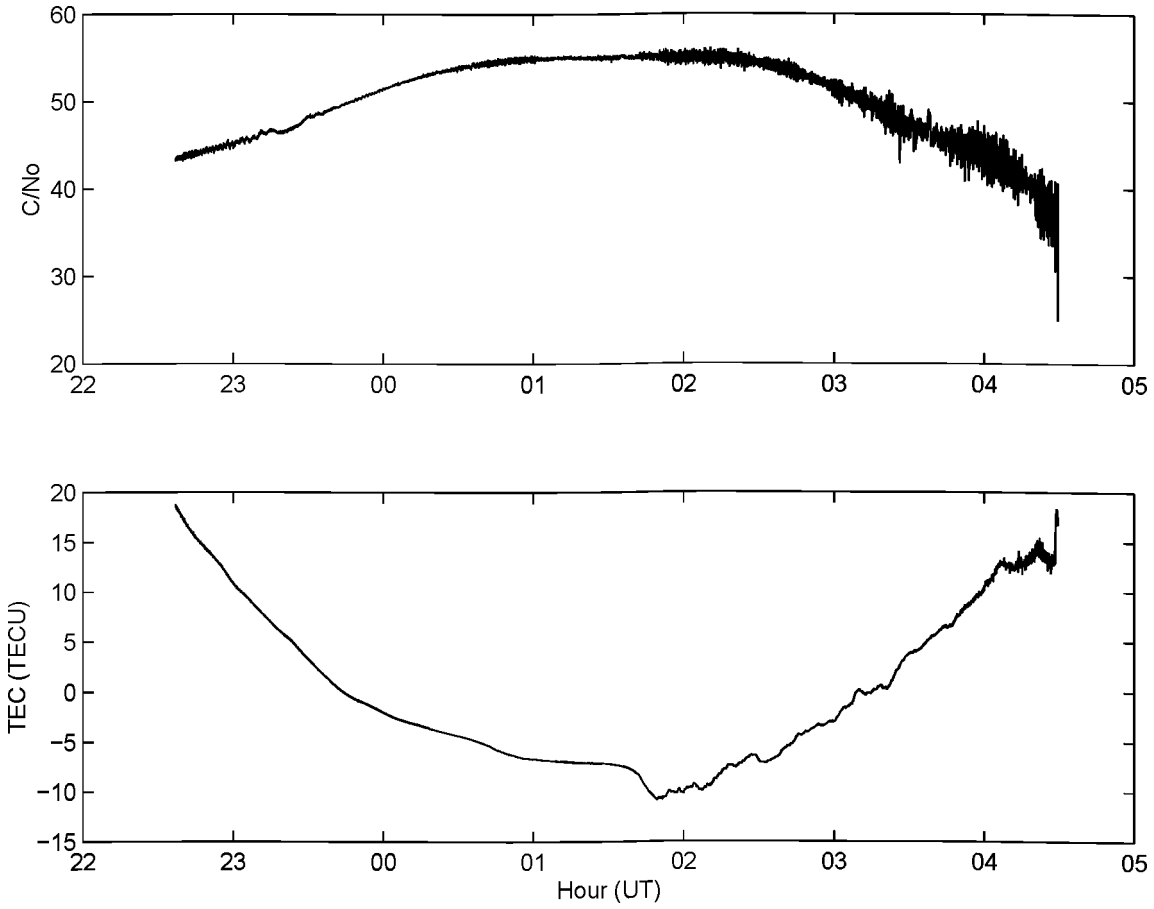

Figure 7.1: Simultaneous amplitude and total electron content (TEC) observations from Ancon for PRN 26, 10–11 April 1997. Rather than wide band power (WBP_k), the dual frequency receiver records the carrier to noise ratio (C/N_0). Also, TEC here is relative TEC derived from phase measurements. The mean is subtracted to emphasize that the correct offset is unknown.

by the dual frequency receiver. The two scintillation monitors at Ancon exhibited similar amplitude fluctuations during this time period for PRN 26. Note the onset of weak amplitude scintillations around 0145 UT (2045 LT). Here the satellite's ionospheric puncture point moves predominantly south to north near the Ancon field line around the time of scintillation onset. The TEC displays a characteristic U-shaped trend which indicates the changing elevation of the satellite and, thus, the changing path length through the ionosphere. Around 0145 UT, a decrease in TEC of about 5 TECU appears, followed by data which are visibly slightly "rougher." Since the satellite essentially tracks along the Ancon field line during the onset of scintillations, what we see is a developed plume drifting eastward across the field line. First the plume appears as a smooth depletion and then we see the more irregular westward portion of the plume.

A more difficult case to interpret is the PRN 5 data on the same night (Figure 7.2). Here no depletion is clearly evident and TEC roughness is barely noticeable during the scintillations from 0400–0530 UT (2300–0030 LT). In this case, the satellite undergoes more complicated motion relative to Ancon and does not stay close to any nearby field line for a substantial length of time as plumes pass. Some combination of changing satellite elevation and ionospheric conditions is likely responsible for the "bump" in TEC between 0200 and 0400 UT. We observed similar bumps of about 10 TECU prior to this day, on 08–09 April (TEC variations and scintillations prior to the bump) and on 09–10 April (no scintillations). The bump, however, did not appear prominently in data we examined for the following week (15–16 April and 16–17 April).

Figure 7.2 also illustrates some data quality issues. Several "glitches" in phase TEC are evident in the figure: before 0000 UT, just after 0100 and also around 0430. These glitches repeat from night to night throughout the campaign, sometimes more

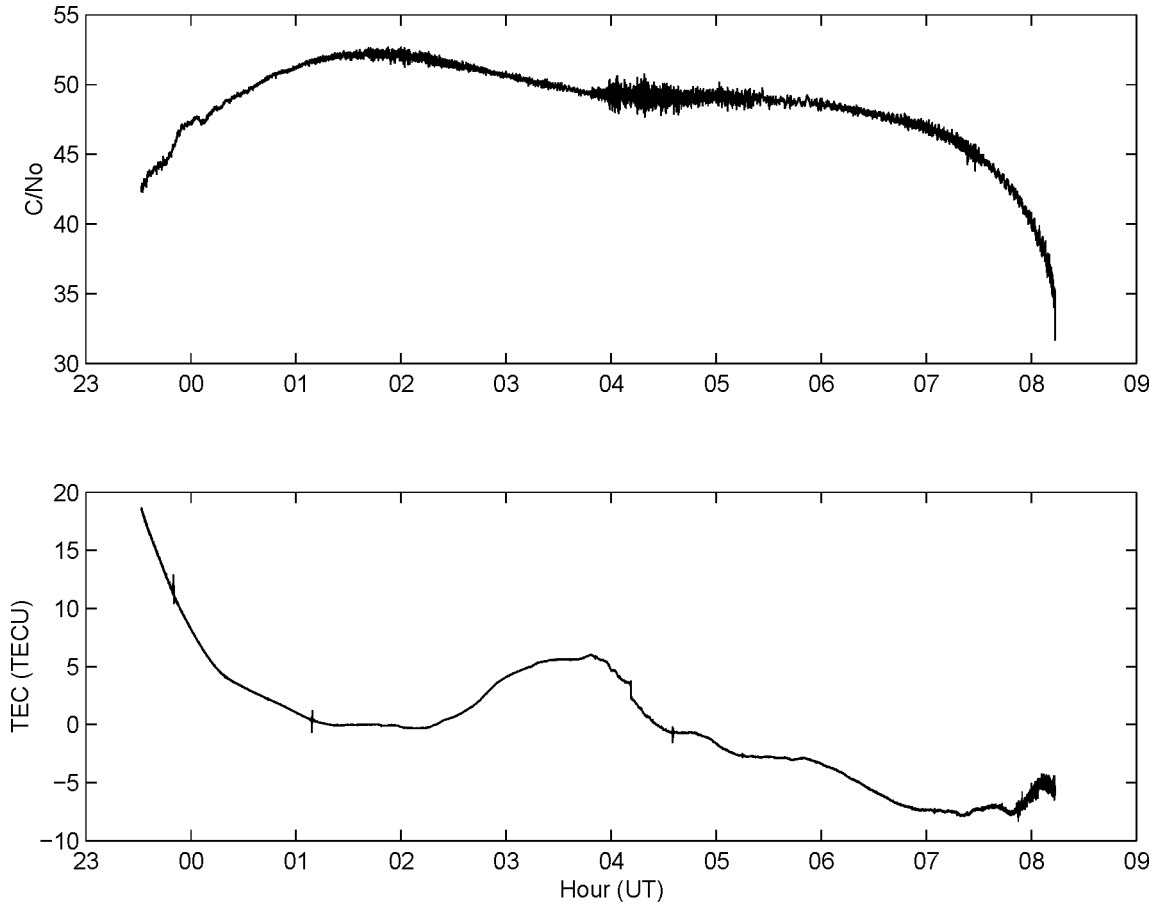

Figure 7.2: Simultaneous amplitude and total electron content (TEC) observations from Ancon for PRN 5, 10–11 April 1997. Same format as Figure 7.1.

evidently and sometimes less evidently, appearing about four minutes earlier in time from day to day. The consistent shifting in accord with the 12 sidereal hour orbits of the GPS satellites suggests that the glitches come from stationary nearby objects, either highly localized multipath or signal blockage. Other researchers have observed similar glitches in IGS data (J. Aarons, private communication, 1997). Also, there is a downward jump in TEC just after 0400 UT which could be a cycle slip. Finally, when GPS signal strength gets low and the satellites are near the horizon the TEC measurements become noisy, as both Figure 7.1 and Figure 7.2 indicate. The glitches, jumps and measurement scatter influence both variance and derivative measures of TEC fluctuation strength.

Figure 7.3 compares various measures of TEC fluctuations for PRN 26 on 10–11 April 1997. The "simulated IGS data" result from averaging the last 10 samples of phase TEC data of every 30 samples of measurements to come up with equivalent data at 30 seconds per sample. The true IGS stations give data at one sample every 30 seconds, and employ only 10 seconds' worth of phase measurements internally to calculate phase related output quantities [*Aarons et al.*, 1997]. Actually, the process used consists of somewhat more than simple averaging: "The receivers are configured to smooth the SNR and pseudorange data over 30-second intervals, and to fit (least-squares) the phase data over 10-second intervals" [*Pi et al.*, 1997]. Unfortunately, the details of the fitting process are proprietary. Also, that the fitting process can be replicated with one second per sample data when the receiver's internal sampling rate may be higher is not clear. Consequently, we adopt the simple averaging process for comparisons.

For this figure, the rate of TEC index (ROTI), the standard deviation of $d\text{TEC}/dt$ (as calculated by simple differencing and expressed in TECU/min), covers five minute

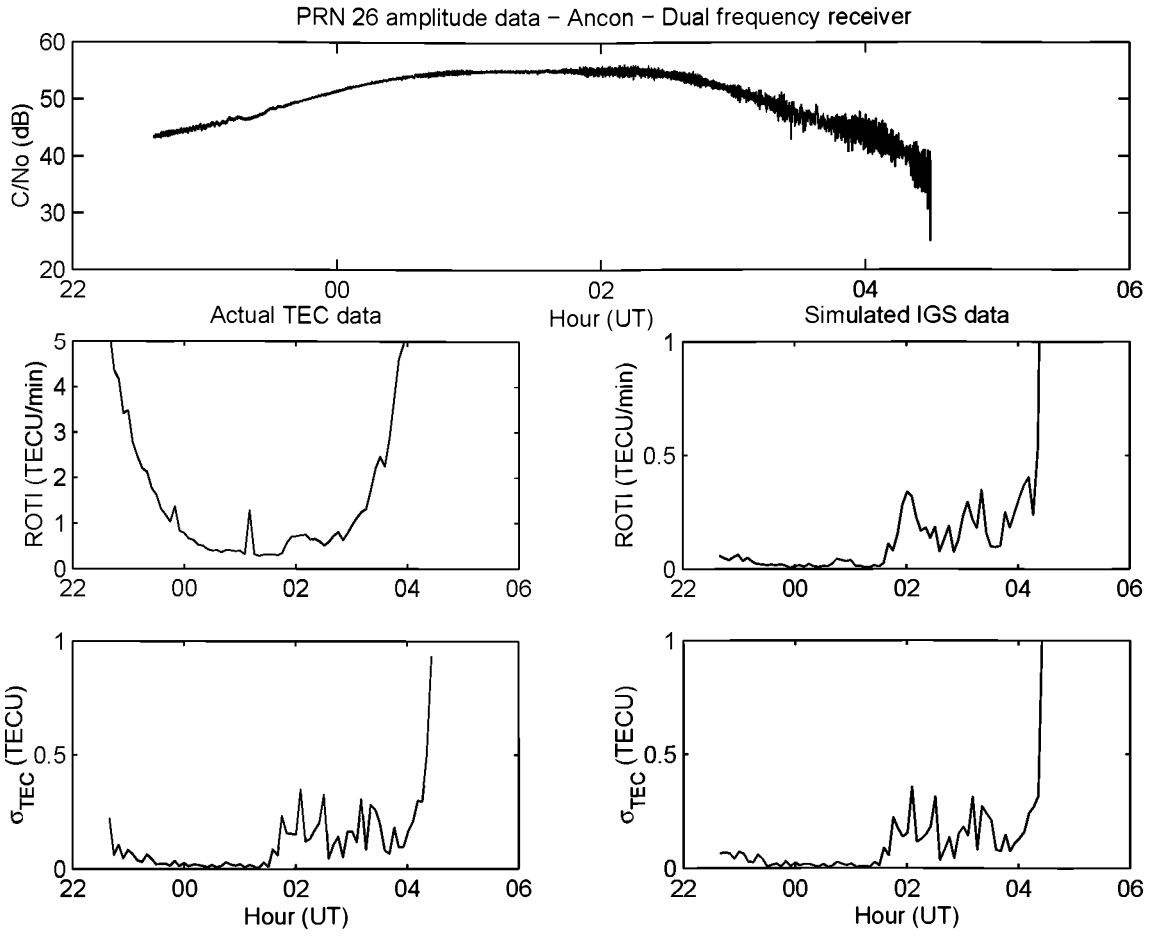

Figure 7.3: Comparative measures of TEC fluctuation strength from PRN 26 data at Ancon, 10–11 April 1997. Here we compare the two TEC fluctuation indices, ROTI and σ_{TEC}, with each other using both simulated IGS data and actual data. The top panel reproduces the amplitude data for comparison. "Actual TEC data" are sampled at one second intervals while the "simulated IGS data" are 30 seconds per sample (see text). Note the different vertical scale in the ROTI graph for the actual data.

intervals as in the work of *Pi et al.* [1997]. The standard deviation σ_{TEC} also covers five minute blocks of data. Prior to computing σ_{TEC} we detrend the phase TEC data by high pass filtering. The high pass filter is a fourth order Butterworth design with a cutoff frequency that corresponds to a 25 minute period. We apply the same processing to both the simulated IGS data and the actual data, adjusting the filter coefficients to compensate for the change in sampling rate.

Except for the ROTI of the actual data, all measures show a similar pattern, the onset of TEC fluctuations just prior to 0200 UT. These TEC fluctuations then continue until the satellite sets, at which point all measures exhibit a large, transient value. This pattern of TEC fluctuations matches the onset of amplitude scintillations around 0200 UT and their subsequent continuation until the satellite sets. The problems with the ROTI for the actual data probably derive from scatter in the TEC measurements. Hence a relatively high average ROTI exists even when scintillations are not present, as compared to the ROTI of the smoothed data. Certainly, averaging the data over part of the 30 second interval is a form of low pass filtering which reduces the high frequency measurement scatter. So the simulated IGS data better reflect the true TEC irregularities rather than the scatter.

Figure 7.4 illustrates a similar comparison of TEC fluctuation measures for PRN 5 on 10–11 April 1997. Here we see the effects of the data glitches on all measures. In fact, the glitches appear to be the predominant source of TEC fluctuations. Except for the ROTI of the one sample per second data, however, all of the indicators of TEC fluctuations again reflect the period of weak amplitude scintillations (scintillation index ≤ 0.1) which last from about 0400 to 0530 UT. Interestingly, the ROTI of the smoothed data actually appears to track the amplitude scintillations more closely than the two σ_{TEC} measures. For example, the σ_{TEC} values die out before 0500 UT,

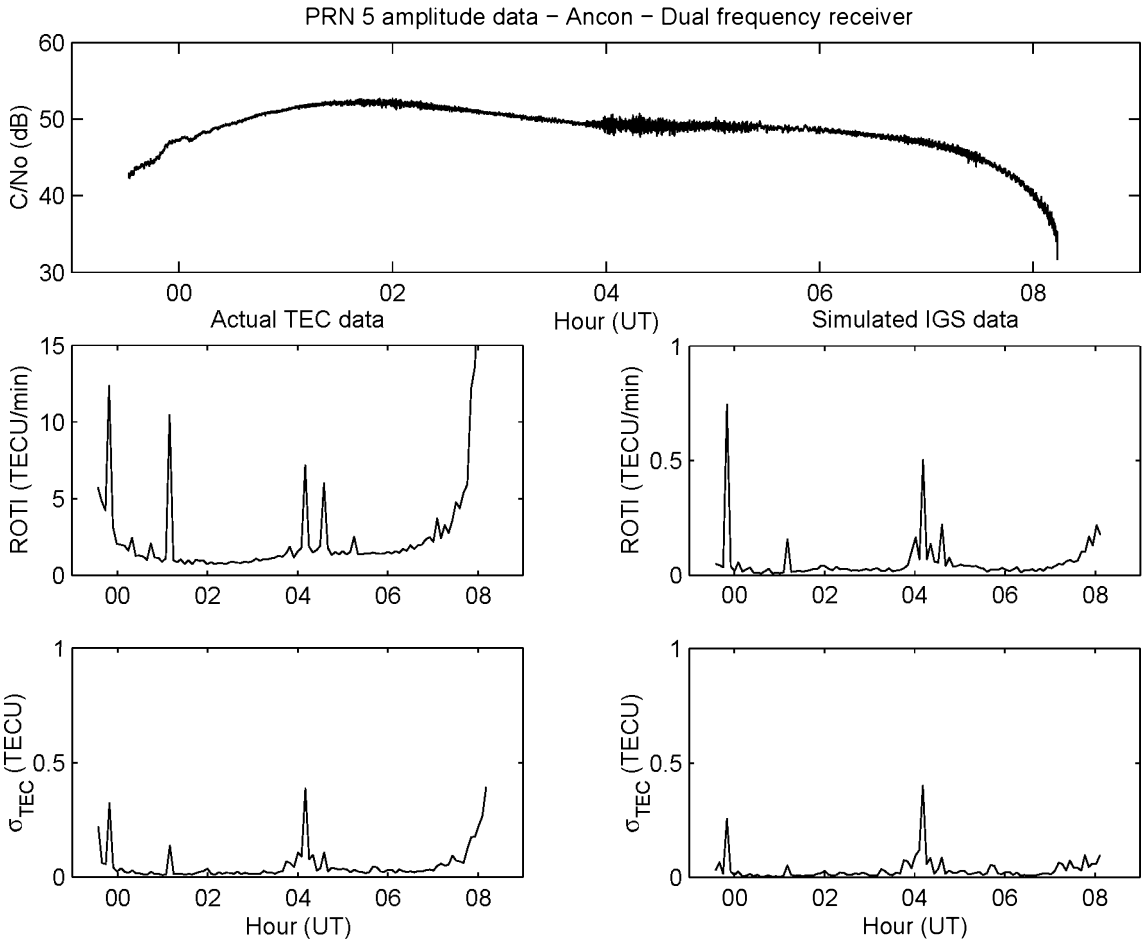

Figure 7.4: Comparative measures of TEC fluctuation strength from PRN 5 data at Ancon, 10–11 April 1997. Same format as Figure 7.3. Again, note the difference in vertical scale of the ROTI for the actual data case.

while the ROTI of the simulated IGS data drops off more slowly until 0530–0600, when it finally merges into the background level.

From these examples and others, then, we conclude that the more useful of the indices we have selected for TEC fluctuations are ROTI for the simulated IGS data and σ_{TEC} for either type of data. We should also like to be able to process the TEC data in such a manner as to reduce the effects of data glitches and cycle slips. Rather than adopt an additional TEC fluctuation measure, such as that of *Musman et al.* [1997], where outlying slopes are rejected from the slope calculations over the measurement interval, we shall simply restrict our comparisons to portions of the TEC data which do not contain glitches for the most part. This approach would not be helpful for more automated data processing programs, however.

7.4 Case Studies

7.4.1 Data

Now we consider all of the cases from the April 1997 campaign where we observed amplitude scintillations and TEC fluctuations. Three nights out of the April campaign had scintillations while both scintillation monitors and the GPS TEC receiver were operating: 08–09 April, 10–11 April and 16–17 April. On each of these nights, scintillations predominantly affected three satellites: PRNs 5, 9 and 26. Figure 7.5 illustrates the scintillations observed on these three satellites' signals on 08–09 April by the eastern scintillation monitor. The paths of the satellites essentially repeat from night to night over short periods of observation, so all three nights on which scintillations occurred have similar patterns of ionospheric sampling by the three satellites.

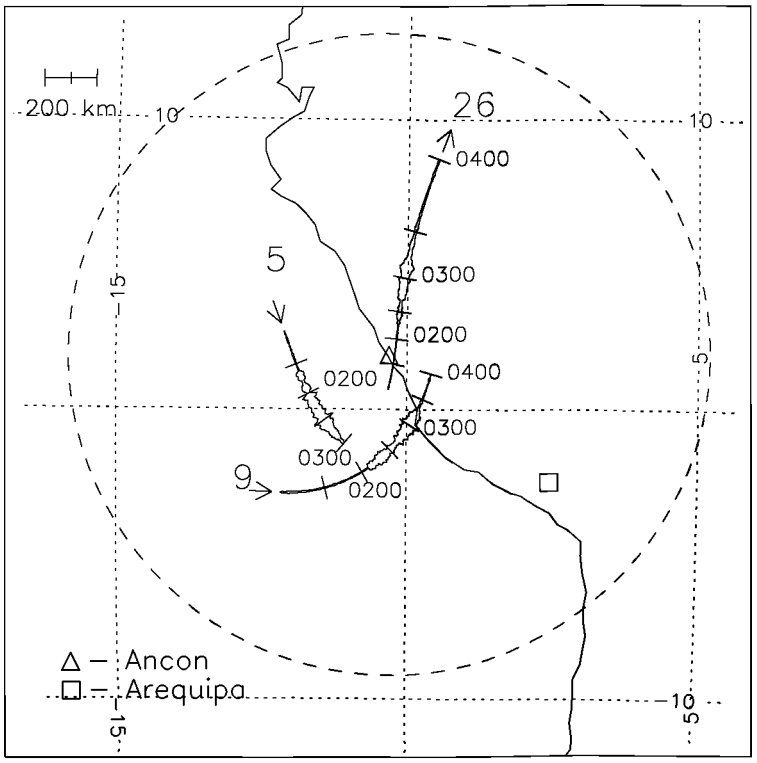

Figure 7.5: Scintillation map from Ancon, 09 April 1997. These traces mark the 350 km ionospheric intersections of the lines of sight to PRNs 5, 9 and 26. The width of the traces indicates the scintillation index. Time ticks denote half hour data segments and all labeled times are UT. For reference, tick width corresponds to a scintillation index of 0.4. Overlaid coordinates are geomagnetic and the dashed circle indicates the 350 km altitude visibility limit at Ancon for 10° elevation.

General characteristics of the irregularities observed by PRNs 5, 9 and 26 follow. All of the amplitude scintillations were weak with scintillation indices m of 0.3 or less, typically. In all cases, amplitude scintillations were accompanied by TEC fluctuations, although when the scintillations were very weak ($m \leq 0.1$), the TEC fluctuation measures barely increased over the background level. The converse is not true, however. There are periods, usually prior to the onset of scintillations, where apparently geophysical TEC fluctuations (i.e., not glitches) exist without concurrently measurable scintillations. Finally, the trend of the TEC fluctuation measures (ROTI for simulated IGS data and σ_{TEC}) generally follows the trend of the scintillation index, although there are exceptions that we will note.

We will go sequentially by date in our discussion. On the first night of activity, 08–09 April 1997, we observe a patch of scintillations to drift from west to east past PRNs 5, 9 and 26 in succession (Figure 7.6; also see Figure 7.5). By the time the patch reaches PRN 26, the scintillations are noticeably weaker, especially if we factor in the satellite's low elevation angle from 0330 UT onward. Also, the onset of the scintillations, when the eastward edge of the patch crosses the line of sight, becomes much less abrupt in going from PRN 9 to PRN 26. In general, the TEC fluctuation measures track the scintillation index. Both ROTI and σ_{TEC} come out to be roughly twice m in value, but σ_{TEC} is usually the lower of the two. Notably, the TEC fluctuations appear to anticipate the onset of scintillations by 15–20 minutes for PRN 26.

Moving on to 10–11 April and Figure 7.7, we see a different pattern of activity. Scintillations first appear on PRN 9 at about 0100 UT. About this time, when PRNs 5 and 9 are close to the same field line, PRN 5 sees a weak patch of scintillations with $m = 0.05$ (not shown in Figure 7.7; see Figure 7.2). By 0200, PRN 26 shows

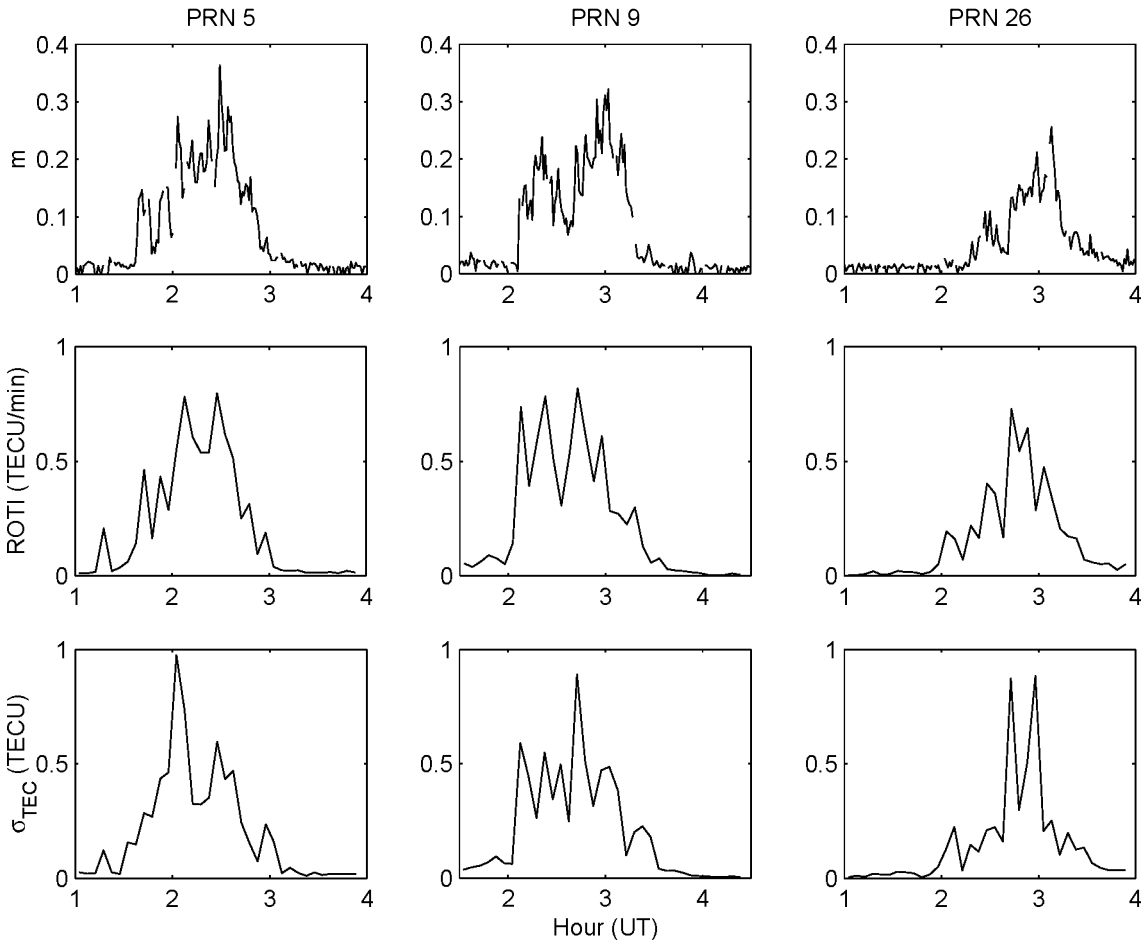

Figure 7.6: Comparison of scintillation index m and TEC fluctuation measures at Ancon for 09 April 1997 UT. The rate of TEC index (ROTI) uses simulated 30 second per sample data while the standard deviation σ_{TEC} employs the actual one second per sample data.

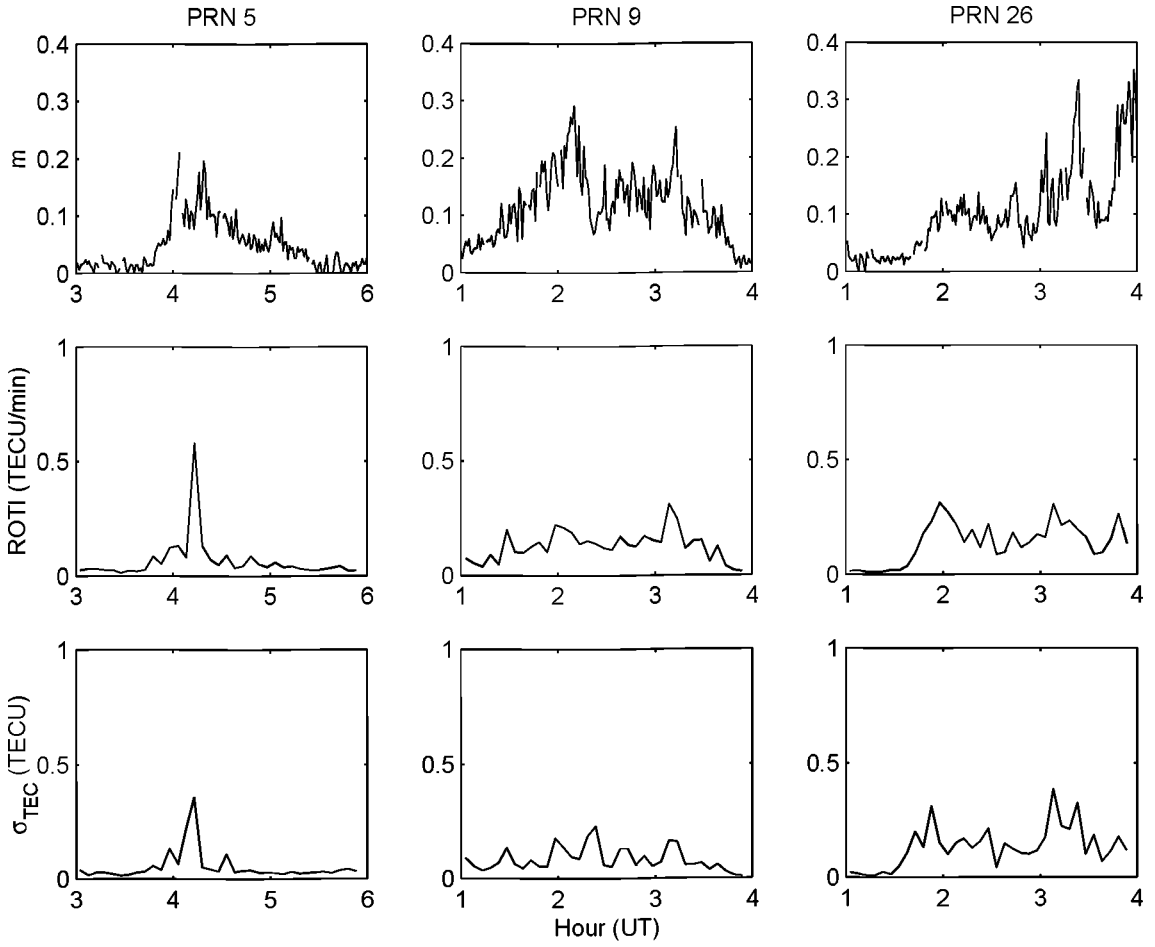

Figure 7.7: Comparison of scintillation index m and TEC fluctuation measures at Ancon for 11 April 1997 UT. Same format as Figure 7.6. Note that scintillation onset for PRN 9 is not shown because there was a glitch in the phase TEC measurement at that time (just prior to 0100 UT). Between 0400 and 0500, PRN 5 phase TEC data had two glitches, as discussed earlier. Also, note that the selected PRN 5 scintillation data occur later than those of the other satellites.

scintillations which continue until it sets at 0430 UT (Figure 7.1). Finally, a weak patch of scintillations with $m = 0.1$ appears from 0350–0530 UT on PRN 5, a patch that does not appear to have influenced any other satellites. We note in passing that these late, post 2300 LT irregularities may be associated with a coronal mass ejection that impacted the earth's magnetosphere on 10 April 1997 and the subsequent geomagnetic disturbance with $K_p \sim 7$ early in UT on 11 April [*Biondi and Meriwether*, 1997].

Generally, the amplitude scintillations and TEC fluctuations again corroborate. Here the ROTI still appears to be about twice the scintillation index m. The standard deviation of TEC (σ_{TEC}) only comes to about half the value of ROTI for PRNs 5 and 9, though, a substantially lower value. Only for PRN 26 do the rate of TEC index (ROTI) and σ_{TEC} become comparable. Qualitatively, the TEC fluctuation indices crudely follow the trend of the scintillation index. Although the indices do not follow some details closely, we should remember the 5 minute time scale of averaging for both ROTI and σ_{TEC}, as opposed to the one minute averages for computing m. The longer time scale for averaging means that the TEC fluctuation indices cannot reflect certain short time scale features, like the dip in m shortly after 0200 UT for PRN 9, perhaps. Note, however, that the large spike in the TEC fluctuation indices shortly after 0400 UT for PRN 5 relates to the "jump" in TEC, the possible cycle slip discussed earlier.

Finally, we turn to Figure 7.8 for the night of 16–17 April 1997. These scintillations appear to be the result of a single patch drifting from west to east, judging by the onset on PRN 5 toward the west, prior to scintillations on PRNs 9 and 26 in the vicinity of the Ancon field line. (Figure 7.5 still holds for the relative positions of the puncture points, although the applicable times on 16–17 April should be about one half hour earlier than the times indicated in that figure.) The general results, such as trend

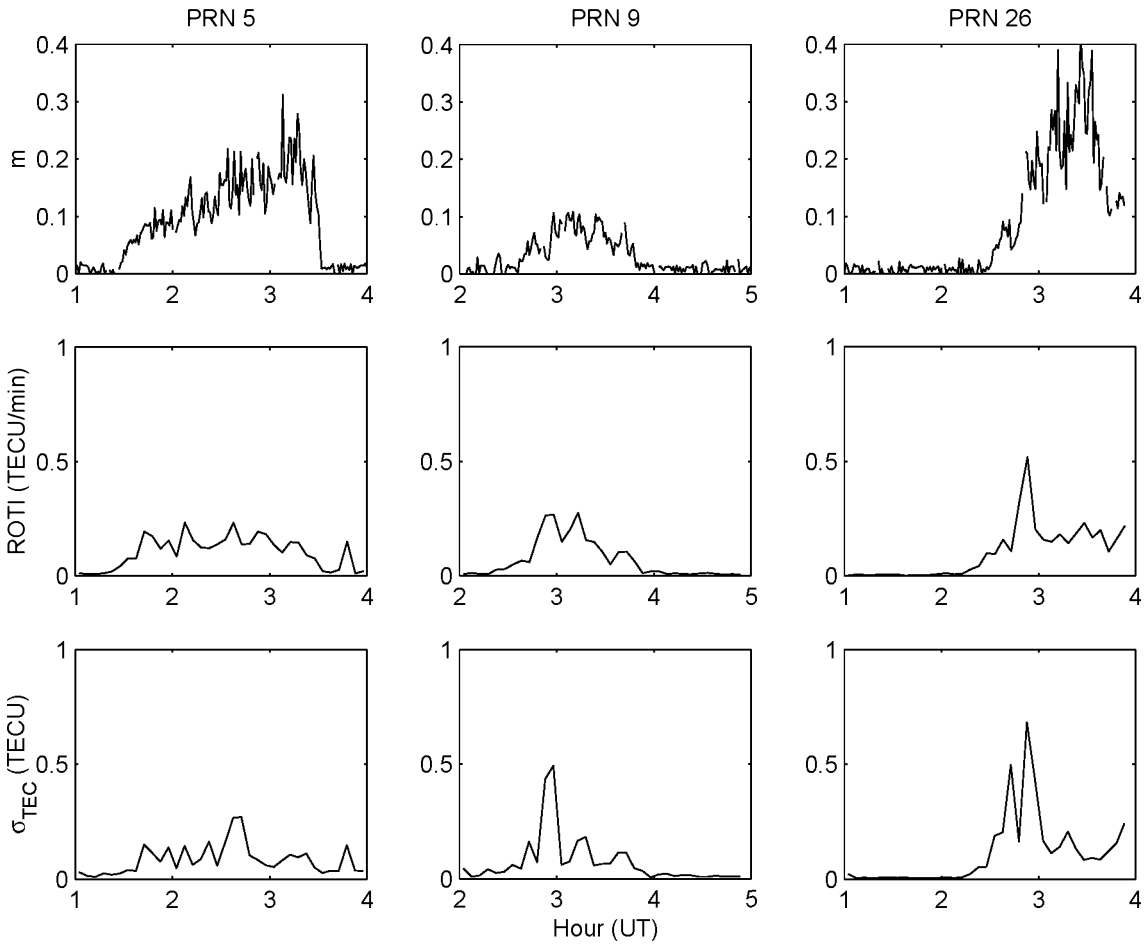

Figure 7.8: Comparison of scintillation index m and TEC fluctuation measures at Ancon for 17 April 1997 UT. Same format as Figure 7.6.

following, ROTI being approximately twice m and σ_{TEC} often coming out lower than ROTI, still hold. More interesting are the anomalies. First, the scintillation index consistently ramps up for PRN 5 during 0130–0315 UT; meanwhile, ROTI levels off at a value consistent with $m \approx 0.1$, judging by previously established behavior. Moreover, if anything, ROTI and σ_{TEC} begin to decrease before the scintillations cease on PRN 5. Also, on PRN 26, only for the early times around 0300 UT do the TEC fluctuation measures reflect the relatively "high" levels of amplitude scintillations observed.

7.4.2 Summary

Overall, these case studies suggest that equatorial TEC fluctuations often, but not always, have associated amplitude scintillations. Further, even TEC data with sampling as coarse as 30 seconds per sample exhibits some correlation between its fluctuations and amplitude scintillations. The rough correspondence for these weak scintillations is that the scintillation index $m \approx 0.5$ ROTI, where ROTI is the rate of TEC index for 30 second sample data, expressed in TECU/min. The relationship of m to σ_{TEC}, the standard deviation of TEC for 1 second sample data and expressed in TECU, is less determinate, but m appears to be roughly proportional to σ_{TEC} with a proportionality constant between 0.5 and unity.

The instances where TEC fluctuations do not follow the amplitude scintillations well provide an interesting study. Without examining the time series data in detail yet, we may hypothesize that the discrepancy relates to sensitivity to different spatial scales of irregularities. Clearly, the standard deviation of TEC (σ_{TEC}) responds to irregularities of all scale sizes, from the low frequency cutoff of the detrending filter down to the resolution limit imposed by the sampling rate. The variance of $d\mathrm{TEC}/dt$

(ROTI, the rate of TEC index) tends to emphasize the smaller scale sizes, again with sampling limitations. On the other hand, weak amplitude scintillations predominantly reflect a narrow range about one particular scale size, the Fresnel scale $\sqrt{2\lambda z}$, where λ is the free space wavelength of the radio signal and z is the line of sight distance to the irregularities. Thus, the TEC fluctuation measures can indicate the presence of irregularities at scales that do not generate scintillations.

Looking at the time series data, we examine the case that appeared on PRN 26 on 09 April 1997, when significant TEC fluctuations appeared 15–20 minute prior to the onset of scintillations. Figure 7.9 shows the PRN 26 TEC and amplitude data alongside the earlier PRN 5 data for comparison. The 3 TECU depletion that appears prior to 0200 UT on PRN 5 is notably absent on PRN 26, a half hour later and a couple hundred kilometers farther east. Meanwhile, the depletion structure appearing between 0200 and 0300 on PRN 5 appears to PRN 26 from 0245–0320. (The difference in apparent widths results from the difference between the satellites in the magnetic eastward velocity components of their ionospheric puncture points.) In going from PRN 5 to PRN 26, then, the first depletion at 0145 apparently fills in by 0230. Although the PRN 26 data show TEC fluctuations between 0200 and 0230 UT, they definitely include less fine scale structure than the later observations, supporting the hypothesis that decay of the small scale irregularities accounts for the discrepancy between the TEC fluctuation measures and amplitude scintillations around this time.

On 17 April, we see another example of a case where the character of the irregularities changed as the ionosphere drifted eastward. Figure 7.10 presents data from PRNs 5 and 9 on this date. Here, the PRN 5 data show little evidence of a depletion, although they do display fairly shallow irregularities of various scales. On the other

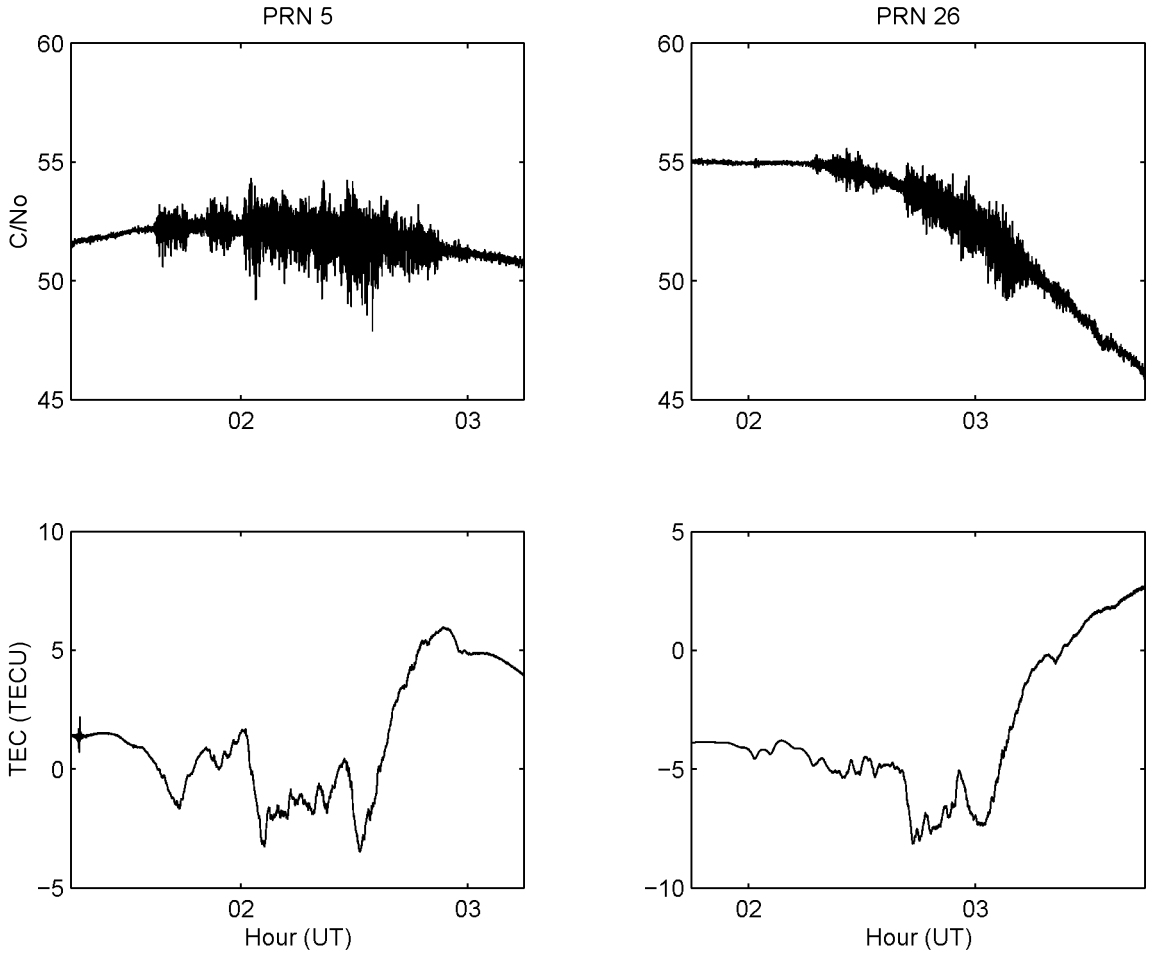

Figure 7.9: Observations of changes in drifting irregularity structure on 09 April 1997. These measurements use one second samples. See Figure 7.5 for relative positions of the satellite lines of sight.

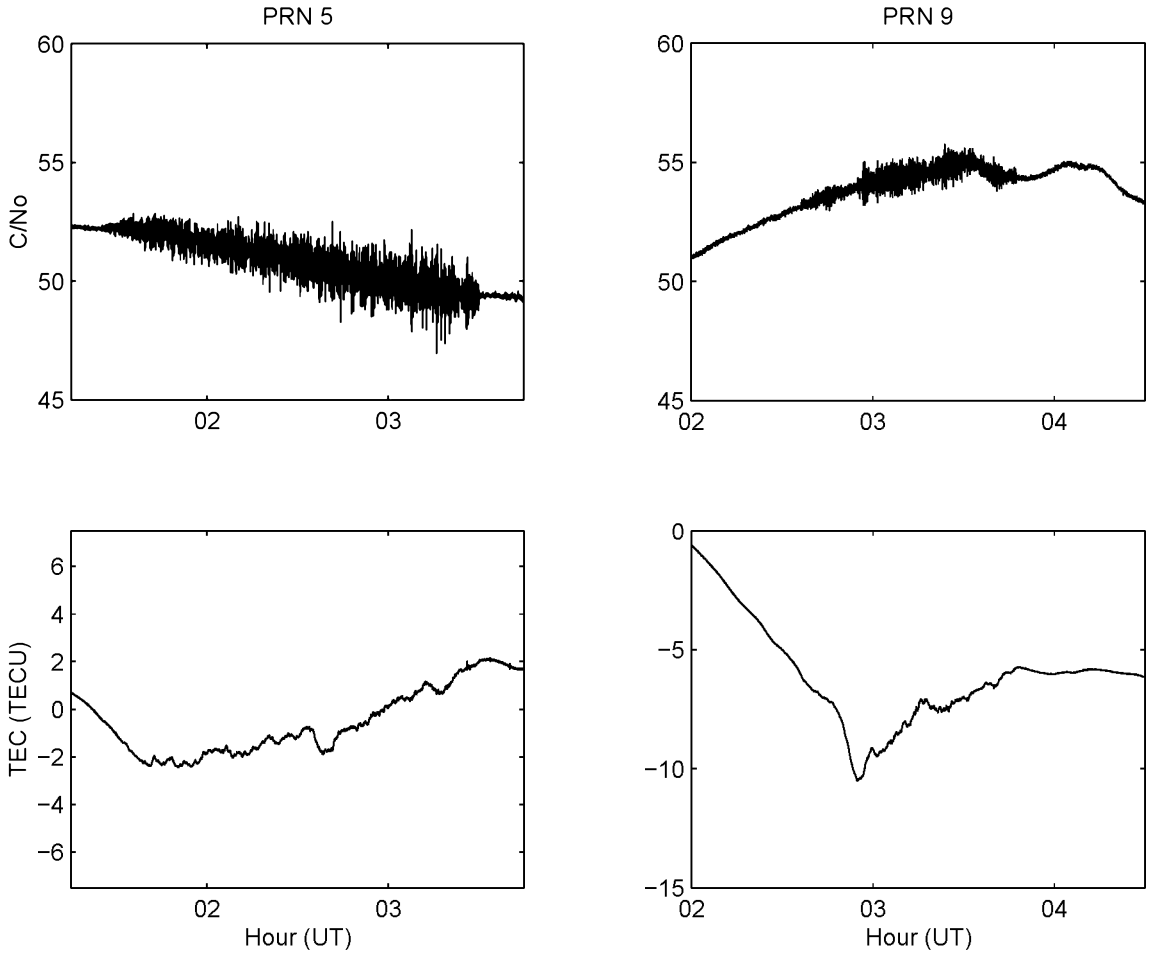

Figure 7.10: Observations of change in drifting irregularity structure on 17 April 1997. These measurements use one second samples.

hand, the PRN 9 data contain a definite depletion feature a little before 0300 UT. Unfortunately, there are few common features between the TEC graphs to use for landmarks, unlike the preceding example. Nonetheless, the graphs give the appearance that some depletion growth has occurred between the satellites. Also, this night is the example where the scintillation index m ramped up slowly on PRN 5 while the TEC fluctuation measures remained relatively constant, suggesting a change in the distribution of scale sizes over time. Specifically, we surmise that we observe energy cascade to the Fresnel scale as the depletion bubbles or plumes develop.

Of course, discussion of the detailed mechanics of depletion growth or decay are beyond the scope of this dissertation. Still, the fact that we observed two likely cases of depletion evolution with time in a very short data set, with few nights of scintillations, indicates that such observations might not be uncommon.

7.5 Theoretical Relationships

As mentioned in the introductory part of this chapter, scintillation index and phase fluctuation strength should be related through the power spectrum of the phase screen's phase. The purpose of this section will be to explore that relationship. Much of the discussion will parallel that of *Rino* [1979*a*], although in a simplified formulation so that the relationships will become more apparent. We emphasize that this discussion applies only to weak scintillations and that in the case of strong scintillations it is much more difficult to obtain analytic results [*Rino*, 1979*b*].

From Chapter 4, the power spectra for intensity ($\Phi_{\mathcal{I}}$) and received phase (Φ_S) relate to the power spectrum of phase at the phase screen (Φ_ϕ) according to

$$\Phi_{\mathcal{I}}(q) = 4\Phi_\phi(q)\sin^2\left(\frac{q^2 {r_F}^2}{4\pi}\right), \tag{7.10}$$

$$\Phi_S(q) = \Phi_\phi(q) \cos^2\left(\frac{q^2 {r_F}^2}{4\pi}\right), \tag{7.11}$$

where q is the horizontal wave number across the phase screen and r_F is the Fresnel radius. These equations apply when the equivalent one dimensional phase screen is perpendicular to the line of sight. For other geometries, see the more detailed formulas of *Rino* [1979*a*]. Also, these relationships become modified when the layer of irregularities that the phase screen represents is thick [*Salpeter*, 1967; *Yeh and Liu*, 1982]. A thick layer of irregularities mitigates the effects of Fresnel filtering [*Rufenach*, 1972].

The spectral form of the equivalent phase screen is generally a power law, q^{-p} [*Rufenach*, 1972; *Yeh and Liu*, 1982; *Basu and Basu*, 1993]. Measurements at Ancon and other equatorial stations suggest that the spectral index p is near 3, usually in the range of 2.5 to 3.2 [*Rino*, 1979*a*; *Basu et al.*, 1986; *Basu and Basu*, 1993]. Figure 7.11 shows several TEC power spectra from the April 1997 campaign at Ancon where p is nearer to 2.6. We adopt a simple, general power law spectral model with an outer scale cutoff for the phase fluctuations at the screen,

$$\Phi_\phi(q) = \frac{C}{({q_0}^2 + q^2)^{p/2}}, \tag{7.12}$$

where C is a constant that determines the strength of the phase fluctuations (C depends on the root-mean-square electron density fluctuations in the ionosphere) while $q_0 = 2\pi/\ell_0$ represents the outer scale of power law applicability. For $q \gg q_0$, $\Phi_\phi(q) \approx Cq^{-p}$. At the opposite extreme of wave numbers, $\Phi_\phi(q) \approx C{q_0}^{-p}$. When converting between wave number q and temporal frequency ω, we shall assume a constant drift V of the phase screen irregularities perpendicular to the line of sight so that $\omega = qV$.

Instruments and data processing introduce modifications to the observed power

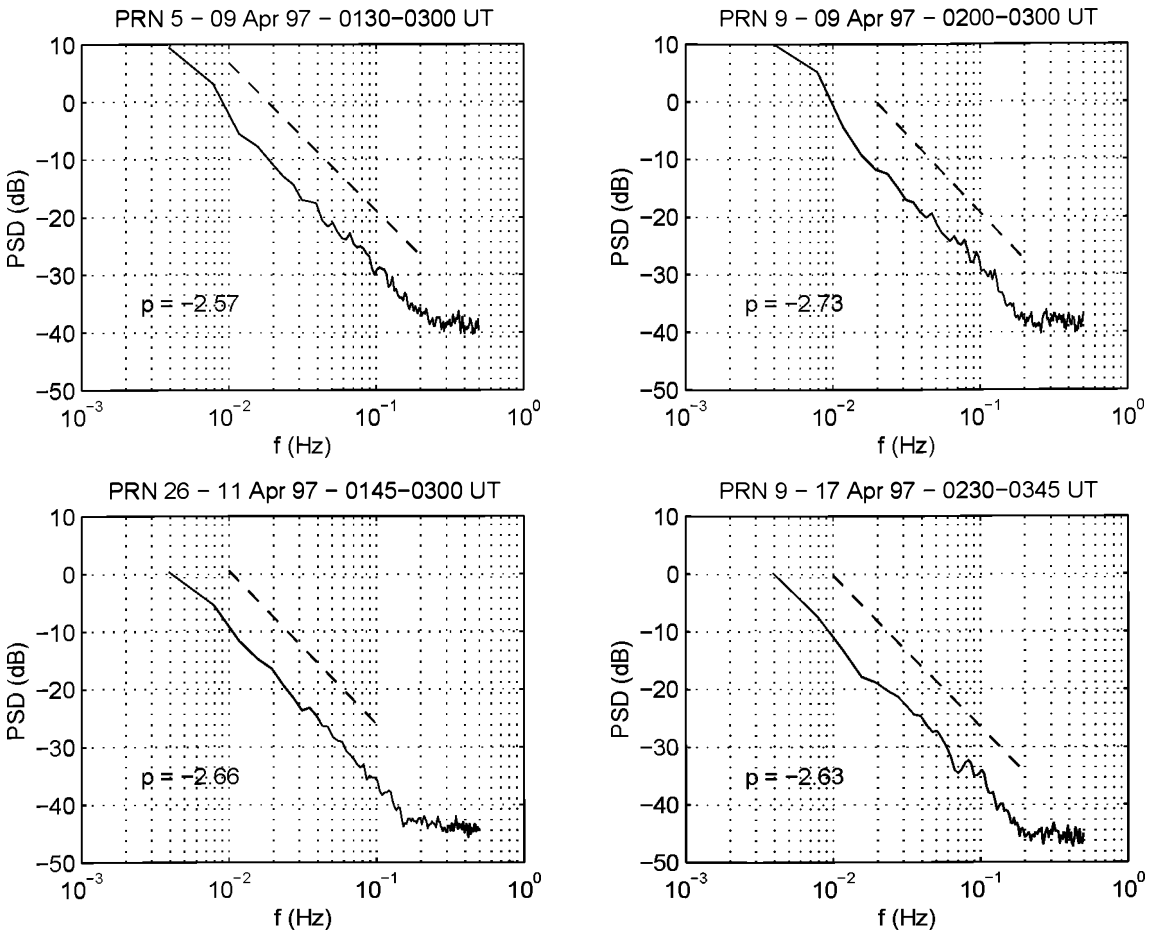

Figure 7.11: Sample TEC fluctuation power spectra at Ancon, Peru from April 1997 campaign. Each panel in this figure includes the power spectrum of detrended phase TEC data (solid line), as calculated by Welch's method, and a power law fit to part of the spectrum (dashed line), which is vertically offset by 10 dB for clarity. The power law exponent p labels each panel. Fitting employs a least squares procedure applied to the logarithms of the frequency and the spectrum. The detrending filter cutoff is approximately 10^{-3} Hz (25 minute period).

spectra. Assuming that the modifications are linear, we represent them by instrument transfer functions $H_{\mathcal{I}}(\omega)$ and $H_S(\omega)$, respectively the intensity and phase measurement transfer functions. Normally, we will perform calculations in the spatial frequency domain and substitute qV for ω in the transfer functions. The measured power spectra become

$$\widehat{\Phi}_{\mathcal{I}}(q) = 4\Phi_\phi(q)\,|H_{\mathcal{I}}(qV)|^2\,\sin^2\left(\frac{q^2{r_F}^2}{4\pi}\right), \tag{7.13}$$

$$\widehat{\Phi}_S(q) = \Phi_\phi(q)\,|H_S(qV)|^2\,\cos^2\left(\frac{q^2{r_F}^2}{4\pi}\right), \tag{7.14}$$

where the hats denote measured quantities. More commonly, we shall treat measurement transfer functions as ideal filters and introduce appropriate spatial frequency cutoffs into the limits of integration, with notation for the cutoffs to be defined as needed.

Ideally, without measurement effects, the scintillation index m and standard deviation of observed phase σ_S are computed from

$$m^2 = \int_{-\infty}^{\infty} dq\ \Phi_{\mathcal{I}}(q), \tag{7.15}$$

$${\sigma_S}^2 = \int_{-\infty}^{\infty} dq\ \Phi_S(q). \tag{7.16}$$

Also,

$${\sigma_{dS}}^2 = \left\langle \left(\frac{dS}{dx}\right)^2 \right\rangle = \int_{-\infty}^{\infty} dq\ q^2\Phi_S(q), \tag{7.17}$$

which derives from the fact that the power spectrum of dS/dx is $q^2\Phi_S(q)$, by theorems of Fourier analysis. The quantity ${\sigma_{dS}}^2$ relates to the rate of TEC index (ROTI).

Evaluating the integrals directly is difficult. The integral for modulation index can be worked out if p is exactly -3, however [*Rufenach*, 1975; *Costa and Kelley*, 1976]. More generally, we follow *Rino* [1979*a*] and approximate the scintillation index

m by

$$m^2 = 4C \int_{-\infty}^{\infty} dq\ q^{-p} \sin^2 \left(\frac{q^2 {r_F}^2}{4\pi} \right). \tag{7.18}$$

This approximation relies on $\pi {r_F}^2 / {\ell_0}^2$ being much, much less than unity so that the $\sin^2$ term is approximately zero when $\Phi_\phi(q) \approx C q_0^{-p}$. For our case, $r_F \sim 300$ m while the outer scale ℓ_0 of power law applicability in ionospheric irregularities can be of the order of 10 km [*Rino*, 1979*a*].

For the root-mean-square phase deviation ${\sigma_S}^2$, we may approximate the integral by noting that, for $\pi {r_F}^2 / {\ell_0}^2 \ll 1$, the bulk of the area under the curve (i.e., the bulk of the integral) occurs when $\cos^2(q^2 {r_F}^2/(4\pi)) \approx 1$ [*Rino*, 1979*a*]. Consequently, diffraction effects on phase may be neglected and

$${\sigma_S}^2 \approx {\sigma_\phi}^2 = \int_{-\infty}^{\infty} dq\ \Phi_\phi(q), \tag{7.19}$$

where ${\sigma_\phi}^2$ is the variance of phase at the screen. Similarly,

$${\sigma_{dS}}^2 \approx \int_{-\infty}^{\infty} dq\ q^2 \Phi_\phi(q), \tag{7.20}$$

although this approximation is less accurate because the q^2 term reduces the area under the curve at low frequencies and emphasizes the high frequency portion of the phase power spectrum where the $\cos^2$ term oscillates. In fact, integral (7.20) does not converge for the assumed form of $\Phi_\phi(q)$ if the spectral index p is less than 3, and it diverges logarithmically at high wave numbers when $p = 3$.

Practically speaking, however, high frequency divergence of (7.20) is not a problem. Sampling of phase TEC at a low rate, as in the IGS data, imposes a high frequency cutoff at the Nyquist frequency (assuming that aliasing in the phase measurement spectrum is negligible in the IGS receivers). If T is the sampling interval of the receiver, the cutoff frequency expressed in radians per second is $\omega_c = \pi/T$, which

yields a cutoff wave number of $q_c = \pi/(VT)$, after accounting for the drift velocity V. With this high frequency cutoff imposed,

$$\hat{\sigma}_{dS}^2 \approx \int_{-q_c}^{q_c} dq\ q^2 \Phi_\phi(q), \tag{7.21}$$

where the hat denotes a measured quantity with inherent spectral limitations. If $V = 100$ m/s and $T = 30$ s, $q_c = 1.05 \times 10^{-3}$ m^{-1}. With $r_F = 300$ m, a typical value at the L1 frequency for F region irregularities, ${q_c}^2 {r_F}^2/(4\pi) = 7.85 \times 10^{-3}$. Thus, the argument of the $\cos^2$ term in $\Phi_S(q)$ is much, much less than unity and $\Phi_S(q) = \Phi_\phi(q)$ within the range of wave numbers $|q| \leq q_c$ covered by the integral (7.21) to a high degree of accuracy.

Having made these approximations, we can evaluate the integrals (7.18), (7.19) and (7.21) to give m^2, ${\sigma_S}^2 \approx {\sigma_\phi}^2$ and $\hat{\sigma}_{dS}^2$, respectively. For the scintillation index,

$$m^2 = -\frac{C}{2} \frac{2^{(5-p)/2}}{{r_F}^{1-p}} \pi^{(1-p)/2} \Gamma\left(\frac{1-p}{2}\right) \cos\left(\frac{(1-p)\pi}{4}\right), \tag{7.22}$$

where $\Gamma(\ldots)$ is the gamma function and the power spectrum exponent is restricted to the range $1 < p < 5$ [*Gradshteyn and Ryzhik*, 1994, 3.823, p. 484] (following a suggestion by *Rino* [1979*a*]). Note that at $p = 3$ the gamma function has a pole, but the $\cos(\ldots)$ term approaches zero. The limit of this product of two terms exists and is -1.57, numerically (i.e., most likely $-\pi/2$).

For the variance of phase,

$${\sigma_\phi}^2 = C\sqrt{\pi}\, {q_0}^{1-p} \frac{\Gamma((p-1)/2)}{\Gamma(p/2)}, \tag{7.23}$$

with $p > 1$ [*Gradshteyn and Ryzhik*, 1994, 3.241.4, p. 340]. Note the explicit dependence on the outer scale via q_0. Finally, a crude estimate of the variance of the derivative of phase across the observation plane gives

$$\hat{\sigma}_{dS}^2 = 2C \int_0^{q_c} dq\ \frac{q^2}{({q_0}^2 + q^2)^{p/2}} \approx \frac{C}{{q_0}^p} \left(\frac{2{q_c}^3}{3} - \frac{p}{5} \frac{{q_c}^5}{{q_0}^2}\right), \tag{7.24}$$

where the fact that q_c/q_0 is of order unity hampers the attainment of accuracy in the approximation. Ordinarily, we will evaluate the integral numerically.

Of greater interest than the values m^2, ${\sigma_\phi}^2$ and $\hat{\sigma}_{dS}^2$ themselves are the interrelationships among them, particularly the ratios $m^2/{\sigma_\phi}^2$ and $m^2/\hat{\sigma}_{dS}^2$. From the above expressions,

$$\frac{m^2}{{\sigma_\phi}^2} = -\sqrt{2}\, 2^{p/2}\, \pi^{p/2-1} \left(\frac{\ell_0}{r_F}\right)^{1-p} \frac{\Gamma((1-p)/2)\cos((1-p)\pi/4)}{\Gamma((p-1)/2)/\Gamma(p/2)}, \tag{7.25}$$

where $\ell_0 = 2\pi/q_0$ is the outer scale length of power law applicability to the phase screen's phase. Also, because of the combined restrictions on evaluating the integrals that contribute to this result, $1 < p < 5$. To examine what value of m/σ_ϕ equation (7.25) predicts for GPS scintillations, we choose $r_F = 300$ m, $\ell_0 = 5$ km (near the low end of rocket observations of one dimensional vertical electron density power spectra [*Costa and Kelley*, 1976]) and $p = 3$. The result is $m/\sigma_\phi = 0.19$ rad^{-1}. To convert to m/σ_{TEC}, the ratio observed in the case studies, we must use the fact that 2π radians of phase advance at L1 corresponds to 1.173 TECU. Thus, the estimate predicts that $m/\sigma_{\mathrm{TEC}} = 1.0$ TECU^{-1}. This value jibes with the high end of the range of m/σ_{TEC} observed in the case studies. Also, m/σ_{TEC} is sensitive to the outer scale cutoff. In the above example, if ℓ_0 doubles in value to 10 km, while all other quantities remain the same, m/σ_{TEC} halves in value to 0.5 TECU^{-1}, the low end of the observed values.

Turning to the relationship between the scintillation index and ROTI, we investigate the ratio $m^2/\hat{\sigma}_{dS}^2$. From the earlier results, the desired ratio becomes

$$\frac{m^2}{\hat{\sigma}_{dS}^2} = -\sqrt{2}\,\pi^{(1-p)/2}\, \frac{2^{-p/2}}{{r_F}^{1-p}}\, \frac{\Gamma((1-p)/2)\,\cos((1-p)\pi/4)}{\int_0^{q_c} dq\; q^2\,({q_0}^2+q^2)^{-p/2}}. \tag{7.26}$$

Again, the restriction on the spectral index p is that $1 < p < 5$. Assuming that $T = 30$ s (measurement sampling period) and $V = 100$ m/s (perpendicular ionospheric drift) as before, with $r_F = 300$ m, $\ell_0 = 5$ km and $p = 3$, $m/\hat{\sigma}_{dS}$ evaluates to 436 m/rad.

Converting $\hat{\sigma}_{dS}$ into the root-mean-square deviation of the rate of change of TEC (i.e., converting into ROTI) by assuming that the drift speed remains constant yields $m/\mathrm{ROTI} = 0.39$, where ROTI is expressed in TECU/min. If the outer scale ℓ_0 increases to 10 km, m/ROTI changes to 0.21 min/TECU. These m/ROTI values are somewhat low according to the case study data but fall into the general range of values observed.

Figure 7.12 shows plots of both m/σ_{TEC} and m/ROTI, as calculated from formulas (7.25) and (7.26) for various values of outer scale (ℓ_0) and power law exponent (p). The caption lists the assumed values of the Fresnel radius r_F and perpendicular ionospheric drift V used to generate the figure. These graphs include the example values calculated above. Generally, $m/ROTI$ is about half the value of m/σ_{TEC} according to the simple model, a ratio that fits in with only some of the observations from the April 1997 campaign. Both m/σ_{TEC} and m/ROTI vary as ${r_F}^{p-1}$, so we may readily factor in dependence on the Fresnel radius.

The effect of drift velocity V on m/ROTI is less straightforward to analyze. Increasing V decreases the upper wave number cutoff q_c for a given sampling period, reducing the value of the integral in (7.26) and increasing m/ROTI overall. On the other hand, V also factors into the conversion from $\hat{\sigma}_{dS}^2$ to ROTI, with the effect that increasing V causes m/ROTI to decrease. These two effects tend to offset each other so that m/ROTI is relatively insensitive to V (Figure 7.13).

Note that we do not expect the low frequency cutoff imposed by detrending to play as significant a role as it does in the discussion of *Rino* [1979*a*]. In our case the satellites are not low earth orbit satellites and we therefore have the luxury of selecting much longer detrend periods. With the 25 minute detrend period applied to the σ_{TEC} calculation, the lower limit on q for integration is 4×10^{-5} m^{-1}, assuming

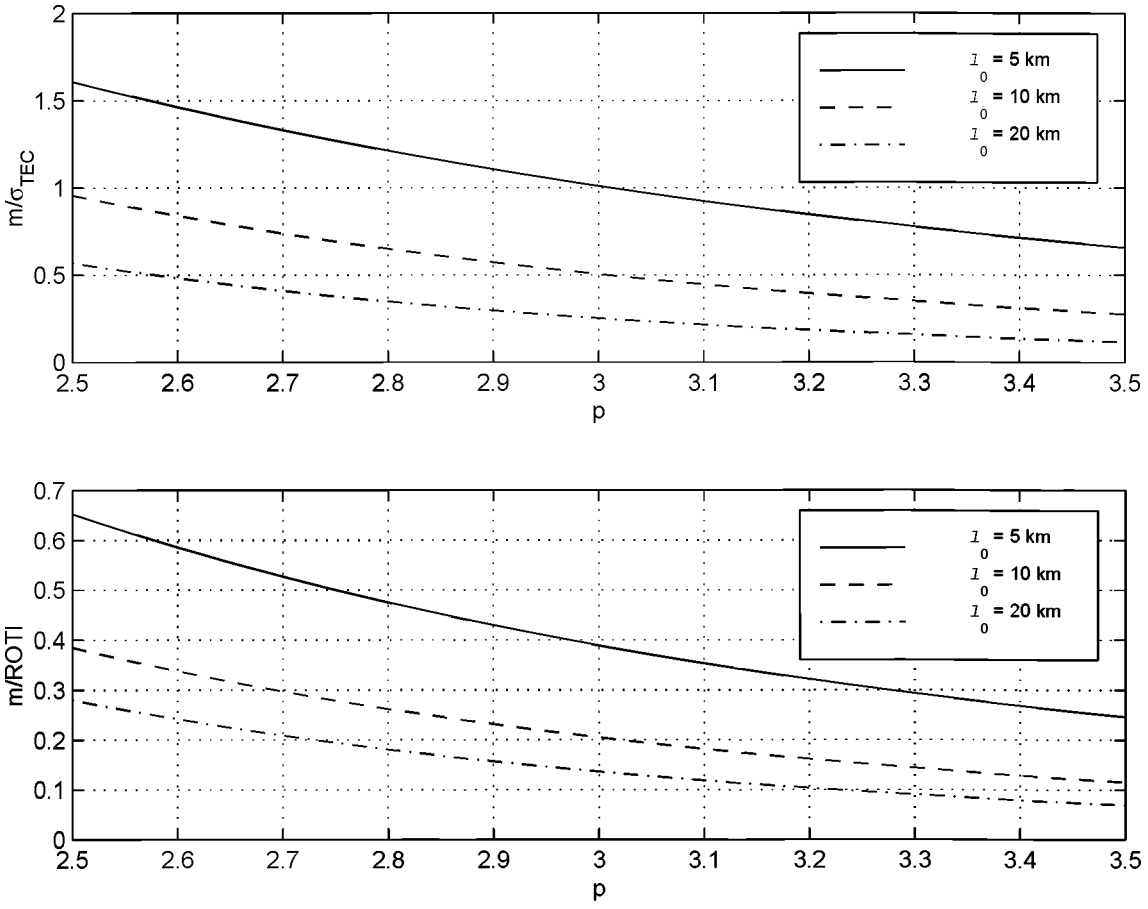

Figure 7.12: Ratios of scintillation index to TEC variance (σ_{TEC}) and rate of TEC index (ROTI) for various outer scale (ℓ_0) and power law index (p) values. These graphs were calculated from the formulas in the text for $r_F = 300$ m. Also, for ROTI, the sampling period used was 30 s with an ionospheric drift of 100 m/s.

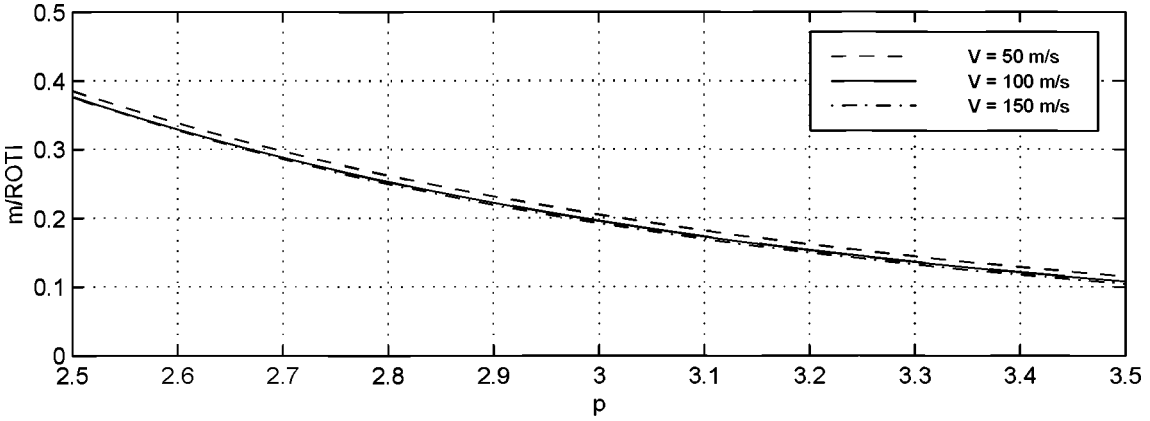

Figure 7.13: Illustration of the insensitivity of m/ROTI versus power law index p to the perpendicular ionospheric drift velocity V. For this graph, the outer scale size $\ell_0 = 10$ km.

100 m/s drift. This value is roughly an order of magnitude smaller than the outer scale cutoff values suggested above.

At the other extreme for the σ_{TEC} calculation, we examine the possibility that the high frequency cutoff imposed by the sampling rate should factor into the model. (Recall that the calculation of ${\sigma_{dS}}^2$ required a cutoff because of the high frequency divergence of its defining integral for $p \leq 3$.) Certainly, the data (Figures 7.3 and 7.4) indicate that changing the sampling period from 1 s to 30 s has little effect on σ_{TEC}. Thus, we already expect the implicit high frequency cutoff to have little influence, at least for this range of sampling rates.

More quantitatively, 30 s sampling corresponds to 6 km scale size at the Nyquist frequency (assuming 100 m/s drift again), a value less than or equal to the range of outer scales suggested above. For a 1 s sampling period, the upper limit of scale sizes sampled is 30 times smaller. Most of the contribution to the integral for ${\sigma_\phi}^2$ is from scale sizes larger than the outer scale (i.e., from the non-power law portion of the phase fluctuation spectrum). So, for sampling periods of roughly 30 seconds or less,

the dominant high frequency cutoff is the one supplied by the outer scale, not the sampling limitations.

In sum, the relatively simple one dimensional, zenith phase screen model we have chosen appears to describe the relationship of the scintillation index m to the variance of TEC (σ_{TEC}) and the rate of TEC index (ROTI). In this model, the most critical parameter affecting the ratios m/σ_{TEC} and m/ROTI is the outer scale of power law applicability and the second most critical parameter is the spectral index p. The modest success of this simple model, at least for weak scattering when the spectrum of irregularities has fully developed into power law form, suggests that more detailed accounting of slanted line of sight geometry (after *Rino* [1979*a*]) may be justified. The *Rino* [1979*a*] results would have to be extended to include the rate of TEC index, however, since that work does not consider such a phase fluctuation measure.

7.6 Discussion and Conclusions

The relationship between weak L1 amplitude scintillations and various measures of total electron content fluctuations from co-located receivers on three nights of the April 1997 campaign at Ancon, Peru has been investigated. Specifically, whenever amplitude scintillations occurred there were accompanying TEC fluctuations. Cases of TEC fluctuations without concurrent amplitude scintillations were noted, however. The asymmetry of this relationship exists because weak amplitude scintillations primarily respond to Fresnel scale ($\sqrt{2}\,r_F$) structures whereas TEC fluctuations encompass a multitude of scale sizes, particularly large scale sizes. In fact, we observe cases of apparent development or decay of short scale length irregularities in which there are TEC fluctuations but very little accompanying amplitude scintillation activity.

Ideally, a better way to relate TEC fluctuations to amplitude scintillations would be to filter the TEC measurements in a narrow band about the Fresnel frequency. Unfortunately, such filtering is not an available option for several reasons. First, the effective relative drift velocity of the ionospheric irregularities with respect to the GPS line of sight is unknown. Neither is the effective distance to the equivalent phase screen known. Both of these problems could theoretically be resolved, however, by allowing the filter bandwidth to be wide enough to accommodate the expected ranges of these parameters (or by using multiple receiver scintillation measurements to estimate the drift speed and the phase screen distance, as in Chapter 5). Another difficulty is that fluctuation strength at the typical Fresnel frequency is quite low, compared to the larger scale sizes. Indeed, fluctuations with periods of 5 seconds or shorter often become lost in the noise level of the dual frequency receiver used at Ancon (see Figure 7.11).

More importantly, the available data rates are not high enough under most circumstances to filter in a window about the Fresnel frequency. Given a typical Fresnel scale size for the GPS L1 frequency of 300–400 m along with 100 m/s ionospheric drift, the dominant period of the scintillations is 3–4 s. Even with velocity matching, when the eastward motion of the line of sight matches the ionospheric drift, capturing the Fresnel scale at 30 seconds per sample is unlikely. The line of sight velocity would have to match the ionosphere's drift to within ± 5–7 m/s to become less than or equal to the Nyquist frequency of 1 min^{-1}. Furthermore, if the line of sight were to follow the irregularities so closely, it is highly doubtful that we would observe "frozen in" irregularities.

Still, the observations demonstrate that TEC fluctuations in 30 second per sample data often follow the scintillation index, provided that the irregularities are well

developed. In particular, ROTI, the root-mean-square deviation of $d\mathrm{TEC}/dt$, seems to follow the scintillation index m well. The quantitative relationship appears to be that $m = 0.3$ ROTI to 0.8 ROTI. The root-mean-square deviation of TEC (σ_{TEC}) follows the scintillation index somewhat less well, and $m \propto \sigma_{\mathrm{TEC}}$ with a proportionality constant that varies from 0.5–1.0.

We have shown that the ratios m/ROTI and m/σ_{TEC} may be estimated from a very simple one dimensional phase screen model and that the model results are in accord with the observations. The model assumes that the phase screen's phase follows a power law spectrum, at least from an outer scale ℓ_0 down to scales smaller than the Fresnel scale. Modeling illustrates the ROTI fluctuation measure's sensitivity to smaller scale sizes, suggesting a theoretical basis for how ROTI often tends to follow the scintillation index more closely than σ_{TEC} (even σ_{TEC} for the high time resolution data). Specifically, ROTI selectively responds to scale sizes nearer to the Fresnel scale, even if the sampling rate is not high enough to include the Fresnel scale. Moreover, the ROTI fluctuation measure performs better at lower sample rates than higher ones because: (1) it tends to amplify high frequency measurement noise, and (2) the defining integral diverges at high frequencies for power law exponents $p \leq 3$, a range of exponents often encountered in equatorial irregularities.

Although ROTI qualitatively follows the scintillation index better than σ_{TEC} does, no other factor seems to recommend one TEC fluctuation measure over the other. For example, both ROTI and σ_{TEC} vary with the outer scale of phase screen irregularities (ℓ_0) and the power law exponent (p), according to the model. Nevertheless, if high rate data were available from IGS, using σ_{TEC} with a detrending cutoff frequency slightly higher than the lowest reasonable Fresnel frequency anticipated might be preferable to ROTI. A high pass detrending filter does not have the extremely sensitive high

frequency response that differentiation does. For the low data rates, however, ROTI may be the more useful measure with respect to estimating scintillation strength, if only for the emphasis of scale sizes nearer to, but still larger than, the Fresnel scale.

Two practical questions remain for future studies. First, is it possible to distinguish scintillating TEC fluctuations from non-scintillating TEC fluctuations given only the low rate data? Second, how well do scintillation strength estimates based on TEC fluctuations translate to receivers at other locations within range? Clearly, the latter involves the issue of slant to vertical TEC conversion. For both questions, some sort of simple irregularity model, with patches of TEC fluctuations identified, their extents estimated and their drift predicted, would be helpful.

Chapter 8

Conclusion

8.1 Summary

We have detailed the design and testing of a new instrument, the Cornell GPS scintillation monitor. The salient feature of this instrument is that it records L1 amplitude measurements at a high data rate (50 samples per second) for up to 12 GPS satellites in view at one time. Alternatively, one channel may be reserved to monitor the ambient noise level in the receiver bandwidth for accurate assessment of the carrier to noise ratio (C/N_0). In addition, the power measurements from the satellites have their sampling tied to the data bit transitions in the received navigation message. Consequently, synchronization of measurements among independent receivers separated by small distances becomes relatively simple, allowing correlation drift measurements to be performed.

The receiver was then employed in several studies of nighttime L band scintillations in equatorial regions during solar minimum. Most of the measurements presented come from Ancon, Peru, a station near the dip equator, during equinox

season. We have verified that the receiver does observe amplitude scintillations associated with equatorial spread F by gross correlation with observations of plumes at the Jicamarca radar and by the consistency of the observed fluctuation time scales with ionospheric drifts and Fresnel scales. Moreover, a comparison of drift measurements between spaced receivers and scintillation fluctuation periods shows that the frequency of fluctuations is proportional to the relative drift speed with a proportionality constant that depends upon the height of the electron density irregularities, as expected for weak scintillations. Beyond verifying receiver operation and logging standard measurements like the scintillation index, several novel applications of the scintillation monitor arise.

First, because several GPS lines of sight through the ionosphere are always available simultaneously, the scintillation monitor is well suited to observe the regional development and distribution of irregularities of scales near the Fresnel scale. While the GPS picture is not nearly so complete as all sky airglow images, GPS is continuously available. We have presented one case of a detailed study of scintillation patch development, motion and decay when airglow and radar measurements were also available. Other researchers have performed similar studies previously for VHF scintillations, but they usually needed chains of ground stations and multiple receivers. What is unique about our study is that the measurements all come from one receiver at one station.

Also, we have observed an unexpected L band propagation phenomenon: cases of apparent edge diffraction from sharp gradients in ionospheric electron density. These diffraction patterns manifest themselves most prominently in the spectrograms of received intensity as V shapes, so we have named them "spectral Vs." Spectral Vs appear to be similar to earlier observations of quasiperiodic scintillations at VHF

frequencies and below and could be generated at altitudes ranging from the E region to the F peak. Observations of edge diffraction patterns at gigahertz frequencies imply that steeper and narrower gradients in electron density exist at times than previously thought. *In situ* measurements of plasma density by the AE-E satellite above the F peak also suggest that gradients sharp enough to form diffraction patterns at the GPS L1 frequency can exist in the depletions associated with equatorial spread F. Notably, observations of diffraction patterns would have been missed if we did not have high sample rate data from the scintillation monitors available.

Finally, an important application of the scintillation monitor is to compare GPS scintillation levels with dual frequency GPS measurements of total electron content (TEC) from another receiver at the same location. The importance of this comparison derives from the existence of global networks of GPS receivers from which low rate TEC measurements can be obtained. Several research groups already study TEC fluctuations using stations in these networks, usually by looking at the rate of change of TEC with respect to time. Questions of great practical concern are whether and how the observed low frequency TEC fluctuations (corresponding to kilometer scale ionospheric structure) relate to L band scintillations (corresponding to irregularities with scale sizes of several hundred meters).

From the simultaneous GPS measurements of scintillation index and TEC fluctuations we have shown examples of their correlation when the spectrum of irregularities is fully developed. We have also shown cases where scintillations are not present at a significant level, although larger scale irregularities exist. The latter cases occur during the development or decay of ionospheric structure. When the irregularities and scintillations are correlated, the TEC fluctuation level and scintillation level are roughly proportional. Specifically, the modulation index $m = 0.3\,\mathrm{ROTI}$ to $0.8\,\mathrm{ROTI}$,

where ROTI is the root-mean-square TEC fluctuation level in TECU/min. The proportionality constant may be estimated from a simple, one dimensional phase screen model if the scintillations are weak, and the model estimates compare favorably with observed values. Lastly, we compared various measures of TEC fluctuation strength and found that the scintillation index followed derivative based measures more closely than other measures (based on variance) for the low sampling rates available in global GPS networks. This advantage undoubtedly stems from the inherent emphasis of smaller scale fluctuations by the process of differentiation.

In sum, equatorial observations using the scintillation monitor illustrate some of the potential of GPS to monitor ionospheric electron density irregularities. As GPS receivers become more prevalent, in more and more critical applications, the ability to characterize the scintillation environment at 1.6 GHz will become increasingly important. Furthermore, many interesting questions undoubtedly remain regarding L band scintillation observations in the equatorial ionosphere. For example, the detection of likely edge diffraction patterns was unexpected. Overall, since the GPS satellites will be available for the indefinite future, it behooves us to take advantage of them.

8.2 Major Results

The research detailed in this dissertation provides the following important results:

1. Technical achievements: development of a successful GPS L1 amplitude scintillation monitor; demonstration of synchronized data collection between spaced receivers.

2. Case study: exploration of ideas of short term, local scintillation predictions

based on activity previously observed to the west.

3. Spectral Vs: demonstration that this phenomenon, of highly probable ionospheric origin, implies the occasional presence of narrow "wall-like" density transitions within a smooth background (estimates: 9 m wide, $\Delta N_e = 1.3 \times 10^{11}$ m^{-3} for E region generation; 16 m wide, $\Delta N_e = 1.2 \times 10^{11}$ m^{-3} for F region).

4. TEC fluctuations: correlation of ROTI (rms deviation of $d\text{TEC}/dt$ expressed in TECU/min) from low rate (30 second per sample) TEC measurements with scintillation index m for developed irregularities; corroboration of simple proportion $m = 0.3\,\text{ROTI}$ to $0.8\,\text{ROTI}$ for weak scintillations using measurements and power law phase screen model.

8.3 Future Directions

Many suggested improvements concern the current state of the scintillation monitor design. As it now stands, the scintillation monitors are glorified prototype units with some residual quirks of operation. First, standalone receivers that can be operated remotely should be developed. Currently, the requirement of periodic operator intervention restricts the siting of the receivers. The receivers also should perform real time data reduction (e.g., computing the scintillation index) to permit remote downloading of data and to reduce the extensive postprocessing burden now incurred. Other "wish list" items include an upgrade to monitor phase scintillations effectively and the development of a receiver with two RF front ends to reduce the amount of hardware needed to conduct drift measurements in the field.

In the category of prospective research projects, many multiple receiver applications recommend themselves. Continental scale studies, such as our work to establish

a regional network across South America, can provide greater insight into the morphology of L band scintillations in the long term. Receivers spaced by hundreds of meters to kilometers can study the decorrelation times of Fresnel scale irregularities and can likely also give insight into their growth and decay time scales.

Specific investigations based on the current research also suggest themselves. The origin of the sharp gradients in electron density which generate spectral Vs should be examined further. The relationship between longer scale TEC fluctuations and scintillations should be investigated on a long term basis for both co-located and separated receivers.

Finally, some applied research programs come to mind. One is to use the scintillation monitor in the field to assess the ability of GPS receivers to maintain lock under scintillation conditions, both for the scintillation monitor itself and by using the scintillation monitor to keep a controlled record of the scintillation environment while other, co-located receivers are tested. Also, scintillation observations could be incorporated into real time predictions of L band scintillations "downstream" from the monitoring station.

Appendix A

Receiver Program Modifications

A.1 Overview

This appendix provides a "tour" of the process of modifying the original Plessey software into the GPS scintillation monitor software (SCINTMON program, Ver. C1.31). It is not intended to be an exhaustive listing of all of the changes to the C source code. Instead, the discussion will highlight some of the more important additions and modifications. The key features of SCINTMON to be documented are: (1) the addition of high data rate power measurements, (2) the treatment of the noise channel, (3) scintillation data logging in FSL (fast scintillation logging) format, and (4) the delayed command processor function.

A.2 Power Measurements

Power measurements have to be collected at the lowest level of receiver operation, the level where the correlations are processed. First, we added storage for power

measurements to the channel control structure chanstruc defined in STRUCTS.H:

```
typedef struct
{
  int channel;                                    /* Channel number. */
  unsigned SV;          /* Current allocated SV, 0=channel is idle. */
  unsigned _SATCNTL;                             /* Register address. */
  unsigned _CARRIER_DCO_INCR_HIGH;               /* Register address. */
  unsigned _CARRIER_DCO_INCR_LOW;                /* Register address. */
  unsigned _CODE_DCO_INCR_HIGH;                  /* Register address. */
  unsigned _CODE_DCO_INCR_LOW;                   /* Register address. */
  unsigned _EPOCH_LOAD;                          /* Register address. */
  unsigned _EPOCH_CHECK;                         /* Register address. */
  unsigned _EPOCH_COUNT;                         /* Register address. */
  unsigned _CODE_PHASE;                          /* Register address. */
  unsigned _CODE_DCO_PHASE;                      /* Register address. */
  unsigned _I_PROMPT;                            /* Register address. */
  unsigned _Q_PROMPT;                            /* Register address. */
  unsigned _I_TRACK;                             /* Register address. */
  unsigned _Q_TRACK;                             /* Register address. */
  unsigned _CARRIER_CYCLE_COUNTER_HIGH;          /* Register address. */
  unsigned _CARRIER_CYCLE_COUNTER_LOW;           /* Register address. */
  unsigned _CARRIER_DCO_PHASE;                   /* Register address. */
  unsigned _ACCUM_RESET;                         /* Register address. */
  unsigned long CARRDCO;   /* Hardware carrier DCO increment * 16. */
  unsigned long CODEDCO;      /* Hardware code DCO increment * 32. */
  unsigned long pCARRDCO;  /* Hardware carrier DCO increment * 16. */
  unsigned long pCODEDCO;     /* Hardware code DCO increment * 32. */
  int CurrDoppBinIndex;/* Index of Doppler bin now being searched. */
  long CodeDoppBin;        /* Code DCO adjustment per Doppler bin. */
  long CarrDoppBin;     /* Carrier DCO adjustment per Doppler bin. */
  long TotalCodeMovement;
                     /* Code srchd in curr Dopp bin, 1/512 chips. */
  unsigned iNXTACCUM;
                   /* Index of next available accumulation entry. */
  unsigned iCURACCUM;
                   /* Index of last accumulation entry processed. */
  unsigned AccumPending;
                   /* How many accums. are pending in the buffer. */
  accumstruc ACCUM[NACCUM];     /* Accumulation data from channel. */
```

```
unsigned _1MS_EPOCH_SLEW;        /* Error in 1-ms epoch counter. */
unsigned _20MS_EPOCH_SLEW;      /* Error in 20-ms epoch counter. */
long EML;                    /* Current Early - Late accumulation. */
unsigned NEML;        /* # samples contained in EML accumulator. */
long EMLOLD;    /* Early - Late accum. at previous filter cycle. */
long IM1;                             /* I, previous millisecond. */
long QM1;                             /* Q, previous millisecond. */
long wdot_c;              /* Carrier frequency dot, carrier loop. */
long phase_error;                /* Carrier phase, carrier loop. */
long avg_phase_change;           /* Carrier phase change per ms. */
long CdLI;                /* Code lock indicator, Av(I**2+Q**2). */
long CrfrLI;                /* Carrier frequency lock indicator. */
unsigned coasting;  /* Remaining # ms to coast before unlocking. */
logical corlk;          /* 1=Correlation lock has been achieved. */
logical carfrlk;  /* 1=Carrier frequency lock has been achieved. */
logical bitlk;                  /* 1=Bit sync has been achieved. */
int BitNumber;                    /* Bit number within subframe. */
logical FrameSync;             /* 1=Frame sync has been achieved */
logical FrameSyncAndTIC;     /* 1=TIC occurred since frame sync. */
logical LostLockDuringLastTIC;  /* 1=lost code or carrier lock . */
logical LostCodeLockDuringLastTIC;          /* 1=lost code lock. */
logical LostCarrierLockDuringLastTIC;    /* 1=lost carrier lock. */
long IPSUM20;         /* Sum of I over current & 19 previous ms. */
long DBINTEG[20];     /* ABS(20-ms I integrals), 1-ms 20 epochs. */
int nDBINTEG;      /* Number of samples in DBINTEG, up to a max. */
int BESTEPOCH;                    /* Index of biggest DBINTEG[]. */
unsigned long BESTSUM;            /* Value of biggest DBINTEG[]. */
unsigned BadDataCntr;
                  /* # data decode errors since last good data. */
unsigned long wordbuff[FRAME_SIZE_PLUS_2];
                                  /* Buffer for 12 GPS words. */
unsigned long codeph;
                /* Code phase, this TIC, units 1/512 of a chip. */
unsigned long old_codeph;
                   /* Code phase, prev TIC, "    "    " "   ".  */
unsigned carrdcophase;
                 /* Carr phase, this TIC, units PI/512 radians. */
unsigned prevcarrdcophase;
                    /* Carr phase, prev TIC, "    "       "   . */
//Ver. C1.20, added below
long ISUM[2][5]; /* Sum of I_Prompt over last two 100 ms epochs. */
```

```
  long QSUM[2][5]; /* Sum of Q_Prompt over last two 100 ms epochs. */
  unsigned long I2PQ2[2][5];
                        /* Sum of I^2+Q^2 over last 100 ms epochs. */
  unsigned int cur100ms;/* Current 100 ms epoch number (modulo 2). */
  unsigned int last20ms;               /* Last 20 ms epoch number. */
  //Ver. C1.30, added below
  int nflag;           /* Flag for channel use as a noise channel. */
} chanstruc;
```

The structure elements added for computing power are `ISUM[2][5]`, `QSUM[2][5]`, `I2PQ2[2][5]`, `cur100ms` and `last20ms` listed near the end. The element `nflag` is used to designate the current channel as a noise channel when set to 1 (`TRUE`). The arrays `ISUM`, `QSUM` and `I2PQ2` store the accumulated sums of correlator output quantities for use in calculating wide band power WBP_k and narrow band power NBP_k (see Chapter 3 for definitions of WBP_k and NBP_k).

The arrays `ISUM`, `QSUM` and `I2PQ2` are used to buffer samples for writing to the FSL file. The first index value specifies the data set to be used. The reason for having two data sets is so that the program can accumulate data in one data set while writing the other. Thus, writing the log file can be asynchronous with the data collection. Each data set contains five samples, specified by the second index and corresponding to sums of correlations over 20 ms intervals (i.e., one GPS navigation message data bit). The value of `cur100ms` indicates which data set is currently being collected (the opposite one should be logged to the file), while `last20ms` indicates which sample within that data set is in the process of being accumulated.

The data are collected by routines in the module `PROCACC.C`. Each active channel runs through the routine `ProcAccum` in that module to read pending accumulations (that were buffered by the fast interrupt driven routine) and update code and carrier lock indicators, close the code tracking loop, etc. Within the function `ProcAccum`

we have inserted the following call to a new routine to collect ISUM, QSUM and I2PQ2 data.

```
//Ver. C1.20, added SNR estimator quantities
//Ver. C1.30, added processing for noise channel
/* Calculate SNR estimator quantities. */
if((CHPTR->coasting == FALSE && CHPTR->FrameSync == TRUE)
      || CHPTR->nflag == TRUE)
   UpdateSNRest(CHPTR, A);
```

The testing in the if statement guarantees that data are collected if the channel is designated as a noise channel. Otherwise, data are collected only if the channel is currently tracking a satellite and the 20 ms epoch counter is synchronized to the GPS subframe boundaries (see Chapter 2).

The UpdateSNRest function accumulates the required sums of the in phase and quadrature correlator outputs, as well as the sums of their squares, into the appropriate array slots:

```
//Ver. C1.20, added function to update SNR estimator quantities
/*****************************************************************
* Function: void UpdateSNRest(register chanstruc _ds *CHPTR,
*                             register accumstruc _ds *A)
*
* Updates the channel SNR estimators.
*
* Input: *CHPTR - parameter block for the channel in question.
*        *A - accumulation data for the channel in question.
*
* Output: *CHPTR - updates to the SNR estimators.
*
* Return Value: None.
*
* Author: Ted Beach, Cornell University, 1996
*****************************************************************/
```

```
void UpdateSNRest(register chanstruc _ds *CHPTR,
  register accumstruc _ds *A)
{
int bitno, set;
long I_Scaled, Q_Scaled, SignBits;

/* Find bit number (bitno) and whether we are on an
   odd 100ms epoch (set==1).  Also, set CHPTR->cur100ms
   if necessary. */
bitno = A->_20ms_epoch % 5;
if (bitno==0 && A->_1ms_epoch==0)
{
   CHPTR->cur100ms = A->_20ms_epoch % 2;
   CHPTR->last20ms = (A->_20ms_epoch + 45) % 50;
}
set = CHPTR->cur100ms;

/* If at the beginning of a bit, clear accumulations. */
if (A->_1ms_epoch == 0)
{
   CHPTR->ISUM[set][bitno] = 0L;
   CHPTR->QSUM[set][bitno] = 0L;
   CHPTR->I2PQ2[set][bitno] = 0UL;
}

/* Scale I and Q prior to squaring. (Extra fiddling is for
   arithmetic shift.) */
SignBits = (A->I_Prompt>=0)?0L:0x8000L;
I_Scaled = ((A->I_Prompt + 1L) >> 1) | SignBits;

SignBits = (A->Q_Prompt>=0)?0L:0x8000L;
Q_Scaled = ((A->Q_Prompt + 1L) >> 1) | SignBits;

/* Accumulate sums (scaled to prevent overflows). */
SignBits = (I_Scaled>=0)?0L:0xE000L;
CHPTR->ISUM[set][bitno] += (I_Scaled + 4L) >> 3;

SignBits = (Q_Scaled>=0)?0L:0xE000L;
CHPTR->QSUM[set][bitno] += (Q_Scaled + 4L) >> 3;

CHPTR->I2PQ2[set][bitno] += ((unsigned long)(I_Scaled*I_Scaled)
```

```
                                + (unsigned long)(Q_Scaled*Q_Scaled)
                                + 32UL) >> 6;
}
```

Note that the `I_Prompt` and `Q_Prompt` samples represent the *sums* of early and late in phase and quadrature accumulations (correlation outputs), respectively.

The arithmetic right shift operations (with rounding) in `UpdateSNRest` accomplish scaling of the sums to prevent overflow. The actual computation of WBP_k and NBP_k from the sums occurs in another routine, the routine which saves the FSL records to disk.

A.3 Noise Channel

The noise channel is a special channel that is deliberately assigned a PRN number to track that does not correspond to any satellite in the current GPS constellation. If the receiver is in the `NOISE_CHANNEL` tracking mode, as determined by the state of the global variable `TrackMode`, the receiver assigns the highest available channel to become and to remain the noise channel. The following added code in the function `UpdateSatelliteAllocation` of the module `ALLOCATE.C` takes care of the assignment;

```
//Ver. C1.30, added NOISE_CHANNEL mode (same as
//     HIGHEST_ELEVATIONS except last channel)
case NOISE_CHANNEL:
    for(i=0;i<ActiveChannels-1;i++)
        assigned[i] = FALSE;
    for(i=0;i<ActiveChannels-1;i++)
    {
        high = 0;
        for(j=0;j<ActiveChannels-1;j++)
```

```
    {
        if(svsel[i] == highest[j])
        {
            if(assigned[j]==TRUE)
                break;                  /* Release duplicates. */
            assigned[j] = TRUE;
            high = 1;
            break;
        }
    }
    if(high==0)
        svsel[i] = 0;
}

for(i=0;i<ActiveChannels-1;i++)
{
    if(svsel[i])
        continue;
    for(j=0;j<ActiveChannels-1;j++)
    {
        if(assigned[j]==TRUE)
            continue;
        svsel[i] = highest[j];
        assigned[j] = TRUE;
        break;
    }
}

for(i=0;i<MAXSATELLITES;i++)
{
   PROTECT++;
   if(alms[i].vflg==2)
   {
      svsel[ActiveChannels-1] = i + 1;
      PROTECT--;
      break;
   }
   else
      PROTECT--;
}
```

```
for(i=0;i<MAXCHANNELS;i++)
{
    if(svsel[i])                          /* Predicted Doppler. */
    {
        SetUpChannel(i,svsel[i],idopp[svsel[i]-1]);
        disable();
        CH[i].nflag = (i==ActiveChannels-1)?TRUE:FALSE;
        enable();
    }
    else                                   /* Idle the channel. */
        SetUpChannel(i,0,0);
}
break;
```

The function `UpdateSatelliteAllocation` is periodically called while the receiver is running. Note that the function ensures that only one channel is designated as a noise channel. There is also a minor addition to the function `SetUpChannel` in `ALLOCATE.C` which guarantees that whenever the `NOISE_CHANNEL` track mode is turned off or the number of channels is changed, the noise channel reverts to an ordinary satellite channel. Note that the module `INIT.C` sets the default tracking mode to `NOISE_CHANNEL`, rather than `HIGHEST_ELEVATION` when the receiver is started.

Several checks of the noise flag (`nflag` in the channel structure) pepper the rest of the `SCINTMON` source code. Many of these changes are cosmetic, e.g., adding the character "N" to the tracking display to indicate the noise channel, but some of them are significant. Probably the most important changes concern preventing the normal Doppler bin search on the noise channel. If the software changes the digitally controlled oscillator (DCO) setting on the noise channel, quasiperiodic transients appear in its power measurements. New `if` statement tests in the modules `BUFFACC.C`, `PROCACC.C` and `TAKEMEAS.C` prevent the update of the DCO on the noise channel. Additional checks in `PROCACC.C` prevent the receiver from declaring code lock or loss

of lock on the noise channel if the channel's correlation power goes above or below the respective power threshold.

The only relevant measurements on the noise channel are the power measurements. No attempt should be made to use quantities like carrier DCO phase, code DCO phase, etc. In particular, since the noise channel does not track any GPS signal, its 1 ms and 20 ms epoch counters are free running. Consequently, when the values of the noise channel 20 ms epoch count are saved to the FSL file, they will not, in general, match the epoch counts of the other channels in the same record.

A.4 FSL Logging

The global variable `ScintillationLogging` controls the state of scintillation logging. It has three possible states, `TRUE`, `FALSE` and `SCINT_WAIT`, where each of the constants is defined in module `DEFINES.H`. If `ScintillationLogging` is `TRUE`, the program logs FSL data records to the stream specified by the global pointer `fpScintLog` with the file name held in `ScintLogFile` (another global variable). If `Scintillationlogging` is `FALSE`, no extra activity occurs. In the third mode, `SCINT_WAIT`, the program waits for a 3D navigation solution to be obtained and for the oscillator error to converge before opening a file, writing an FSL header and setting `ScintillationLogging` to `TRUE`.

The following new functions from the new module `SCINT.C` take care of getting FSL logging started:

```
/*********************************************************************
*
* Function: void ScintLogStart (void)
*
```

```
* Start scintillation logging (open logging file, etc.) only if we
* are navigating and clock model has stabilized. Otherwise, hold off.
*
* Input: None.
*
* Output: None.
*
* Return Value: None.
*
* Author: Ted Beach, Cornell University, 1996
*****************************************************************/
void ScintLogStart(void)
{
fslhdrstruc header;
obsstruc *obs;                    /* Copy of current observation. */
clockmodelstruc CLK;              /* Copy of current clock model. */
navstatestruc N;             /* Copy of current navigation state. */

time_t t;
struct tm *tblock;

static char datestr[21];

int i, gwk, y, m, d, hh, mm;
unsigned long nowTIC, obsTIC;
double gsec, ss;

static double lastRCOrate = 0;

/* Exit if any mode other than SCINT_WAIT */
if (ScintillationLogging != SCINT_WAIT) return;

/* Make local copies of current clock model and navigation state */
PROTECT++;
CLK = CurClkModel;
PROTECT--;

PROTECT++;
N = CurNavState;
PROTECT--;
```

```
/* Exit if not in 3D navigation mode */
if (N.navmode != FIX_3D) return;

/* Exit if clock has not converged to GPS time */
if (fabs(CLK.RCOrate - lastRCOrate) > 5E-10L)
{
   lastRCOrate = CLK.RCOrate;
   return;
}
lastRCOrate = 0;

/* Open scintillation logging file. */
if((fpScintLog = OpenLogFile("FSL","b",ScintLogFile)) == NULL)
{
   ScintillationLogging = FALSE;
   return;
}

/* Get time information for current observation. */
obs = obsbuff + pobs;
obsTIC = obs->obstm;
TICToGpsTime(obs->obstm, &gwk, &gsec);
GpsTimeToGregorianDate(gwk, gsec, &y, &m, &d, &hh, &mm, &ss);

/* Compute value of first TIC of program */
nowTIC = ((unsigned long)(10.0F*gsec+0.5F)) % TICS_IN_DAY;

if (obsTIC > nowTIC)
   FirstTIC = TICS_IN_DAY + (obsTIC - nowTIC);
else
   FirstTIC = nowTIC - obsTIC;

/* Setup header for fast log file */
PROTECT++;
header.FSLversion = FSL_VERSION;

sprintf(header.pgm,"GPSBUILDER %s", CONFIG_CODE);
sprintf(header.run_by,"");

t = time(NULL);
tblock = localtime(&t);
```

```
strftime(datestr,20,"%d-%b-%y %H:%M",tblock);
for(i=3; i<6; i++) datestr[i]=toupper(datestr[i]);
strcpy(header.date, datestr);

strncpy(header.comment,StationCom,60);
strncpy(header.marker_name,StationMrk,60);
strncpy(header.observer,StationObs,20);
strncpy(header.agency,StationAgn,40);

sprintf(header.rec_no,"PLESSEY GP2010/2021");
sprintf(header.rec_type,"SCINT MON");
sprintf(header.rec_vers,"VER C%s",C_VERSION);

strncpy(header.ant_no,StationAnm,20);
strncpy(header.ant_type,StationAty,20);

header.x = CurNavState.x;
header.y = CurNavState.y;
header.z = CurNavState.z;

header.delta_h = 0.0;
header.delta_e = 0.0;
header.delta_n = 0.0;

header.yy = y;
header.mm = m;
header.dd = d;
header.h = hh;
header.m = mm;
header.s = ss;

fwrite(&header, sizeof(header), 1, fpScintLog);

/* Set global variables associated with fast logging */
ScintillationLogging = TRUE;
DontMove = FALSE;
PROTECT--;
}

/*****************************************************************
*
```

```
* Function: FILE *OpenLogFile(char *suffix, char *type, char *f)
*
* Generate a new file name for logging (based on current GPS date and
* station id character), open it for writing and return the file
* pointer and file name.
*
* Input: suffix - up to three character suffix to use for filename.
*        type   - one character file type ('b' - binary or
*                 't' - text);
*
* Output: f     - name of newly opened file.
*
* Return Value: Pointer to open file, or NULL if open failed.
*
* Author: Ted Beach, Cornell University, 1996
*****************************************************************/
FILE *OpenLogFile(char *suffix, char *type, char *f)
{
FILE *logfile;
obsstruc *obs;

char mode[3], fname[13], buff[90];
int gwk, y, m, d, hh, mm;
int ffound, fileno=0;
double gsec, ss;

/* Get current date to construct filename */
obs = obsbuff + pobs;
TICToGpsTime(obs->obstm, &gwk, &gsec);
GpsTimeToGregorianDate(gwk, gsec, &y, &m, &d, &hh, &mm, &ss);

/* Construct filename based on current GPS date and
   station ID character and check whether it exists */
sprintf(mode,"r%1.1s",type);
sprintf(fname,"%02d%02d%02d%1c%1d.%-3.3s", y%100, m, d,
StationId, fileno, suffix);
while((ffound = ((logfile = fopen(fname,mode)) != NULL)) != FALSE
   && fileno < 9)
{
   fclose(logfile);
   fileno++;
```

```
   sprintf(fname,"%02d%02d%02d%1c%1d.%-3.3s", y%100, m,
           d, StationId, fileno, suffix);
}

if (ffound && fileno==9)
{
   sprintf(buff,"Can't open .%-3.3s file: all names used",
                   suffix);
   WarningMessage(buff);
   logfile = NULL;
}
else
{
   sprintf(mode,"w%1.1s",type);
   logfile = fopen(fname, mode);
   if(logfile == NULL)
   {
      sprintf(buff,"Error opening .%-3.3s file",
              suffix);
      WarningMessage(buff);
   }
}

if (logfile != NULL)
{
           setvbuf(logfile,NULL,_IOFBF,256);
           strcpy(f,fname);
}
else
           strcpy(f,"");

return logfile;
}
```

`OpenLogFile` is an automatic file name generation routine that the RINEX logging facilities have also been upgraded to use. It opens a file of the name *YYMMDDSN* with the specified suffix, where *YY* is the year, *MM* is the month, *DD* is the day, *S* is the station ID character from the global variable `StationId` (set by the user), and *N*

is a sequence number (0–9).

The FSL header structure, `fslhdrstruc`, is an addition to module `STRUCTS.H`. To save space, the definition of `fslhdrstruc` is not listed here, but it may be found in Appendix B as part of the program fragment for reading FSL files. Many of the items that go into the FSL header are global variables which can also be used in the RINEX header. Several of them (`StationCom`, `StationMrk`, `StationObs`, `StationAgn`, `StationAnm` and `StationAty`) have been added in the revision of its software from its original form. These variables are set by new commands in the module `CMD.C`.

The actual data logging takes place in the module `NAV.C`, which is essentially called for every TIC (measurement interrupt at 0.1 s intervals). The structure of the modification is rather convoluted, as will be revealed shortly, because two different cases must be accommodated. If the current TIC is one at which the navigation solution is computed (every 100th TIC if `ScintillationLogging` is `TRUE`, every 10th TIC otherwise), the receiver software automatically computes pseudoranges and these may be incorporated into the FSL file directly. At all other TICs, the FSL logging routine must compute the pseudoranges for itself.

Here is the modified version of the routine `Navigate` from the module `NAV.C` which incorporates fast scintillation logging:

```
/*********************************************************************
* Function: void Navigate(obsstruc *obs)
*
* Attempts to produce a navigation fix or updates the integrated
* carrier phase data using the current observation block.
*
* Input: obs - pointer to the observation block to be processed.
*
* Output: None.
```

```
*
* Return Value: None.
*
* Modified:  T. L. Beach, Cornell University, 1996
*****************************************************************/
//Ver. C1.00, added scintillation logging option every TIC
void Navigate(obsstruc *obs)
{
    //Ver. C1.20, changed to nav solution only every 10 seconds
    //            to reduce processor loading.
    /* Only do a full solution every 100th TIC else just update the
       integrated carrier phase data or do scintillation log */

    if((ScintillationLogging==TRUE && obs->obstm%100==0) ||
       (ScintillationLogging!=TRUE && obs->obstm%10==0))
    {
    //Ver. C1.20, added call to ScintLogStart
       if (ScintillationLogging == SCINT_WAIT) ScintLogStart();
    //Ver. C1.00, has to have its own scintillation logging for 10th
    //  TICs (see GetNavDataFull)
       NavigateFull(obs);
    }
    else
    {
       if (ScintillationLogging == TRUE)
          GetNavDataScintLog(obs);
       else
          GetNavDataICP(obs);
    }
}
```

Scintillation data logging appears in two places, `GetNavDataFull` and also in `GetNavDataScintLog`. `GetNavDataScintLog` is a new routine and is listed below (the definition of `fslsatstruc` appears in Appendix B):

```
//Ver. C1.00, new function for fast data logging
/*****************************************************************
*
* Function: void GetNavDataScintLog(obsstruc *obs)
```

```
*
* Logs current observation to fast (scintillation) logging file
* and also does ICP update.
*
* Input: obs - pointer to the observation block to be processed.
*
* Output: None.
*
* Return Value: None.
*
* Author: Ted Beach, Cornell University, 1996
**********************************************************************/
void GetNavDataScintLog(obsstruc *obs)
{
//Ver. C1.20, added sizeUC
size_t sizeUC, sizeUL, sizeRecord;  /* Sizes of data blocks saved. */

//Ver. C1.20, added checksum variable
unsigned char chksum = 0;
                       /* Checksum to be attached to time/SV tag. */

//Ver. C1.20, added int variables below
int set;            /* Index used for correlator samples (0 or 1). */
int sample;                              /* SNR sample number (0-4). */

int channel;                                     /* Channel number. */
int satellite;                             /* Satellite being used. */
int gps_week;                                /* At the observation. */

/* The following variable indicates if this satellite has been
   used in the current solution already. This is to stop
   redundant data being used when the same satellite is being
   tracked on more than one channel. */

int used_this_SV[MAXSATELLITES];

unsigned long svcurrent; /* Bitmap of satellites used in solution. */
unsigned long timeTIC;           /* Holder for TIC of observation. */

double code_minus_icp;             /* Code minus icp pseudo-range. */
double code_time;            /* Code time of the pseudo-range (s). */
```

```
double carrier_dco_freq;            /* Carrier DCO frequency (Hz). */
double gps_second;                          /* At the observation. */

pseudostruc pseudo;                /* Holds the pseudo-range data. */
static fslsatstruc record[MAXCHANNELS];      /* Satellite records. */
static fslsatstruc *index[MAXSATELLITES];
        /* Indices of satellite records for ordering by SV number. */

//Ver. C1.10, added checkpoint
Checkpoint("GetNavDataSL",1);

/* Check for missed observations which would mean that the
   integrated carrier phase data are not continuous. */

if(MissedObservations()) return;

/* First do some initialization. */
svcurrent = 0;

// Ver. C1.20, modified timeTIC
timeTIC = SYNC_MSB | ((obs->obstm + FirstTIC) % TICS_IN_DAY);

sizeUC = sizeof(unsigned char);  //Ver. C1.20, added
sizeUL = sizeof(unsigned long);
sizeRecord = sizeof(fslsatstruc);

for(satellite=0;satellite<MAXSATELLITES;satellite++)
   used_this_SV[satellite] = FALSE;

for(satellite=0;satellite<MAXSATELLITES;satellite++)
   index[satellite] = NULL;

//Ver. C1.30, added noise channel record below
if (TrackMode==NOISE_CHANNEL)
{
   timeTIC |= 0x80000000UL;
   channel = ActiveChannels-1;
   record[channel].pseudorange = 0.0;
   record[channel].range_rate = 0.0;
   record[channel].int_carrier_phase = 0.0;
   record[channel].epoch = 0U;
```

```
   record[channel].flags = 0U;

   /* Add correlator power entry. */
   /* 100 ms sample set to use is opposite of current one. */
   set = CH[channel].cur100ms ? 0 : 1;

   for (sample=0;sample<5;sample++)
   {
      long I = CH[channel].ISUM[set][sample];
      long Q = CH[channel].QSUM[set][sample];

      record[channel].NBPk[sample] = (unsigned int)
         ((unsigned long)((I*I)/SNR_SAMPLES +
         (Q*Q)/SNR_SAMPLES) >> 7);
      record[channel].WBPk[sample] = (unsigned int)
         (CH[channel].I2PQ2[set][sample] >> 7);
    }
}

/* Compile records for each channel in a loop. */
for(channel=0; channel<ActiveChannels; channel++)
{
   if(obs->obspresent[channel]==YES)
   {
      satellite = obs->sv[channel];

      if(used_this_SV[satellite]==FALSE)
      {
         used_this_SV[satellite] = TRUE;

         /* Discard satellites without ephemeris data. */

         if(ephs[satellite-1].vflg==0)
            continue;

         /* Discard satellites with bad health codes. */

         if(ephs[satellite-1].s1hlth)
            continue;

         /* Discard satellites below the elevation mask except
```

```
   when in Cold Start. */

if(ielvd[satellite-1] < ElvMask)
   if(TrackMode != COLD_START)
      continue;

/* Add carrier phase entry. */
/* Get the code time for the measurement block and make
   it modulo 1 second. */

code_time = 20.0*(obs->epoch_count[channel]>>8)
            +(obs->epoch_count[channel]&0x1F)
            +(obs->code_phase[channel])/2046.0
            +(obs->code_dco_phase[channel])/
            (2046.0*1024.0) - 0.2443792766E-3;
code_time /= 1000.0;          /* Convert from ms to s. */
if(code_time<0.0)
   code_time += 1.0;
code_time = fmod(code_time,1.0);

UpdateICP(obs->LostLockDuringLastTIC[channel],
          obs,channel,code_time,&code_minus_icp,
          &pseudo.icp_range);
record[channel].int_carrier_phase =
                        ICP.Beat_Phase[channel];

/* Add pseudorange entry. */
/* The observed code time is modulo 1 second.  Compute
   the pseudorange by assuming that the current GPS time
   estimate is accurate to 1/2 second or better. */

TICToGpsTime(obs->obstm,&gps_week,&gps_second);

pseudo.range = fmod(gps_second,1.0) - code_time;
if(pseudo.range > 0.5)
   pseudo.range -= 1.0;
else if(pseudo.range < -0.5)
   pseudo.range += 1.0;

pseudo.range = pseudo.range*SPEED_OF_LIGHT;
```

```
record[channel].pseudorange = pseudo.range;

/* Add range_rate entry. */

carrier_dco_freq = -(obs->carrdco[channel]/
   CARRIER_DCO_SCALE - NOMINAL_CARRIER_DCO)*
   CARRIER_DCO_RESOLUTION;

pseudo.range_rate = -SPEED_OF_LIGHT*carrier_dco_freq/L1;

record[channel].range_rate = pseudo.range_rate;

//Ver. C1.20, modified to use I, Q and I2PQ2 samples
/* Add correlator power entry. */
/* 100 ms sample set to use is opposite of current one. */
set = CH[channel].cur100ms ? 0 : 1;

for (sample=0;sample<5;sample++)
{
   long I = CH[channel].ISUM[set][sample];
   long Q = CH[channel].QSUM[set][sample];

   record[channel].NBPk[sample] = (unsigned int)
         ((unsigned long)((I*I)/SNR_SAMPLES +
         (Q*Q)/SNR_SAMPLES) >> 7);
   record[channel].WBPk[sample] = (unsigned int)
         (CH[channel].I2PQ2[set][sample] >> 7);
}

record[channel].epoch = CH[channel].last20ms;

/* Add flag entries. */
record[channel].flags = 0U;

if (obs->LostLockDuringLastTIC[channel])
   record[channel].flags |= 0x04U;

if (obs->LostCodeLockDuringLastTIC[channel])
   record[channel].flags |= 0x02U;

if (obs->LostCarrierLockDuringLastTIC[channel])
```

```
            record[channel].flags |= 0x01U;

         /* Mark this SV in the SV used bitmap and set
            pointer for this satellite record. */

         //Ver. C1.30, changed bit positions in svcurrent
         svcurrent |= (1UL<< (satellite-1));
         index[satellite-1] = &record[channel];
      }                                  /* Satellite used already. */
   }                                    /* Observation not present. */
}                                                 /* Channel count. */

/* Emit data record to logging stream. */

/* Header information first. */
fwrite(&timeTIC, sizeUL, 1, fpScintLog);
fwrite(&svcurrent, sizeUL, 1, fpScintLog);

//Ver. C1.20, added CRC generation and saving
CRCgen(timeTIC, svcurrent, &chksum);
fwrite(&chksum, sizeUC, 1, fpScintLog);

//Ver. C1.30, added noise channel record
if (TrackMode==NOISE_CHANNEL)
{
   channel = ActiveChannels-1;
   Checksum(&record[channel]);
   fwrite(&record[channel], sizeRecord, 1, fpScintLog);
}

/* Individual satellite records next. */
for (satellite=0; satellite < MAXSATELLITES; satellite++)
   if (index[satellite] != NULL)
   {
      //Ver. C1.20, added checksum
      Checksum(index[satellite]);
      fwrite(index[satellite], sizeRecord, 1, fpScintLog);
    }

//Ver. C1.10, added checkpoint
Checkpoint("GetNavDataSL",2);
```

```
}
```

The functions `CRCgen` and `Checksum` are part of the new module `SCINT.C` and are almost identical to the checksum checking routines listed in Appendix B for the FSL reading program.

The code to perform scintillation logging in the function `GetNavDataFull` is substantially the same as that of `GetNavDataScintLog` and so is not shown. The only difference between the two logging routines is that `GetNavDataFull` already computes its own pseudoranges. Also, `GetNavDataScintLog` must update integrated carrier phase values itself since it replaces the call to `GetNavDataICP`.

Why is scintillation logging split into two separate pieces? The answer lies in arcane revision history: early ultraconservative programming concerns over the timing overhead of added subroutine calls and simple inertia.

A.5 Delayed Commands

The delayed command function allows for a very rudimentary form of automation: the execution of any receiver command at a particular time, especially those to start and stop data logging. This function exemplifies the use of the original software's built in multitasking system.

The task `TDelayed` is added to the module `RTEXEC.C` in place of the RTCM (differential GPS) task originally provided:

```
/* Real-time executive functions are collected together in this
   module. */

extern void TBeep(void);       /* Beeper management task */
extern void TDisplay(void);    /* Display update task */
```

```
//Ver. C1.20, added TDelayed task
extern void TDelayed(void);   /* Delayed command task. */
extern void TProcSbf(void);   /* Process subframes task */
//Ver. C1.00, removed RTCM task

/*****************************************************************
* Task definitions.  The context that exists when the program begins
*  executing becomes the lowest priority task, which must have the
*  task name "MAIN".  Since the list is in priority order, MAIN is
*  always at the end of the list.
*****************************************************************/

//Ver. C1.00, removed RTCM task from list
//Ver. C1.20, added TDelayed task to list
tcbstruc TCB[] =
{
    {"TBeep",2000,TBeep,NULL}, /* Beep task (mostly a case study). */
    {"TDisplay",10000,TDisplay,NULL},      /* Display update task. */
    {"TDelayed",2000,TDelayed,NULL},      /* Delayed command task. */
    {"TProcSbf",4000,TProcSbf,NULL},    /* Process subframes task. */
    {"MAIN",0,NULL,NULL}               /* MAIN must be at the end. */
};
```

The new module DELAY.C contains the TDelay task as well as some routines to add and remove commands to and from the queue.

```
//Ver. 1.20, added module
//Ver. 1.30, put log file closing and re-opening here,
//           rather than in NAV.C
#include "includes.h"

#define MAXCMDS 4          /* Maximum number of commands in queue. */

typedef struct                         /* Define a delayed command. */
{
    unsigned long ExeTIC;           /* TIC number on which to run. */
    char command[80];                          /* Command to run. */
} CmdEntry;

CmdEntry CmdQ[MAXCMDS];                         /* Command queue. */
```

```
volatile unsigned NInCQ;
                    /* Number of items currently in command queue. */
/*****************************************************************
* Function: void TDelayed(void)
*
* Execute a delayed command request.
*
* Input: None.
*
* Output: None.
*
* Return Value: None.
*
* Author: Ted Beach, Cornell University, 1996
*****************************************************************/
void TDelayed(void)
{
   char delayed_cmd[80];
   char buff[16];
   unsigned long NowTIC, RunTIC;
   //Ver. C1.30, added below
   unsigned long FSLCloseTIC=0;

   /* Do forever: examine request queue, execute any commands that
      are due, then go to sleep for a while. */
   while(TRUE)
   {
      /* Display number of commands in queue. */
      Checkpoint("TDelayed",1);
      sprintf(buff,"%3d CMD(S)",NInCQ);
      TCBComment(buff);

      /* Get current TIC. */
      CurrentTIC(&NowTIC);

      Checkpoint("TDelayed",2);
      if(NInCQ>0)
      {
         /* Indivisibly access command queue. */
         PROTECT++;
         RunTIC = CmdQ[NInCQ-1].ExeTIC;
```

```
      strncpy(delayed_cmd,CmdQ[NInCQ-1].command,80);
      PROTECT--;

      /* Compare current TIC to run time. */
      if (NowTIC>RunTIC)
      {
         /* Make truncated command for task display. */
         strncpy(buff,delayed_cmd,15);
         TCBComment(buff);

         /* Set current command line to stored command. */
         cmdmode = DISPLAY;
         ClearToEndOfLine(1,25);
         strncpy(cb,delayed_cmd,80);
         cbready = TRUE;

         /* Remove command from queue. */
         NInCQ--;
      }
   }

   /* If on task display (DisplayFunc==DISPLAY_F9), print a
      list of the pending commands. */
   Checkpoint("TDelayed",3);
   if (DisplayFunc==DISPLAY_F9)
   {
      int i, j, gwk, hh, mm, y, m, d;
      double gsec, ss;

      OutputString(3,18-MAXCMDS,"DELAYED COMMAND QUEUE:");
      for(i=0;i<MAXCMDS;i++)
         OutputString(3,18-i,
                      "                                          ");
      if(NInCQ==0) OutputString(3,19-MAXCMDS,"<empty>");

      for(i=NInCQ-1,j=0;i>=0;i--,j++)
      {
         PROTECT++;
         RunTIC = CmdQ[i].ExeTIC;
         strncpy(buff,CmdQ[i].command,15);
         PROTECT--;
```

```
            TICToGpsTime(RunTIC,&gwk,&gsec);
            GpsTimeToGregorianDate(gwk,gsec,&y,&m,&d,&hh,&mm,&ss);
            sprintf(delayed_cmd,"[%1d] %2.2d%2.2d%2.2d "
                    "%2d:%2.2d:%2.2d %15.15s",j,y%100,m,d,hh,
                    mm,(int)ss,buff);
            OutputString(3,19-MAXCMDS+j,delayed_cmd);
         }
      }

      //Ver. C1.30, added closing and re-opening of FSL file to flush
      //            buffer to disk.
      /* Check whether it is time to close the log file to minimize
         data loss in the event of a power failure. */
      if (ScintillationLogging==TRUE)
      {
         fflush(fpScintLog);

         /* Close file every 2 hours. */
         if (NowTIC>FSLCloseTIC)
         {
            FSLCloseTIC = NowTIC + 72000UL;  //Next time is in
                                             //2 hours.
            PROTECT++;
            fclose(fpScintLog);
            if ((fpScintLog = fopen(ScintLogFile,"a+b")) == NULL)
               ScintillationLogging = FALSE;
            PROTECT--;
         }
      }

      /* Suspend for 2 sec (20 TICS) while awaiting command
         requests. */
      Checkpoint("TDelayed",4);
      Suspend(20);
   }
}   /* Note: GPS Builder tasks must never attempt to terminate.  */

/*********************************************************************
* Function: void Delayed(unsigned hh, unsigned mm, char *c)
*
```

```
* This is TDelayed's enqueuing routine.  The application task calls
* it with a specified time to start a delayed command and the delayed
* command string.  After the request is enqueued, we return to the
* caller.
*
* Input: hh        - GPS hour to start command
*        mm        - GPS minute to start command
*        c         - pointer to command string
*
* Output: None.
*
* Return Value: None.
*
* Author: Ted Beach, Cornell University, 1996
**********************************************************************/
void Delayed(int hh, int mm, char *c)
{
   int gwk, i, j;
   unsigned int inserted = FALSE;
   unsigned long curTIC, dayTIC, startTIC, runTIC;
   double gsec;

   /* Ignore requests in excess of the queue capacity. */
   if (NInCQ >= MAXCMDS)
   {
      WarningMessage("Delayed command buffer full "
                     "(command not entered).");
      return;
   }

   /* Check whether requested hour and minute are valid. */
   if (hh<0 || hh>23)
   {
      WarningMessage("Command start hour must be 0-23.");
      return;
   }

   if (mm<0 || mm>59)
   {
      WarningMessage("Command start minute must be 0-59.");
      return;
```

```
}

/* Compute starting TIC (within day) from hour and minute. */
startTIC = (((unsigned long)hh * 60UL)+(unsigned long)mm) * 600UL;

/* Get time of current TIC (within day). */
CurrentTIC(&curTIC);
TICToGpsTime(curTIC, &gwk, &gsec);
dayTIC = ((unsigned long)(10*gsec+0.5)) % TICS_IN_DAY;

/* Compute TIC to start delayed command.  Add in (and later
   subtract) TICS_IN_DAY to avoid problems with negative
   numbers. */
runTIC = curTIC + TICS_IN_DAY - dayTIC;      /* Next midnight. */
if (dayTIC>startTIC)
   runTIC += TICS_IN_DAY + startTIC;
else
   runTIC += startTIC;
runTIC -= TICS_IN_DAY;

/* Add command to delayed command queue.  If there are already
   other commands in the queue, ensure that the new command is
   filed among them in time sequence order (earliest at top). */

/* Find first time that is earlier or equal to requested
   time and insert new request into queue at this point. */
PROTECT++;
for(i=0;i<NInCQ;i++)
{
   if (CmdQ[i].ExeTIC<=runTIC)
   {
      inserted = TRUE;
      for (j=NInCQ;j>i;j--)
         CmdQ[j] = CmdQ[j-1];

      CmdQ[i].ExeTIC = runTIC;
      strncpy(CmdQ[i].command,c,80);
      NInCQ++;
      break;
   }
}
```

```
   /* If not inserted into queue, new request is earliest time
      in queue; therefore, put command at the top. */
   if(inserted==FALSE)
   {
      CmdQ[NInCQ].ExeTIC = runTIC;
      strncpy(CmdQ[NInCQ].command,c,80);
      NInCQ++;
   }
   PROTECT--;

   /* Let the queue server have a look at the new queue. */
   Activate("TDelayed");
   return;
}

/*********************************************************************
* Function: void DequeueCommand(int ll)
*
* This is the dequeuing routine for TDelayed.  Dequeues a command
* from the delayed command queue.
*
* Input: ll       - level of command to dequeue (0 is nearest to
*                   execution).  Level is reverse of order in queue.
*
* Output: None.
*
* Return Value: None.
*
* Author: Ted Beach, Cornell University, 1996
*********************************************************************/
void DequeueCommand(int ll)
{
   int i, N=(int)NInCQ, j=(int)NInCQ-ll-1;

   if(ll<0 || ll>(N-1))
   {
      WarningMessage("Invalid command number to dequeue.");
      return;
   }
```

```
   PROTECT++;
   for (i=j;i<N-1;i++)
      CmdQ[i]=CmdQ[i+1];
   NInCQ--;
   PROTECT--;

   Activate("TDelayed");
   return;
}
```

Finally, the delayed command queue is controlled by the user through the new DX ("Delayed eXecute") and DQ ("De-Queue") commands in module `CMD.C`:

```
   //Ver. C1.20, added DX command
   /* DX hh:mm cmd - Delayed eXecution.
      Execute cmd at time hh:mm. */

   if(cc1=='D' && cc2=='X')
   {
      int hh, mm, i, j;

      i = 2;
      j = 0;
      while(TRUE)
      {
         buff[j] = cb[i];
         i++;
         j++;
         if(cb[i-1] == ':') break;
         if(i>78 || cb[i-1]=='\0')
         {
            WarningMessage("Format not DX hh:mm command");
            return;
         }
      }
      buff[j-1]='\0';
      hh = atoi(buff);

      j=0;
```

```
   while(TRUE)
   {
      buff[j] = cb[i];
      i++;
      j++;
      if(cb[i-1] == ' ') break;
      if(i>78 || cb[i-1]=='\0')
      {
         WarningMessage("Format not DX hh:mm command");
         return;
      }
   }
   buff[j-1] = '\0';
   mm = atoi(buff);

   Delayed(hh,mm,&cb[i]);
   return;
}



//Ver. C1.20, added DQ command
/* DQ n - DeQueue command.
   Remove command n from the delayed command queue. */
if(cc1=='D' && cc2=='Q')
{
   int n = atoi(&cb[2]);
   DequeueCommand(n);
   return;
}
```

Appendix B

Reading FSL Files

B.1 Description

This appendix lists fragments of a C program used to read fast scintillation logging (FSL) files. The program fragments constitute an operational definition of the FSL format. These routines, as written, only work on PC compatible computers due to byte order considerations and possible variations in the number of bytes used for certain data types on other platforms. Nevertheless, they should provide guidance in reading the FSL file format on other platforms.

B.2 Usage

Ideally, the list of definitions, type definitions and function prototypes should go into a header file to foster good program organization. The main program skeleton declares the variables needed to use the given subroutines. It also shows a simple example of how to sequentially scan through an FSL file but does not illustrate

how to pick out the desired data (pseudorange, wide band power samples, etc.). In addition to the data reading routine `ReadFSLRecord` (and its attendant routines `CRCcheck` and `ChecksumCheck`), the listing includes a simple error message printing routine (`PrintStatus`) and a subroutine (`PrintHeader`) to print the FSL file header information in a format similar to the RINEX observation file header.

After opening the file, FSL reading programs should read the header immediately using the `fread` function as shown. The header gives three main types of information useful to data analysis: the version of the FSL format used (currently set to 0), the ECEF coordinates of the receiver from the navigation solution and the starting time of the observations. The starting time, when converted to TICs (0.1 second intervals) past midnight should match the TIC of the first data record in the file. This condition is not stringently enforced in the current format, however, so programs should check and make appropriate corrections if the header TIC does not match the TIC in the first data record.

The heart of the program is the `while` loop incorporating the `ReadFSLRecord` routine. This routine automatically accounts for the variable length record structure of the FSL format, verifies checksums and returns the data from all available channels (including the noise channel) in arrays. The return `numsats` gives the number of satellites in the record or `ERROR` if there was an error in reading the record. If an error occurred, the parameter `status` will contain the error code (see `PrintStatus` for a description of the codes). The parameter `obstic` returns the TIC value for the current record, which is restricted to range from 0 to 863,999. Finally, `satmarkers` gives a simplified list of satellites in the file for quick and easy comparisons. The list is encoded in a 32 bit word so that if bit 0 is set to 1, the record contains PRN 1; if bit 1 is set, the record contains PRN 2; etc.

The data are returned in `PRNEntries` and `NoiseEntry`. (If no noise channel data are present, the address of `NoiseEntry` points to `NULL`.) The data for channel `i` are in `PRNEntries[i]`, where $0 \leq$ `i` $\leq$ `numsats-1`, and `PRNTable[i]` contains the PRN number assigned to channel `i`. The data in channel `i` may be accessed as elements of `fslsatstruc`. For example to access the loss of lock flags for channel `i`, use `PRNEntries[i].flags`. To access entry `j` of wide band power, where $0 \leq$ `j` ≤ 4, use `PRNEntries[i].WBPk[j]`. Note that only the wide band power and narrow band power entries are well defined in the `NoiseChannel` structure.

The skeleton, as given, does not account for cases where the value of the `epoch` element does not increment by 5 (modulo 50) from one sample to the next, as mentioned in Chapter 3. Generally speaking, in this case, the wide band and narrow band power samples repeat their previous set of values and the repeated values should be discarded to leave a data gap. Also, for synchronization between receivers, adjusting the current TIC number to conform to the epoch count is desirable; i.e., the TIC number should equal 0 (modulo 10) when the epoch count is 0. Again, this refinement is not illustrated.

Finally, several improvements on the search algorithm could be made, as suggested in the Chapter 3 text. The given program fragment merely scans through the FSL file records sequentially. The straightforward, albeit slow, approach is then to process data in a record only when desired time and PRN number conditions are met. A more sophisticated search algorithm might implement some form of quasi-random access. Also, the program should have more "graceful" recovery in the event of media errors or checksum errors. As written, the reading program simply exits with an error message in these instances.

B.3 Listing

```
/*********************************************************************
* Program fragment to read FSL files (FSL version 0).
*
* By:  Ted Beach, Cornell University, 1996-8
*********************************************************************/

/* List of standard libraries to include. */ #include <stdio.h>
#include <stdlib.h>

/* List of definitions. */
#define FSL_VERSION 0     //FSL version number.
#define MAXSATELLITES 32  //Maximum number of satellites allowed.
#define MAXCHANNELS 12    //Maximum number of channels per record.

#define SYNC_MASK 0x00FFFFFFUL //Mask to get TIC without sync byte.
#define SYNC_MSB 0x57000000UL  //Sync byte is 0x57 in MSB of TIC.

#define FLAG_MASK 0x00FF  //Mask to get flags without CRC checksum.

/* List of error codes for ReadFSLRecord. */
#define ERROR -1
#define OK 0
#define TIME_UNREAD 1
#define MARKERS_UNREAD 2
#define CRC_UNREAD 3
#define ENTRY_UNREAD 4
#define CRC_INVALID 5
#define CHECKSUM_INVALID 6
#define SYNC_LOST 7

/* Set up special structures for data read from files. */
/* Header information for scintillation log file. */
typedef struct {
   int FSLversion;                        /* FSL version number. */
   char pgm[21];                        /* Program name for RINEX. */
   char run_by[21];                   /* Run by listing for RINEX. */
   char date[21];                           /* Date for RINEX. */
   char comment[61];                      /* Comment for RINEX. */
   char marker_name[61];                /* Marker Name for RINEX. */
```

```
   char observer[21];              /* Observer listing for RINEX. */
   char agency[21];                  /* Agency listing for RINEX. */
   char rec_no[21];                 /* Receiver number for RINEX. */
   char rec_type[21];                /* Receiver type for RINEX. */
   char rec_vers[21];              /* Receiver version for RINEX. */
   char ant_no[21];                  /* Antenna number for RINEX. */
   char ant_type[21];                 /* Antenna type for RINEX. */
   double x;                            /* X-position for RINEX. */
   double y;                            /* Y-position for RINEX. */
   double z;                            /* Z-position for RINEX. */
   float delta_h;                    /* Antenna height for RINEX. */
   float delta_e;                     /* Antenna east for RINEX. */
   float delta_n;                    /* Antenna north for RINEX. */
   int yy;                           /* Starting year for RINEX. */
   int mm;                          /* Starting month for RINEX. */
   int dd;                            /* Starting day for RINEX. */
   int h;                           /* Starting hour for RINEX. */
   int m;                         /* Starting minute for RINEX. */
   double s;                      /* Starting second for RINEX. */
} fslhdrstruc;

/* Satellite entry in scintillation log file. */
typedef struct {
   double pseudorange;                          /* Pseudorange (m). */
   double range_rate;                    /* Pseudorange rate (m/s). */
   double int_carrier_phase;      /* Carrier beat phase (cycles). */
   unsigned int NBPk[5];   /* Correlator based narrow band power. */
   unsigned int WBPk[5];     /* Correlator based wide band power. */
   unsigned int epoch;     /* Time of first SNR estimator sample. */
   unsigned int flags;    /* Checksum and flags: e.g., lost lock. */
} fslsatstruc;

/* Abbreviations to simplify use of unsigned types. */
typedef unsigned char uchar;
typedef unsigned int uint;
typedef unsigned long ulong;

/* Function prototypes. */
/*********************************************************************
* I/O routines.
*********************************************************************/
```

```
int ReadFSLRecord(int *status, FILE *infile, ulong *obstic,
                  ulong *satmarkers, uint PRNTable[],
                  fslsatstruc PRNEntries[],
                  fslsatstruc *NoiseEntry);
int CRCcheck(ulong t, ulong s, uchar crc);
int ChecksumCheck(fslsatstruc *rec);
void PrintStatus(int s);
void PrintHeader(fslhdrstruc Hdr);

/*****************************************************Main Program*/
int main(void) {
   FILE *infile;

   fslhdrstruc Hdr;
   fslsatstruc *PRNEntries;
   fslsatstruc NoiseEntry;

   uint *PRNTable;

   int numsats, status;

   ulong obstic;
   ulong recordnumber=1;
   ulong satmarkers;


   /* Allocate space for arrays. */
   PRNEntries = (fslsatstruc *) calloc(MAXCHANNELS,
                sizeof(fslsatstruc));
   PRNTable = (uint *) calloc(MAXCHANNELS, sizeof(uint));


   /*************************************************************
    * Open file here with fopen command and mode "rb".  Assign
    * the stream to the pointer infile...
    *************************************************************/


   /* Read FSL header. */
   if (!fread(&Hdr,sizeof(fslhdrstruc),1,infile)) {
      puts("\n***Error! Could not read FSL data header.");
```

```
      exit(1);
   }
   if (Hdr.FSLversion != FSL_VERSION) {
      puts("\n***Error! Incompatible FSL version.");
      printf("Program FSL version: %d.  File version is %d.\n",
             FSL_VERSION, Hdr.FSLversion);
      exit(1);
   }

   /* Read in entries for each TIC. */
   while (!feof(infile)) {
      if ((numsats=ReadFSLRecord(&status,infile,&obstic,&satmarkers,
          PRNTable,PRNEntries,&NoiseEntry))==ERROR) {

         printf("\n***Error reading input file at record %lu!\n",
                recordnumber);
         PrintStatus(status);
         break;
      }
      if (feof(infile)) break;
      recordnumber++;


      /*********************************************************
       *Data processing goes here...
       *********************************************************/


   }


   /*********************************************************
    * Close stream infile here with fclose command...
    *********************************************************/


}

/*********************************************************Subroutines*/
/*****************************************************************
* I/O routines.
```

```
*****************************************************************/
/* Read in an FSL record. */
int ReadFSLRecord(int *status, FILE *infile, ulong *obstic,
                  ulong *satmarkers, uint *PRNTable,
                  fslsatstruc *PRNEntries,
                  fslsatstruc *NoiseEntry) {

   uchar chksum, numsats;
   int i, nflag;

   /* Read in time TIC. */
   if (!fread(obstic,sizeof(ulong),1,infile)) {
      if (feof(infile)) {
         *status = EOF;
         return 0;
      } else {
         *status = TIME_UNREAD;
         return ERROR;
      }
   }

   /* Check for synchronization byte. */
   if ((*obstic & 0x7F000000UL) != SYNC_MSB) {
      *status = SYNC_LOST;
      return ERROR;
   }

   /* Read in satellite markers. */
   if (!fread(satmarkers,sizeof(ulong),1,infile)) {
      *status = MARKERS_UNREAD;
      return ERROR;
   }

   /* Read in Cyclic Redundancy Checksum (CRC) for record header. */
   if (!fread(&chksum,sizeof(uchar),1,infile)) {
      *status = CRC_UNREAD;
      return ERROR;
   }

   /* Verify CRC for record header. */
   if (!CRCcheck(*obstic,*satmarkers,chksum)) {
```

```
   *status = CRC_INVALID;
   return ERROR;
}

/* Extract noise channel flag and TIC number. */
nflag = ((*obstic & 0x80000000UL) == 0x80000000UL);
*obstic &= SYNC_MASK;

/* Count up satellites in record and mark PRNTable. */
numsats=0;
for (i=0;i<MAXSATELLITES;i++) {
   if ((*satmarkers >> i) & 0x00000001UL) {
      PRNTable[numsats]=i+1;
      numsats++;
   }
}

/* Read noise channel entry (if present). */
if (nflag==1) {
   if (fread(NoiseEntry,sizeof(fslsatstruc),1,infile)!=1) {
      *status = ENTRY_UNREAD;
      return ERROR;
   }
   if (!ChecksumCheck(NoiseEntry)) {
      *status = CHECKSUM_INVALID;
      return ERROR;
   }
   NoiseEntry->flags &= FLAG_MASK;
} else {
   NoiseEntry = NULL;
}

/* Read satellite entries into table. */
if (fread(PRNEntries,sizeof(fslsatstruc),numsats,infile)
    != numsats) {
   *status = ENTRY_UNREAD;
   return ERROR;
}

for (i=0;i<numsats;i++) {
   if (!ChecksumCheck(&PRNEntries[i])) {
```

```
         *status = CHECKSUM_INVALID;
         return ERROR;
      }
      PRNEntries[i].flags &= FLAG_MASK;
   }

   *status = OK;
  return numsats;
}

/*****************************************************************/
/* Check CRC checksum of header block. */
int CRCcheck(ulong t, ulong s, uchar crc) {
   static union {
      struct {
         ulong sf;
         ulong tm;
      } hdr;
      uchar byte[8];
   } bytes;

   static const uchar CRCMASK = 0x1D;
   uchar check, data;
   int i, j;

   bytes.hdr.tm = t;
   bytes.hdr.sf = s;

   check = bytes.byte[7];

   for (i=7;i>=0;i--) {
      if (i>0)
         data = bytes.byte[i-1];
      else
         data = crc;

      for (j=0;j<8;j++) {
         if (check & 0x80)
            check = ((check << 1) | ((data & 0x80) == 0x80))
                    ^ CRCMASK;
         else
```

```
            check = (check << 1) | ((data & 0x80) == 0x80);
         data <<= 1;
      }
   }
   return (check == 0);
}

/*****************************************************************/
/* Verify checksum of satellite record. */
int ChecksumCheck(fslsatstruc *rec) {
   #define NUM_BYTES 48              /* no. bytes in fslsatstruc. */

   static union {
      fslsatstruc sat;
      uchar byte[NUM_BYTES];
   } data;

   uchar chk = 0;
   int i;

   data.sat = *rec;

   /* Generate simple checksum (relies on PC byte order:
      low->high). */
   for (i=0;i<(NUM_BYTES-1);i++)
      chk = (uchar)((chk + data.byte[i]) % 256);

   /* Compare checksum to high byte of flags. */
   return (chk == data.byte[NUM_BYTES-1]);
}

/*****************************************************************/
/* Print status after FSL file reading error. */
void PrintStatus(int s) {
   if (s==TIME_UNREAD) puts("Failed to read time word.");
   if (s==MARKERS_UNREAD) puts("Failed to read satellite markers.");
   if (s==CRC_UNREAD) puts("Failed to read record header CRC.");
   if (s==ENTRY_UNREAD) puts("Failed to read a satellite entry.");
   if (s==CRC_INVALID) puts("Invalid CRC for record header.");
   if (s==CHECKSUM_INVALID) puts("Invalid checksum for satellite "
                                 "entry.");
```

```
   if (s==SYNC_LOST) puts("Sync word not found in record header.");
   return;
}

/*****************************************************************/
/* Print header information in RINEX format. */
void PrintHeader(fslhdrstruc Hdr) {
   puts("\nRINEX-Type Header Information:\n");
   printf("%-20.20s%-20.20s%-20.20sPGM / RUN BY / DATE\n",
   Hdr.pgm, Hdr.run_by, Hdr.date);
   printf("%-60.60sCOMMENT\n", Hdr.comment);
   printf("%-60.60sMARKER NAME\n", Hdr.marker_name);
   printf("%-20.20s%-40.40sOBSERVER / AGENCY\n",
   Hdr.observer, Hdr.agency);
   printf("%-20.20s%-20.20s%-20.20sREC # / TYPE / VERS\n",
   Hdr.rec_no, Hdr.rec_type, Hdr.rec_vers);
   printf("%-20.20s%-20.20s                    ANT # / TYPE\n",
   Hdr.ant_no, Hdr.ant_type);
   printf("%14.4f%14.4f%14.4f                  "
          "APPROX POSITION XYZ\n", Hdr.x, Hdr.y, Hdr.z);
   printf("%14.4f%14.4f%14.4f                  "
          "ANTENNA:DELTA H/E/N\n", Hdr.delta_h, Hdr.delta_e,
          Hdr.delta_n);
   printf("%6d%6d%6d%6d%6d%12.6f               "
          "   TIME OF FIRST OBS\n", Hdr.yy, Hdr.mm, Hdr.dd,
          Hdr.h, Hdr.m, Hdr.s);
   printf("\n");

   return;
}
```

Appendix C

Phase Screen Program

C.1 Description

This appendix lists the MATLAB program which propagates a complex wave field emerging from a phase screen to the observation plane a distance z away. It is a very straightforward implementation of the one dimensional propagation formula of Chapter 4 by the Fourier transform technique. For reference, the propagation formula is

$$\mathcal{A}(x,z) = \frac{1}{r_F}\int dx'\ \mathcal{A}^+(x')\exp\left[i\pi\left(\frac{x-x'}{r_F}\right)^2\right], \tag{C.1}$$

where $r_F = \sqrt{\lambda z}$ is the Fresnel radius (λ is the radio wavelength), x is the horizontal distance across the screen, $\mathcal{A}^+(x)$ is the complex amplitude of the scalar wave field just as it emerges from the screen and $\mathcal{A}(x,z)$ is the complex amplitude across the observation plane.

C.2 Usage

All vectors of complex amplitude data to be used should be powers of two in length. Amplitude vectors may be either row vectors or column vectors. If the vector of phase values across the screen is `phi`, the input vector `b = exp(i*phi)`. Note that this program can propagate waves from amplitude changing screens as well. For example, to generate a classical knife edge diffraction pattern, set the elements of `b` to 0 on the shadow side and to 1 on the other side. Since `a` represents the amplitude values across the observation plane, the intensity pattern is `abs(a).^2`.

All that this program does is to transform the propagation equation into Fourier space, where the convolution integral becomes a product. After evaluating the product, the result is transformed back into regular space. The vector `w` in the program represents the Fourier transform of the Gaussian kernel of the scattering integral. The only "tricky" aspect of the program is the manipulation of the index vector `j` to ensure that its last half actually corresponds to the negative frequency values that frequencies above the Nyquist frequency represent.

Given that the program uses discrete, rather than continuous, Fourier transforms to calculate the convolution, the results are only approximate. Although the accuracy of the approximation in some cases is impressive [*Beach and Lovelace*, 1997], one must exercise great care not to misapply the simulation. The following general guidelines apply. Always keep in mind that the discrete Fourier transform implicitly assumes that the phase screen is periodic. For example, the suggestion given above to calculate diffraction from a knife edge yields an unintended side effect: a second knife edge diffraction pattern where the end of the screen "wraps around" to meet the beginning. Consequently, screens should be made wide enough to separate features of interest

in the center of the screen from the edges by several Fresnel radii (depending on the width of the diffraction pattern and how well the edge values match up on either side). Diffraction patterns from truly periodic screens, such as the sinusoidal phase screen, are computed accurately if an integer number of periods fit on the screen. Screens should also be made as wide as possible to give adequate frequency resolution if intensity power spectra are to be studied.

C.3 Listing

```
function a=propagate(b,rfmod)
%function a=propagate(b,rfmod)
%
%Propagate a wave through space in the longitudinal direction
%(small scattering angle model).
%
%Notes: (1) Vectors should be of size 2^n.
%       (2) All distances are expressed in grid spacings.
%       (3) Works for either row or column vectors; output is
%           same dimension as input.
%
%Inputs:
%[vector] b - input complex amplitudes in x (position) space
%[scalar] rfmod - modified Fresnel radius=sqrt(z)*wavelength
%
%Output:
%[vector] a - output complex amplitudes in x (position) space
%
%By: Ted Beach, Cornell University, 1996

%Set up parameters
sz = size(b);
n = max(sz);
nz = n/2+1;
rg = rfmod*rfmod/(n*n);

%Indices of vectors in "shifted" format
```

```
j1 = 0:n-1;
j2 = n:-1:1;
j = j2;
j(1:nz) = j1(1:nz);

%Make propagator
w = reshape(exp(i*pi*(0.25-rg*j.^2)), sz);

%Propagate wave to observation plane
a = ifft(w.*fft(b));
```

Appendix D

Photos of Author

Per the request of the chair of the author's special committee, these images are recorded for future reference.

Bibliography

Aarons, J., Global morphology of ionospheric scintillations, *Proc. IEEE*, *70*, 360, 1982.

Aarons, J., The longitudinal morphology of equatorial *F*-layer irregularities relevant to their occurrence, *Space Science Reviews*, *63*, 209, 1993.

Aarons, J., Global positioning system phase fluctuations at auroral latitudes, *J. Geophys. Res.*, *102*, 17,219, 1997.

Aarons, J., M. Mendillo, and R. Yantosca, GPS phase fluctuations in the equatorial region during sunspot minimum, *Radio Sci.*, *32*, 1535, 1997.

Aarons, J., M. Mendillo, R. Yantosca, and E. Kudeki, GPS phase fluctuations in the equatorial region during the MISETA 1994 campaign, *J. Geophys. Res.*, *101*, 26,851, 1996.

Aarons, J., J. P. Mullen, H. E. Whitney, and E. M. MacKenzie, The dynamics of equatorial irregularity patch formation, motion, and decay, *J. Geophys. Res.*, *85*, 139, 1980.

Abramowitz, M., and I. A. Stegun, *Handbook of Mathematical Functions*, Dover, Mineola, N.Y., 1972.

Basu, S., and S. Basu, Ionospheric Structures and Scintillation Spectra, in V. I. Tatarskii, A. Ishimaru and V. U. Zavorotny (eds.), *Wave Propagation in Random*

Media (Scintillation), pp. 139–155, SPIE–The International Society for Optical Engineering, Bellingham, Wash. and Institute of Physics Publishing, Philadelphia (copublishers), 1993.

Basu, S., S. Basu, R. Eastes, R. E. Huffman, R. E. Daniell, P. K. Chaturvedi, C. E. Valladares, and R. C. Livingston, Remote sensing of auroral *E* region plasma structures by radio, radar, and UV techniques at solar minimum, *J. Geophys. Res.*, *98*, 1589, 1993.

Basu, S., S. Basu, J. LaBelle, E. Kudeki, B. G. Fejer, M. C. Kelley, H. E. Whitney, and A. Bushby, Gigahertz scintillations and spaced receiver drift measurements during project Condor equatorial *F* region rocket campaign in Peru, *J. Geophys. Res.*, *91*, 5526, 1986.

Basu, S., and A. Das Gupta, Scintillations of satellite signals by ionospheric irregularities with sharp boundary, *J. Geophys. Res.*, *74*, 1294, 1969.

Basu, S., E. Kudeki, S. Basu, C. E. Valladares, E. J. Weber, H. P. Zengingonul, S. Bhattacharya, R. Sheenan, J. W. Meriwether, H. A. Biondi, H. Kuenzler, and J. Espinoza, Scintillations, plasma drifts, and neutral winds in the equatorial ionosphere after sunset, *J. Geophys. Res.*, *101*, 26,795, 1996.

Basu, S., E. MacKenzie, and S. Basu, Ionospheric constraints on VHF/UHF communications links during solar maximum and minimum periods, *Radio Sci.*, *23*, 363, 1988.

Basu, S., J. P. McClure, S. Basu, W. B. Hanson, and J. Aarons, Coordinated study of equatorial scintillations and in situ and radar observations of nighttime *F* region irregularities, *J. Geophys. Res.*, *85*, 5119, 1980.

Beach, T. L., and R. V. E. Lovelace, Diffraction by a sinusoidal phase screen, *Radio Sci.*, *32*, 913, 1997.

Biondi, M. A., and J. W. Meriwether, Measured equatorial thermospheric winds and temperatures during the severe geomagnetic storm of 11 April 1997, poster presented at 1997 Fall Meeting, AGU, San Francisco, December 8–12, 1997.

Bishop, G., S. Basu, E. Holland, and J. Secan, Impacts of ionospheric fading on GPS navigation integrity, in *Proceedings of ION GPS-94*, p. 577, The Institute of Navigation, Arlington, VA, September, 1994.

Booker, H. G., J. A. Ferguson, and H. O. Vats, Comparison between the extended-medium and the phase-screen scintillation theories, *J. Atmos. Terr. Phys.*, *47*, 381, 1985.

Booker, H. G., J. A. Ratcliffe, and D. H. Shinn, Diffraction from an irregular screen with applications to ionospheric problems, *Phil. Trans. R. Soc. London A*, *242*, 579, 1950.

Born, M., and E. Wolf, *Principles of Optics (5th ed.)*, Pergamon Press, Oxford, England, 1975.

Bramley, E. N., The accuracy of computing ionospheric radio-wave scintillation by the thin-phase-screen approximation, *J. Atmos. Terr. Phys.*, *39*, 367, 1977.

Briggs, B. H., and I. A. Parkin, On the variation of radio star and satellite scintillations with zenith angle, *J. Atmos. Terr. Phys.*, *25*, 339, 1963.

Briggs, B. H., G. J. Phillips, and D. H. Shinn, The analysis of observations on spaced receivers of the fading of radio signals, *Proc. Phys. Soc. London B*, *63*, 106, 1950.

Buckley, R., Diffraction by a random phase-changing screen: A numerical experiment, *J. Atmos. Terr. Phys.*, *37*, 1431, 1975.

Cahn, C. R., D. K. Leimer, C. L. Marsh, F. J. Huntowski, and G. D. Larue, Software implementation of a PN spread spectrum receiver to accommodate dynamics, *IEEE Trans. Comm.*, *COM-25*, 832, 1977.

Coker, C., R. Hunsucker, and G. Lott, Detection of auroral activity using GPS satellites, *Geophys. Res. Lett.*, *22*, 3259, 1995.

Cordes, J. M., A. Pidwerbetsky, and R. V. E. Lovelace, Refractive and diffractive scattering in the interstellar medium, *Astrophys. J.*, *310*, 737, 1986.

Costa, E. O., and M. C. Kelley, Calculations of equatorial scintillations at VHF and gigahertz frequencies based on a new model of the disturbed equatorial ionosphere, *Geophys. Res. Lett.*, *3*, 677, 1976.

Davies, K., and J. D. Whitehead, A radio lens in the ionosphere, *J. Atmos. Terr. Phys.*, *39*, 383, 1977.

Doherty, P. H., E. Raffi, J. A. Klobuchar, and M. B. El-Arini, Statistics of time rate of change of ionospheric electron content, in *Proceedings of the International Beacon Satellite Symposium*, p. 33, University of Wales, Aberystwyth, UK, July 11-15, 1994.

Evans, J. V., Satellite beacon contributions to studies of the structure of the ionosphere, *Rev. Geophys. Space Phys.*, *15*, 325, 1977.

Fowles, G. R., *Introduction to Modern Optics (2nd ed.)*, Dover, Mineola, N.Y., 1989.

Franke, S. J., C. H. Liu, and J. P. McClure, Interpretation and modeling of quasiperiodic diffraction patterns observed in equatorial VHF scintillation due to plasma bubbles, *J. Geophys. Res.*, *89*, 10,891, 1984.

Fremouw, E. J., R. L. Leadabrand, R. C. Livingston, M. D. Cousins, C. L. Rino, B. C. Fair, and R. A. Long, Early results from the DNA Wideand satellite experiment — Complex-signal scintillation, *Radio Sci.*, *13*, 167, 1977.

Gradshteyn, I. S., and I. M. Ryzhik, *Table of Integrals, Series, and Products (5th ed.)*, Academic Press, San Diego, 1994.

Hajkowicz, L. A., Radio transmissions from two satellites as a possible cause of

quasiperiodic scintillations in amplitude recordings, *J. Atmos. Terr. Phys.*, *36*, 1689, 1974.

Hajkowicz, L. A., Morphological and ionospheric aspects of quasiperiodic scintillations, *J. Atmos. Terr. Phys.*, *39*, 833, 1977.

Hanson, W. B., D. R. Zuccaro, C. R. Lippincott, and S. Sanatani, The retarding-potential analyzer on Atmosphere Explorer, *Radio Sci.*, *8*, 333, 1973.

Hewish, A., The diffraction of radio waves in passing through a phase-changing ionosphere, *Proc. R. Soc. London A*, *209*, 81, 1951.

Hewish, A., A user's guide to scintillation, *J. Atmos. Terr. Phys.*, *51*, 743, 1989.

Hofmann-Wellenhof, B., H. Lichtenegger, and J. Collins, *Global Positioning System: Theory and Practice (3rd ed.)*, Springer-Verlag, Wien, Austria, 1994.

Huff, D., *How to Lie with Statistics*, Norton, New York, 1954.

Ireland, W., and G. F. Preddey, Regular fading of satellite transmissions, *J. Atmos. Terr. Phys.*, *29*, 137, 1967.

Kelleher, R. F., and P. Martin, Fresnel-type fading on satellite records at low latitudes, *J. Atmos. Terr. Phys.*, *37*, 1109, 1975.

Kelley, M. C., *The Earth's Ionosphere: Plasma Physics and Electrodynamics*, Academic Press, San Diego, Calif., 1989.

Kelley, M. C., D. Kotsikopoulos, T. Beach, D. Hysell, and S. Musman, Simultaneous Global Positioning System and radar observations of equatorial spread F at Kwajalein, *J. Geophys. Res.*, *101*, 2333, 1996.

Klobuchar, J. A., S. Basu, Q. Hua, and A. J. Van Dierendonck, A versatile amplitude and phase scintillation monitor using a GPS commercial single frequency C/A code receiver, in *Proceedings of the International Beacon Satellite Symposium*, p. 250, University of Wales, Aberystwyth, UK, July 11-15, 1994.

Lovelace, R. V. E., *Theory and Analysis of Interplanetary Scintillations*, Ph.D. thesis, Cornell University, Ithaca, New York, 1970.

Mannucci, A. J., B. D. Wilson, and C. D. Edwards, A new method for monitoring the earth's ionospheric total electron content using the GPS global network, in *Proceedings of ION GPS-93*, p. 1323, The Institute of Navigation, Arlington, VA, September, 1993.

Mejias, P. M., Fresnel approximation applicability to ultrasonic diffraction, *Appl. Opt.*, *19*(2), 263, 1980.

Mercier, R. P., Diffraction by a screen causing large random phase fluctuations, *Proc. Camb. Phil. Soc.*, *58*, 382, 1962.

Musman, S., J.-M. Jahn, J. LaBelle, and W. E. Swartz, Imaging spread-*F* structures using GPS observations at Alcântara, Brazil, *Geophys. Res. Lett.*, *24*, 1703, 1997.

Parkinson, B. W., Introduction and Heritage of NAVSTAR, in B. W. Parkinson and J. J. Spilker (eds.), *Global Positioning System: Theory and Applications*, Vol. I, pp. 3–28, AIAA, Washington, DC, 1996.

Pi, X., A. J. Mannucci, U. J. Lindqwister, and C. M. Ho, Monitoring of global ionospheric irregularities using the worldwide GPS network, *Geophys. Res. Lett.*, *24*, 2283, 1997.

Pidwerbetsky, A. P., *Simulation and Analysis of Wave Propagation through Random Media*, Ph.D. thesis, Cornell University, Ithaca, New York, 1988.

Plessey, *Global Positioning: Products Handbook*, GEC Plessey Semiconductors, Publication No. HB4305, 1996.

Press, W. H., B. P. Flannery, S. A. Teukolsky, and W. T. Vetterling, *Numerical Recipes in C (2nd ed.)*, Cambridge University Press, Cambridge, 1992.

Rino, C. L., A power law phase screen model for ionospheric scintillation: 1. Weak

scatter, *Radio Sci.*, *14*, 1135, 1979*a*.

Rino, C. L., A power law phase screen model for ionospheric scintillation: 2. Strong scatter, *Radio Sci.*, *14*, 1147, 1979*b*.

Rino, C. L., and E. J. Fremouw, The angle dependence of singly scattered wavefields, *J. Atmos. Terr. Phys.*, *39*, 859, 1977.

Rino, C. L., and J. Owen, The time structure of transionospheric radio wave scintillation, *Radio Sci.*, *15*, 479, 1980.

Rino, C. L., and J. Owen, Numerical simulations of intensity scintillation using the power law phase screen model, *Radio Sci.*, *19*, 891, 1984.

Rufenach, C. L., Power-law wavenumber spectrum deduced from ionospheric scintillation observations, *J. Geophys. Res.*, *77*, 4761, 1972.

Rufenach, C. L., Ionospheric scintillation by a random phase screen: Spectral approach, *Radio Sci.*, *10*, 155, 1975.

Ryder, L. H., *Quantum Field Theory*, Cambridge University Press, Cambridge, 1985.

Salpeter, E. E., Interplanetary scintillations, I, theory, *Astrophys. J.*, *147*, 433, 1967.

Schaer, S., M. Rothacher, and G. Beutler, Global ionospheric maps based on GPS carrier phase data from the IGS network produced by the CODE analysis center, paper presented at 1996 Spring Meeting, AGU, Baltimore, May 20–24, 1996.

Slack, F. F., Quasiperiodic scintillations in the ionosphere, *J. Atmos. Terr. Phys.*, *34*, 927, 1972.

Snow, R. W., P. Romanowski, P. H. Doherty, and J. A. Klobuchar, A comparison of ionospheric total electron content measurements with code and codeless GPS receivers, in *Proceedings of the International Beacon Satellite Symposium*, p. 17, University of Wales, Aberystwyth, UK, July 11-15, 1994.

Spilker, J. J., GPS Navigation Data, in B. W. Parkinson and J. J. Spilker (eds.),

Global Positioning System: Theory and Applications, Vol. I, pp. 121–176, AIAA, Washington, DC, 1996*a*.

Spilker, J. J., GPS Signal Structure and Theoretical Performance, in B. W. Parkinson and J. J. Spilker (eds.), *Global Positioning System: Theory and Applications*, Vol. I, pp. 57–119, AIAA, Washington, DC, 1996*b*.

Tatarskii, V. I., *The Effects of the Turbulent Atmosphere on Wave Propagation*, Israel Program for Scientific Translations, Jerusalem, 1971.

Uscinski, B. J., Multi-Phase-screen Analysis, in V. I. Tatarskii, A. Ishimaru and V. U. Zavorotny (eds.), *Wave Propagation in Random Media (Scintillation)*, pp. 346–357, SPIE–The International Society for Optical Engineering, Bellingham, Wash. and Institute of Physics Publishing, Philadelphia (copublishers), 1993.

Van Dierendonck, A. J., GPS Receivers, in B. W. Parkinson and J. J. Spilker (eds.), *Global Positioning System: Theory and Applications*, Vol. I, pp. 329–407, AIAA, Washington, DC, 1996.

Van Dierendonck, A. J., J. Klobuchar, and Q. Hua, Ionospheric scintillation monitoring using commercial single frequency C/A code receivers, in *Proceedings of ION GPS-93*, p. 1333, The Institute of Navigation, Arlington, VA, September, 1993.

Vladimer, J. A., M. C. Lee, P. H. Doherty, D. T. Decker, and D. N. Anderson, Comparisons of TOPEX and Global Positioning System total electron content measurements at equatorial anomaly latitudes, *Radio Sci.*, *32*, 2209, 1997.

Wanninger, L., Ionospheric monitoring using IGS data, paper presented at the 1993 Berne Workshop, Int. GPS Serv. for Geodyn., Berne, March 25–26, 1993.

Wanninger, L., E. Sardón, and R. Warnant, Determination of the total ionospheric electron content with GPS—Difficulties and their solution, in *Proceedings of the International Beacon Satellite Symposium*, p. 13, University of Wales, Aberystwyth,

UK, July 11-15, 1994.

Weber, E. J., S. Basu, T. W. Bullett, C. Valladares, G. Bishop, K. Groves, H. Kuenzler, P. Ning, P. J. Sultan, R. E. Sheenan, and J. Araya, Equatorial plasma depletions signatures and onset observed at 11° south of the magnetic equator, *J. Geophys. Res.*, *101*, 26,829, 1996.

Wernik, A. W., C. H. Liu, and K. C. Yeh, Model computations of radio wave scintillation caused by equatorial ionospheric bubbles, *Radio Sci.*, *15*, 559, 1980.

Woodman, R. F., and C. La Hoz, Radar observations of *F* region equatorial irregularities, *J. Geophys. Res.*, *81*, 5447, 1976.

Yeh, K. C., and C. H. Liu, Radio wave scintillations in the ionosphere, *Proc. IEEE*, *70*, 324, 1982.